Heat Transfer in Helically Coiled Small Diameter Tubes for Miniature Cooling Systems

By

Ahmed Mohamed Elsayed
MSc., BSc. (Mechanical Engineering)

Thesis Submitted in Partial Fulfilment of Requirements for the Degree of Doctor of Philosophy

The School of Mechanical Engineering
University of Birmingham
Edgbaston, Birmingham, B15 2TT

SEPTEMBER 2011

UNIVERSITY OF
BIRMINGHAM

University of Birmingham Research Archive

e-theses repository

Abstract

This thesis describes experimental and theoretical investigation on the use of small diameter helically coiled tubes for the evaporator of miniature refrigeration systems. A detailed review of past experimental and theoretical work on boiling heat transfer inside helically coiled tubes is presented. As most of past work was conducted on helical coils with tube diameters larger than 6 mm, a brief review of the flow boiling heat transfer process inside straight tubes with small diameters of less than 3 mm is also presented.

An experimental facility was constructed and instrumented to investigate the flow boiling of refrigerant R134a in helically coiled tubes with diameters ranging from 2.8 mm to 1.1 mm and coil diameter ranging from 30 mm to 60 mm. The experimental results showed that decreasing the tube diameter increases the boiling heat transfer coefficient by up to 58% while decreasing the coil diameter increased the boiling heat transfer coefficients more significantly by up to 130% before dryout. Dimensional analysis using Pi theorem and Artificial Neural Network (ANN) techniques were used to develop correlations to predict the flow boiling heat transfer coefficients inside helically coiled tubes. The ANN method produced a better prediction of the experimental results with ±30%.

The experimental facility was equipped with a reciprocating compressor and a manual expansion device and instrumented to assess the performance of miniature vapour compression refrigeration system. A mathematical model of this miniature system was developed, validated and then used to optimise the system performance in terms of the geometry of the helical coils used in the evaporator and condenser. It was shown that the smaller the coil diameter, the better the performance of cooling system. For the same evaporator length, the larger the tube diameter, the larger surface area and better COP. Smaller tube diameters showed better performance at lower area ratios. However, smaller tube diameters showed lower performance at high area ratios due to the large pressure drop caused by smaller tubes in case of using high area ratios.

Finally, the addition of AL_2O_3 nanoparticles to pure water was investigated using computational fluid dynamics technique (CFD) in terms of heat transfer and pressure drop of single phase laminar and turbulent fluid flow in both straight and helically coiled tubes. The tested AL_2O_3 nanofluid in helical coils produced up to 350% increase in the heat transfer coefficient of the laminar flow compared to pure water in straight tubes for the same flow conditions. However, insignificant enhancement of the heat transfer was obtained in the turbulent flow regime. Also, the use of high AL_2O_3 nanofluid concentration of above 2% was found to produce significant pressure drop penalty factor of 5 times that of pure water in straight tubes.

Acknowledgment

Thanks to Allah; the lord of the universe and all that exists; for his guidance, blessing and helping me to complete my thesis.

I submit my highest appreciation to **Dr. Raya Al-Dadah** for her help in applying for the project, continuous support, scientific discussions and reviewing both the thesis and scientific papers. I am deeply indebted to her continuous supervision, original ideas and guidance.

My gratefulness directed to **Dr. Saad Mahmoud** for his various invaluable suggestions and reviewing the published research papers. Many thanks are also to **Dr. Michael Ward** for accepting co-supervision on the current project.

I would like also to express my thanks to **Simon Rowan**, the best technician I have ever met, for his help in constructing the test facility and helping in solving the technical problems. I would like also to express my deep and special appreciation to all staff members of the school of Mechanical Engineering, University of Birmingham who have supported me and to my colleagues who offered all the help I needed. Finally, Thanks to the **ORSAS** organization for giving me the chance to study in UK.

Ahmed Mohamed Elsayed
September 2011

Publications

1. Ahmed Elsayed ; R K Al-Dadah; Saad Mahmoud; Ahmed Rezk. Experimental and Theoretical Investigation of Small Scale Cooling System Equipped with Helically Coiled Evaporator and Condenser. IMechE Journal Part C. Accepted manuscript.

2. A. Elsayed, R. Al-Dadah, S. Mahmoud and L. Soo (2010). Experimental investigation of heat transfer in flow boiling inside a helically coiled small diameter tube. *Microfluidic 2010 Toulouse, France.*

3. Ahmed M. Elsayed, Raya K. Al-Dadah, Saad Mahmoud, Abdel Fattah Mahrous (2011). Numerical investigation of heat transfer through helically coiled tubes using nanofluids.*UK-China Particle Technology Forum III, UK.*

4. A. Elsayed , R. Al-Dadah , Saad Mahmoud, A. Rezk (2011). Prediction of flow boiling heat transfer in helically coiled tubes using neural network. *The 23 IIR International Congress of Refrigeration*, Czech Republic.

5. Ahmed M. Elsayed, Raya K. Al-Dadah, Saad Mahmoud, Abdel Fattah Mahrous(2011). Numerical Investigation of laminar flow heat transfer through helically coiled tubes using Al_2O3 Nanofluid. *3rd Micro and Nano Flows Conference MNF 2011, Greece.*

6. Ahmed M. Elsayed, Raya K. Al-Dadah, Saad Mahmoud, Abdel Fattah Mahrous. Numerical investigation of heat transfer through helically coiled tubes using nanofluids. *under review.*

7. Ahmed M. Elsayed, Raya K. Al-Dadah , Saad Mahmoud, A. Rezk. Flow boiling heat transfer inside helically coiled tubes- effect of tube and coil diameter. Under preparation.

8. Ahmed M. Elsayed, Raya K. Al-Dadah , Saad Mahmoud, A. Rezk. Artificial neural networks prediction of boiling heat transfer coefficient inside helical coils. Under preparation.

DEDICATION

To my beloved parents and sisters,
To my daughter Arwa and my wife,
And to the soul of my uncle Elsayed

Table of contents

LIST OF FIGURES

List of Tables

Nomenclature

AR	Area Ratio
Bo	Boiling Number, $q/(G\ h_{fg})$
C_p ,C	Specific heat (J/kg K)
Co	Convective Number $((1-x)/x)^{0.8}\ (\rho_l/\ \rho_v)^{0.5}$
COP	Coefficient of performance
d	Diameter (m)
Dn	Dean number $Re(d_i/d_{coil})$
f	Friction factor
He	Helical number $(Dn/(1+(\delta_{coil}/\pi d_{coil})^2)^{0.5}$
g	Gravitational acceleration (m/s^2)
G	Mass velocity (kg/m^{2}s)
h	Enthalpy (J/kg)
h_{fg}	Latent heat of vapour change(J/kg)
I	Current (Amp)
j	*Total superfacial velocity (m/s)*
Ja	Jacob number $Cp_l\,\Delta T_{wall\text{-}ref}/h_{fg}$
k	Thermal conductivity (W/m K)
L	Length (m)
$m^{\bullet}$	Refrigerant mass flow (kg/s)
Nu	Nusselt number $\alpha\ d_i/k$
P	Pressure (Pa)
Pr	Prandtl number $C_p\mu/k$
ΔP	Pressure drop (Pa)
Q	Heat transfer rate (W)
q	Heat flux (W/m^2)
Re	Reynolds number $Gd_i\ /\mu$
R	Radius (m)
Rev/Min	Compressor speed (rev/min)
St_{tp}	Stanton number $Nu/(Re_{lo}Pr_l)$
T	Temperature (K)
ΔT_s	Temperature difference between water and refrigerant (K)
u	Velocity (m/s)
U	Uncertainty
V	Volume (m3), Volt (V)
x	Vapour quality
X_{tt}	Martinelli parameter
W	Electric power (W)
We	Weber number $G^2d_i/(\rho\ \sigma)$

Greek symbols

σ	Surface tension (N/m)
δ	Pitch (m)
α	Heat Transfer coefficient (W/m^{2}K)
ρ	Density (kg/m^3)
γ	Dimensionless pitch
η	Efficiency
μ	Viscosity (N s/m^2)
ϕ	Volume fraction
ϕ^2	Two-phase multiplier

Subscripts

b	Bulk
cb	Convective boiling
coil	Coil
cond	Condenser
comp	Compressor
cr	Critical
dis	Discharge
evap	Evaporator
elect	Electric
h	Hydraulic
i	Inner
in	Inlet
l	Liquid
lo	Liquid only
nb	Nucleate boiling
o	Outer
out	Outlet
Pre	Preheater
ref	Refrigerant
sat	Saturation
suc	Suction
tp	Two-phase
w	Water
wall	Wall
wall-ref	Wall to refrigerant
v	Vapour
vol	Volumetric
II	Second law

CHAPTER 1

Introduction

Microchannels are recently developed for different industrial and medical applications including cooling of micro-processors and portable cooling devices for cooling personnel in military, chemical and biological industries. Several organizations are engaged in research of personal air conditioning system including Pacific Northwest National Laboratory (PNNL), Natick solider Centre and Aspen systems (Zhong et al., 2008). The application of vapour compression cycles in electronic cooling seems promising since they have high coefficient of performance (between 3 to 2), low refrigerant charge is required and the ability to remove the thermal load away from the chip, and finally the junction temperature may be below the ambient temperature offering better performance for the processors. Therefore, heat transfer enhancement techniques offer attractive features for using it to develop such miniaturized cooling systems.

Heat transfer enhancement techniques have been one of the main thermal engineering research fields since the fuel crisis in 1970s. Active, passive and compound heat transfer enhancement methods have been developed. Helical coils, additives to fluids, swirl flow devices, rough and extended surfaces are all passive enhancement techniques while application of electric, acoustic and magnetic fields and fluid /system vibration are active techniques (Bergles, 2002). Passive methods were preferred due to their simplicity in manufacturing, lower cost and longer operating life.

Many researchers are currently interested in investigating flow boiling inside channels with small diameters due to their high surface area to volume ratio and the increase of heat transfer coefficients leading to high heat transfer rates (Thome, 2010). The heat transfer coefficient is inversely proportional to the channel diameter (α=Nu×k/d). As a result, decreasing the channel diameter would result in higher heat transfer coefficient. Additionally, for the same cross sectional flow area, dividing the flow to large number of channels produces larger surface area for heat transfer compared to flow in single tube with large diameter leading to high heat transfer rates. Several investigations have been done on flow boiling through straight tubes proving their enhanced heat transfer performance compared to conventional channels with diameters larger than 6 mm. Yan and Lin (1998) compared their minichannel boiling measurements with tube diameter of 2 mm to different conventional channels and found enhancement as high as 30% for mean vapour qualities less than 0.7. Afterwards more research groups were interested in carrying more investigations using different fluids and tube diameters such as (Shiferaw et al., 2006 and Shiferaw et al., 2008) in UK and (Owhaib, 2007 and Fernando et al., 2008) in Sweden, (Saitoh et al., 2005 and Saitoh et al., 2007) in Japan, (Choi et al., 2007, Choi et al., 2009 and Oh et al., 2011) in Korea and (Thome, 2004, Ong and Thome, 2009) in Switzerland.

Flow boiling inside helical coils is a passive heat transfer enhancement technique. They have been widely used in once-through high pressure boilers for nuclear and conventional power stations, as they can withstand high heat fluxes and retard the dryout of the liquid film on the tube wall due to the centrifugal forces that redistribute the liquid film on the wall surface. Additionally, they had been utilized in tubular chemical reactors to make use of the very vigorous mixing of the phases (Ishida, 1981). Other researchers were interested in using helically coiled tubes in steam generator for steam powered automotives. Additionally, they have been applied for use as receivers of concentrating type solar collector in a large scale power generation system (Jensen, 1980).

Helical coils are found to be very effective in enhancing heat transfer compared to straight tube in single phase flow (Kumar et al., 2006), boiling heat transfer (Wongwises and Polsongkram 2006a and Akhavan-Behabadi et al., 2009) and condensation (Wongwises and Polsongkram, 2006b and Shao et al., 2007). Enhancement ratio as high as 1.37 and 2.15 has been reported for flow boiling in helical coils by Wongwises and Polsongkram (2006a) and Akhavan Behabadi et al.(2009) for vertical and horizontal helical coils respectively.

To develop miniature cooling systems, small diameter helical coils for evaporation and condensation are needed. However, research on the heat transfer performance of boiling inside helical coils with small diameter tubes is very limited while significant amount of research had been done for large helical coils. The use of small diameter tubes in helical coils have the potential of increasing the heat transfer rate due to increased heat transfer coefficients and increased surface area per unit volume leading to compact and light weight evaporators necessary for miniature cooling systems. However, attention should be paid to the increase in pressure drop associated with reducing channel diameters. There are very limited experimental studies of helically coiled tubes with tube diameters less than 4 mm. Therefore, an investigation into flow boiling in small diameter tube helical coils is performed to provide knowledge on this process and supply miniature cooling system designers with quantitative data of flow boiling of R134a in small diameter tube helical coils.

1.1 Heat transfer enhancement and secondary flow in coiled tubes

In helical coils, the radial velocity component generated from the centrifugal force results in secondary flow. A pair of generally symmetrical vortices in the vapour core affecting the main fluid stream is produced as depicted in figure 1.1. The main differences in heat transfer and fluid flow characteristics between helical coils and straight tube are related to this secondary flow effect caused by centrifugal forces. The liquid droplets are pushed from the inner tube wall to the outer tube wall through the center of the tube then liquid moves to the inner wall due to pressure difference between the outer and inner surfaces. This phenomenon improves the heat transfer and retards the dry out and prevents stratification in helical coils compared to straight tubes as proved for large tube diameters (Owhadi, 1968 and Akhavan-Behabadi et al., 2009). The combination of the spreading and thinning of the liquid film results in a higher average heat transfer coefficient. The coiled tube geometry apparently delays the transition from a wetted to a dry wall condition when compared to a straight tube; this transition occurred at qualities of nearly 100 % in some cases as reported for large tube diameters (Jensen, 1980).

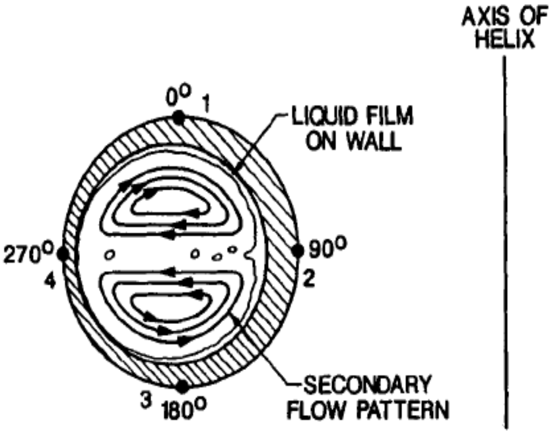

Figure 1.1 Two-phase secondary flow pattern in helical coils (Young and Bell, 1991).

The large radial accelerations induced by the helical path would continuously de-entrain any liquid droplets in the vapour stream and force all the liquid to remain on the hot surface until total vaporization is achieved. The liquid on the wall has a longitudinal velocity much lower than the vapour and therefore is subject to very small radial acceleration effects making the return of liquid film from outer to inner sides possible. Bell and Owhadi (1969) found that the secondary flow imposes a shear stress on the inner surface of the liquid film, causing liquid flow from the 270° (position 4) to the 90° (position 2) thus improving the rewetting of the surface. It is clear from figure 1.2 that the liquid film disappeared first at the top of the coil 0° (position 1) and then from the bottom of the coil 180° (position 3) in case of measuring the local heat transfer coefficient along the length and circumference of the coil (Young and Bell, 1991).

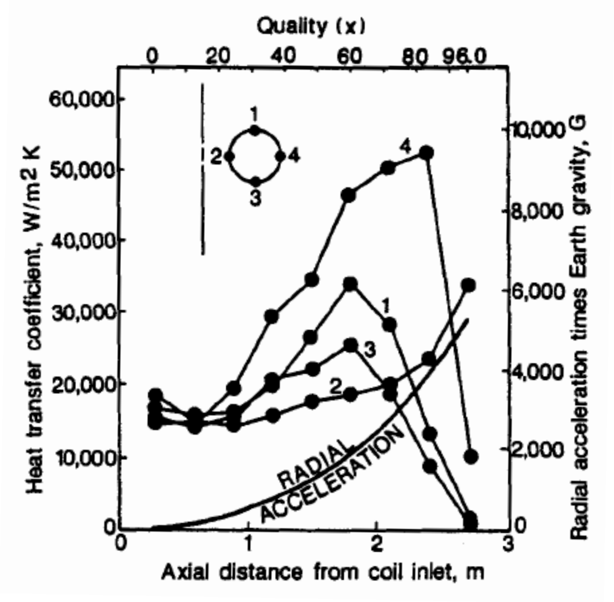

Figure 1.2: Local heat transfer coefficient distribution (Young and Bell, 1991).

1.2 Objectives and overview

It has been shown that significant experimental research has been reported for single and two-phase flow in mini/micro straight tubes with small diameter (Shiferaw et al., 2008; Shiferaw et al., 2006, Owhaib, 2007; Del Col et al., 2008). However, very limited heat transfer studies have been reported in the literature for small helical coils with diameters less than 4 mm. Additionally, very limited number of studies reported on using nanofluids in helical coils. Combining such two passive heat transfer enhancement techniques could lead to beneficial improvement in cooling systems with double pipe heat exchangers. The present research is an investigation for the heat transfer augmentation in helical coils for cooling applications with the following objectives:

- Conduct experimental measurement of boiling inside helical coils with different tube diameters and different helical diameters. Namely coil A, B, C, and D with tube diameters of 2.8 mm, 2 mm, 1.55 mm and 1.1 mm.
- Develop accurate and generalized predictive methods for boiling heat transfer coefficient for the design of small cooling systems.
- Developing a simulation code for the miniature cooling system and validating it against experiments then conducting an optimisation study for the effect of coil diameter and tube diameter on the enhancement of performance of thermal systems.
- Conduct numerical investigation on combining the helical coil and nanofluids in single phase flow to study their heat transfer enhancement compared to straight tube with pure fluids in both laminar and turbulent flow.

1.3 Thesis Outline

The thesis starts with a review of the research done on two-phase flow boiling and heat transfer mechanisms in helical coils and its applications in miniature cooling systems and the opportunities to utilize nanofluids in helical coils. Next, the details of the designed test facility are mentioned followed by experimental measurements of boiling heat transfer and new predictive techniques. Lastly, a numerical study using fluent CFD code was done to study the effect of combining both tube coiling and nanofluids. The thesis could be summarized as follow:

Chapter one contains the introduction, practical applications of the helically-coiled and thesis overview.

Chapter two reviews the experimental and prediction methods, critical heat flux, flow patterns for flow boiling heat transfer inside helical coils. Also, a review of boiling inside straight tubes highlights the effect of reducing tube diameter is presented. Then, a review of miniature cooling systems and the effect of nanoparticles addition on heat transfer enhancement are also discussed.

Chapter three describes the experimental test facility. A miniature vapour compression refrigeration system has been designed to measure the flow boiling in different helical coils. The components of the test facility and uncertainties associated with the measurements have been presented.

Chapter four investigate the enhancement of flow boiling heat transfer measurements through four configurations of helically-coiled tubes. Coils A, B, C, and D are with tube diameters of 2.8 mm, 2 mm 1.55 mm and 1.1 mm respectively. All coils have 60 mm coil diameter and helical pitch of 8 mm respectively except coil A has 30 mm coil diameter.

Chapter five presents two new prediction models for flow boiling in helical coils. The first model is an empirical correlation based on dimensional analysis. The second model is an application of artificial intelligence techniques using ANNs (artificial neural networks).

Chapter six is an optimisation study for performance of a miniature refrigeration system equipped with helically coiled evaporator and condenser.

Chapter seven is a CFD investigation for heat transfer enhancement for single phase flow in helical coils using Al_2O_3 nanofluids in both the laminar and turbulent flow regimes. The CFD model has been validated against experimental data in literature and empirical correlations. Additionally the effect of nanofluids on the pressure drop was incorporated for better assessment on the nanofluid performance.

Chapter eight presents the conclusions from the empirical and theoretical findings and recommendation for future work.

CHAPTER 2

Literature Review

2.1 Introduction

This chapter presents a review of the research done on flow boiling heat transfer in helical coils and its applications in miniature cooling systems. The chapter begins with the fundamental parameters used in two-phase flow that are essential for the calculations of boiling heat transfer and pressure drop were described. Secondly, a review of experimental work of boiling heat transfer in helical coils is presented. Next, boiling heat transfer predictive methods, pressure drop, flow regimes, and dryout in helical coils are presented. Afterwards, a detailed review of the research work done on miniature cooling systems and the opportunities of using helical coils has been discussed. Next, a review of using nanofluids in channels has been done for the sake of using combined passive enhancement heat transfer methods using tube coiling and nanofluids. Lastly, a summary of the main findings from the review is presented.

2.2 Two-phase flow fundamentals and basic definitions

The two-phase flow is more complicated than single phase flow as it is affected by the interfacial forces between phases and the wetting of liquid to the tube wall, and momentum exchange between phases. Flow boiling is divided into two main categories: the subcooled flow boiling and saturated flow boiling. In subcooled flow boiling, the boiling process is initiated as the wall temperature becomes higher than the saturation temperature of the fluid while the fluid bulk temperature is lower than its saturation temperature corresponding to the operating pressure.

Saturated boiling occurs when the fluid is boiling while its bulk temperature is at the saturation temperature corresponding to the operating pressure. In refrigeration systems, the refrigerant enters the evaporators as saturated mixture with low dryness fractions hence the boiling process is of the saturated boiling type. Therefore, in the present study, saturated flow boiling is investigated where R134a after being throttled in the expansion valve, it enters the test section as saturated mixture with initial vapour quality. Generally, the flow boiling process is affected by two different mechanisms: the nucleate boiling (Boiling in a stagnant liquid) and convective boiling (Balakrishnan et al. 2009). In nucleate boiling where vapour bubbles are formed (usually at the solid surface), the heat transfer process is mainly affected by the applied heat flux and evaporating pressure. In the convective boiling process where the heat is conduct through a thin film of liquid which evaporates at liquid vapour interface with no bubble formation (Whalley, 1996), is mainly affected by the mass velocity and vapour quality. The effect of different mechanisms on the boiling heat transfer coefficient (Wadekar, 2001) is depicted in Figure **2.1**. In two-phase flow in order to maintain the mass flow rate through the channel and satisfy the conservation of mass, the mean density decreases and the mixture velocity increases. The main reason for the appearance of different flow regimes is the flow acceleration which increases the difference between the mean liquid and vapour velocities. This section includes the basic definitions related to two-phase flow as described below. The gas mass velocity is defined as:

$$\mathrm{G_v} = \frac{\text{gas mass flow rate}}{\text{tube cross sectional area}} = \frac{\overset{\bullet}{m}_v}{A_{cs}} \qquad \textbf{(2.1)}$$

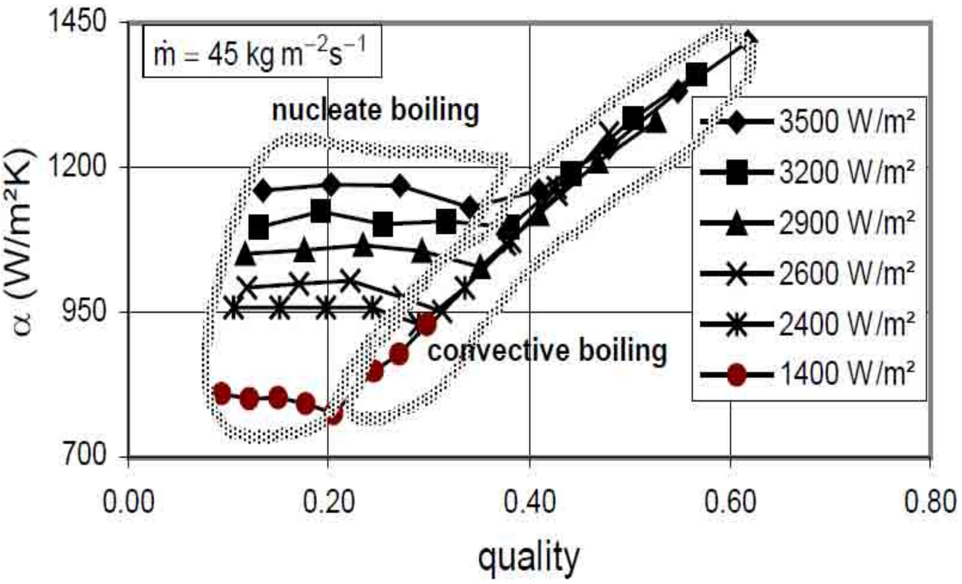

Figure 2.1: Local heat transfer coefficient as a function of local vapour quality (d_i=3.1 mm) straight tube using R114 (Wadekar, 2001).

The liquid mass velocity is defined as:

$$G_l = \frac{\text{liquid mass flow rate}}{\text{tube cross sectional area}} = \frac{\dot{m}_l}{A_{cs}} \tag{2.2}$$

Total mass velocity is defined as the product of mean density by the mean velocity:

$$G = \frac{\text{total mass flow rate}}{\text{tube cross section area}} = \frac{\dot{m}_v + \dot{m}_l}{A_{cs}} \tag{2.3}$$

The vapour quality in two-phase flow is defined as:

$$x = \frac{G_v}{G} \tag{2.4}$$

2.2.1 Phase velocities

The liquid or vapour superficial velocity is defined as the velocity of liquid or gas as it flows alone in the channel (based on the total channel area):

$$V_v = \frac{G_v}{\rho_v} \qquad V_l = \frac{G_l}{\rho_l} \tag{2.5}$$

$$V_v\rho_v + V_l\rho_l = G \tag{2.6}$$

The total superficial velocities defined as:

$$j = V_l + V_v \tag{2.7}$$

The total superficial velocity expresses the total volume flux of the two-phase flow. The relative velocity between the two phase's velocities to the total superficial velocity is used to obtain the void fraction (Whalley, 1996). The actual phase velocity (liquid or gas based on the phase flow area) are given as:

$$u_l = \frac{V_l}{(1-\varepsilon)} \qquad u_v = \frac{V_v}{\varepsilon} \tag{2.8}$$

ε is the void fraction defined in section 2.2.2.

2.2.2 Void fraction

The cross sectional void fraction represents the cross sectional area occupied by the gas to the total cross sectional area. The void fraction is utilized to identify the flow regimes since the pressure drop and heat transfer coefficient calculations are dependent on the flow regimes. Flow regimes could be identified based on variation of void fraction with time using measurement techniques such as densitometer (Whalley, 1996) that measure the average density of a mixture across the tube. The void fraction is the ratio between vapour to total cross sectional areas as illustrated in Figure **2.2**.

$$\varepsilon = \frac{A_v}{A_{cs}} = \frac{A_v}{A_v + A_l} \tag{2.9}$$

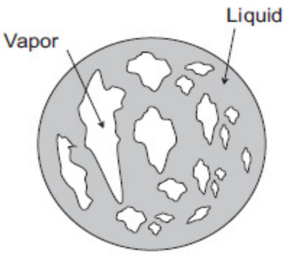

Figure 2.2: Cross sectional void fraction.

Butterworth developed a generalized equation for the void fraction (Chowdhury, 2008):

$$\varepsilon = \left[1 + A \left(\frac{1-x}{x} \right)^{p} \left(\frac{\rho_v}{\rho_l} \right)^{q} \left(\frac{\mu_l}{\mu_v} \right)^{r} \right]^{-1} \quad \textbf{(2.10)}$$

Where A, p, q and r are empirical constants given in table 2.1.

Table 2.1: Constants for various void fraction models (Chowdhury, 2008).

Correlation	A	p	q	R
Homogeneous Model	1	1	1	0
Lochart Martinelli Model	0.28	0.64	0.36	0.07
Baroczy Model	1	0.74	0.65	0.13
Zivi Model	1	1	0.67	0
Thome Model	1	1	0.84	0.18

Both homogenous and Zivi models do not incorporate the effect of phases viscosity ratio on the void fraction calculations. The homogeneous model is derived by equating the velocity of phases and latter model is derived from kinetic energy of the two-phase flow (Thome, 2010). The gas phase velocity could be correlated to total mass velocity using the void fraction as (Whalley, 1996):

$$G_v A = AGx = \rho_v u_v A_v = \rho_v u_v \varepsilon A \;\Rightarrow\; \qquad u_v = \frac{Gx}{\rho_v \varepsilon} \quad \textbf{(2.11)}$$

Similarly for liquid phase:

$$G_l A = AG(1-x) = \rho_l u_l A_l = \rho_l u_l \varepsilon A \Rightarrow \qquad u_l = \frac{G(1-x)}{\rho_l \varepsilon} \tag{2.12}$$

The slip ratio is defined as the ratio between the gas phase velocities to liquid one:

$$S = \frac{u_v}{u_l} \tag{2.13}$$

The cross sectional void fraction is related to slip ratio as:

$$\varepsilon = \frac{1}{1 + ((1-x)/x)(\rho_v/\rho_l)S} \tag{2.14}$$

Since S≥1, the void fraction is maximum when the slip ratio equal to 1(homogeneous void fraction where both phases have the same phase flow velocity). In the heat transfer calculations, we are interested in the cross sectional void fraction. However, the void fraction that is measured from the quick-closing valve method is the volumetric void fraction. The relation between the volumetric and cross sectional void fraction is given by (Thome, 2004).

$$\varepsilon_{vol} = \frac{\varepsilon}{(1-\varepsilon)/S + \varepsilon} \tag{2.15}$$

2.2.3 Density of two-phase mixture

The two-phase density is defined as:

$$\rho_{tp} = \rho_v \varepsilon + \rho_l (1-\varepsilon) \tag{2.16}$$

Since there are several proposed expressions for the void fractions as described in table 2.1, there will be different values for the two-phase density according to the selected void fraction model. It is widely used in correlating the two-phase heat transfer coefficient is to use the liquid density which was used in the current study.

2.2.4 Viscosity of two-phase mixture

Several definitions for mixing rules for the two-phase viscosity exist in the literature. Table 2.2 summarizes some of these formulas.

Table 2.2: Viscosity of two-phase mixture.

Proposed correlation for mixture viscosity	Formula
Mc Adams	$1/\mu_{tp} = (x/\mu_v) + (1-x)/\mu_l$
Dukler	$\mu_{tp}/\rho_{tp} = x\mu_v/\rho_v + (1-x)\mu_l/\rho_l$
Cicchitti	$\mu_{tp} = x\mu_v + (1-x)\mu_l$

The liquid viscosity (μ_l) is widely used in correlating the two-phase heat transfer coefficient and hence it was used in the current study.

2.2.5 Two-phase dimensionless parameters

This section presents the most commonly utilized dimensionless groups in two-phase flow. These dimensionless parameters are utilized in correlating the heat transfer coefficient and/or the pressure drop as described in sections 2.4 and 2.7.

2.2.5.1 Boiling Number

It is defined as the actual heat flux over the potential heat flux required for complete evaporation.

$$Bo = \frac{q}{Gh_{fg}} \tag{2.17}$$

Where h_{fg} is the latent heat of evaporation.

2.2.5.2 *Jacob Number*

It is the ratio of sensible to latent energy absorbed during liquid-vapour phase change. Some researchers utilize the Jacob number instead of the boiling number (Jokar et al., 2006):

$$Ja = \frac{Bo}{St} \tag{2.18}$$

Where Stanton number (St) is a modified Nusselt Number defined as:

$$St = \frac{Nu}{\mathrm{Re}\cdot \mathrm{Pr}} \tag{2.19}$$

2.2.5.3 *Martinelli parameter*

Martinelli parameter is defined as the ratio of the pressure drop per unit length in the liquid phase to that of vapour phase utilizing the mass velocity of each phase to flow separately through the total cross sectional area.

$$\chi = \sqrt{\frac{(dP_F/dz)_l}{(dP_F/dz)_v}} \tag{2.20}$$

Where:

$$(dP_F/dz)_l = 2\frac{f_{fl}}{d_i}\frac{G_l^2}{\rho_l} = 2\frac{f_{fl}}{d_i}\frac{G^2(1-x)^2}{\rho_l} \tag{2.21}$$

$$(dP_F/dz)_v = 2\frac{f_{fv}}{d_i}\frac{G_v^2}{\rho_v} = 2\frac{f_{fv}}{d_i}\frac{G^2x^2}{\rho_v} \tag{2.22}$$

f_{fl}, f_{fv} are the fanning factors for liquid and vapour flow respectively. The fanning factor for straight tube is found by:

Laminar flow: $f_{f,st} = \frac{16}{\mathrm{Re}}$ $\quad \mathrm{Re} < 2000$ **(2.23)**

Turbulent flow: $f_{f,st} = 0.079\mathrm{Re}^{-0.25}$ $\quad \mathrm{Re} > 2000$ **(2.24)**

For Martinelli number >>1 the mixture is mostly liquid and for Martinelli number <<1 the mixture is dominantly vapour. The analogy between the energy and momentum in single phase turbulent flow leads to the following relation between the heat transfer and pressure drop (Gungor, 1986):

$$\frac{\Delta P}{\Delta L} \propto G^n \quad \Rightarrow \alpha \propto \left(\frac{\Delta P}{\Delta L}\right)^{\frac{n-1}{n}} \tag{2.25}$$

Where n is an empirical constant.

Several authors assumed a similar relationship between the two-phase heat transfer coefficient and two-phase pressure drop. Since the two-phase pressure drop is correlated as a function of Martinelli parameter, the two-phase heat transfer coefficient to liquid only or liquid flow ratio may also be expressed as a function of the Martinelli parameter as:

$$\frac{\alpha_{tp}}{\alpha_l} = fn(\chi_{tt}) \quad \text{or} \quad \frac{\alpha_{tp}}{\alpha_{lo}} = fn(\chi_{tt}) \tag{2.26}$$

Where χ_{tt} is the Martinelli parameter for turbulent liquid – turbulent vapour flow condition. In the nucleate boiling region, the ratio of two-phase heat transfer coefficient to liquid only heat transfer (α_{lo}) coefficient is nearly constant with the Martinelli parameter, increases with the decrease in the mass velocity, and is less dependent on the quality. At lower Martinelli parameter values, the forced convection becomes apparent and the ratio increases with the increase in mass velocity (Mitsutake et al., 2004) as shown in figure 2.3.

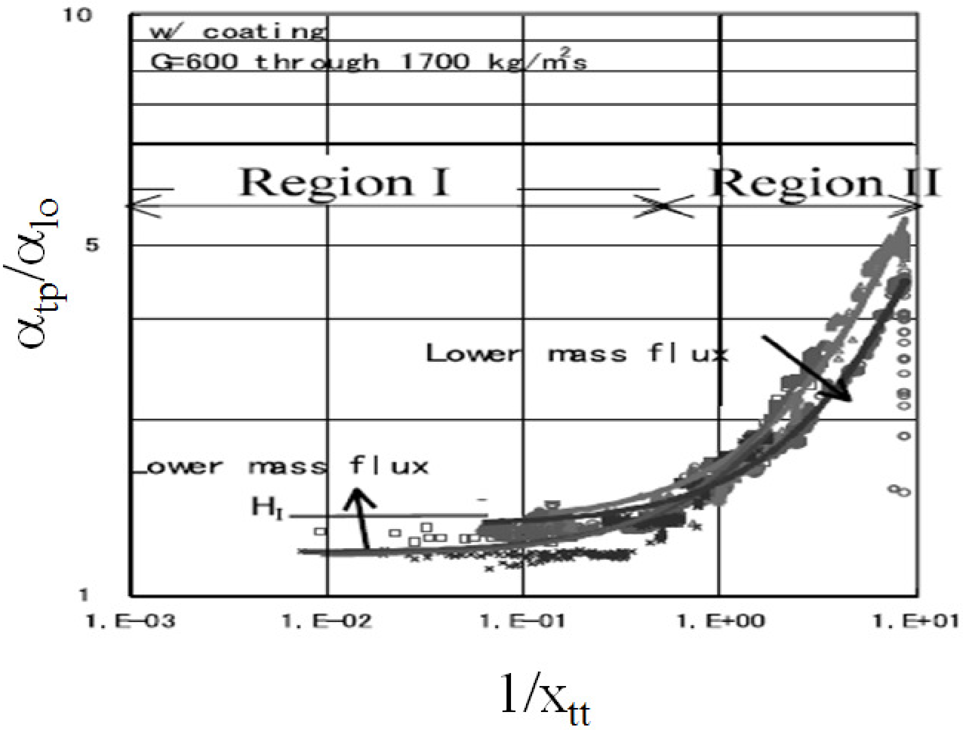

Figure 2.3: Variation of two-phase to liquid film heat transfer coefficients ratio for coated surfaces (Mitsutake et al., 2004) correlated in Martinelli parameter.

Researchers usually correlate the two-phase to liquid only (assuming the entire mass velocity as liquid) heat transfer coefficient ratio in the following form (Mitsutake et al., 2004):

$$\frac{\alpha_{tp}}{\alpha_{lo}} = A\left(\frac{1}{X_{tt}}\right)^{B} \tag{2.27}$$

Other researchers combine the effect of both convective and nucleate boiling mechanisms as (Gungor, 1986):

$$\frac{\alpha_{tp}}{\alpha_{l}} = C_1\left[Bo + C_2\left(\frac{1}{X_{tt}}\right)^{m1}\right]^{m2} \tag{2.28}$$

A, B, C_1, C_2, m_1, m_2 are constants determined from regression and fitting of experimental data.

2.2.5.4 Reynolds Number

The Reynolds number is defined as the ratio between inertia to viscous forces. Researchers utilized different approaches in correlating their measurement to Reynolds number. Table 2.3 summarizes the different definitions of Reynolds number utilized in literature.

Table 2.3: Two-phase Reynolds number definitions in literature.

Reynolds number definition	Formula	Developed correlations
Liquid phase Reynolds number	$\mathrm{Re}_l = G(1-x)d_h / \mu_l$	Chen (Thome, 2010) Shah (Thome, 2010) and Winterton (Thome, 2010)
Vapour phase Reynolds number	$\mathrm{Re}_v = Gxd_h / \mu_v$	
Liquid-only Reynolds number	$\mathrm{Re}_{lo} = Gd_h / \mu_l$	Lazarek and Black (Fernando et al.,2008) Kandlikar and Balasubramanian (Thome,2010)
Vapour-only Reynolds number	$\mathrm{Re}_{vo} = Gd_h / \mu_v$	Mikielewicz (2004)
Two mixture Reynolds number	$\mathrm{Re}_m = \left[x\left(\left(\rho_l / \rho_v\right)-1\right)+1\right] * Gd_h / \mu_l$	Cui et. al.(2006)

2.2.5.5 Weber Number

It is the ratio between the inertia to surface tension forces. Weber number relates the effects of surface tension and inertia forces on the flow patterns in microchannels. Similar to Reynolds number, one can find in the literature several definitions for Weber number as shown in table 2.4.

Table 2.4: Two-phase Weber number definitions in literature.

Reynolds number definition	Formula	Authors
Liquid phase Reynolds number	$We_l = G^2 d_h (1-x)^2 / (\rho_l \sigma)$	
Vapour phase Reynolds number	$We_v = G^2 d_h x^2 / (\rho_v \sigma)$	
Liquid-only Reynolds number	$We_{lo} = G^2 d_h / (\rho_l \sigma)$	Tran et al. (Fernando et al.,2008)
Vapour-only Reynolds number	$We_{vo} = G^2 d_h / (\rho_v \sigma)$	Saitoh et al. (2007)

2.2.5.6 Dean number

The Dean number is the product of the Reynolds number and the ratio of centrifugal force to inertia force (Balakrishnan et al., 2009). The dean number is defined as:

$$Dn = \mathrm{Re}\sqrt{\frac{d_i}{d_{coil}}} \qquad \textbf{(2.29)}$$

2.2.5.7 Convective number

The convective number is utilized to express the convective contribution in the boiling process. The convective number is a function of vapour quality and density ratio between liquid and vapour phases.

$$Co = \left(\frac{1-x}{x}\right)^{0.8} \left(\frac{\rho_l}{\rho_v}\right)^{0.5} \qquad \textbf{(2.30)}$$

For convective number less than 0.65, the effect of convective boiling becomes significant compared to nucleate boiling (Kakaç and Liu, 2002).

2.3 Flow boiling in helical coils

Several researchers have investigated flow boiling in helical coils using different fluids, coil dimensions and orientations, however much of the early work understandably has involved steam. Owhadi et al. (1968) performed tests using two vertical helical coils with a 12.5 mm inside diameter at constant atmospheric pressure and with heat fluxes ranging from 60 to 255 kW/m^2. They reported that nucleate boiling appeared only in the low quality region.

Kozeki et al. (1970) evaluated the effect of varying pressure (from 5 to 21 bar) in a helically coiled steam generator comprising a tube having an inside diameter of 15.5 mm and coil diameter of 628 mm. Their results showed that the local heat transfer coefficient was hardly affected either by the steam quality, mass flow rate or operating pressure due to the thicker liquid film produced by the centrifugal force inherent in helical coils, which causes nucleate boiling to dominate the boiling process as few liquid droplets hold through the vapour core. Additionally, the heat transfer coefficients on the concave side (outer side) were higher than on the convex side (inner side). The authors concluded that the Martinelli-Neslon’s method did not adequately correlate their data as they defined their two phase multiplier as the ratio between two-phase pressure drop in coils to single phase in straight tube such deviation was interpreted by the secondary flow effect. Experimental investigations by Nariai et al. (1982) on the flow boiling of steam for cooling nuclear reactors with tubes having inside diameters of 14.3 mm (coil diameters ranging from 420 to 620 mm), concluded that the effect of coiled tubes on the average heat transfer coefficient was negligible, while correlations relating to straight tubes were only applicable to helical coils under operating pressures less than 35 bar. The insignificant effect of tube coiling in Nariai experiment may be related to the large diameters they used so that the effect of secondary flow was insignificant.

Zhao et al. (2003) measured the boiling heat transfer of steam in a 9 mm diameter tube with a 292 mm coil diameter and found that the heat transfer coefficient was dependent on the mass velocity and heat flux which indicated that both nucleate and convective boiling mechanisms were important. From the previous research on steam it could be concluded that secondary flow effect was not significant for large coil diameter as reported by Nariai. Straight tube pressure drop methods were not applicable to predict the pressure drop in helical coils with reasonable accuracy.

Over the past decade, research on the topic has begun to incorporate alternatives to steam, including refrigerants R113 and R134a, as well as refrigerant mixtures such as M09. Kaji et al. (1998) carried out experimental studies on the flow boiling of R113 in 10 mm diameter tubes with coil diameters of 165 and 320 mm respectively. The heat flux was varied between 30 and 200 kW/m^2 while the operating pressure was fixed at 3.9 bar. Their results showed that in the high quality region, the heat transfer coefficient was greatest at the outer periphery of the coil but lowest at the inside of the coil. This could be explained by the effect of secondary flows generated by centrifugal forces causing a thinner liquid film at the outer periphery of the coil compared to that at the inside of the coil. Nucleate boiling was dominated at high and intermediate Martinelli number and convective boiling dominates at low Martinelli numbers.

Wongwises and Polsongkram (2006a) similarly utilized a vertical helical coil with tube and coil diameters of 8.3 and 305 mm respectively to investigate the flow boiling of R134a in a heat exchanger at applied heat fluxes of 5 to 10 kW/m^2. Their results revealed that the average heat transfer coefficient increased with mass velocity, heat flux and saturation temperature, indicating that both mechanisms of boiling were active under the conditions tested. The trend of helical coil measurement was similar to straight tubes since the heat transfer coefficient was increasing with vapour quality and mass velocity as published in their work. Helical coils heat transfer were higher compared to straight tubes due to the effect of centrifugal force as shown below.

Similarly, Jitian et al. found from their measurements of R134a boiling inside a 600 mm diameter horizontal coil of 7.6 mm diameter tube that the effect of mass velocity on heat transfer coefficients was less significant at low vapour qualities and becomes pronounced at high vapour quality. More recently, boiling heat transfer coefficient measurements of M09 refrigerant mixture (R134a/ R290/ R600a of 91%, 4.068%, 4.932% by mass) and R12 flowing through a vertical coil (141.5 mm coil diameter, 6.35 mm diameter tube) were undertaken by Balakrishnan et al. (2009) at refrigerant mass flow rates ranging from 0.3-0.9 g/s. They found that the heat transfer coefficient was strongly dependent on the mass velocity, which suggests that the primary boiling mechanism was largely convective.

A detailed investigation of the variation of the boiling heat transfer coefficient around the circumference of helically coiled tube was performed by Bell and Owhadi (1969). They fitted four thermocouples at 0° (top), 90° (inner to helical axis), 180° (bottom), 270° (outer far from helical axis) around the circumference at different stations along the coil to measure the local heat transfer coefficient. They plotted their two-phase heat transfer coefficient divided by the liquid heat transfer coefficient in helical coil against turbulent liquid - turbulent vapour Martinelli parameter. The liquid heat transfer coefficient was calculated from Seban and McLaughlin (1963) liquid single phase heat transfer correlation. The scatter of data at low Martinelli number less than 10 is due to the dominance of nucleate boiling mechanism. At low and medium vapour qualities the boiling heat transfer coefficients at (270°) were higher than those at bottom and top due to the thin liquid film formed as a result of the secondary flow while the inner side of the coil (90°) was significantly lower than the outer side. At high vapour qualities, the coefficients at the 90° and 270° were comparable and significantly higher than those at top (0°) and bottom (180°). The heat transfer at the top of the tube was higher than those at the bottom due to the effect of gravity thickening the liquid film at 180°. The experimental results were comparable to a correlation previously developed by the authors for predicting the circumferentially average heat transfer coefficient.

On the other hand Jensen (1980) reported that near the coil inlet, the heat transfer coefficients were highest at the convex side (inner side), and lowest at the concave side (outer side). The convex heat transfer coefficients decreased to a minimum further down the tube while the concave side heat transfer coefficient increased to become larger. The higher coefficients at the inlet on the convex side were postulated to be due to:

1. Larger nucleate boiling component (caused by the larger heat flux at that surface due to the non-uniform heating). The boiling is then suppressed further down the tube due to the effect of turbulence on nucleation. As the vapour quality increases, the vapour velocity increases and the single-phase heat transfer dominates.

2. The change in the heat transfer mechanism associated with the change in the flow regime. Before the annular flow regime is attained at higher qualities, other flow regimes must first occur leading to vigorous boiling at convex side (surface close to coil axis). In annular flow the liquid layer on the concave surface becomes thinner than that on the convex because of the secondary flow and a thicker film formed on the convex surface as it is a stagnation point of the secondary flow. At this point the heat transfer coefficients become larger at the concave side than those on the convex side.

Chen et al. (2011a) measured the local heat transfer coefficient using 128 thermocouples distributed along 32 axial positions on a 4 turns horizontal helical coil where 4 thermocouples fitted on the circumference of the coil at each position. The coil was 7.6 mm inner diameter, 300 mm coil diameter and 40 mm coil pitch and heated length of 7.07 m. The wall temperature trend was monotonically decreasing at high and intermediate mass velocities but repetitive saw-edge behaviour at low mass velocity. The heat transfer coefficient was highest at the outer side (0°) and lowest on the inner side (180 °) which was very clear at low mass velocities. The front side (270°) and offside (90°) has intermediate heat transfer coefficients. The heat transfer coefficient was increasing with the mass velocity, heat flux, vapour quality but the effect of pressure seemed to be insignificant.

In conclusion, most researchers reported that the boiling heat transfer performance coefficient were enhanced by helically coiling tubes due to the centrifugal force and secondary flow effects where the liquid film is pushed from the outer side to the inner side of the tube wall then the liquid droplets circulated from the inner side to the outer side leading to better heat transfer coefficients and redistribution of the liquid film (Owhadi et al., 1968, Wongwises and Polsongkram, 2006a and Akhavan Behabadi et al., 2009). An enhancement ratio of up to 2.15 was reported in the literature. Most studies used tube diameter larger than 4 mm using different fluids such as steam/water, R134a, R113, and refrigerant mixtures. Studies with large coil diameter reported that the enhancement of tube coiling may be insignificant such as reported by Nariai. Flow boiling studies in helical coils with small diameters less than 4 mm are very limited. The current experimental is directed to investigate the effect of different small tube diameters in helical coils which has not been investigated in literature.

2.4 Heat transfer predictive methods in helical coils

Prediction of boiling in vertical straight tubes was performed using different approaches such as superposition models: Chen boiling correlation, enhancement models such as Shah correlation, asymptotic models such as Steiner and Taborek correlation (García-Cascalesa et al., 2007). The superposition and asymptotic models combine two thermal mechanisms nucleate boiling and convective boiling which are expressed in the form (García-Cascalesa et al., 2007):

$$\alpha_{tp} = \left(\alpha_{nb}^{n} + \alpha_{cb}^{n}\right)^{1/n} \qquad \textbf{(2.31)}$$

Where n=1 Chen correlation

n=2 Kutateladze correlation

n=3 Steiner and Taborek correlation

There have been several methods utilized by researchers to predict heat transfer coefficients during flow boiling inside helical coils. Cui et al. (2006) described the two-phase heat transfer Nusselt number for a helical coil as a function of the convective number. This was achieved by adapting the well established straight tube boiling correlation of Klimenko (1988) to a helical coil by incorporating the Dean number.

$$Nu_{tp} = 8.76\,\mathrm{Re}_{m}^{0.6}\,\mathrm{Pr}_{l}^{1/6}\left(\frac{\rho_v}{\rho_l}\right)^{0.2}\left(\frac{k_{l,wall}}{k_{l,b}}\right)^{0.09} Dn^{0.1}Co^{-0.414} \qquad \textbf{(2.32)}$$

Dn is the Dean number and *Co* is the convective number. It is utilized to model the effect of the secondary flow within the helical coil. Cui et al. (2006) postulated that there is a critical value for the convective number, after which convective boiling becomes dominant.

The second methodology that is widely used involves correlating the two-phase heat transfer coefficient as a function of the Martinelli parameter. Table 2.5 summarizes the proposed relationships by different researchers. The Martinelli number (χ_{tt}) for turbulent-turbulent flow is defined as:

$$\chi_{tt} = \left(\frac{1-x}{x}\right)^{0.9}\left(\frac{\rho_v}{\rho_l}\right)^{0.5}\left(\frac{\mu_l}{\mu_v}\right)^{0.1} \qquad \textbf{(2.33)}$$

Table 2.5: Boiling heat transfer coefficient correlated to the Martinelli number for helical coils.

Correlation	Fluid	Mathematical Formulation
Kozeki et al. (Zhao et al.,2003)	Water	$\alpha_{tp}/\alpha_{lo} = 2.5(1/\chi_{tt})^{0.75}$
Schrock-Grossman (Zhao et al.,2003)	Water	$\alpha_{tp}/\alpha_{lo} = 1.11(1/\chi_{tt})^{0.66} + 7400Bo$
Zhao et al.(2003)	Water	$\alpha_{tp}/\alpha_{lo} = 1.6(1/\chi_{tt})^{0.74} + 183000Bo^{1.46}$
Jitian et al.	R134a	$\alpha_{tp}/\alpha_{lo} = 2.8446(1/\chi_{tt})^{0.27} + \left(46162Bo^{1.15} - 0.8762\right)$
Kaji et al. (1998)	R113	$\alpha_{tp}/\alpha_{lo} = \left[\left(2.6(1/\chi_{tt})^{0.95}\right)^3 + \left(4*10^4 Bo\,\mathrm{Re}_{lo}^{-0.12}\right)^3\right]^{1/3}$
Bai (Chen et al. ,2011a)	Water	$\alpha_{tp}/\alpha_{lo} = 1 + 2.21(1/\chi_{tt})^{0.3} \quad 1/\chi_{tt} < 1.2$ $\alpha_{tp}/\alpha_{lo} = 3.06(1/\chi_{tt})^{0.47} \quad 1/\chi_{tt} \geq 1.2$
De la Harpe (Isheda, 1981)	Helium	$\alpha_{tp}/\alpha_{l} = 1.8(1/\chi_{tt})^{0.75}$

The two-phase heat transfer coefficient (α_{tp}) is calculated from these correlations as a ratio to the liquid-only single phase heat transfer coefficient (α_{lo}). This liquid-only heat transfer coefficient can be calculated from the liquid only Nusselt number (Nu_{lo}) obtained either from the Mori-Nakayama's equation (Nariai et al. 1982; Kaji et al., 1998):

$$Nu_{lo} = \frac{1}{41}\mathrm{Re}_{lo}^{5/6}\,\mathrm{Pr}_l^{0.4}\left(\frac{d_i}{d_{coil}}\right)^{1/12}\left(1+\frac{0.061}{\left(\mathrm{Re}_{lo}\left(d_i/d_{coil}\right)^{2.5}\right)^{1/6}}\right) \quad \text{for Liquid only} \tag{2.34}$$

$$Nu_{l} = \frac{1}{41}\mathrm{Re}_{l}^{5/6}\,\mathrm{Pr}_l^{0.4}\left(\frac{d_i}{d_{coil}}\right)^{1/12}\left(1+\frac{0.061}{\left(\mathrm{Re}_{l}\left(d_i/d_{coil}\right)^{2.5}\right)^{1/6}}\right) \quad \text{for Liquid flow}$$

or from the Seban and McLaughlin relationship (Young, 1991; Zhao et al. 2003):

$$Nu_{lo} = 0.023\,\mathrm{Re}_{lo}^{0.8}\,\mathrm{Pr}_l^{0.4}\left[\mathrm{Re}_{lo}^{0.05}\left(\frac{d_i}{d_{coil}}\right)^{0.1}\right] \qquad \text{for liquid only flow} \tag{2.35}$$

$$Nu_{l} = 0.023\,\mathrm{Re}_{l}^{0.8}\,\mathrm{Pr}_l^{0.4}\left[\mathrm{Re}_{l}^{0.05}\left(\frac{d_i}{d_{coil}}\right)^{0.1}\right] \qquad \text{for liquid flow}$$

The Chen boiling correlation based on the sum of convective and nucleate boiling components was adopted by Owhadi et al. (1968) and Zhao et al. (2003) to describe the boiling of water in helical coils. The two-phase heat transfer coefficient can be estimated from the following equation:

$$\alpha_{tp} = 0.00122\frac{k_l^{0.79} Cp_l^{0.45} \rho_l^{0.49}}{\sigma^{0.5} \mu_l^{0.29} h_{fg}^{0.24} \rho_v^{0.24}} \Delta T_{sat}^{0.24} \Delta p_{sat}^{0.75} * S + 0.023 \mathrm{Re}_l^{0.8} \mathrm{Pr}_l^{0.4} \frac{k_l}{d_i} * \mathrm{Re}_l^{0.05} \left(\frac{d_i}{d_{coil}}\right)^{0.01} * F \qquad \mathbf{(2.36)}$$

S is the nucleate boiling Suppression factor and *F* is the convective boiling Enhancement factor.

Balakrishnan et al. (2009) developed a correlation for R12 evaporating inside helical coils based on the Dean and Pierre numbers:

$$Nu_{tp} = 0.0382(DnPe)^{0.658} \qquad \mathbf{(2.37)}$$

$$Dn = \mathrm{Re}_{lo}\sqrt{\left(\frac{d_i}{d_{coil}}\right)} \qquad \& \qquad Pe = \frac{\Delta x h_{fg}}{L\, g}$$

Pe denotes the Pierre Number, *Δx* is the quality difference over the length *L* and *g* is the gravitational acceleration.

Wongwises and Polsongkram (2006a) fitted their data to a mathematical formulation (also employed by Akhavan-Behabadi et al. , 2009) based on a modified Cavallini and Zecchin (1974) correlation for straight tubes, which is shown in Eq. (2.38):

$$Nu_{tp} = j_1 Dn_{eq}^{j_2} \mathrm{Pr}^{j_3} X_{tt}^{j_4} Bo^{j_5} \qquad \mathbf{(2.38)}$$

Where j_1, j_2, j_3 , j_4, *and* j_5 denote the correlation empirical constants. Most of researchers developed their correlation by fitting only their measurements for specific fluid and limited geometric and operating conditions within error band of 30%.

2.5 Boiling heat transfer and pressure drop in straight tubes

Flow boiling in minichannel straight tubes was tested by several researchers for a wide range of operating conditions and fluids. Flow boiling heat transfer and pressure drop characteristics of Refrigerant R134a in vertical micro-tubes was measured by Owhaib (2007) using three diameters were tested 1.7, 1.224, and 0.826 mm. Additionally, The author visualized the flow boiling for developing a micro channel flow pattern map where bubble nucleation to dry out regimes were observed.

Choi et al. (2007) experimentally studied flow boiling of CO_2 in horizontal micro-tubes of 1.5 and 3 mm in diameter with 2 and 3 m in length. The dry out started earlier with the increase of heat flux, mass flux, saturation temperature and with decreasing the tube diameter. They found that all the correlations utilized for validation under predicted the experimental data and were unable to predict the high nucleate boiling of CO_2, they developed asymptotic models and modified the nucleate boiling suppression factor and convective boiling enhancement factor to be suitable for both turbulent and laminar flow. The dry-out of CO_2 was starting earlier compared to R134a as a result of its lower ratios of liquid/vapour viscosity and density resulting in more nucleation.

Ribatski et al. (2006) reviewed the suitability of micro and macro scale correlations for microchannel flow heat transfer and pressure drop. Generally, the pressure drop increases with the increase in mass velocity G and decreases in the saturation temperature. Furthermore, none of heat transfer correlations were able fully to predict their data set. This was a result of the contrasting trends between experimental data itself. Generally, the heat transfer coefficient increases as the diameter decreases and with the increase in heat flux. From the comparison of rectangular and circular channels, they found that the heat transfer coefficient in rectangular channels 3 times that in circular. The authors suggested an explanation as the liquid film is concentrated at the corners of the rectangular channel; a thinner liquid film is formed on the side causing a better heat transfer process. The heat transfer coefficient seems to decrease for qualities larger than 0.7.

Yun et al. (2005) tested the flow boiling of carbon dioxide in microtube with diameters of 2 and 0.98 mm and 1.2 and 0.4 m test section length. The mass flux ranged from 500 to 3570 kg/m^2.s and the heat flux ranged from 7 to 48 kW/m^2 with 5 °C and 10 °C saturation temperature. The heat transfer coefficient before dry out was strongly dependent on the heat flux and mass flux up to Weber number of 100 after this limit it was only function in the heat flux. As the superficial liquid Weber number in their data was greater than 100, nucleate boiling was the dominant where the heat transfer coefficient was a strong function in heat flux before dry out.

Lie at al. (2006) tested the flow boiling of R134a and R407c inside microtubes of 0.83 and 2 mm. They found that the heat transfer coefficient is dependent on the heat flux, mass flux and saturation temperature. In addition the heat transfer coefficient was increasing linearly with the vapour quality except at low mass fluxes with high applied heat fluxes where dry out occurred in case of R134a. The change in heat transfer coefficient to the operating parameters was higher for R407C compared to R134a.

Ong and Thome (2009) examined extensively the flow boiling of three working fluids R134a, R236fa, R245fa with a microchannel tube diameter of 1.03 mm. They classified the flow regime during boiling into three main categories as isolated bubbles, coalescing bubbles and annular flow. The heat transfer coefficient showed a dependence on the heat flux at low vapour qualities for all working mediums. The heat transfer was uniform or decreasing in the isolated bubbles and coalescing bubble regime, the authors interpreted this by the transition from pure bubbly flow to elongated bubbles. The heat transfer was increasing with the mass velocity in the high quality regime (i.e, annular flow regime) with negligible effect of heat flux especially for both R236fa and R245fa. The effect of degree of subcooling was negligible in the saturated boiling regime compared to the subcooled boiling regime.

Huo et al. (2007) tested the available pressure drop correlation against their experimental data on R134a in vertical tubes with diameters 4.26 mm (500 mm length) and 2.01 mm (211 mm length). They considered the acceleration component in their measurement of frictional pressure drop and the churn flow pattern was dominant in their observation. The pressure drop per tube length was larger for the tube with small diameter. The pressure drop was increasing with both the mass velocity and exit vapour quality but decreasing with pressure due to the increase in liquid film viscosity.

Pamitran et al. (2008) examined the pressure drop in micro-tubes with CO_2 as a working fluid. The effect of vapour density, liquid viscosity and surface tension was significant on pressure drop compared to liquid density and vapour viscosity. As a result carbon dioxide has a lower pressure drop when compared to R22 due to its high vapour density (i.e. lower flow to same mass flux) and lower liquid viscosity and surface tension.

It could be concluded that the flow boiling heat transfer in straight tubes has been investigated extensively where early dry out occurs for vapour qualities less than 0.7. The minichannel straight tubes produced high heat transfer coefficient before dryout compared to conventional scale tubes (larger than 6 mm). Most researchers support that nucleation is dominant in straight tubes where the heat flux effect is significant. Extensive research has been done using R134a and CO_2 on such tube scales.

2.6 Flow regimes in helical and curved tubes

In helical or vertical U-curved tubes, centrifugal force has a strong influence on the distribution of the phases, which in turn affects the flow and heat transfer characteristics. In helical coils, stratified wavy flow is dominant at low quality regimes in helical coils. At high qualities, the flow is annular or semi-annular. Stratified wavy flow is similar to stratified (effect of gravity overcomes the vapour shear effect) but the vapour shear is larger at the interface. Intermittent flow (slug flow) is a special stratified flow but with large amplitude waves that reach the top of the tube. The annular flow is characterized by a liquid film between the vapour core and tube wall.

Cui et al. (2008) investigated the diabatic flow pattern of R134a through 3D-micro finned tube with 11.2 mm inner diameter. The mass velocity varied from 61 to 315 kg/m^2.s and the heat flux varied from 2 to 21.8 kW/m^2. The authors observed three different regimes stratified wavy, intermittent flow, and annular flow as shown in figure 2.4. Transition from the intermittent flow to annular flow occurred at Martinelli Number of 0.7 compared to 1.6 in straight tubes. Mass velocity /vapour quality based flow pattern map was utilized to predict the transition from stratified wavy to annular or intermittent flow. Transition vapour quality between intermittent to annular was found between 0.2 and 0.3. Stratified flow was dominant at mass velocities less than 100 kg/m^2.s.

(a) Stratified flow (b) Stratified wavy flow

(c) Intermittent flow (d) Annular flow

Figure 2.4: Flow regimes observed by Cui et al. (2008).

Li et al. studied the flow pattern through helical coil with 7.6 mm internal diameter, 300 mm coil diameter, and 30 mm helical pitch. The mass velocities varied from 50 to 500 kg/m^2.s. In ascending flow, they observed stratified wavy (SW), annular (A), and wavy annular (WA), and intermittent flow (I) which includes bubbly flow and plug flow. In the descending flow, they observed stratified flow (S), super-slug flow (SS), annular flow (A) and intermittent flow (I). Due to the effect of centrifugal force, it is depicted that the transition to annular flow starts early compared to straight tube (nearly at vapour quality of 0.12 and 0.13 for ascending and descending flow respectively). At low vapour quality the intermittent flow occupies a narrow margin as depicted in figure 2.5.

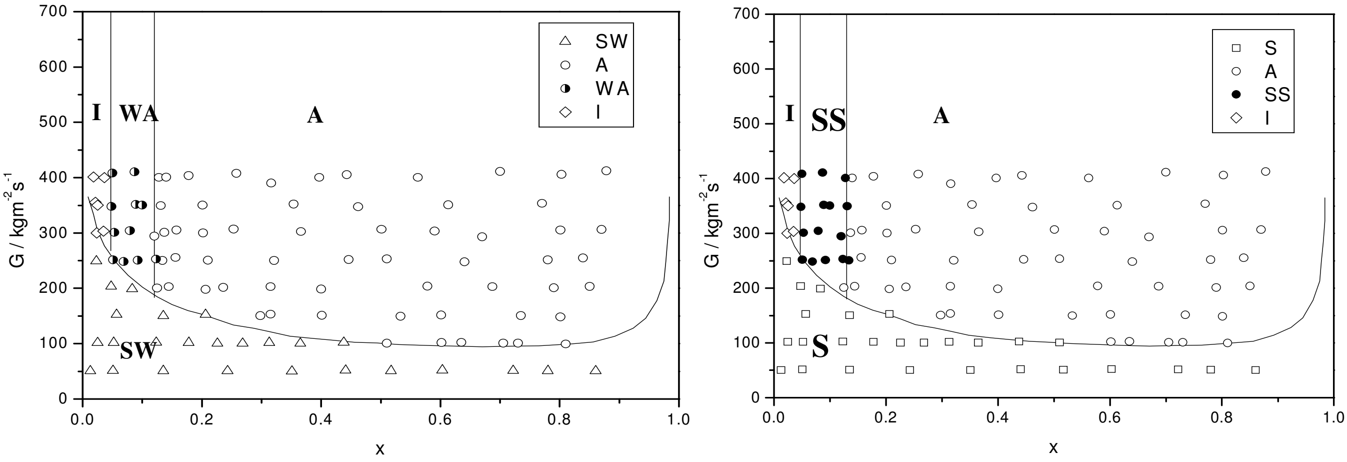

A. Ascending flow pattern map

B. Descending flow pattern map

Figure 2.5: Flow pattern map in helical coils observed by Li et al.

Banerjee (Isheda, 1981) suggested that as the liquid density is usually considerably larger than that of the gas, it is reasonable to suppose that liquid would be forced to the outer wall of the coiled tube by centrifugal forces. However, the most significant effects of coiling are seen in annular flow. It was observed that for certain ranges of liquid and gas flow rates the liquid travelled on the inner wall of the tube as shown in figure 2.6. This phenomenon is called "Film inversion". The film inversion was found to occur at low liquid but high gas flow rates. At low gas flow rates, the liquid film in upward helical concurrent flow was located mainly on the outer wall of the tube figure 2.6a. As gas velocity increased, the liquid film moves first into the neutral position shown in figure 2.6b and then into the inverted position in figure 2.6c. As the gas velocity continued to increase, the film moved further and further up the inner wall of the tube as shown in figure 2.6d. At higher velocities liquid was entrained from the film and thrown onto the outer part of the wall as in figure 2.6e.

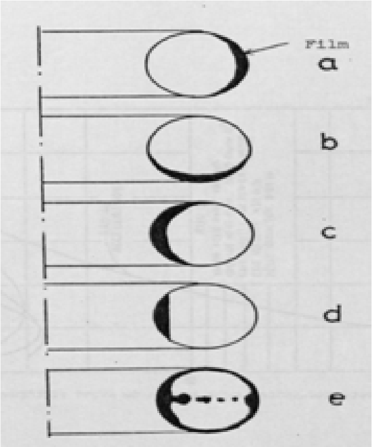

Figure 2.6: Liquid film movement at various gas mass flow rates.

Yi et al. (2003) tested small tube diameter (4mm) helical coiled pipes for evaporators in looped heat pipe systems. The authors found the following flow regimes: single phase liquid, bubbly flow, slug flow and unsteady stratified flow as shown in figure 2.7. No annular flow was observed as the flow velocity was quite small.

(a) bubbly flow (b) slug flow

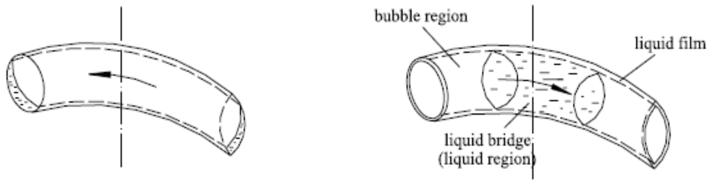

(c) the stratified flow in the pulsatile ascent of two-phase fluid (d) the slug flow in the pulsatile descent of two-phase fluid

Figure 2.7: Two-phase flow patterns in coiled pipes.

It could be concluded that annular flow appears at high mass velocities in intermediate to high vapour qualities. Stratified flow appears for low mass velocities for the entire range of vapour quality. Film inversion was observed at high gas flow rates and low liquid mass flow rates.

2.7 Dryout

It is important to monitor the CHF for the safety of thermal operation of heat exchangers in nuclear reactor bundles, refrigeration evaporators and once through boilers. In the case of miniature cooling, CHF is important for microevaporators used in cooling electronic devices to avoid their failure and for evaporators used in air conditioning and refrigeration to properly size such evaporators (Thome, 2010).

Several definitions are associated with critical heat flux such as burn out, Departure from Nucleate Boiling (DNB), and dryout. The transition from highly efficient nucleate boiling or forced convective vaporization heat transfer to inefficient vapour dominated heat transfer mechanism occurs at CHF (critical heat flux) i.e., general definition of phenomenon. The DNB describes this transition in subcooled flow boiling and low quality region occurs in nuclear reactors applications. The dryout describes the breakup of thin liquid film on the wall in annular flow in saturated flow boiling. Burnout (BO) is used when the actual physical destruction of the test section occurs due to DNB or dryout (Jensen, 1980).

In dryout, evaporating annular film starts to break up at some parts of tube surface and liquid entrains in the vapour core and no liquid exist to absorb the heat supplied to the wall at such points, hence the wall temperature starts to increase. This condition occurs at high values of vapour qualities. A progressive dryout in horizontal straight tubes tends to occur along a region of the tube length instead of occurring “simultaneously” around the entire perimeter as typically imagined in vertical tubes. Since the annular film is thinner at the top of the tube compared to the bottom in horizontal tubes, dryout tends to occur first at the top and then progress around the perimeter towards the bottom, creating a dryout zone along the tube.

In figure 2.8A dryout first occurs at the top of the tube where the liquid film is thinner denoted as $x_{d,i}$ (Onset dry out quality) and then progresses downward around the perimeter (section B-B) until reaching the bottom section (C-C) at vapour quality $x_{d,e}$ (complete dryout quality) afterwards fully developed mist flow starts to occur where the wall is completely dry. The onset of dry out at the top of the tube is accompanied by drastic drop in the heat transfer coefficient relative to that prior dry out (annular flow typically) and then becomes uniform in the mist flow regime. As depicted in figure 2.8B, Regions AB, BC, CD represent the annular flow, dryout, and mist flow regions with onset of dryout at $x_{d,I}$ and complete dryout at $x_{d,e}$.

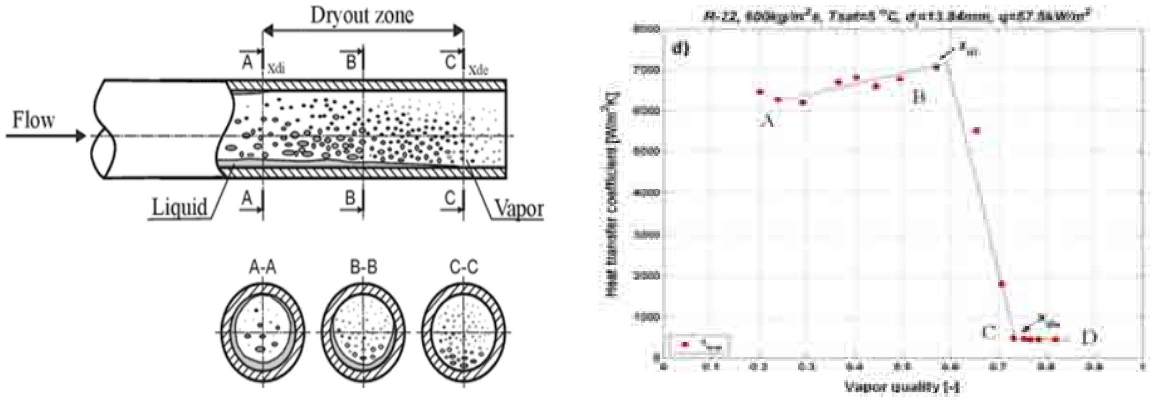

(A) Dryout zone in a horizontal tube. (B) Variation in local heat transfer coefficient.

Figure 2.8: Dry out in straight tubes using R22 in 13.84 tube diameter (Thome, 2010).

Researchers use different methods to identify dry out (Rashid and Palm, 2010) such as using the boiling curve or following the standard deviation in wall temperature. In case of using the boiling curve (figure 2.9), where the temperature close to the tube outlet is measured (usually last thermocouple position on tube surface , the heat flux at the first shift from the boiling curve is termed dryout incipience heat flux and the corresponding vapour quality is termed as dryout incipience quality. Beyond the dryout incipience point, a small increase in heat flux gives a much larger increment in wall superheat as compared to the conditions before dryout incipience. Further increment in heat flux raises the average wall temperature continuously even after waiting for long time and as the average wall superheat becomes very large and dryout completion occurs and the power is cut-off.

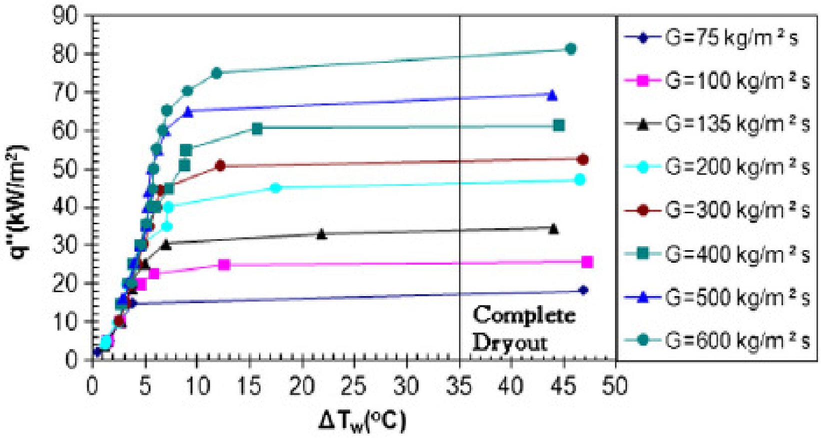

Figure 2.9: Boiling curves near the tube exit at T_{sat}=27 °C for tube diameter d_i=1.22.

The other method is to track the change in wall temperature (Rashid and Palm, 2010). For instance in figure 2.10, the temperature distribution at different thermocouple axial position is uniform at heat flux q=65 kW/m^2 for microchannel tube with diameter d_i = 1.55 and mass velocity G=500 kg/m^2.s. By increasing the heat flux in stepwise to q=69 kW/m^2 the wall temperature monotonically increased at the tube exit until complete dryout occurs.

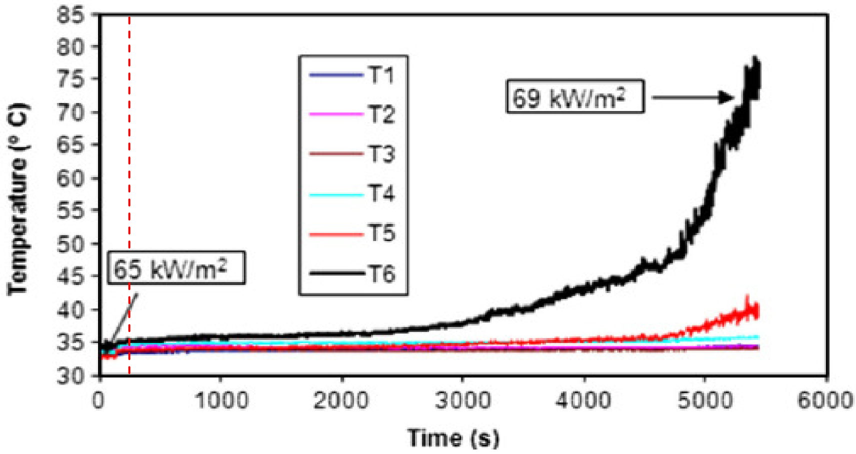

Figure 2.10: Variation of wall temperature at critical heat flux condition.

In case of helical coils as depicted in figure 2.11, the position at which the first dry out would start would be the inner and top sides thermocouple at position A (dashed line at quality 0.72). Then the dryout of the film will creep towards other radial position where the film dry out occurs then at bottom side and then outer side (position c) and completely vanish at local quality close to 1. The outlet flow condition from the test section is in superheated condition as the equilibrium vapour quality larger than 1.

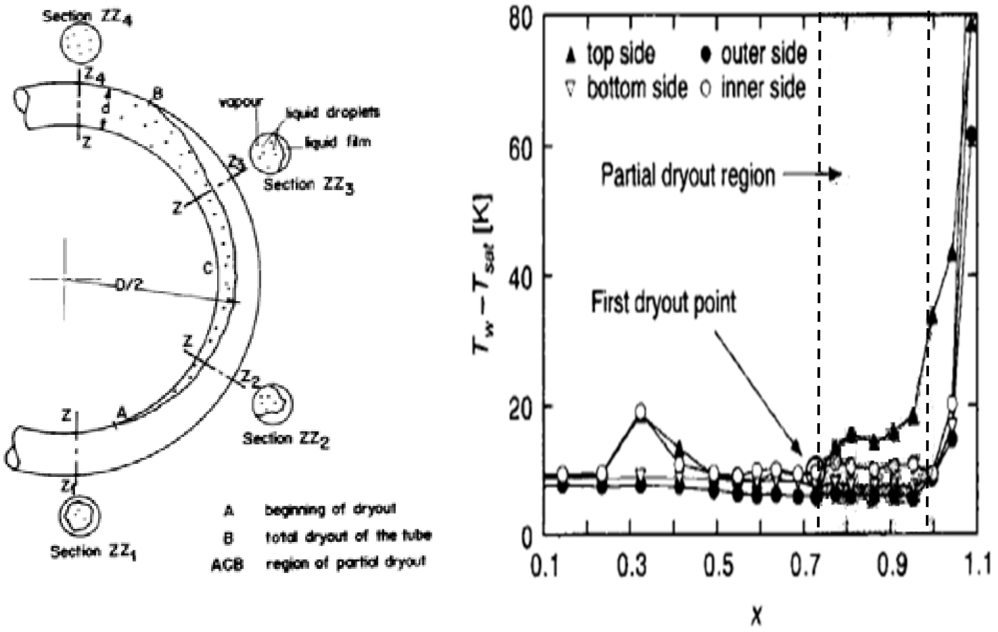

Figure 2.11: Partial dryout in helical coils.

In annular flow with moderate heat flux, the inlet subcooling has insignificant effect on the first dryout quality. Decreasing the pressure reduces the vapour density and leads to a higher vapour superficial velocity for the same mass velocity. This makes the effect of secondary flow much stronger and more liquid is pushed from the outer side to the inner side. Accordingly, the first dryout quality is retarded where dryout first occurs on the inner side. The coil diameter affects both the flow regime and first dryout quality. Increasing the coil diameter reduces the centrifugal forces on the droplets and reduces the effect of the secondary flow and redeposition rate. Accordingly, the first dryout decreases (faster dryout) with increasing the coil diameter. Increasing the heat flux generates more bubbles and activates more nucleation sites. As a result the liquid entrainment (liquid leaving the liquid film) increases with the increase of heat flux and faster dryout occurs (less first dryout quality). The effect of heat flux was found to be insignificant at high dryout qualities as the nucleation mechanism is suppressed.

The effect of mass velocity at two extreme cases: the first one when the pressure is low and coil diameter is small (large redeposition) and second case when the pressure is high and coil diameter is large (large entrainment). Increasing the mass velocity will decrease the critical quality in case of large redeposition but increase it in case of large entrainment (Chung et al., 2002). Dry out starts from the top and bottom of the tube in case of significant centrifugal forces. On the other hand, as gravity becomes significant the dryout is retarded at the bottom of the tube. In case of dryout starting at the outer surface rather than the inner surface, it is usually explained by film inversion. Dryout occurs at large vapour quality (0.9 to 1) in case of low pressure, large mass velocity, small coil diameter (P=5 bar, G=500 kg/m^2.s, d_{coil}=215 mm) as shown in figure 2.12a. Early dryout at vapour quality of 0.2 occurred in case of large pressures, low mass velocities, large coil diameters (P=7 bar, G=300 kg/m2.s, d_{coil}=485 mm) as shown in figure 2.12b.

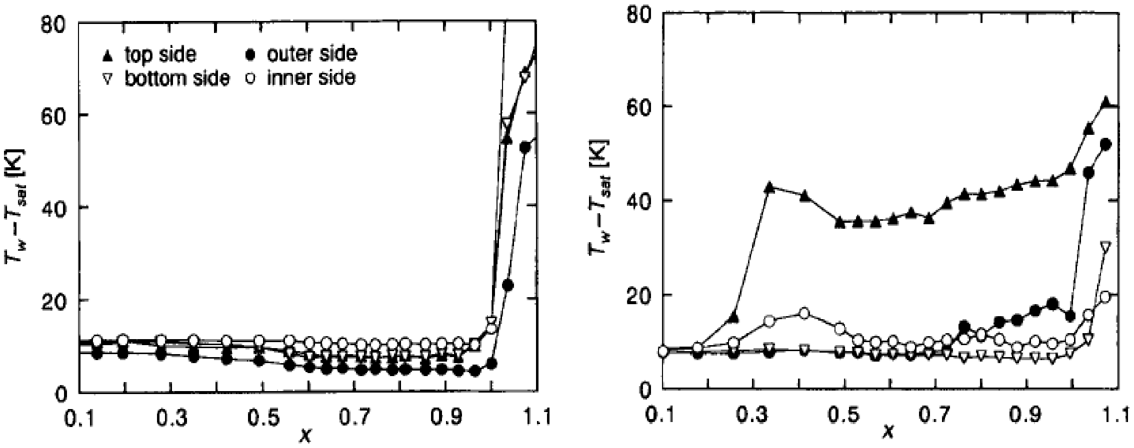

A. Wall temperature in high mass velocity, low pressure, small coil diameter.

B. Wall temperature in low mass velocity, high pressure, large coil diameter.

Figure 2.12: Spread of dry out in helical coils (Chung et al., 2002)

Styrikovich et al. (1984) reported that the dryout region in coils is better than in straight tubes i.e., the wall temperature jump is smaller and the dry out temperature profile is smoother in coils as depicted in figure 2.13. The temperature jump was lower at high pressure and mass velocities. Additionally, the temperature rise on the internal side is much higher than that on the external side. The authors found that the flow direction (upward or downward) does not affect the critical heat flux. The critical quality (coil exit quality) was decreasing with the mass velocity and heat flux. The upward flow shows better heat transfer coefficients in the dry out region compared to the downward flow (lower wall temperature).

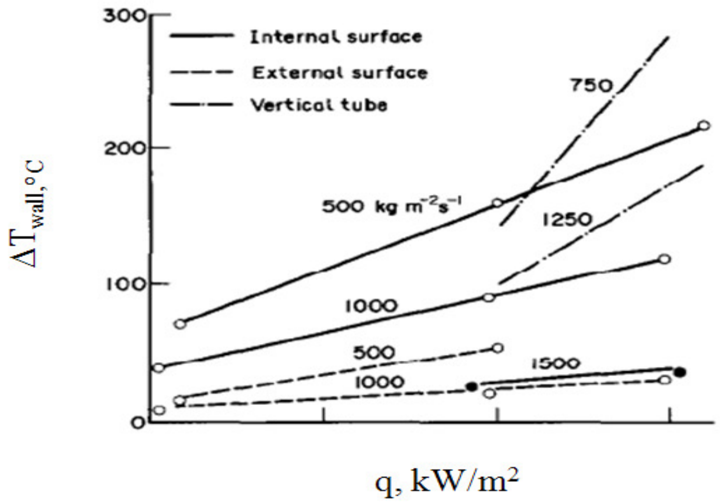

Figure 2.13: Temperature jump ($T_{wall,max}$-T_{sat}) at helical coil sides and vertical straight tubes (P=176 bar).

It could be concluded that better critical heat flux characteristics could be achieved by operating at lower pressures and using small coil diameters due to the improvement in secondary flow at such operating conditions. Some discrepancies exist in literature for the effect of mass velocity on dryout quality. Helical coils has better CHF characteristics as the temperature profiles of the tube surface are smoother after dryout compared to straight tubes.

2.8 Pressure drop in helical coils correlations

Several authors developed correlations to predict the two-phase pressure drop in helical coils. Usually, the two-phase pressure drop is correlated in terms of the liquid-only two-phase multiplier as followed by Zhao (2003) and Guo (2001). Other researchers developed their correlations based on the liquid two-phase multiplier as followed by Cui (2008). Cioncolini et al. (2008) found that Zhao correlation was the most accurate in predicting their data at low test pressures although the correlation was originally developed at high pressures.

Adiabatic two-phase pressure drop has been extensively investigated including air/water, air/glycerin/water, air/butanol/water, air/water/glycol, and air/ isobutyl/alcohol. Lochart Martinelli correlation has shown satisfactory agreement with the experimental measurement for adiabatic pressure drop systems. However, correlations that have been proposed to predict two-phase diabatic flow (phase change) pressure drop fails to predict the data outside their validity range especially for subcooled flow boiling. Straight tube pressure drop models were able to predict the pressure drop in helical coils with very high accuracy after incorporating the effect of heating during saturated boiling as suggested by Trasasova (Cioncolini et al., 2008). A correction factor has been multiplied to two-phase Lochart-Martinelli straight tube correlation as:

$$\phi_l^2 = \frac{\Delta P}{\Delta P_l} = \left(1 + \frac{C}{X_{tt}} + \frac{1}{X_{tt}^2}\right)\left[1 + 0.0044\left(\frac{q}{G}\right)^{0.7}\right] \tag{2.39}$$

It should be mentioned that the liquid two-phase flow multiplier ϕ_l^2 is based on the liquid flow $G(1-x)$ but the liquid-only two-phase multiplier ϕ_{lo}^2 is based on the total flow of the mixture as a liquid G.

Hart et al. (1988) measured the pressure drop and developed the criterion for film inversion based on their measurements for air/water and air/water/glycol (25%) for small liquid hold-up (void fraction) ≤0.3. The tube diameter was 14.66 mm with coil diameter of 421 mm. The superficial air velocity was within 10 m/s to 40 m/s. On the other hand, the liquid superficial velocity was between 8×10^{-4} to 3×10^{-2} m/s. The authors measured the radial (perpendicular to main flow direction) and axial (in the main flow direction) pressure drops in two-phase flow. They found that the axial pressure drop increases with the liquid hold-up, and that the two-phase pressure drop in helical coils was up to 30% higher compared to single-phase gas flow in helical coils. However, the two-phase pressure gradient in straight tubes was higher by 70% compared to gas flow in straight tubes in straight tubes i.e., the two-phase multiplier in helical coils is smaller than that in straight tubes. The authors developed analytical model to predict the film inversion where the liquid is accumulated on the inner side of the coil as:

$$\frac{\dot{m}_v}{\dot{m}_l} > 195\left(\frac{\rho_g}{\rho_l}\right)^{0.5}\left(\frac{\mu_g}{\mu_l}\right)^{3/4} \qquad \textbf{(2.40)}$$

Bi et al. (1997) measured experimentally the pressure drop of water/steam mixture upward flow through stainless-steel helical coil of 1.3 m coil diameter and 16 mm inner tube diameter and 2 mm wall thickness. They tested their coil at pressures of 40 to 180 bar, mass velocities of 400 to 1400 kg/m^2.s and heat fluxes from 100 to 700 kW/m^2. The two-phase multiplier was increasing with increasing the vapour quality and reducing the system pressure as depicted in figure 2.14. They developed a correlation for the two-phase multiplier for liquid only flow as:

$$\varphi_{lo}^2 = 1 + \left(\frac{\rho_l}{\rho_v} - 1\right)\left(C + x^2\right) \qquad \textbf{(2.41)}$$

They correlated the C – coefficient according to the system pressure range as:

$C = 1.955x^{0.698}(1-x)^{0.291}$ for pressures from 40 to 100 bars. **(2.42)**

$C = 1.378x^{0.277}(1-x)^{0.0738}$ for pressures from 140 to 180 bars. **(2.43)**

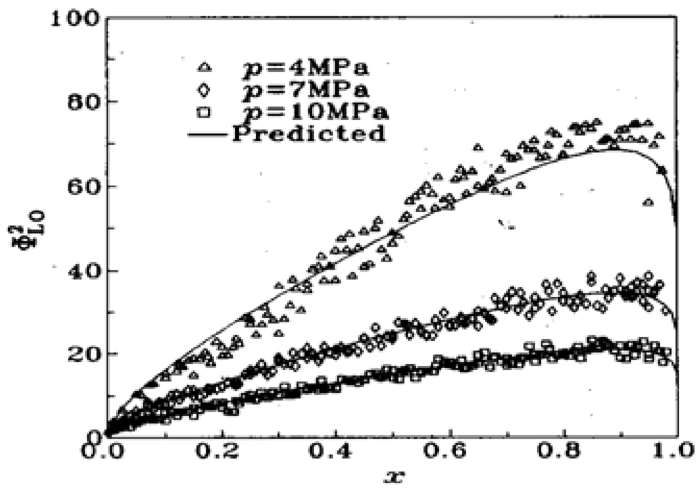

Figure 2.14: Variation of liquid only two-phase multiplier and x.

Banerjee et al. (1967) (from: Ishedia, 1981) tested nine coils with different coil diameter and helical angles with three liquids of different viscosities with air at various pressures. They used the Lochart-Martinelli method but with friction factors of helical coils (Modified Lochart-Martinelli) so that:

$$-\left(\frac{dP_F}{dZ}\right)_{tp,c}=\phi_v^2\left(\frac{dP_F}{dZ}\right)_{v,c}=\phi_l^2\left(\frac{dP_F}{dZ}\right)_{l,c} \tag{2.44}$$

Where c and *F* subscripts denote to helically coiled tubes, and frictional pressure drop component respectively. They derived Martinelli parameters for helical coils as:

$$\chi=\sqrt{\left(\frac{dP_F}{dZ}\right)_{l,c}/\left(\frac{dP_F}{dZ}\right)_{v,c}} \tag{2.45}$$

The authors found no effect of coil pitch on pressure drop and hold up for the range of pitches investigated.

Kim et al. (2000) developed a new correlation for the friction factor of two-phase flow in helical coils using a correction factor for straight tube two-phase friction factors in the following form:

$$f_{tp,c} = f_{tp,st}(1+\mathrm{Re}_{lo}(d_i/d_{coil})^2)^{1/20} \qquad \mathrm{Re}_{lo}(d_i/d_{coil})^2 > 6 \tag{2.46}$$

Where $f_{tp,st} = 0.079(Gd_i/\mu_{tp})^{-0.25}$ and $\mu_{tp} = \rho_{tp}\left[\frac{x\mu_g}{\rho_g}+\frac{(1-x)\mu_l}{\rho_l}\right]$

Domanski and Hermes (2006) developed a new correlation for predicting the pressure drop in 180 ° bend (U-bend or return bend) for R22 and R410A with tube diameters 3.3 mm and 11.6 mm, bend diameter 12.8 mm to 75 mm and curvature ratio (d_i/D_{bend}) from 2.3 to 8.2. The authors provided excellent review for the correlations developed for predicting the pressure drop in return bends. The two-phase pressure drop correlation was formulated using the Buckingham-PI theorem as a function of refrigerant properties, flow characteristics, and bend geometry. They modified Müller-Steinhagen correlation for straight tubes by using a curved multiplier as shown in equation (2.47).

$$\left(\frac{\Delta P_F}{\Delta L}\right)_{tp,bend} = \Lambda\left(\frac{\Delta P_F}{\Delta L}\right)_{tp,st} \tag{2.47}$$

$$\Lambda = a_0\left(\frac{Gxd_i}{\mu_v}\right)^{a_1}\left(\frac{1-x}{x}\right)^{a_2}\left(\frac{\rho_l}{\rho_v}\right)^{a_3}\left(\frac{2R_{bend}}{d_i})\right)$$

Santini et al. (2008) measured the diabatic pressure drop in stainless steel helical coil with tube inner diameter of 12.53 mm and coil diameter of 1 m. The mass velocity varied from 192 to 824 kg/m^2.s and heat flux range from 50 to 200 kW/m^2. They correlated the single phase friction factor in helical coils using equation (2.48) and two-phase pressure drop using equation (2.49). They reported that both gravitational and acceleration pressure drops are insignificant except at low quality region with low mass velocity and high pressure. The authors reported that pressure drop decrease with increasing the pressure leading to lower specific volume of the mixture i.e; lower two-phase velocity. The two-phase pressure drop in helical coils confirmed to be higher than that in straight tube as the pressure drop was proportional to the mass velocity to the power 1.91 instead of the 1.8 used in straight tubes.

For single phase flow: $f = 0.00206 + 0.085\,\mathrm{Re}^{-0.278}$ **(2.48)**

For two-phase flow $\left(\frac{\Delta P_F}{dz}\right)_{tp} = k(x)\frac{G^{1.91}}{d_i^{1.2}\rho_m}$ **(2.49)**

where $k(x) = -0.0373x^3 + 0.0387x^2 - 0.00479x + 0.0108$ **(2.50)**

Table 2.6 provides a list of the correlations developed specifically for helical coils. It could be concluded that several authors investigated the pressure drop in helical coils using different fluids where the two-phase pressure drop is correlated using the two-phase multiplier. Guo correlation has been utilized to predict the two-phase pressure drop due its reasonable average prediction compared to other pressure models (Guo et al., 2001).

Table 2.6: Pressure drop empirical correlations in helical coils.

Correlation	Coil Type	Fluid	Mathematical Formulation
Zhao et al. (2003)	Smooth	Steam/Water	$\phi_{lo}^2 = 1 + \left(\frac{\rho_l}{\rho_v} - 1\right)\left(0.303x^{1.63}(1-x)^{0.885}\,\mathrm{Re}_{lo}^{0.282} + x^2\right)$
Guo correlation (Zhao et al.,2003)	Smooth	Steam/Water	$\phi_{lo}^2 = \psi_1\psi\left(1 + x\left(\frac{\rho_l}{\rho_g} - 1\right)\right)$ $\psi = 1 + \frac{x(1-x)(1000/G-1)(\rho_l/\rho_g)}{1 + x(\rho_l/\rho_g - 1)}$ G≤1000 $\psi = 1 + \frac{x(1-x)(1000/G-1)(\rho_l/\rho_g)}{1 + (1-x)(\rho_l/\rho_g - 1)}$ G≥1000 $\psi_1 = 142.2\left(\frac{P}{P_{cr}}\right)^{0.62}\left(\frac{d_i}{D_{coil}}\right)^{1.04}$
Guo et al. (2001)	Smooth	Steam/Water	$\phi_l^2 = 1 + (4.25 - 2.55x^{1.5})G^{0.34}$
Bi correlation (Zhao et al.,2003)	Smooth		$\phi_{lo}^2 = 1 + \left(\frac{\rho_l}{\rho_v} - 1\right)\left(c + x^2\right)$ $c = 0.14691x^{1.3297}(1-x)^{0.59884}(d_i/D_{coil})^{-1.2864}$
Chen and Zhou (Guo et al.,2001)	Smooth	Air /Water	$\xi = 2.06\left(\frac{d}{D}\right)^{0.05}\mathrm{Re}_{tp}^{-0.025}\left[1 + \varepsilon\left(\frac{\rho_v}{\rho_l} - 1\right)\right]^{0.8}$ $* \left[1 + x\left(\frac{\rho_l}{\rho_v} - 1\right)\right]^{1.8}\left[1 + \varepsilon\left(\frac{\mu_v}{\mu_l} - 1\right)\right]^{0.2}$ ε =void fraction ξ dimensionless parameter similar to ϕ_{lo}^2
Li et al.	Smooth	R134a	$\phi_{lo}^2 = 1 + CC\left(\frac{\rho_l}{\rho_v}\left(\frac{\mu_g}{\mu_l}\right)^{0.25} - 1\right)$ $CC = 2.477\left(\frac{G}{100}\right)^{0.35} x^{1.1}(1-x)^{0.4} + x^{2.5}$
Cui et al. (2008)	3D microfin	R134a	$\phi_l^2 = 1 + \frac{48.2}{\chi_{tt}} + \frac{1}{\chi_{tt}^2}$ Stratified Flow Regime $\phi_l^2 = 1 + \frac{59.8}{\chi_{tt}} + \frac{3.5}{\chi_{tt}^2}$ Annular Flow Regime

2.9 Miniature cooling systems with helical coil evaporator

Miniature cooling systems have shown advantages in applications such as electronics cooling and personal cooling systems for hazardous environments. Nowadays, the computational requirements for simulating complicated phenomena led to the need of producing more efficient CPUs (computer processing units). The development of higher power CPUs requires more effective cooling technologies than those currently used e.g. air cooled and liquid cooled heat sinks. Also, currently used cooling technologies are not sufficient to cool the CPU whose integration rate is becoming much denser. Using miniaturized vapour compression systems offer lower junction temperature and increase in processing speed using highly compact evaporators attached to the CPU for heat rejection.

Additionally, portable cooling is an important application for using miniaturized cooling systems where light weight cooling systems with reasonable cost and reliable operation are required in special applications such as military or fire fighting operations or working in chemical processes with toxic environments. Due to the need for developing reliable and efficient cooling systems operating at comfortable and safe temperature range, many research carried out including experimental and theoretical investigations of different heat exchanger designs.

Table 2.7 shows recent studies carried out to develop miniature cooling systems with maximum dimensions reported of 318 mm in Ernst (2005). He developed a cooling suit based on vapour compression system with the evaporator consisting of semi-circular tubes attached to aluminium foil integrated inside the garment with 1.9 mm hydraulic diameter. Mongia et al.(2006), Trutassanawin et al. (2006), and Nnanna (2006) have developed systems for cooling electronic devices where the microchannel evaporators integrated to the CPU unit. Heydari (2002) developed a mathematical model for a miniature cooling system to supply cold air for personal computer cooling. For developing a cooling suit, Wu et al. (2010) utilized a Wankel compressor, a multiport extruded tube (MPET) condenser and a spirally coiled tube in a shell evaporator with the chilled water passing through the tube and refrigerant R22 boiling in the shell. The tested system had a coefficient of performance up to 3.25.

As discussed in chapter 1, helical coils may be used as passive heat transfer enhancement techniques in both single and two-phase heat transfer processes. The enhancement is produced by centripetal forces that produce a pressure gradient in the cross section of the tube thus inducing a secondary flow in the vapour core in the form of double vortices (known as Dean Eddy or Double Eddy).

In addition, the fluid elements with high axial velocity are pushed toward the outer wall thus improving the distribution of liquid film on the tube wall (Welti-Chanes et al., 2003). Enhancement ratios of up to 2.15 were reported by Akhavan Behabadi et al. (2009). Therefore utilising helical coils in the evaporator and condenser of refrigeration systems have the potential of producing compact system and/or improved performance.

Kim et al. (2000) measured the local flow boiling heat transfer of R-22 in helically coiled evaporator with 1 mm tube diameter and coil diameters of 31, 34, and 46.2 mm. the heat transfer coefficient was found to increase with the mass velocity and heat flux. Dryout was found to occur at vapour quality close to 0.6. They observed from their measurements that the smaller coil diameter the higher heat transfer coefficient. The pressure drop was found to increase with both the heat flux and mass velocity. Next, they tested experimentally the performance of miniature air cooled helically coiled evaporators using R-22 (Kim, 2001). Finally, they analytically modelled the performance of the helically coiled miniature evaporator (Kim et al., 2006). The authors utilized fixed dry out quality of 0.6 and the single phase heat transfer correlation and void fraction to express their boiling heat transfer coefficient after dryout quality.

Table 2.7: Miniature cooling systems.

Author	Cooling load [w]	System Description	Application	Refrigerant	COP
Ernst (2005)	100 to 300	Evaporator tubes were integrated in the garment, multiport extruded tube condenser, reciprocating compressor, expansion valve. Overall System Dimensions 318 mmx273 mmx152 mm.	Portable cooling suits	R134a	-
Mongia et al. (2006)	50 to 60	Copper cold plate microchannel array (80 μm wide) evaporator, reciprocating compressor, multiport extruded tube condenser, capillary tube	Electronic cooling	R600a (Isobutane)	(2.25 to 4) $Cop_{system,exp}$
Trutassanawin et al. (2006)	up to 286	Rotary compressor, Directly attached microchannel cold plate 41 channel (0.8 mmx2.3 mm) evaporator, air cooled microchannel condenser, manual expansion valve Evaporator Dimensions 32.8 mmx2.3 mm Overall condenser dimensions 45 mmx180 mmx25 mm. Compressor dimensions 85mmx166mm	Electronic cooling	R134a	(2.8 to 4.7) $Cop_{system,exp}$
Nnanna (2006)	606, 343, 271, 152	Evaporator directly attached cold plate 89 mmx152 mm to the simulated electronic device, TXV valve, air cooled condensing unit	Electronic cooling	R134a	-
Heydari (2002)	120 to 150	Reciprocating compressor, Air cooled evaporator, air cooled condenser, capillary tube.	Electronic cooling	R134a	(1.5 to 5) $Cop_{system,pred}$
Wu et al. (2010)	50 to 350	Water cooled miniaturized spiral-tube type evaporator (Refrigerant in shell), multiport extruded tube condenser, Wankel rotary compressor, capillary tube. Overall system dimensions of 250 mmx260 mmx120 mm.	Portable cooling	R22	(1.7 to 3.25) $Cop_{system,exp}$

Wessapan et al (2010) developed a portable cooling system with helically coiled condenser and air cooled evaporator using R22 as a refrigerant. The diameters of the helical coil and the tube used were 150mm and 9.3mm respectively. They showed that helically coiled tube condenser gave higher heating capacity and cooling COP compared to conventional condensers.

It could be concluded that very limited work has been reported on incorporating helically coiled evaporators and condensers with the refrigerant passing through the coil in a small vapour compression cooling systems. An investigation of the performance of small scale vapour compression refrigeration system equipped with helically coiled evaporator and condenser using both theoretical analysis and experimental testing has been performed and presented in chapter 6.

2.10 Heat transfer enhancement using nanofluids in helical coils

Nanoparticles improve the energy transport properties of the base fluid by increasing the effective thermal conductivity and heat capacity, which enhances the heat transfer rate of the nanofluid. The chaotic movement of ultra fine particles accelerates the thermal dispersion process in the fluid which leads to a steeper temperature gradient between the fluid and the wall augmenting heat transfer rate (Li and Xuan, 2002). Nanoparticles increases the thermal conductivity and reduces the specific heat of the fluid leading to a better dispersion of heat inside the fluid which will reduce the accumulation of heat in fluid elements near the heated wall and the nanofluid becomes cooler close to the wall compared to the case of base fluid i.e, steeper temperature gradient close to wall. The applications using these Nanofluids include engine cooling to reduce the engine weight and fuel consumption (Saripella et al.,2007) increasing the critical heat flux in boilers (Cheng, 2009) and developing compact heat exchangers for medical applications (Sundar et al., 2009).

Recently, many researchers have experimentally investigated the effect of nanofluids in enhancing the heat transfer coefficient in straight tubes in laminar flow such as Heris et al. (2006) using alumina (Al_2O_3), copper oxide (CuO) and copper (Cu) nanoparticles dispersed in water, Murshed et al. (2007) using titanium dioxide (TiO_2) dispersed in water, and Rea et al. (2009) using Al_2O_3 and zirconia in the laminar flow regime. Heris et al.(2006) reported enhancement of 35% compared to pure water flow at the same test conditions using Al_2O_3, CuO, and Cu particles. Murshed et al. (2007) found an enhancement by up to 14% using TiO_2 with volume fractions between 0.2% to 0.8%. Rea et al. (2009) reported up to 27% enhancement using Al_2O_3 up to 6% volume fractions.

Also some researchers investigated the nanofluids performance in straight tube in the turbulent flow regime such as Nguyen et al. (2005) who investigated numerically the utilization of two nanofluids water/γ-Al_2O_3 (Re=2000, and 4000) for the cooling of microprocessors. The authors examined copper rectangular slot-type heat sink with flow cross-sectional area of 3 mm x 48 mm with supplied heat over 10 mm × 10 mm contact area. The authors tested volume fractions of nanoparticles from 0% to 7.5%. The wall shear stress was increasing appreciably with the particle volume concentration since the nanofluid viscosity was considerably increased with respect to that of the base fluid. The wall friction was higher in case of Ethylene Glycol/γ-Al_2O_3 compared to water/γ-Al_2O_3. The reduction of the microprocessor temperature using nanofluid was insignificant at lower levels of heat supplied.

Vasu et al. (2008) developed empirical model with ε – NTU method under turbulent flow conditions with Al_2O_3 dispersed in ethylene glycol/H_2O mixture as coolant in automobile flat tube plain fin compact heat exchanger with 3.73 mm tube diameters. The increase of the volume fraction of the nanoparticle concentration increases the cooling capacity in moderate manner and pressure drop decreases with the increase of nanfluid inlet temperature. Rostamani et al. (2010) numerically investigated the turbulent flow (Reynolds number 20,000 to 100,000) of nanofluids with different volume concentrations (0 to 6%) of nanoparticles flowing through a two-dimensional duct under constant heat flux ($50W/cm^2$) condition using copper oxide (CuO), alumina (Al_2O_3) and titanium oxide (TiO_2) nanoparticles and water as the base fluid. The results showed an increase of volume concentration resulted in an increase in both the heat transfer coefficient and shear stress. Due to the higher value of viscosity of CuO in comparison with other nanofluids, the shear stress of CuO nanofluid was higher than other fluids. The enhancement of heat transfer at lower Reynolds number was significant.

Torii (2007) measured the convective heat transfer of nano diamond particles in water flow in 1m long, 4 mm diameter tube at three volume fractions 0.1%, 0.4%, 1% with Reynolds number ranged from 3000 to 6000. The particles were assumed circular based on the TEM image (Transmission Electron Microscope). Significant enhancement relative to water especially at high Reynolds number and volume fractions were observed. The enhancement in heat transfer (up to 25 %) was higher than the enhancement in thermal conductivity (up to 15% at 5% volume fraction) and was explained by several factors including the reduction in boundary layer thickness, suspension and migration of particles.

Bianco et al. (2011) numerically investigated the turbulent flow in straight tube with 1 meter long and 10 mm diameter with heat flux of 500W/m^2. The turbulent flow was modelled using the single phase and mixture model approaches. The particle size was assumed 38nm with volume concentration 0%, 1%, 4%, and 6% and varying the Reynolds number from 10,000 to 100,000. The velocity profile became fully developed at larger dimensionless axial distance (Z/D) with increasing the Reynolds number due to the effect of thinning (suppression) the boundary layer at the same location. The enhancement ratio was estimated to be 4%, 19%, 33% for Al_2O_3 volume concentrations of 1%, 4%, and 6% respectively. The CFD prediction was close to Pak and Cho (1998) correlation (originally developed for Al_2O_3) and Maiga correlation (2006) but lower than Li and Xuan correlation (2002) that was originally developed for Cu and is based on dispersion model.

Experimental data of Heat transfer and pressure drop using nanofluids in helical coils are very limited. Wallace (2010) measured the heat transfer rate using nanofluids in helically coiled cooler however the author did not report any measurements of heat transfer coefficients or wall temperatures. Akhavan-Behabadi and Hashemi (2010) tested the pressure drop using CuO dispersed in oil flow in a helical coil but no heat transfer measurements were carried-out. With the lack of experimental data, the CFD prediction of single phase heat transfer becomes a useful tool to investigate the performance of nanofluids in helical coils. Chapter 7 investigates the effect of particle concentration and Reynolds number on the thermal performance of Al_2O_3 nanofluid in helically coiled tubes.

2.11 Summary

From the literature review the following conclusions can be made:

- Flow boiling in small helical coils studies are very limited except the work done by Kim et al. (2000) using R22 in 1 mm diameter tube. Therefore, it would be beneficial to test other fluids such as R134a using different fluids for better understanding of the flow behaviour through helical minichannels.
- The secondary flow effect was found to be significant at low testing pressures and small coil diameters.
- Although there are several methods for the prediction of heat transfer in helical coils, much of those correlations are limited to a specific fluid, mass velocities, and heat fluxes ranges. There is a necessity to predict the boiling heat transfer accurately for better design of helical coil heat exchangers.
- Dry out in helical coils was found to have lower surface to fluid temperature difference at the critical heat flux compared to straight tubes thus reducing the deterioration in thermal performance compared to straight tube at dryout conditions.
- Although there were helical coils tested for miniature systems such as the work done by Wu et al. (2010) and Kim (2000) the performance, tests were carried out using R22 and no data was reported for such systems using R134a. As the thermal properties of R134a (Pr_l= 3.472 at 15°C saturation temperature) do not differ significantly from those of R22(Pr_l= 2.443 at 15°C saturation temperature), it is expected that the trends of the results will not be qualitatively different from those produced with R22. However, investigating the heat transfer performance of R134a in small diameter tubes helical coils is necessary

to provide quantitative results that can be used in the design of small scale evaporators in addition to emphasizing the trends of flow boiling in small diameter tubes.

CHAPTER 3

Experimental Facility

3.1 Introduction

The literature review presented in chapter 2 indicated the possibility of enhancing the flow boiling process by helically coiling the tubes. Also, reducing the diameter of heat transfer channels was shown to increase the boiling heat transfer coefficients. Generally channels with hydraulic diameter larger than 3 mm are denoted as conventional channels. Channels with diameters between 3 mm to 1 mm are denoted as minichannels. Microchannels are denoted for tubes with hydraulic diameter less than 1 mm (Thome, 2010). Research on flow boiling in helical coils with small and micro tube diameters is limited. Therefore an experimental facility was constructed to investigate flow boiling heat transfer inside helically coiled tubes with internal diameters smaller than those reported in literature. Four helical coils were tested, three of which were electrically heated and the fourth was heated by water flow outside the coil. As the heat transfer performance of small diameter coils was necessary for the development of miniature vapour compression cooling system, the helical coils were tested in a system where a compressor is used to circulate the working fluid. Thus results will be representative of practical applications. This chapter reports on the design, installation, commissioning of the experimental test facility and its instrumentation. A detailed description of the test rig was made, followed by a detailed description of the helical coil test sections and the instrumentation used to measure the boiling heat transfer coefficient. The process of data reduction and the formula used in deriving the heat transfer coefficients of boiling inside the helical coils was then described. Finally, the calibration of the various instrumentation used then described followed by the method used in estimating the uncertainty in the results.

3.2 Description of the experimental rig

Figure 3.1 shows a schematic diagram of the experimental facility. It is a vapour compression system with R134a serving as the refrigerant. The system consists of a reciprocating compressor, water cooled condenser, manual expansion valves and the helical evaporators. The compressor is Danfoss BD35F with displacement volume of 2 cm^3 directly driven by a dc 12 Volt power supply. The compressor was designed to operate at cooling capacity lower than 100W and especially manufactured for R134a which commonly used in portable fridges. The compressor was driven by TTi TSX1820 Power Supply (18V, 20A, 360W). The compressor is supplied with electronic unit as depicted in figure 3.2 to control the compressor speed via a resistor (R1) as depicted in the circuit diagram. 2 kilo Ohm Vishay resistor (manufacturer number: 534-8872-202) has been selected to control the compressor speed. A jumper connection has been used instead of the Thermostat to ensure continuous operation of the compressor during the experimentation. The compressor speed was varied between 2000 to 3500 rpm.

Heat transfer preliminary calculations were performed assuming water temperature difference through the evaporator and condenser of 5 °C to determine the length of the evaporator and condenser. Both suction and discharge pressures were used to size the manual expansion valve and hot gas bypass valves were selected based on liquid or gas valve sizing methods described in Skousen (2004).

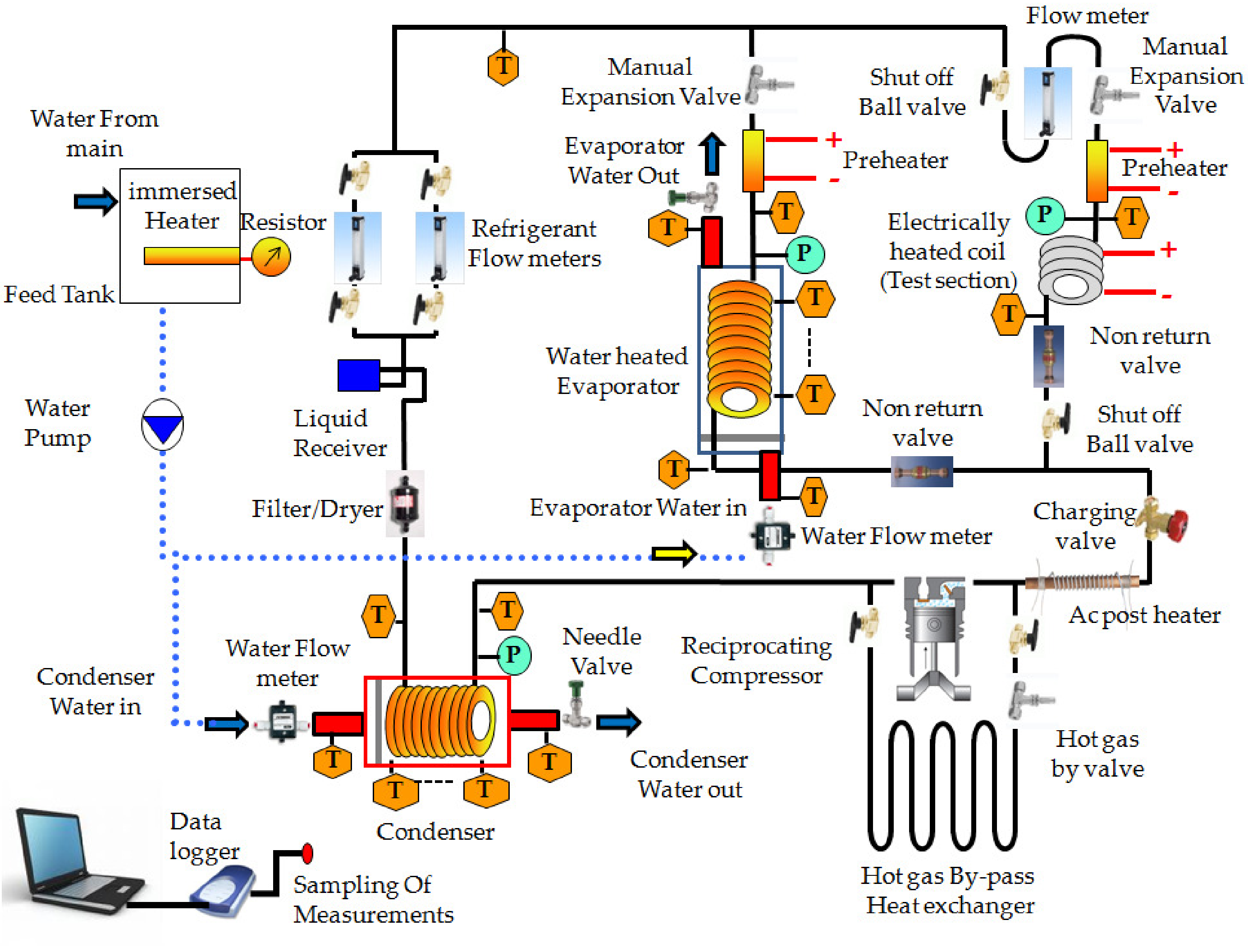

Figure 3.1: Schematic diagram of helically coiled tubes experimental test facility

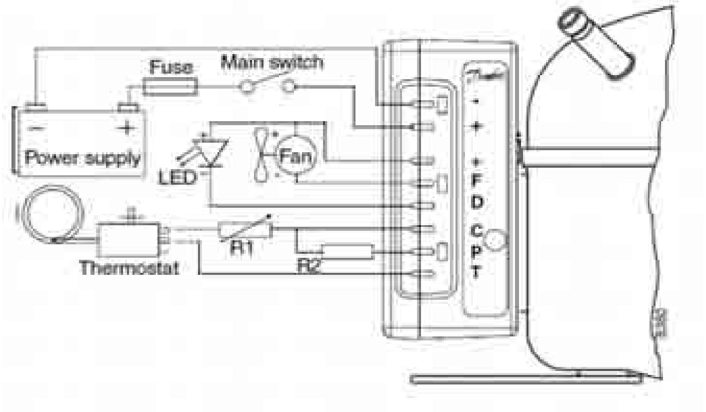

Figure 3.2: Danfoss reciprocating compressor BD35F and the electronic control unit.

A counter flow helically coiled condenser was made from copper tube length of 1.5 m and 2.8 mm tube diameter. The coil diameter was 30 mm with 7 mm coil pitch and 16 turns. Figure 3.3 shows the shell side of the condenser with 16.5 cm long where flanges were welded then drilled to fit the gasket and caps at both ends of the condenser to seal the water side. The outside and inside diameters of the shell were 57.25 mm and 50 mm respectively.

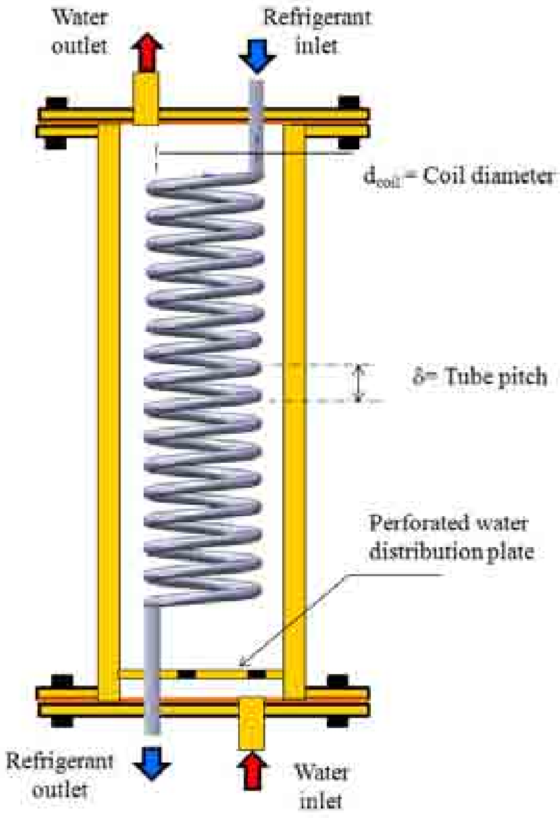

Figure 3.3: Condenser shell and end caps connected to the shell flanges.

Manual expansion valves with flow discharge coefficient (C_v) up to 0.004 of the small series (Swagelok B-SS6mm) were utilized to throttle the refrigerant from the condensation pressure to the evaporation pressure. A manual expansion valve has been fitted before each coil.

After the condenser, the refrigerant flow was split into two parallel circuits to direct the refrigerant to the tested coil. One circuit contained the water heated evaporator and the second contained the electrically heated evaporator. Before each evaporator a preheater was used to control the refrigerant inlet conditions to the test section. The preheaters were heated using 15 m electrically insulated wires with 0.5 mm diameter wrapped around the tube before the evaporator. After the evaporator test sections, non return valves were installed to prevent backflow of refrigerant. Danfoss NRV6 with ¼ inch flare connection non-return valves were used. Also the electrically heated evaporator was fitted with shut off valves at the inlet and outlet to allow changing the test section easily. Swagelok B-42s shutoff valves with 6 mm connections were used. The valves are ¼ turn between the position of fully open and completely closed position. After the evaporator flow circuits and before the compressor, rope heaters were utilized to ensure complete evaporation of the refrigerant before entering the compressor suction. The heaters were model FGR-030/240V with total length 1 m with 125 W heating powers at 240 V. The power was controlled Via Dimmer switch that control the applied voltage to the heaters.

To control the flow rate through the compressor, hot gas bypass line was installed. The bypass line has a hot gas by pass valve and heat exchanger as shown in figure 3.1 and pictorially in figure 3.4. A brass hot gas by pass valve of medium series with flow discharge coefficient (C_v) up to 0.04 (Swagelok B-4MG) with ¼ in connections has been used to control the recirculation ratio of refrigerant through the compressor. The bypass valve was connected to serpentine heat exchanger to make the refrigerant reject the heat before returning to the compressor suction. A serpentine tube air cooled heat exchanger was fitted after the hot gas bypass valve to avoid compressor overloading. The heat exchanger is 2 m long with 8 segments each 25 mm long with ¼ OD tubing.

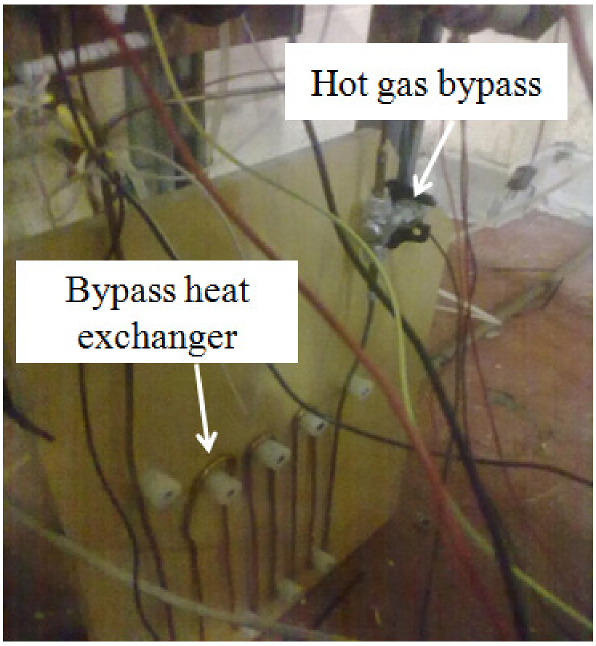

Figure 3.4: Hot gas by-pass heat exchanger and By-pass valve.

After the condenser, Danfoss DML-032 filter dryer with ¼ inch flare was installed to purify the refrigerant from moisture and solid particles in the system. The refrigerant leaves the compressor as superheated vapour at the condenser pressure, passes to the condenser where it condenses and leaves the condenser as subcooled liquid. The liquid refrigerant passes in the manual expansion valve which controls both the pressure and flow rate of the refrigerant. The refrigerant passes through the evaporator test sections followed by the post heater and then returns to the compressor.

3.3 Evaporator test sections

Four helical coils were tested to evaluate the flow boiling heat transfer coefficient inside tubes with different diameters. Three of the coils were electrically heated and the fourth was heated using water flow in a shell surrounding the coil. The water heated evaporator is a counter flow helically coiled tube in a shell evaporator. The helical coil was made from copper tube with length of 1 m and 2.8 mm tube diameter. The coil diameter was 30 mm with 7 mm coil pitch and 10.5 turns. The shell side of the evaporator was 12 cm long where flanges were welded then drilled to fit the gasket and caps at both ends of the evaporator to seal the water side. For water heated evaporator, the thermocouples wires were soldered to the coil surface then sealed by heat insulation then passed through an opening in the shell which was sealed using Araldite see figure 3.5a. The electrically heated coiled were electrically insulated from the test rig by using refrigeration hoses made from Synthetic rubber and clips (Rs No: 288-4080) to tighten the hoses to electrodes at both ends of the test section as depicted in figure 3.5. The clips are designed to seal pressures up to 136 bar and the minimum and maximum internal diameters of the clips are 9 to 12 mm (see figure 3.5b).

Figure 3.6 shows the preparation process of the electrically heated coils. The thermocouples were first attached to the coil surface then fixed by using adhesive aluminium foil sheets as shown in figure 3.6A. The coil pitch was then adjusted using electrically insulating tape as shown in figure 3.6B. The coil was thermally insulated using fiber wool layers and finally covered by insulating tape layer as shown in figure 3.6C.

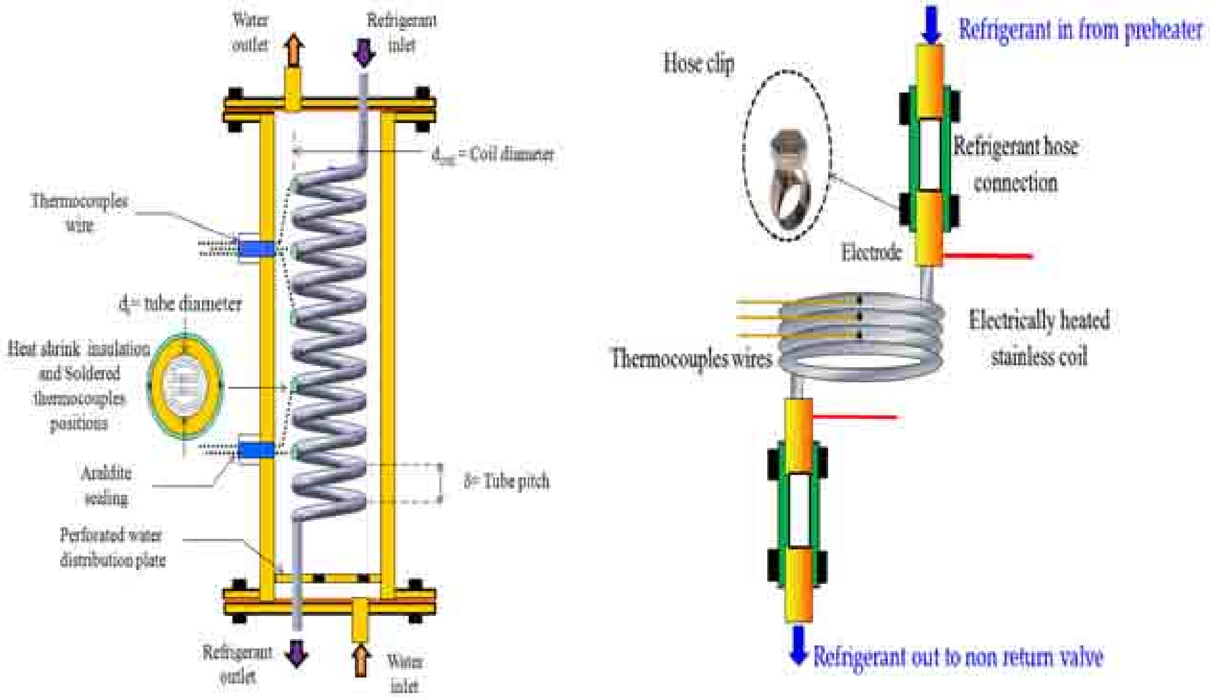

A. Water heated evaporator B. Electrically heated evaporator

Figure 3.5: Schematic of evaporator coils.

A. Wall thermocouples fixed to the tube surface using aluminium foil tape.

B. Adjustment of coil pitch using insulating tape.

C. Thermal insulation using fiber wool and insulation tape.

Figure 3.6: Preparation of electrically heated helical coils.

Table 3.1 summarizes the geometrical specifications of the four coils tested and the method utilized for heating and the surface material.

Table 3.1: Geometric specification of the different coils tested (all dimension in mm)

Coil	Heating Method	Coil material	d_{coil}	d_o	d_i	δ_{coil}	N_{turn}	L_{evap}
Coil A	Water heated	Copper	30	4	2.8	7	10.6	1
Coil B	Electrically heated	Stainless steel	60	2.65	2	8	3	0.56
Coil C	Electrically heated	Stainless steel	60	2.05	1.55	8	3	0.56
Coil D	Electrically heated	Stainless steel	60	1.47	1.1	8	3	0.56

3.4 Instrumentation

The test facility was instrumented by temperature, pressure and flow rate measuring devices to enable evaluating the boiling heat transfer coefficient in the helical evaporator and analyse the overall performance of the refrigeration system. These measuring devices will be described in the following sections.

3.4.1 Thermocouples

All thermocouples utilized in the measurements were T-type thermocouples. The thermocouples attached to the surface of the helical coils were Omega 5TC-TT-TI-36-1M with specification described in Table 3.2.

Table 3.2: Specification of wall surface thermocouples.

Thermocouple specification	Code	Code interpretation
Thermocouple Insulation	TT	PFA
Thermocouple type	T	T type thermocouple
Wire Gauge	36	36 AWG
Thermocouple Length	1M	1 m

To measure the refrigerant temperature at different position in the test rig probe thermocouples model: Omega TJC100-CPSS-M050G-100 with specifications summarized in table 3.3 was used. The positions of different thermocouples utilized in the experiment are summarized in table 3.4. Twelve probe thermocouples were utilized to measure the temperature of the refrigerant and water at the various points in the refrigeration system. The surface thermocouples were positioned each 2 turns for the water heated coil since it has 10.5 turns. In case of the electrically heated coil, the thermocouples were positioned each half turn.

Table 3.3: Specification of probe type thermocouples.

Thermocouple specification	Code	Code interpretation
Lead wire length	100	91cm
Thermocouple type	CP	T thermocouple
Sheath material	SS	Stainless steel
Sheath diameter	M050	0.50 mm
Junction	G	Grounded
Probe length	100	100 mm

Table 3.4: Positions of thermocouples utilized in the experiment.

Probe TC	Thermocouple location	Surface TC from inlet	EH	WH
Probe-1	Refrigerant evaporator inlet	Surf-1	1/2 turn	2.5 turn
Prob-2	Refrigerant evaporator outlet	Surf-2	1/2 turn	4.5 turn
Prob-3	Refrigerant condenser inlet	Surf-3	1 turn	6.5 turn
Prob-4	Refrigerant condenser outlet	Surf-4	1 turn	8.5 turn
Prob-5	Water condenser inlet	Surf-5	1 .5 turns	
Prob-6	Water evaporator inlet	Surf-6	1 .5 turns	
Prob-7	Water condenser outlet	Surf-7	2 turns	
Prob-8	Water evaporator outlet	Surf-8	2 turns	
Prob-9	Refrigerant evaporator steel coil inlet	Surf-9	2.5 turns	
Prob-10	Refrigerant evaporator steel coil outlet	Surf-10	2.5 turns	
Prob-11	Compressor suction line			
Prob-12	Before expansion valve			

TC=Thermocouple, EH= electrically heated, WH= water heated

3.4.2 Pressure transducers

The pressure transducers utilized were Druck 4-20 mA output signals model PTX-7517. 100 ohms resistances have been connected to the data logger terminal board to convert the current signal to voltage signal (up to 2 Volt). The pressure at the evaporator side was measured by 10 bar absolute pressure transducer while 15 bar pressure transducer was used at the compressor discharge line. The electrical wiring of the transducer with the data logger is illustrated in figure 3.7.

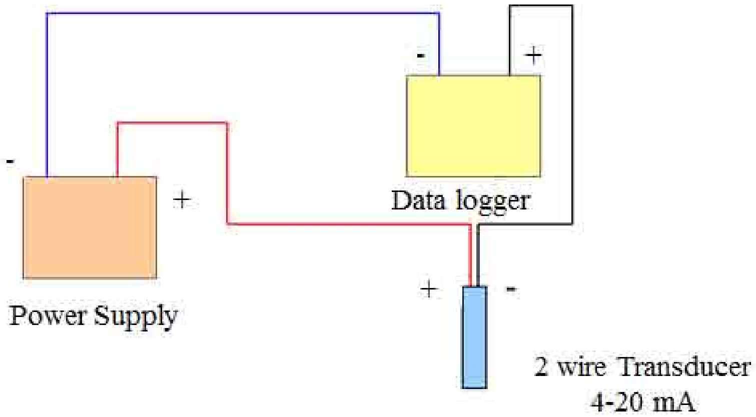

Figure 3.7: Electrical wiring diagram of pressure transducers.

3.4.3 Flow meters

Omega FLR-1009 flow meters with 50-500 ml/min was used to measure the water flow through the water cooling evaporator while Omega FLR 1010 with 100-1000 ml/min was used for measuring the water flow rate through the condenser. The electrical wiring diagram for the water flow meters is depicted in figure 3.8. The output signal from the flow meter varies between 0 to 5 V DC. In order to adapt the signal to the data logger two resistances were connected on the data logger terminal board to resize the signal to be less than 2.5 Volt.

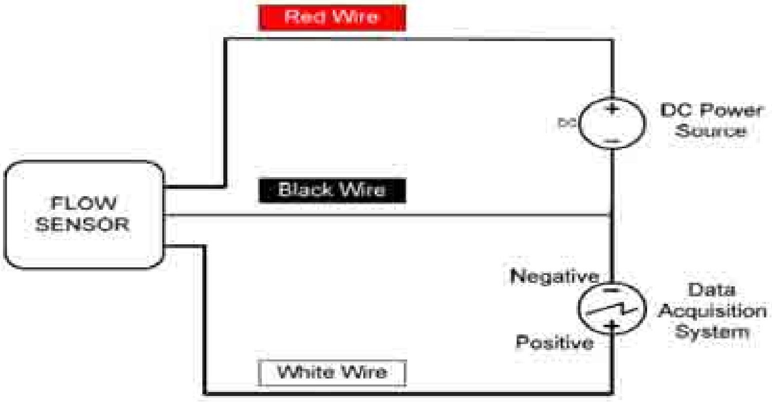

Figure 3.8: Electrical wiring diagram of mass flow meters.

The refrigerant mass flow meters are VA (variable area) flow meter manufactured by Roxspur measurement and control ltd. The flow meter scaled from 7 to 47 ml/min calibrated for R134a with uncertainty of 1.25% FS (full scale) according to manufacturer.

3.4.4 Power measurements

Three helical coil evaporators were heated electrically by passing dc current through the tube wall directly. The rate of power supplied was determined from the measured current and voltage across the coil. The dc current was measured using the power supply digital reading with accuracy ± (2.5% reading + 2 digits) while the voltage was measured using Maplin-M5010 with accuracy of ± (0.5% reading) based on manufacturer data. This would lead to uncertainty less than 0.4 Amp and 0.02 v.

3.4.5 Data acquisition

Thermocouples were connected to Pico TC-08 data loggers which were connected to a personal computer. Each Pico-logger contains 8 thermocouple ports which were connected to miniature thermocouple connections fitted at the open end of the thermocouples. The pressure transducers and water flow meters were connected to Pico 1012 general purpose voltage input datalogger which was connected to terminal board to convert current signal into readable voltage signal. The heating dc voltage, current and refrigerant volume flow rates were recorded manually.

After the start up of the rig, it was allowed to run long enough at the desired data point to achieve steady state condition where the change in thermocouples readings was not exceeding 0.2 °C (Generally 15 minutes were required to reach the steady state) then the temperature and pressures were recorded. Fifty readings were taken at a time interval of

2 seconds for each data point. The average value of the recorded fifty readings was utilized in the analysis of heat transfer calculations.

3.5 Instrument calibration

In the experimental study, a number of measuring instruments have been used for determination of heat transfer coefficient and fluid flow through the helical coils. These include thermocouples and pressure transducers to measure the temperatures and absolute pressure at the coil inlet. Additionally, water and refrigerant flow meters were used to measure flow rates, dc voltage and current meters were used to measure the power input. All measuring devices were calibrated and their uncertainties were determined.

3.5.1 Calibration of thermocouples

The T-type thermocouples were calibrated with respect to standard PT 100 Platinum Resistance Temperature Detector (RTD). All thermocouples immersed in water bath at the same level and the RTD was connected to DataTaker data logger utilized in the calibration process as the RTD has 4 wiring cable. The water bath equipped with a thermostat that can be used to control the rate of heat supplied to water bath. The calibration process was started by adjusting the thermostat to a specific temperature. The bath was left for approximately 15 minutes to reach steady state temperature. Reading of thermocouples and RTD were recorded then the thermostat was then set to a new point and the procedure was repeated. The calibration curve for thermocouple SURF-8 thermocouple is shown in figure (3.9). The calibration formulas for different thermocouples are summarized in section 3.8.2.

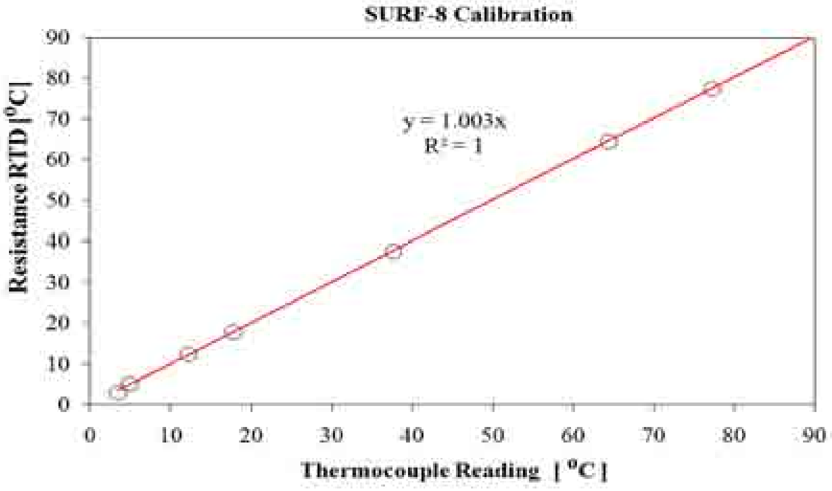

Figure 3.9: Calibration of thermocouples.

3.5.2 Calibration of pressure transducers

The absolute pressure transducers were calibrated against accurate pressure gauge in pressurized water cylinder (Water Dead-Weight Testers). The pressure was increased to the desired value using a rotating screwed shaft. The voltage reading from the transducer was recorded against the summation of the gauge pressure and atmospheric pressure. The stability error of transducer was ± 0.1% FS per one year and the uncertainty of the standard gauge was ± 0.04 bar. According to manufacturer catalogue the uncertainty associated with the temperature variation (-10 to 50 °C temperature range) would be less than ± 1% FS. The hysteresis, repeatability, curve fit uncertainties has been combined and are listed in appendix A.

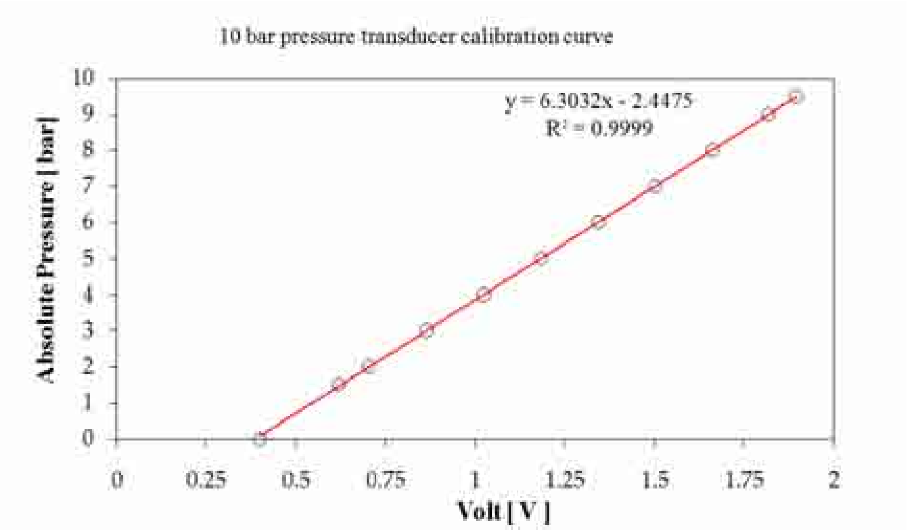

Figure 3.10: Calibration of suction pressure transducer.

3.5.3 Calibration of water flow meters

The water flow meters have been calibrated by calculating the time required to fill a tank with 500 ml capacity. For each data point, the turbine flow meter voltage signal was recorded and the volume flow rate was calculated as the volume (500 ml) divided by the time required to fill it. The uncertainty associated with collecting tank method was found to be 9.7 ml/min and the uncertainty associated with curve fitting was found to be 5.1 ml/min. The overall uncertainty (including calibration and curve fitting uncertainties) of the calibrated flow meters was found to be 11 ml/min (1% Fs for condenser flow meter (Omega FLR-1010) and 2% FS for the evaporator flow meter (Omega FLR-1009)). The details of uncertainty calculations are listed in appendix A.

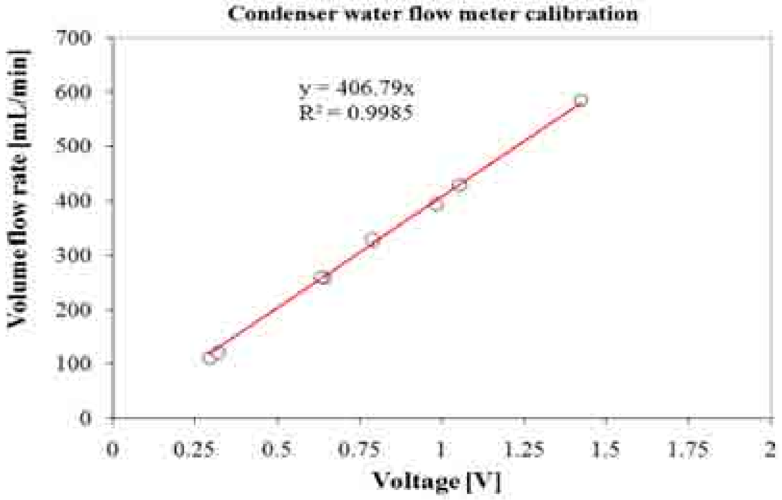

Figure 3.11: Calibration of Omega FLR-1010 water flow meter.

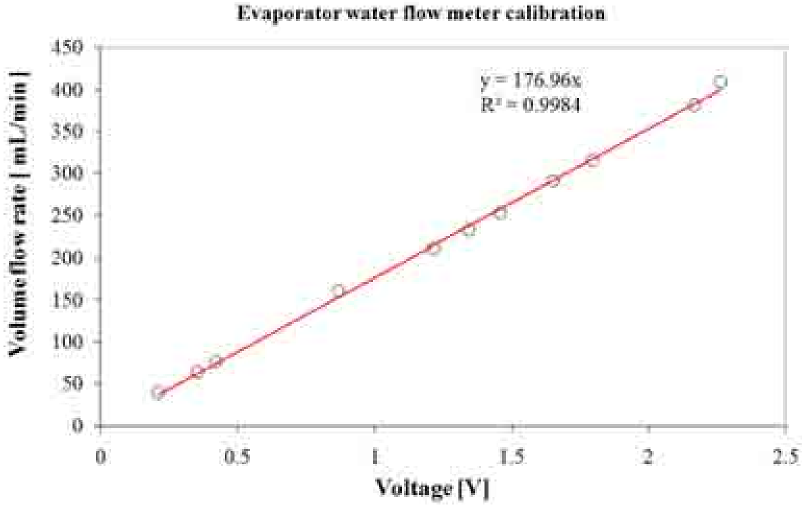

Figure 3.12: Calibration of Omega FLR-1009 water flow meter.

3.6 Experimental procedure

Once the construction of the test rig was completed, it was charged with nitrogen under the pressure of 16 bars. Soap solution was utilized around connections and fittings to verify that the system has no leaks. Then the test rig was evacuated and the system was charged with R134a where the throttle valve was kept at small opening and the heaters were turned off. Water was fed by gravity from water tank to the condenser. The system was kept charging until no bubbles appeared in the flow meter glass tube. The expansion valve was then opened until maximum refrigerant flow rate was reached. The post heaters and the condenser water pump were on while keeping the system charging with refrigerant until stable operation was achieved and no bubbles were observed at the flow meter glass. After charging the system, testing commenced where the mass velocity was controlled via the expansion valve, the pressure at the coil inlet was controlled using the compressor speed and hot gas bypass valve opening, and the heat flux was controlled by controlling the supplied electrical current from TTi TSX1820 digital power supply. The thermocouples, pressure transducers, and flow meters readings were recorded and averaged for the analysis of heat transfer. The equations utilized for deriving the heat transfer coefficient from experimentally measured flow rates, pressures and temperatures will be described in the following sections. The main difference between electrical heating and water heating is the method of calculating the wall temperature inside the tube by deriving it from heat conduction governing equations. Section 3.6.1 describes the experimental methods used in studying flow boiling heat transfer coefficients. Section 3.6.2 describes the analysis used for water heated evaporator and section 3.6.3 is for the electrically heated one.

3.6.1 Techniques in heat transfer coefficients calculation

Researchers in the field of flow boiling have used different methods in evaluating the boiling heat transfer coefficient. Some researchers measured the local heat transfer coefficient at the axial and circumference of the tube utilizing the local wall and refrigerant temperature profiles where the refrigerant pressure distribution is assumed linear in the two-phase region. Other researchers measured circumferentially averaged heat transfer coefficient at different locations along the coil where the wall temperatures are averaged at each axial position by measuring the top and bottom and side wall temperature. Another approach is to measure the boiling heat transfer by averaging the inlet and outlet refrigerant temperatures and averaging all thermocouples temperatures attached to surface. The last approach requires the inlet and outlet condition to be in two-phase conditions and the averaged heat transfer coefficient is plotted versus the mean vapour quality in the test section. The first two approaches are usually used in long test sections or high heat flux conditions where large range of local vapour qualities could be measured during each experimental run. However, the last approach is used when there is no significant change in vapour quality through the test section such as testing high mass velocities or low heat fluxes and a preheater is usually connected before the test section to control the mean quality in the test section. Table 3.5 summarizes the utilization of these three approaches by different researchers and the condition of their test section. In this investigation, the length of test sections was only 560 mm, used heat fluxes less than 12000 W/m^2, and the change in vapour quality through the test section for most of the measured data was less than 0.4 making the last measurement technique suitable for the current study. As a result, all heat transfer coefficient measurements presented in chapter 4 were based on the mean vapour quality.

3.6.2 Data reduction for water heated evaporator

The water temperature difference has been measured to calculate the evaporator load and then divided by the surface area of the coil to determine the heat flux as shown in equations (3.1) and (3.2):

$$Q_{evap} = \dot{m}_w C_w \left(T_{w,in} - T_{w,out}\right) \tag{3.1}$$

$$q = Q_{evap} / \left(\pi d_i L_{evap}\right) \tag{3.2}$$

The inlet enthalpy to the preheater was evaluated at the condenser pressure and the temperatures before throttling from the condenser:

$$h_{in,pre} = enthalpy(P_{cond} \& T_{probe-12}) \tag{3.3}$$

Table 3.5: Boiling heat transfer coefficient measurement approaches.

Measurement Technique	Heat transfer measurement Techniques by researchers
Approach I	Owhid et al.(1968) Steam, Helical coil, d_i=12.5 mm, L_{tube}=3060 mm ,q=60 to 255 kW/m^2
	Kaji(1998) R113, Helical coil, d_i=10 mm, d_{coil}=165 mm, L_{tube}=2000 mm, q=30 to 200 kW/m^2
Approach II	Zhao et al.(2003) Electric Heating Steam, Helical coil, d_i=9 mm, d_{coil}=292 mm, L_{tube}=1380 mm, q=70 to 470 kW/m^2
	Oh et al.(2011) R134a, Straight tube, di=3 mm, L_{tube} = 2000 mm, q=5 to 10 kW/m^2 R134a, Straight tube, di=1 mm, L_{tube} = 1000 mm, q=5 to 10 kW/m^2
	Saithoh et al.(2005) R134a, Straight tube, di=3 mm, L_{tube} = 3235 mm, q=5 to 39 kW/m^2 R134a, Straight tube, di=1.12 mm, L_{tube} = 935 mm, q=5 to 39 kW/m^2
Approach III	Akahavan Behabadi et al.(2009) Water Heating R134a, Helical coil, di=8.28 mm, d_{coil}=305 mm, L_{tube} = 5870
	Cui et al. (2006) Electric heating R134a, Helical coil, di=10 mm, d_{coil}=180 mm, L_{tube} = N/A, q=2 to 22.8 kW/m^2
	Wongwises and Polsongkram (2006) Water heating R134a, Helical coil, di=8.3 mm, d_{coil}=305 mm, L_{tube} = 5786.8, q=5 to 10 kW/m^2
	Yan and Lin (1998) copper plate heating R134a, Straight tube, di=2 mm, L_{tube} = 100 mm, q=5 to 20 kW/m^2
	Kaew-on and wongwises (2009) heating wire R410, multiport tube, di=3.48 mm, L_{tube} = 1250 mm, q=5 to 14.25 kW/m^2

The exit quality from the preheater is equal to the inlet quality to the evaporator which was calculated from:

$$x_{in,evap} = x_{out,pre} = x_{in,pre} + \frac{Q_{pre}}{\dot{m}_{ref} h_{fg}} \tag{3.4}$$

The heat transfer at the preheater was calculated using:

$$Q_{preheater} = V_{pre} . I_{pre} \tag{3.5}$$

Where V_{pre} and I_{pre} are voltage across the preheater wire and supplied electric current to the preheater. The exit quality from the tested coil was calculated from:

$$x_{evap,out} = x_{evap,in} + \frac{Q_{evap}}{\dot{m}_{ref} h_{fg}} \tag{3.6}$$

The mean quality through the tested coil was then defined as:

$$x_m = \frac{x_{out,evap} + x_{in,evap}}{2} \tag{3.7}$$

where x_m is the mean vapour quality through the test section, $x_{evap,in}$ is the inlet vapour quality to the test section and $x_{evap,out}$ is the outlet vapour quality from the test section. The average inside wall temperature was determined from the outside wall temperatures via the relationship detailed in equation (3.8):

$$T_{wall,i} = T_{wall,o} - q * d_i \ln\left(\frac{d_o}{d_i}\right) / (2 * k_{wall}) \tag{3.8}$$

Where $T_{wall,i}$ is the inner average wall temperature, $T_{wall,o}$ is the outer average wall temperature, k_{wall} is the tube copper wall thermal conductivity. The average outer wall temperature was calculated as:

$$T_{wall,o} = (1/N)\sum_{i=1}^{N} T_{wall,o,i} \tag{3.9}$$

Where $T_{wall,o,i}$ is the temperature reading of the ith thermocouple. N is the number of thermocouples used. Finally, the two-phase heat transfer coefficient was calculated as:

$$\alpha_{tp} = \frac{q}{(T_{wall,i} - T_{ref})} \tag{3.10}$$

Where α_{tp} is the average boiling heat transfer coefficient through the helical coil and T_{ref} is the refrigerant saturation temperature measured as an average between the values at the evaporator inlet and outlet.

3.6.3 Data reduction for electrically heated coils

The heat supplied to the evaporator coil was calculated from the electric current measured by the power supply multiplied by the voltage across the test coil measured by the multimeter:

$$Q_{evap} = V_{evap} I_{evap} \tag{3.11}$$

The inner wall temperature was calculated after estimating the heat generation by direct heating in the coil by equation (3.13).

$$V_{metal} = \frac{\pi}{4}\left(d_o^2 - d_i^2\right)L_{evap} \tag{3.12}$$

$$q_{gen} = \frac{Q_{evap}}{V_{metal}} \tag{3.13}$$

After solving the heat conduction governing equations with heat generation in cylindrical co-ordinates (Chung et al., 2002), the inner wall temperature was determined as:

$$T_{wall,i} = T_{wall,o} - \frac{q_{gen}}{k_{wall}}\left(\frac{\left(\frac{d_o}{2}\right)^2 - \left(\frac{d_i}{2}\right)^2}{4} - \frac{\left(\frac{d_o}{2}\right)^2}{2}\ln\left(\frac{d_o}{di}\right)\right) \tag{3.14}$$

The heat flux and heat transfer coefficients were calculated using equations (3.2) and (3.10) respectively.

3.7 Measurements accuracy

Pressure transducers, thermocouples, and flow meters have been calibrated to ensure accurate measurements. The overall accuracy of any measuring device contains random (Precision) and systemic (bias) errors. The random errors (repeatability error) are statistical in nature and are determined from the mean standard deviation with 95 % confidence level as:

$$U_{random} = t_{N-1,95\%} S_{\bar{x}} \tag{3.15}$$

Where: $S_{\bar{x}} = \frac{1}{\sqrt{N}} \sqrt{\frac{\sum_{i=1}^{N} \left(X_i - \overline{X}\right)^2}{N-1}}$, $t_{N-1,95\%}$ is the student distribution factor for a degree of freedom N-1. Where N is the number of data points in the sample.

The systemic errors include the calibration errors, data acquisitions error, and hysteresis errors. The systematic error could be estimated using:

$$U_{systemtic} = \sqrt{\sum_{i=1}^{M} U^{2}{}_{i,systematic}} \tag{3.16}$$

M is the number of systematic error sources. $U_{systematic}$ could be based on the manufacturer data if available or laboratory calibration. The overall uncertainty was estimated using the RSS (Root Square Sum) of the random and systematic errors:

$$U_{overall} = \pm\sqrt{U_{systematic}^{2} + U_{random}^{2}} \tag{3.17}$$

3.8 Uncertainty propagation

In order to estimate the uncertainty in the physical quantities were deduced through the data reduction, uncertainty propagation has been carried out. Considering the objective function (y), for instance the heat flux, is a function of *k* independent variables (x_1, x_2, x_3,…, x_k) such as pressure, temperature, and flow rate in the following form:

$$y = f(x_1, x_2, x_3, x_4, \dots, x_k) \tag{3.18}$$

The overall uncertainty in the dependent variable y would be:

$$U_y = \pm\sqrt{\left[\frac{\partial y}{\partial x_1}U_{x1}\right]^2 + \left[\frac{\partial y}{\partial x_2}U_{x2}\right]^2 + \dots + \left[\frac{\partial y}{\partial x_k}U_k\right]^2} \tag{3.19}$$

Table 3.6 summarizes the range of experimental boiling measurements for different tube diameters, heat fluxes, mass velocities and mean vapour qualities. The next sections describe the uncertainty in the various measurements taken in the project and the uncertainty in the derived results.

Table 3.6: Range of experimental parameters.

Parameters	Range
Internal diameter (d_i)	2.88-1.1 mm
Coil diameter (d_{coil})	30-60 mm
Coil length (L_{evap})	1-0.56 m
Mass velocity(G)	100-450 kg/m^2.s
Heat flux (q)	2500-12000 W/m^2
Pressure	3.5-6 bars
Vapour quality	0.2-0.95

3.8.1 Uncertainties in internal tube diameter (d_i) and coil diameter (d_{coil})

Based on the stainless steel tube manufacturer catalogues, Coppers Needles, the uncertainty in the internal and outside tube diameters is ±0.04 mm (40μm). The coil diameter was measured using Vernier Caliper with accuracy of ± 100 μm (10^{-4} m).

3.8.2 Uncertainty in temperature measurement

T-type thermocouples have been utilized in the current test rig as the maximum temperature does not exceed 120 °C. The wall surface thermocouples of type 5TC-TT-

TI-36-1M has been fixed to the wall surface using aluminium foil tape. Using the foil tape enables the use of the same thermocouples with the different coils thus reducing the uncertainly associated with changing the thermocouples and other fixing methods such as epoxy and minimizing the heat transfer measurement errors. The probe thermocouples of type TJC100-CPSS- M050G-100 have been fitted at different positions to measure the refrigerant and water temperatures. All thermocouples were calibrated using water bath equipped with a thermostat that controls the temperature of the water. The calibration process was conducted over the temperature range 0 to 100 °C.

The thermocouples were calibrated against Platinum (PT100) RTD thermocouple with ±0.025 K accuracy. Table 3.7 summarize the location and calibration curves for the evaporator surface thermocouples. Table 3.8 summarizes the location and calibration curves for the probe thermocouples. The average uncertainty of thermocouples was found to be ±0.15 K. All the thermocouples used an internal reference point (cold junction compensation), which was regulated by the data logger.

Table 3.7: Uncertainty of wall surface thermocouples.

Thermocouple code	Position from coil inlet	Curve fit formula	Uncertainty (K)
SURF-1	1/2 turn	1.001 × T	± 0.13
SURF-2	1/2 turn	T	± 0.17
SURF-3	1 turn	1.001× T	± 0.15
SURF-4	1 turn	1.002× T	± 0.18
SURF-5	1 .5 turns	1.005× T	±0.14
SURF-6	1 .5 turns	1.004× T	± 0.25
SURF-7	2 turns	1.002× T	± 0.18
SURF-8	2 turns	1.003× T	± 0.19
SURF-9	2.5 turns	0.999× T	± 0.32
SURF-10	2.5 turns	0.998× T	± 0.18

Table 3.8: Uncertainty of Probe thermocouple measurements.

Thermocouple	Thermocouple location	Curve fit formula	Uncertainty (K)
Prob-1	Refrigerant evaporator inlet	$1.001\times T- 0.2926$	± 0.12
Prob-2	Refrigerant evaporator outlet	$0.9999 \times T- 0.2106$	± 0.12
Prob-3	Refrigerant condenser inlet	$0.9983\times T - 0.0679$	± 0.11
Prob-4	Refrigerant condenser outlet	$0.9973\times T + 0.1702$	± 0.06
Prob-5	Water condenser inlet	$0.9971\times T+ 0.1338$	± 0.12
Prob-6	Water evaporator inlet	$0.9984\times T- 0.1825$	± 0.13
Prob-7	Water condenser outlet	$0.9986 \times T- 0.316$	± 0.14
Prob-8	Water evaporator outlet	$0.9999\times T - 0.3642$	± 0.14
Prob-9	Refrigerant evaporator steel coil inlet	$0.997 \times T$	± 0.15
Prob-10	Refrigerant evaporator steel coil outlet	T	± 0.19
Prob-11	Compressor suction line	$1.005\, T$	± 0.14
Prob-12	Before expansion valve	T	± 0.15

3.8.3 Uncertainty in pressure measurement

15 bar pressure transducer (PTX-7517) was fitted at the condenser inlet and two 10 bar pressure transducers (PTX-7517) were fitted at the two parallel evaporator inlets. Because the transducers were 4-20 mA transducers, 100 ohm resistances were soldered on the datalogger terminal board to convert the amperes signal to voltage signal that the data logger can process. The pressure-volt calibration curves have been plotted by calibrating the pressure transducer against accurate gauge pressure with accuracy of ± 0.04 bars. The uncertainties of the pressure transducers including the hysteresis, stability, dead weight tester, repeatability, temperature effect errors and the overall uncertainties of the three transducers are shown in table 3.9. The details of uncertainty calculations are listed in Appendix A.

Table 3.9: Uncertainties associated with pressure transducers.

Transducer	Pressure transducer location	Curve fit formula (bar)	Uncertainty (bar)
Transducer-1	Condenser inlet	$9.3552\times \text{volt}-3.6896$	±0.17
Transducer-2	Water cooling evaporator inlet	$6.2496 \times \text{volt} - 2.4151$	±0.12
Transducer-3	Electrically heated evaporator	$6.3032 \times \text{volt} – 2.4475$	±0.12

3.8.4 Uncertainty in flow rate measurement

A 0-5 voltage output signal turbine flowmeter transducers have been utilized in measuring the water flow through the condenser and evaporator. Omega FLR-1009 with measuring range of 50-500 ml/min was connected to the water passing through the evaporator. Omega FLR-1010 with measuring range of 60-1000 ml/min was connected to the condenser water flow circuit. Two resistance each 5 kilo-ohm have been connected to the terminal board of the data logger to resize the voltage signal to be 0 to 2.5 volt as described in the data logger manual. The uncertainty of the condenser and evaporator water flow meters were 1.096% FS and 2.053% FS based on the uncertainty calculations listed in appendix A. The refrigerant flow meter is Roxspur rotameter with measuring range of 7-47 ml/min with uncertainty of ± 1.25% FS as calibrated by the manufacturer. Table 3.10 summarizes the uncertainties associated with the different flow meters.

Table 3.10: Flow meters uncertainties.

Flow meter	Curve fit formula(mL/min)	Uncertainty (mL/min)
Condenser water flow meter	Flow rate= 406.79*volt	± 10.96
Evaporator water flow meter	Flow rate=176.96*volt	± 10.26
Refrigerant flow meter	Analogue [-]	± 0.5875

3.8.5 Uncertainty in electrical power measurements

The power is calculated as the product of current and voltage. The current and voltage ranges used in the experiment (4 to 15) amperes and (1 to 3) volt respectively. The uncertainty in the measured power was calculated from equation (3.21):

$$U_{Q_{evap}} = \sqrt{\left(\left(\frac{\partial Q_{evap}}{\partial I}\right)U_I\right)^2 + \left(\left(\frac{\partial Q_{evap}}{\partial V}\right)U_V\right)^2} \qquad \textbf{(3.20)}$$

$$U_{Q_{evap}} = \sqrt{(VU_I)^2 + (IU_V)^2} \tag{3.21}$$

3.8.6 Uncertainty in coil length and surface area

The uncertainty in the coil length can be calculated using the coil diameter uncertainty by equation (3.23):

$$L_{evap} = \pi d_{coil} N_{coil} \tag{3.22}$$

$$U_{L_{evap}} = \sqrt{\left(\left(\frac{\partial L_{evap}}{\partial d_{coil}}\right) U_{d_{coil}}\right)^2} = \pi N_{coil} U_{d_{coil}} \tag{3.23}$$

The uncertainty in the surface area could be calculated using:

$$A_{evap} = \pi d_i L_{evap} \tag{3.24}$$

$$U_{A_{evap}} = \sqrt{\left(\left(\frac{\partial A_{evap}}{\partial d_i}\right) U_{d_i}\right)^2 + \left(\left(\frac{\partial A_{evap}}{\partial L_{coil}}\right) U_{L_{evap}}\right)^2} \tag{3.25}$$

$$U_{A_{evap}} = \pi \sqrt{(L_{evap} U_{d_i})^2 + (d_i U_{L_{evap}})^2} \tag{3.26}$$

For the electrically heated coils the internal diameter varied from 2 to 1.1 mm leading to uncertainty in the surface area to be 70.4 to 70.6 mm^2 (2 % to 4% evaporator area) at 1.1 mm and 2 mm respectively.

3.8.7 Uncertainty in heat flux (q)

The heat flux is defined as the heat transfer rate in the evaporator divided by the surface area as given by equation 3.2. The uncertainty in heat flux can be calculated using equation (3.28):

$$U_q = \sqrt{\left(\frac{\partial q}{\partial Q_{evap}} U_{Q_{evap}}\right)^2 + \left(\frac{\partial q}{\partial A_{evap}} U_{A_{evap}}\right)^2} \quad \textbf{(3.27)}$$

Since the heat flux is the ratio of the heat transfer to the surface area of the evaporator ($q=Q_{evap}/A_{evap}$), the uncertainty in the heat flux would be:

$$U_q = \sqrt{\left(\frac{1}{A_{evap}} U_{Q_{evap}}\right)^2 + \left(\frac{-Q_{evap}}{A_{evap}^2} U_{A_{evap}}\right)^2} \quad \textbf{(3.28)}$$

3.8.8 Uncertainty in refrigerant temperature

The refrigerant temperature was defined as the average between the inlet and outlet of the test section. The average uncertainty in thermocouples was found to be ± 0.15 K. As a result, the uncertainty in the refrigerant temperature would be:

$$U_{Tref} = \sqrt{\left(\frac{\partial T_{ref}}{\partial T_{evap,in}} U_{T_{evap,in}}\right)^2 + \left(\frac{\partial T_{ref}}{\partial T_{evap,out}} U_{T_{evap,out}}\right)^2} \quad \textbf{(3.29)}$$

Since the refrigerant temperature was defined as the average of evaporator inlet and outlet temperatures , $T_{ref}=0.5\ (T_{evap,in}+T_{evap,out})$, then its uncertainty was estimated as:

$$U_{Tref} = \frac{1}{2}\sqrt{\left(U_{T_{evap,in}}\right)^2 + \left(U_{T_{evap,out}}\right)^2} \quad \textbf{(3.30)}$$

3.8.9 Uncertainty in wall temperature

First the uncertainty in the outside wall temperature has been calculated using equation (3.9) then the uncertainty in the inner wall temperature was calculated from (3.32) by expressing the inner wall temperature as function in heat flux by modifying equation (3.14):

$$T_{wall,i} = T_{wall,o} - \frac{4qd_i}{\left(d_o^2 - d_i^2\right)k_{wall}} \left(\frac{\left(\frac{d_o}{2}\right)^2 - \left(\frac{d_i}{2}\right)^2}{4} - \frac{\left(\frac{d_o}{2}\right)^2}{2} \ln\left(\frac{d_o}{di}\right) \right) \quad \textbf{(3.31)}$$

$$U_{T_{wall,i}} = \sqrt{\left(\frac{\partial T_{wall,i}}{\partial T_{wall,o}} U_{T_{wall,o}}\right)^2 + \left(\frac{\partial T_{wall,i}}{\partial d_i} U_{d_i}\right)^2 + \left(\frac{\partial T_{wall,i}}{\partial d_o} U_{d_o}\right)^2 + \left(\frac{\partial T_{wall,i}}{\partial q} U_q\right)^2} \quad \textbf{(3.32)}$$

3.8.10 Uncertainty in heat transfer coefficient

Finally the uncertainty in heat transfer coefficient was calculated from equation (3.33) using equation (3.10):

$$U_\alpha = \sqrt{\left(\frac{\partial \alpha}{\partial T_{wall,i}} U_{T_{wall,i}}\right)^2 + \left(\frac{\partial \alpha}{\partial T_{ref}} U_{T_{ref}}\right)^2 + \left(\frac{\partial \alpha}{\partial q} U_q\right)^2} \quad \textbf{(3.33)}$$

The uncertainty propagation in all calculated results was performed using Engineering Equation Solver (EES). The software has a spread sheet where the uncertainty of measured variables was set in uncertainty propagation table in the calculate menu. Table 3.11 summarizes the uncertainty in heat transfer coefficient for different tested coils.

Table 3.11: Summary of uncertainties associated with the experimental measurements.

Flow meter	Units	Uncertainty
Evaporator inlet temperature	°C	± 0.15
Evaporator outlet temperature	°C	± 0.15
Outside wall thermocouple temperatures	°C	± 0.15
Heating current	amp	± 0.4
Heating voltage	V	± 0.02
Tube inside diameter	m	0.00004
Tube outside diameter	m	0.0001
Coil diameter	m	0.0001
Evaporator water flow meter	ml/min	11
	Boiling heat transfer coefficient uncertainties [%]	
Coil A		9.323- 16.11
Coil B		6.38 - 10.2
Coil C		6.0 - 13.23
Coil D		7.76 - 16.78

CHAPTER 4

Flow Boiling In Small Helical Coils

4.1 Introduction

In this chapter, the experimental results for flow boiling inside helical coils are presented. It was clear from the literature review that the experimental flow boiling heat transfer measurements in miniature helical coils are very limited. Kim et al. (2000) tested three coils with coil diameters of 30, 34, and 46.2 mm with tube diameters of 1 mm using refrigerant R22 as the working fluid. Decreasing the coil diameter was found to enhance the heat transfer coefficient. Additionally, the authors found that dry out in coils occur at vapour quality of 0.6 (Kim et al., 2006). No data has been reported for R134a for such small helical tubes. Furthermore, the effect of tube diameter of a coil has not been reported in literature. This experimental work aims to clarify the flow boiling behaviour of R134a in miniature coils with different coil and tube diameters. The effect of mass velocities and heat flux on the heat transfer coefficient at different vapour qualities have been investigated for each coil.

The experimental study includes four coils where coil A is heated by water and the other three coils were heated electrically for better control on the heat supplied for such small size coils. The results are presented for each coil separately starting from coil A to coil D at different mass velocities and heat fluxes then the effect of tube diameter and coil diameter are presented.

4.2 Validation of test facility

A straight tube has been utilized for validating the test facility measurements. A tube with 2 mm diameter and 81 mm long was used to check the measurement technique and data reduction methodology. Data has been collected at heat fluxes varying from 2500 up to 12000 W/m^2 at mass velocity of 100 kg/m^2.s. The results were compared to experimental data measured by Yan and Lin (1998) and to empirical correlations commonly used in literature. In figure 4.1, the heat transfer coefficient was presented as a function of the mean vapour quality of the test section at different heat fluxes at mass velocity of 100 kg/m^2.s and inlet saturation temperature of 15 °C through the 2 mm internal diameter tube. The mean vapor qualities obtained in this study were limited to 0.7 due to the power supply limitations. The figure shows that the heat transfer coefficient is independent of vapour quality at low quality region and it increases with heat flux. At intermediate qualities with low heat flux values, the heat transfer coefficient was slightly increasing with the vapour quality as the two-phase flow velocity increases and convective boiling component effect becomes significant. At intermediate qualities ($0.3<x<0.6$) the heat transfer coefficient starts to increase at higher mean vapour quality compared to lower heat flux as the nucleate boiling component becomes significant with increasing the heat flux. Additionally, figure 4.1 shows that the measurements are comparable to measurements carried out by Yan and Lin (1998) based on mean vapor quality for a bundle (parallel tubes stacked to a copper plate heater) of straight tubes with 100 mm heated length and similar test conditions. The difference between measurements is within 30% which is acceptable for heat transfer coefficient measurements. This difference is attributed to the difference in test section material and uncertainties associated with experimental measurements as the current experiment and Yan and Lin (1998) experiment have uncertainties of ± 10 %

and ± 16 % respectively. The quality of surface finish has also a significant effect on boiling process; a rough surface offer higher number of bubble nucleation sites and increases the heat transfer coefficient.

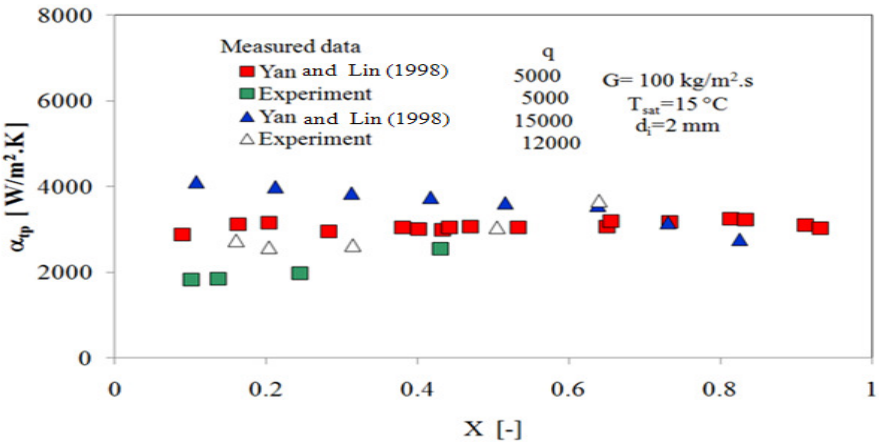

Figure 4.1: Comparison between straight tube data with Yan and Lin data (1998)

The difference between the two experiments is highest (30%) at low vapour quality region and lowest at high vapour quality. In the low quality region, the nucleate boiling has significant effect where bubbles are generated on the surface. In high quality region the convective boiling effect is significant where the boiling is controlled via the vapour liquid interface and not the surface. Therefore the surface material can contribute significantly to the difference between the measured results and those of Yan and Lin (1998).

In figure 4.2 and 4.3, the heat transfer coefficient measured at four heat fluxes for mass velocity of 100 kg/m^2 has been compared to Kandlikar correlation (1990) and Gungor and Winterton correlations (1987) to validate the experimental procedures. The Kandlikar correlation presents a general correlation for saturated boiling in straight tubes and annuli. Fernando et al. (2008) used Kandlikar correlation (1990) to predict their boiling data in minichannels with hydraulic diameter of 1.42 mm with ±30% deviation. Additionally, the correlation predicts the local flow boiling heat transfer coefficient in the two-phase region as the heat transfer coefficient is correlated to vapour quality as given in equation 4.1.

$$\alpha_{tp} = \alpha_l \left(c_1 Co^{C_2} \left(25 Fr_{lo} \right)^{C_5} + C_3 Bo^{C_4} F_{fluid} \right) \tag{4.1}$$

$F_{fluid} = 1.63$ For R134a (Xiande et al., 2011)

$$Co = \left(\frac{1-x}{x} \right)^{0.8} \left(\frac{\rho_v}{\rho_l} \right)^{0.5} \quad \mathrm{Re}_l = \frac{G(1-x)d_i}{\mu_l} \quad \alpha_l = 0.023 \mathrm{Re}_l^{0.8} \mathrm{Pr}_l^{0.4} \left(\frac{k_l}{d_i} \right) \quad Fr_{lo} = \frac{G^2}{\sigma \rho_l^2 d_i}$$

$if\,(Co < 0.65)$ Convective boiling region

$\mathrm{C}_1 = 1.136 \qquad \mathrm{C}_2 = -0.9 \qquad \mathrm{C}_3 = 667.2 \qquad \mathrm{C}_4 = 0.7 \qquad \mathrm{C}_5 = 0$

$if\,(Co > 0.65)$ Nucleate boiling region

$\mathrm{C}_1 = 0.6683 \qquad \mathrm{C}_2 = -0.2 \qquad \mathrm{C}_3 = 1058 \qquad \mathrm{C}_4 = 0.7 \qquad \mathrm{C}_5 = 0$

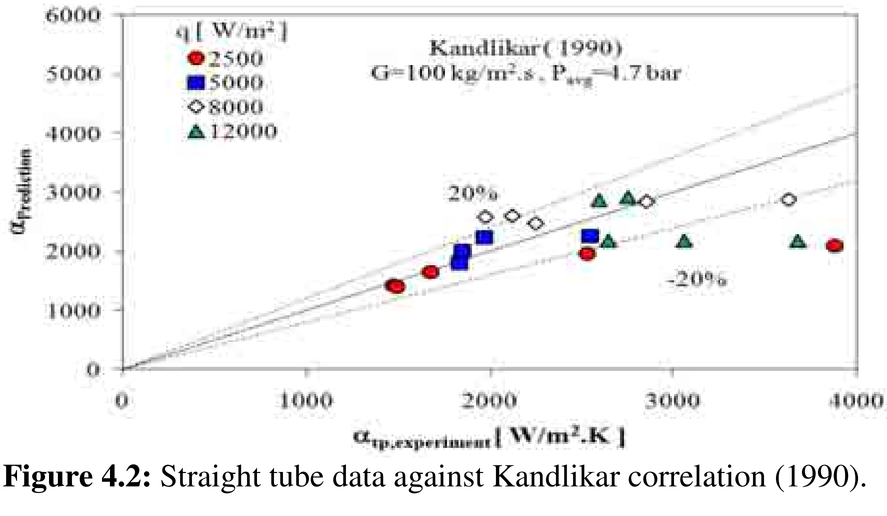

Figure 4.2: Straight tube data against Kandlikar correlation (1990).

Gungor and Winterton correlation (1987) was also used to predict the experimental results. Xiande et al. (2011) tested 18 correlations for flow boiling of R134a in minichannels and found that Gungor and Winterton (1987) correlation was the best correlation predicting 1158 data point for boiling in minichannel tubes. Gungor and

Winterton (1987) correlation was developed using a large data bank including experimental results with water, CFCs and hydrocarbons in tube diameters ranging from 2.95 to 32 mm (Fernando et al., 2008). The correlation parameters are described in equation 4.2. The deviation of experimental measurements and the mentioned correlations is within ± 20 %.

$$\alpha_{tp} = \alpha_l \left(1 + 3000 Bo^{0.86} + 1.12 \left(\frac{x}{1-x} \right)^{0.75} \left(\frac{\rho_l}{\rho_v} \right)^{0.41} \right) \tag{4.2}$$

$$\alpha_l = 0.023 \mathrm{Re}_l^{0.8} \mathrm{Pr}_l^{0.4} \left(\frac{k_l}{d_i} \right) \qquad Bo = \frac{q}{G h_{fg}} \qquad \mathrm{Re}_l = \frac{G(1-x) d_i}{\mu_l}$$

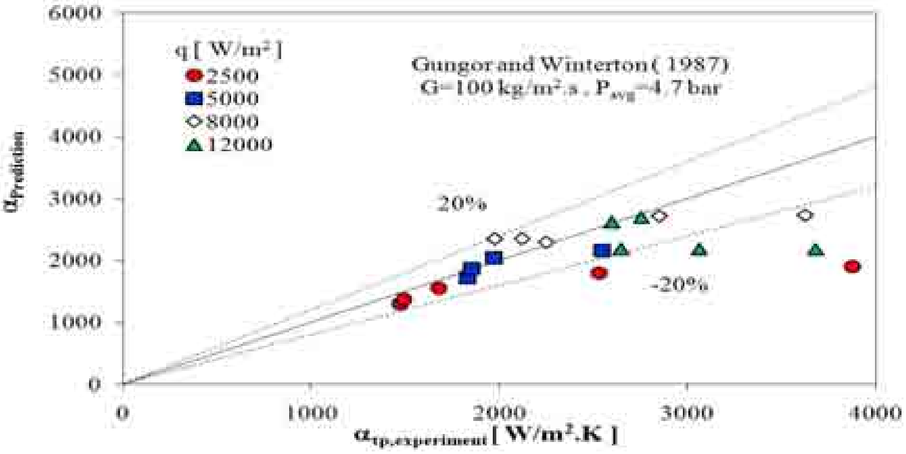

Figure 4.3: Straight tube data against Gungor and Winterton correlation (1987).

4.3 Flow boiling heat transfer in coil A

Coil A was tested at two mass velocities namely; 123 and 187 kg/m^2.s where the vapour inlet quality was varied using a preheater fitted before the test section. The preheater heating power was calculated using the voltage applied across the preheater measured using a multimeter multiplied by the electrical current from the power supply. Coil A was installed in a shell where water was circulated outside the coil and used to heat the refrigerant flowing inside the coil. During the tests, the heat flux was fixed to 7600 W/m^2 by varying the water flow through the test section and the saturation temperature was adjusted to 6 °C by varying the compressor speed. The refrigerant flow was controlled using the manual expansion valve. In figure 4.4, the heat transfer coefficient was plotted against the mean vapour quality at the test section through two different mass velocities of 187 and 123 kg/m^2.s where the mean vapour quality was changed by increasing the inlet vapour quality using the preheater and mass velocity was adjusted using the manual expansion valve.

It has been found that as the mass velocity increases, the heat transfer coefficient increases. As the mass velocity increases, the liquid film becomes thinner and more turbulent secondary flow is generated augmenting the heat transfer. The effect of mass velocity becomes significant at high vapour qualities. On the other hand the heat transfer coefficient increases with the vapour quality as more vapour is generated with increasing the quality causing a higher two-phase mixture velocity since the density of vapour is much lower than that of liquid. It is notable from figure 4.4 that Coil A was able to retard the dry out to higher vapour qualities larger than 0.75 which is higher than the values reported for straight tubes (Shiferaw et al., 2006). Shiferaw reported that dryout occurs in straight tubes with diameter 4 mm at vapour qualities between 40%-50% and tube with diameters 2 mm at vapour qualities between 20%-30% at mass velocities of 300 kg/m^2.s and heat fluxes between 13 kW/m^2 to 108 kW/m^2.

Initially, the coil was installed in a configuration that mimic a miniature water chilling system where the water was used to supply the heat required for boiling the refrigerant. However, using this method produced limitation on the amount of heat that can be supplied where very small water flow rate would be required and uncertainties of experiment would be large in such cases. Therefore, to cover a wider range of operating conditions smaller coils were heated using direct heating (Joule effect or electrification).

Coils B, C, and D with diameters of 2, 1.55 and 1.1 mm respectively were heated electrically and the results will be described in the following sections.

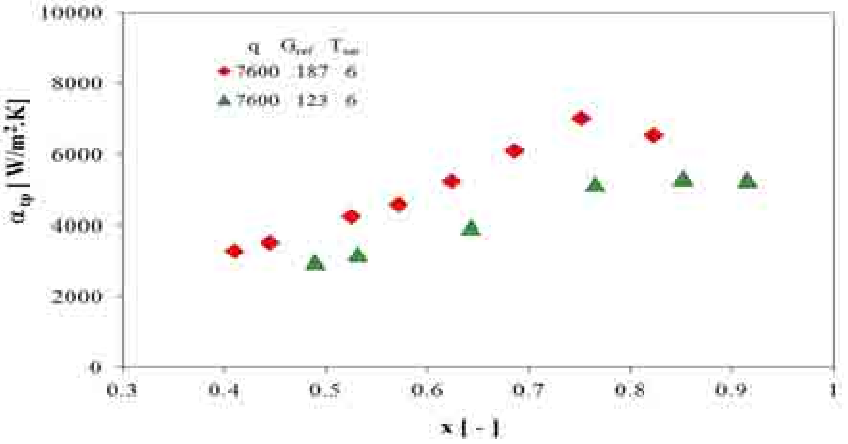

Figure 4.4: Variation of heat transfer coefficient with mass velocity and vapour quality.

4.4 Flow boiling heat transfer in coil B

Figures 4.5A, 4.5B, 4.5C show the variation of heat transfer coefficient with vapour qualities at different mass velocities and three levels of heat flux 2500, 5000 and 12000 W/m^2 respectively. In figure 4.5A, the heat transfer coefficient is nearly uniform with vapour quality at low heat flux (q=2500). Increasing the vapour quality increases the two-phase velocity which reduces the liquid film thickness close to the wall and augments the heat transfer coefficient but the nucleate boiling contribution is suppressed in the same time causing such uniform behaviour of heat transfer coefficient at low heat fluxes. In some cases, the heat transfer coefficient may not increase with vapour quality where the suppression of nucleate boiling is significant with increasing the vapour quality as reported by Cary (1992).

Comparing figures 4.5A and 4.5B, the effect of mass velocity becomes larger with increasing the heat flux. Increasing the heat flux activates more nucleation sites and generates more vapour per unit length causing significant effect of mass velocity at higher heat fluxes. The heat transfer coefficient increases with both vapour quality and mass velocity at intermediate quality region. Furthermore, Comparison of figures 4.5A and 4.5C shows that the heat transfer coefficients at the same quality and mass velocity increase with increasing the heat flux. It could be concluded that the heat transfer coefficient changes with both the heat flux and mass velocities where the effect of mass velocities becomes significant at high levels of heat fluxes. Zhao et al. (2003) tested water/steam mixture inside 9 mm tube diameter helically coiled tube where the heat transfer coefficient was changing with both the heat flux and mass velocity. Based on the current results such observations are extended for tube diameter as small as 2 mm.

Additionally, the effect of heat flux variation on heat transfer coefficient is nearly three to five times that of mass velocity in the current measurements. This highlights the advantage of operating in high heat flux region to obtain high heat transfer coefficient hence producing compact evaporators while handling small refrigerant charge. However, the dryout phenomenon described in section 2.7 should be avoided.

Several authors concluded from their experimental measurements of flow boiling in straight minichannels that the smaller the tube diameter the earlier the dryout (Saitoh et al. 2005, Oh et al. 2011 and Choi et al., 2009). They explained this phenomenon by the increase in contact area between tube wall and fluid causing more active nucleate boiling thus causing dry patches to appear earlier. Using smaller tubes makes the liquid film thinner during flow boiling making it easier for breakup and occurrence of early dryout. Dryout in this experimental work with the 2 mm tube diameter was not clearly observed as the peak behaviour in heat transfer coefficient with vapour quality as described in section 2.7 was not found.

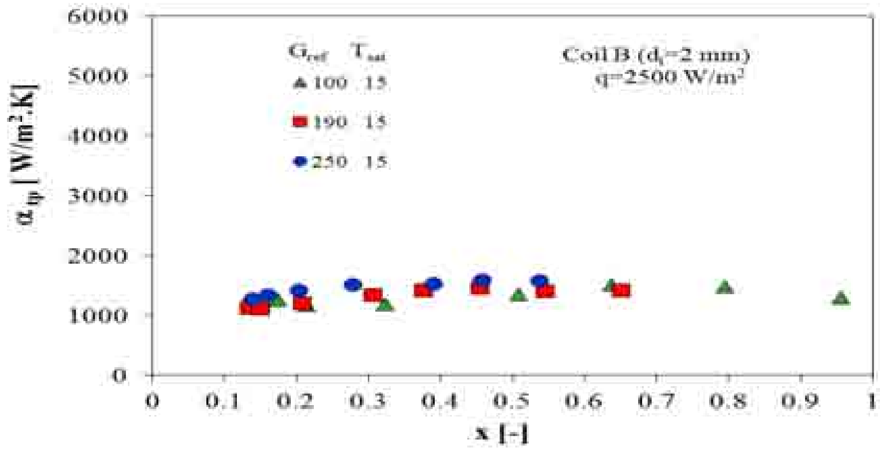

(A) q=2500 W/m^2

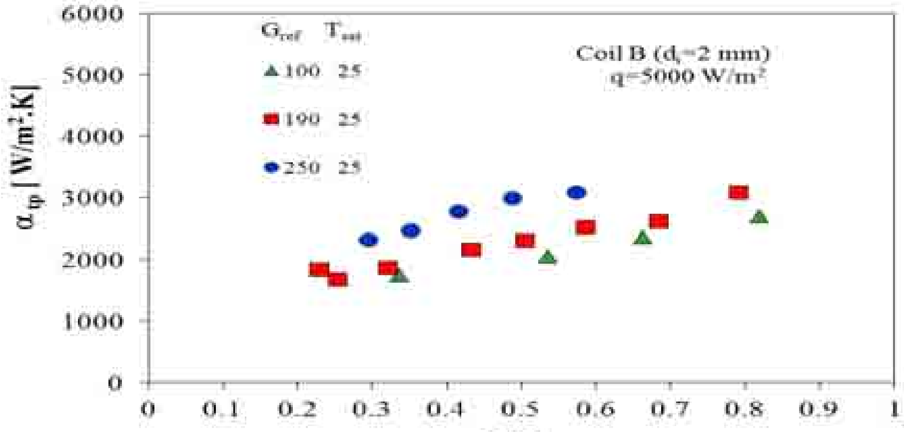

(B) q=5000 W/m^2

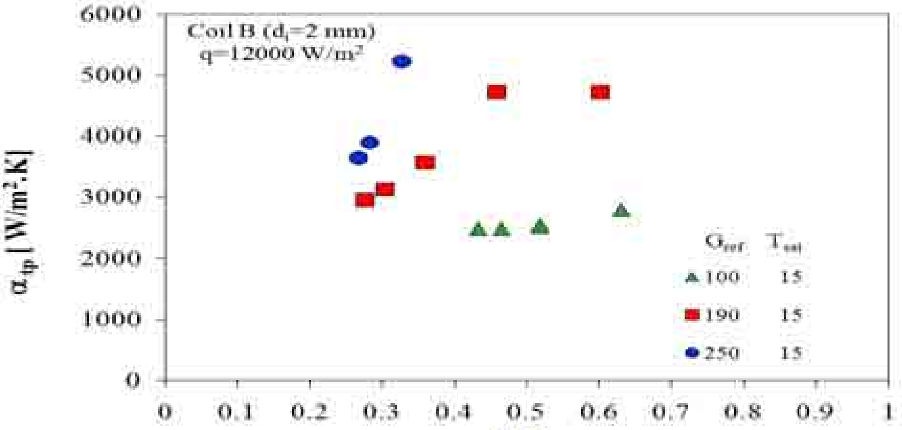

(C) q=12000 W/m^2

Figure 4.5: Boiling heat transfer coefficient in coil B at different levels of heat fluxes.

4.5 Flow boiling heat transfer in coil C

Coil C has 1.55 mm inside diameter with 3 turns and 8 mm coil pitch. The heat transfer coefficient was measured at different mass velocities and two levels of heat fluxes. In figure 4.6A at (q= 5000 W/m^2), for low mass velocity (G< 250kg/m^2.s), the heat transfer coefficient starts to increase with vapour quality up to qualities close to 0.5 due to the effect of vapour quality in accelerating the two-phase mixture as the vapour velocity becomes high compared to liquid velocity to satisfy the continuity flow governing rules since the density of vapour (ρ_v) is much smaller than that of liquid (ρ_l). After vapour quality of 0.5, the heat transfer coefficient starts to decline with vapour quality as an indication of dry out. The dry out was found to start earlier (x_m=0.5) in case of low mass velocities of 190 kg/m^2 but at higher mean vapour quality of 0.65 in case of high mass velocity of 300 kg/m^2. Increasing the mass velocity increases the effect of secondary flow and centrifugal force which helps in redistribution of the liquid film and retard the dry out to higher qualities in case of increasing the mass velocity.

With applying high heat fluxes of (q=12000 W/m^2) in figure 4.6B, the heat transfer coefficient values becomes higher compared to figure 4.6A. In conclusion, heat transfer coefficient varies with both the mass velocity and heat flux inside tube diameter of 1.55 mm. By comparing coil B and coil C, dryout occurs in coil C with decreasing the diameter from 2 mm to 1.55 mm for the same heat flux used. Saitoh et al. (2005) tested straight tube diameters of 0.51, 1.12, and 3.1 mm using R134a and found that decreasing the straight tube diameter causes earlier dryout.

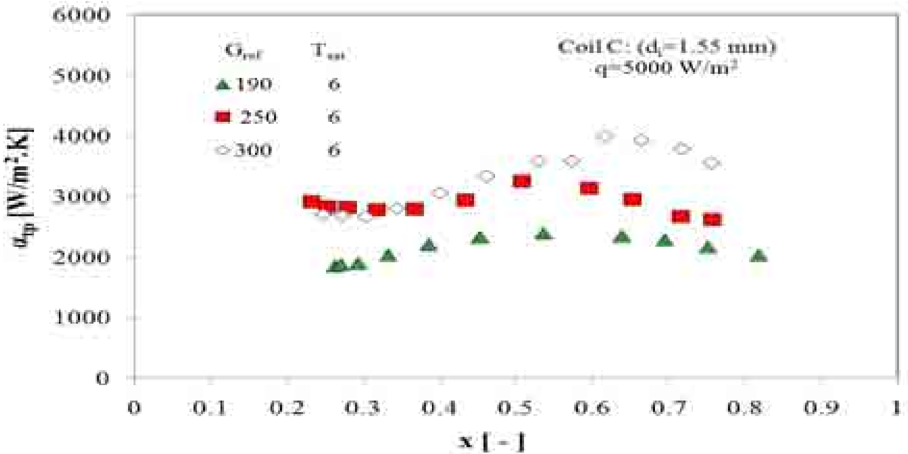

(A) q=5000 W/m^2

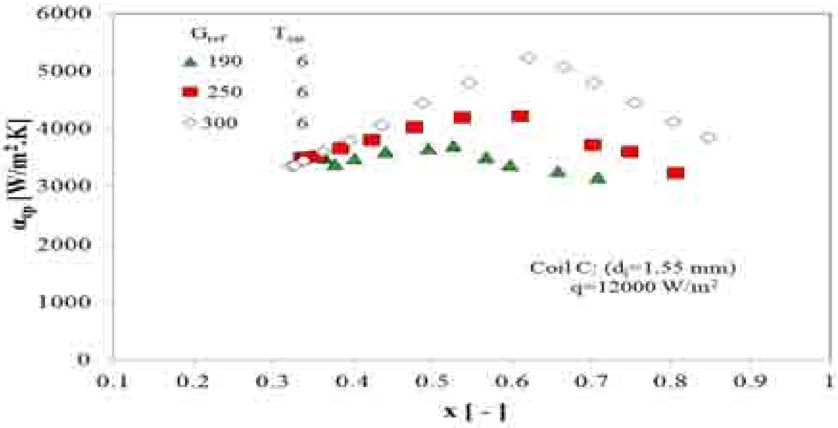

(B) q = 12000 W/m^2

Figure 4.6: Boiling heat transfer coefficient in coil C.

4.6 Flow boiling heat transfer in coil D

Coil D is 1.1 mm inside diameter with 3 turns and 8 mm coil pitch. The heat transfer coefficient was measured at different mass velocities at three levels of heat fluxes as shown in figures 4.7. In case of mass velocity of 450 kg/m^2.s in figure 4.7A, the heat transfer coefficient reach a peak then becomes uniform with vapour quality as the dry out is counteracted by the droplet deposition caused by the significant secondary flow at high mass velocity of 450 kg/m^2.s. Jayanti and Berthoud (1990) reported that the dry out region in helical coils is governed by four mechanisms that control the liquid film thickness. Both secondary flow and liquid redeposition improve the liquid film distribution. However, the evaporation of liquid and entrainment mechanisms decreases the liquid film thickness. Therefore the counteracting effects of these mechanisms cause leveling off trend observed at high vapour quality. The effect of saturation was found insignificant from measurements as will be discussed in section 4.10. This makes the comparison correct even at different levels of saturation temperatures.

Comparing figure 4.7A, figure 4.7B after dry out region, there is sharper reduction in the heat transfer coefficient at the high heat flux (q=8000 W/m^2) compared to lower heat fluxes (q=5000 W/m^2). In figure 4.8C, the heat transfer coefficient was presented against the mean vapour quality at heat flux of 12000 W/m^2. At mass velocity of 250 kg/m^2.s, the heat transfer coefficient was found to decreases monotonically with vapour quality. This trend was observed by several researchers who tested straight minichannels (Yan and Lin, 1998 and Shiferaw et al., 2006). In conclusion, both convective and nucleate boiling mechanisms affect the boiling process in tube diameter as small as tube diameter of 1.1 mm. Below the dryout, the heat transfer coefficients increase with the heat flux but decrease with the heat flux above the dryout. As tube surface becomes dry and no sufficient liquid to wet the surface, increasing the heat flux would lead to higher wall temperature and larger temperature difference between the refrigerant and tube wall, i.e., lower heat transfer coefficient after dryout. Such behaviour was approved by measurement of Yan and Lin (1998) and Kaew-on and Wongwises (2009).

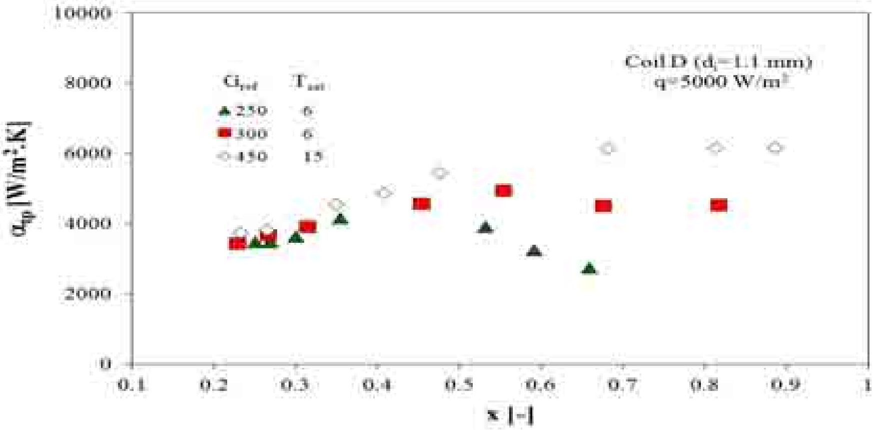

(A) q= 5000 W/m^2

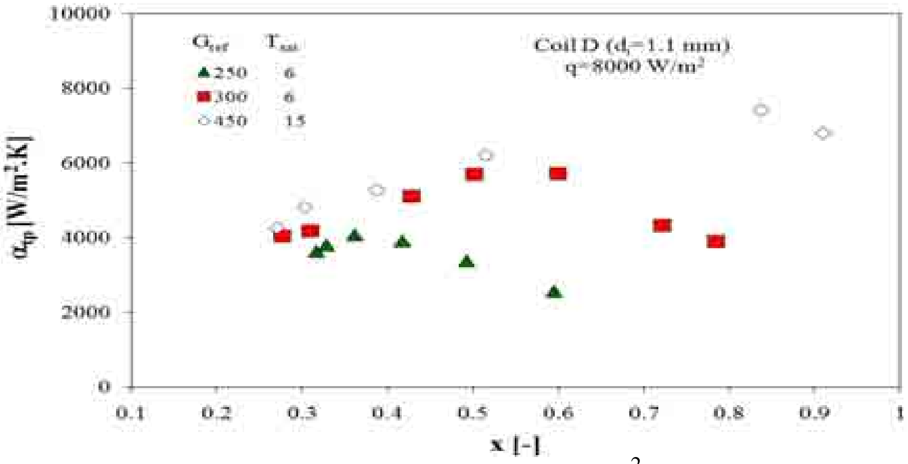

(B) q= 8000 W/m^2

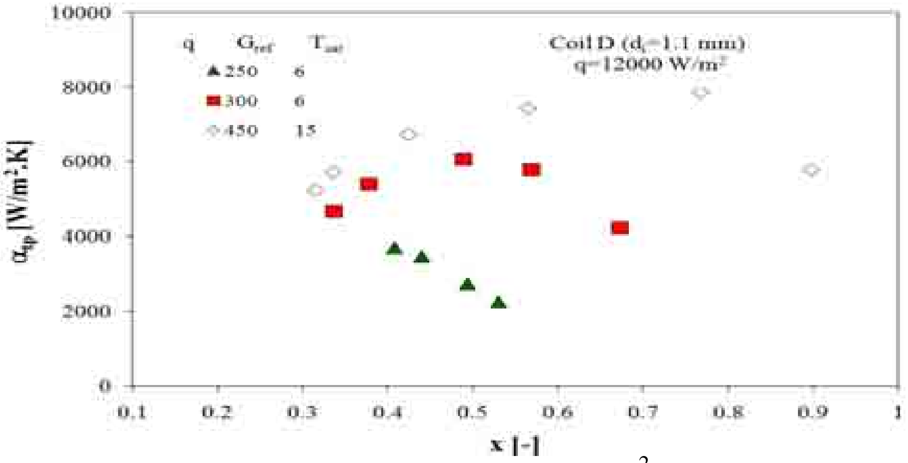

(C) q= 12000 W/m^2

Figure 4.7: Boiling heat transfer coefficient in coil D at different heat fluxes.

4.7 Repeatability of measurements

In addition to calibration of measuring instruments and testing the straight tube, repeatability of the measured data was also checked. Repeatability results can be affected by factors, other than measuring instruments, such as fouling, surface conditions and environmental conditions. This is more probable in boiling tests, which is affected by a large number of factors in contrast with single phase. Figure 4.8 shows the heat transfer coefficient of two helical coils, coil C and coil D versus the refrigerant quality. Coil C was tested at 12000 W/m^2 heat flux and 190 kg/m^2.s mass velocity while coil D was tested at 5000 W/m^2 heat flux and 250 kg/m^2.s mass velocity.

The tests were conducted at two different days to ensure that the results are repeatable. Figure 4.8 shows that the heat transfer coefficients repeatability was good with ± 5 % at low vapour qualities and ± 16 % at high vapour qualities. The deviation was large at high vapour qualities due the dryout which makes it too difficult to reach the exact operating condition. The boiling results are repeatable within the uncertainty limit of ±16%. Overall, the patterns of the heat transfer dependence and the magnitude of the coefficient are repeatable with an acceptable accuracy.

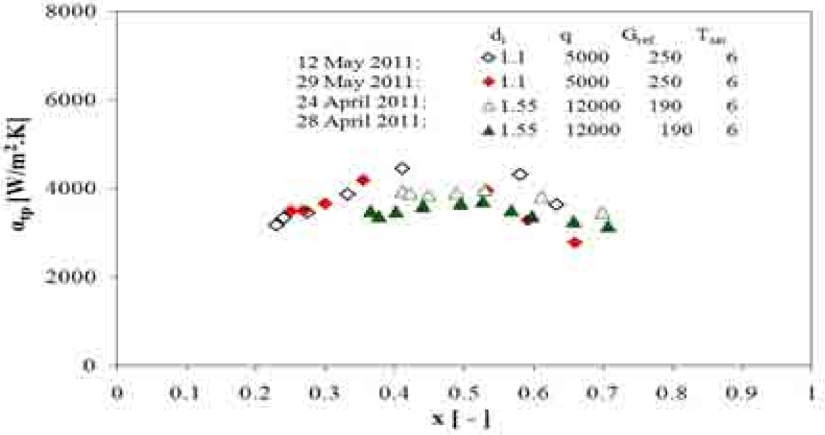

Figure 4.8: Repeatability of measurements.

4.8 The effect of tube diameter on flow boiling in helical coils

To illustrate the effect of tube diameter of a helical coil, the heat transfer coefficient was presented versus the vapour quality in figure 4.9. The experimental data at heat flux of 5000 W/m^2 and mass velocity of 250 kg/m^2.s are presented in figure 4.9A. In case of the 2 mm diameter tube, the heat transfer coefficient increases monotonically with the vapour quality as a result of the enhancement caused by convective mechanism with increasing the vapour quality. At tube diameter of 1.1 mm, early dry out was clearly observed between 0.4 and 0.5. The increase in heat transfer coefficient by decreasing the channel diameter is not linear as the increase in heat transfer coefficient by decreasing the channel from 1.55 to 1.1 mm is higher than that in case of decreasing the channel from 2 mm to 1.55 mm.

In figure 4.9B, the heat transfer coefficient presented versus the vapour quality at heat flux of 5000 W/m^2 and mass velocity of G=300 kg/m^2.s flow condition. The decrease in tube diameter causes a higher heat transfer coefficient. Comparing figure 4.9A and 4.9B, the increase in mass velocity retard the dryout mean quality.

In figure 4.9C, the heat transfer coefficient was presented with vapour quality at heat flux of 12000 W/m^2 and mass velocity of G=250 kg/m^2.s. It can be seen that for tube diameter 1.1 mm, the tube measurements are dominantly in the dryout region causing sharp degradation of heat transfer coefficient with vapour quality. Increasing the coil diameter to 1.55 mm causes a smoother behaviour of heat transfer coefficient against vapour quality. The dryout for the 1.55 mm tube occurs at mean vapour quality of 0.6. In case of the 2 mm tube, the heat transfer coefficient was increasing with vapour quality due to the convective contribution. Operating condition has a significant effect on the thermal performance as dryout may suppress the enhancement caused by reducing the channel size.

It could be concluded that decreasing the tube diameter enhances the heat transfer coefficient except for high heat fluxes with the smallest tube diameter where the dryout dominates most of the tube length as depicted in figure 4.9C. The dryout was found to occur at lower vapour quality with decreasing the tube diameter which was observed at higher heat fluxes q=12000 W/m^2. This is in agreement with the measurements of Kim et al. (2000) using R22 in tube diameters of 1 mm where the dryout occurs close to 0.6. Decreasing the tube diameter makes it confined with vapour bubbles which make the liquid film very thin which easily vanish at relatively high heat fluxes and causes early dry out.

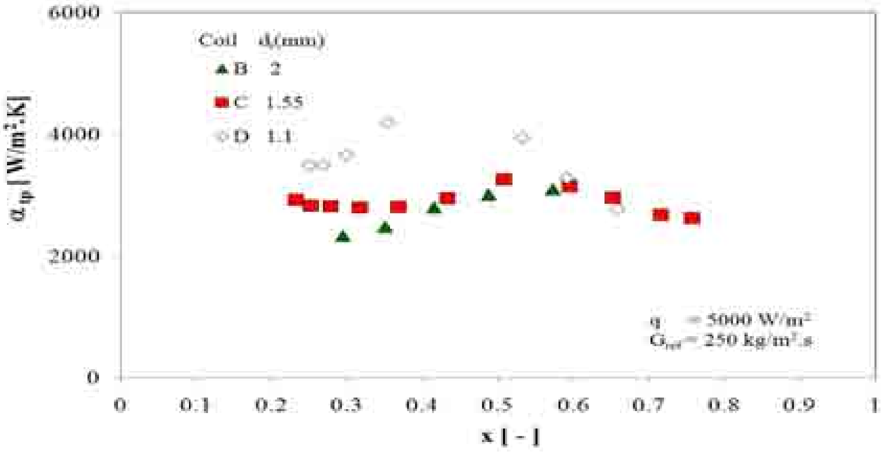

(A) G=250 kg/m^2.s, q=5000 W/m^2

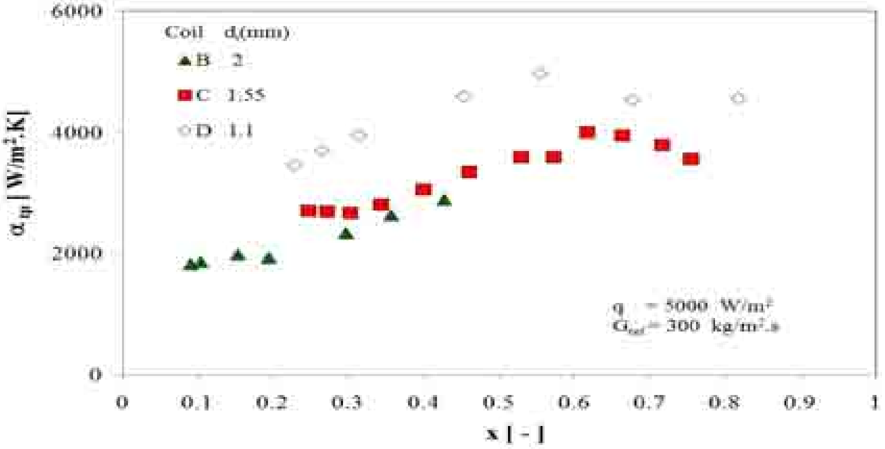

(B) G=300kg/m^2.s, q=5000 W/m^2

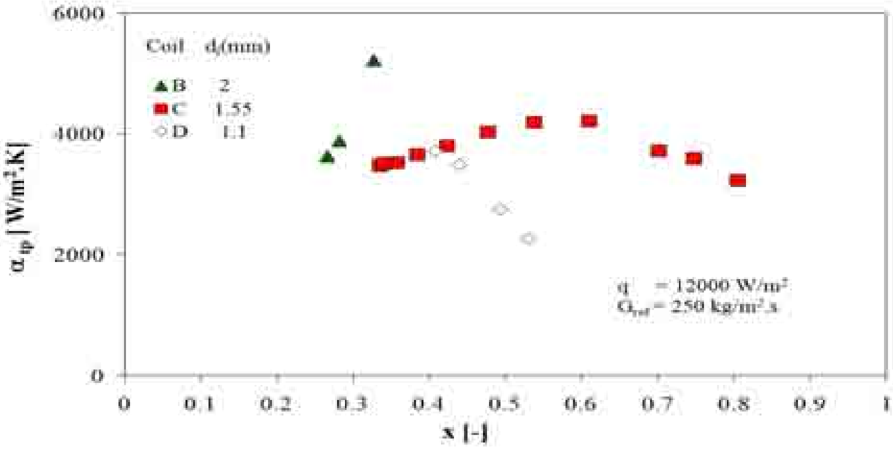

(C) G=250 kg/m^2.s, q=12000 W/m^2

Figure 4.9: Tube diameter effect on heat transfer coefficient.

4.9 The effect of coil diameter on flow boiling in helical coils

To illustrate the effect of coil diameter, the heat transfer coefficient was presented against vapour quality for both coil A and coil B. Coil A has a tube diameter of 2.8 mm and coil diameter of 30 mm while coil B has a diameter of 2 mm and coil diameter of 60 mm. For Coil B, the heat transfer coefficient increases slowly with the vapour quality at both mass velocities ($G=100$ kg/m^2.s and $G=190$ kg/m^2.s). The mass velocity and heat flux used in both Coil A and B tests are nearly similar. Also, the Material effect (as Coil A made from Copper and Coil B from Stainless steel) is mainly significant at lower quality. However, as the main difference appears in the high quality region then the observed change in heat transfer coefficient could be explained by effect of coil diameter. Decreasing the coil diameter to 30 mm (coil A) was found to intensify the effect of convective contribution in the boiling process hence the heat transfer coefficient increases sharply with vapour quality and mass velocity effect becomes more apparent at high vapour qualities.

It could be concluded that decreasing the coil diameter has a significant effect on enhancing the heat transfer coefficient and its effect is significant compared to tube diameter as shown in figure 4.10. Similar effect has been found by Kim et al. (2000) for R22 who tested three different coil diameters. Using smaller coil diameters makes larger number of turns for same coil length causing continuous change of flow direction and redistribution of liquid film. Additionally, smaller coil diameter causes larger centrifugal forces and secondary flow effects.

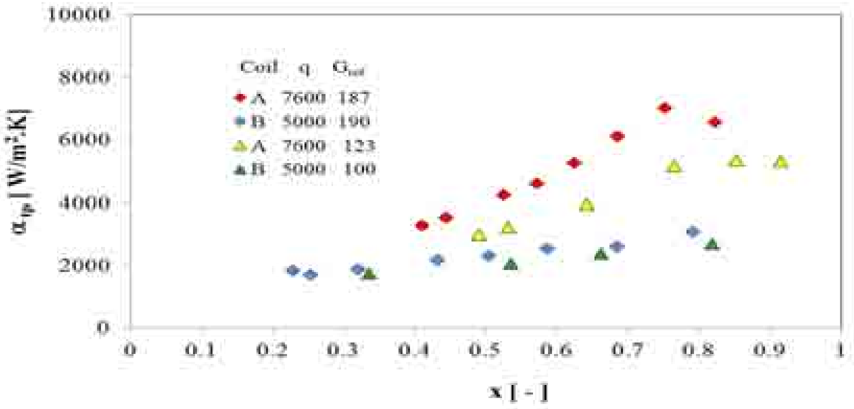

Figure 4.10: Coil diameter effect on boiling heat transfer coefficient.

4.10 The effect of saturation temperature

The saturation temperature has insignificant effect on the heat transfer coefficient except for tube diameters less than 1 mm where its effect becomes clear in the dryout region as reported by Saitoh et al.(2005) for straight tube using R134a. Additionally, Agostini et al. (2005) found no effect of saturation temperature on the boiling heat transfer coefficient through their measurements on rectangular minichannel with hydraulic diameter of 2.01 mm using R134a. Even nucleate boiling correlations such as Cooper correlation (Agostini et al., 2005) predict 17% increase in heat transfer coefficient for the 2.01 mm tube with varying the pressure from 4 bar to 6 bar which is simply within the experimental uncertainties. In order to check the effect of saturation temperature data has been collected at mass velocity of 350 kg/m^2.s and heat flux of 5000 W/m^2.K for the 1.1 mm tube diameter as shown in figure 4.11. No significant effect of saturation temperature on the heat transfer coefficient was observed.

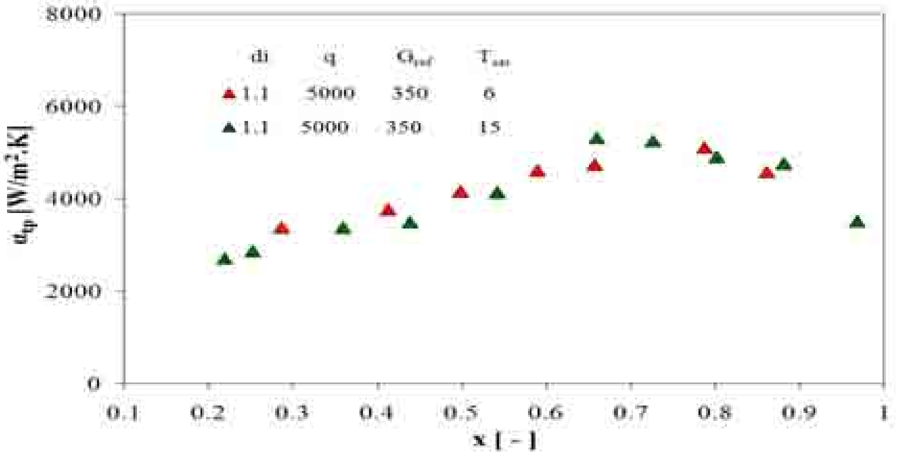

Figure 4.11: Saturation temperature effect on boiling heat transfer coefficient.

4.11 Summary

A parametric study has been carried out to find the effect of coil geometrical parameters on the flow boiling heat transfer performance. The tested coils have tube diameters range from 1.1 to 2.8 and coil diameters from 30 mm to 60 mm. The heat fluxes varied from 2500 to 12000 W/m^2 and mass velocities from 100 to 450 kg/m^2.s. The conclusions are summarized as:

- Both the heat flux and mass velocities found to have significant effect on the tested coils heat transfer process found to be applicable to small tube diameters as low as 1mm.
- Decreasing the tube diameter improves the heat transfer coefficient but early dryout has been observed especially at high heat fluxes and low mass velocities.
- Decreasing the coil diameter improves the heat transfer coefficient as it intensifies the effect of secondary flow.

CHAPTER 5

Boiling Prediction Techniques

5.1 Introduction

Cioncolini (2003) reported in their review of flow boiling in helical coils that there is a considerable difference between the correlations proposed by various researchers. Also most of the published correlations for helical coils were developed for a specific fluid, operating conditions, or specific dimensions. As a result, it was necessarily to develop new generalized predictive techniques for the sake of accurate design of helical coil evaporators using a wide range of heat fluxes, mass velocities, working fluids, tube and coil diameters. This chapter introduces a new correlation based on dimensional analysis using Pi-theorem and application of artificial neural network as another prediction method. Data were collected from five published research papers in literature and the current experimental results.

5.2 Dimensional analysis of flow boiling in helical coils

The heat transfer coefficient can be assumed as a function in the following parameters including the thermophysical properties, heat flux, mass velocity, and coil geometry.

$$f(\alpha_{tp}, G_{ref}, d_i, \Delta T_{ref-wall}, h_{fg}, \mu_l, \mu_v, C_{p,l}, k_l, \rho_l, \rho_v, \sigma, x, d_{coil}, \delta_{coil}) = 0 \qquad \textbf{(5.1)}$$

As a result, fifteen parameters are affecting the boiling process in helically coiled tube evaporators. All these parameters could be expressed using four basic dimensions (length, time, temperature, and mass). The tube diameter, liquid viscosity, liquid specific heat, liquid densities were selected as fundamental parameters while the remaining parameters were utilized to formulate the dimensionless groups. The dimensions of each parameter are given below in figure 5.1.

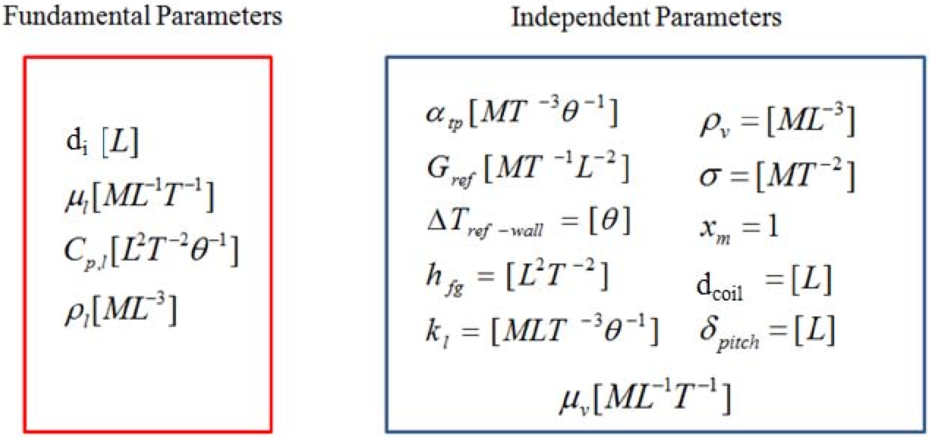

Fundamental Parameters

$d_i\ [L]$
$\mu_l[ML^{-1}T^{-1}]$
$C_{p,l}[L^2T^{-2}\theta^{-1}]$
$\rho_l[ML^{-3}]$

Independent Parameters

$\alpha_{tp}[MT^{-3}\theta^{-1}]$
$G_{ref}[MT^{-1}L^{-2}]$
$\Delta T_{ref-wall} = [\theta]$
$h_{fg} = [L^2T^{-2}]$
$k_l = [MLT^{-3}\theta^{-1}]$
$\rho_v = [ML^{-3}]$
$\sigma = [MT^{-2}]$
$x_m = 1$
$d_{coil} = [L]$
$\delta_{pitch} = [L]$
$\mu_v[ML^{-1}T^{-1}]$

Figure 5.1: Fundamental and independent parameters.

The number of dimensionless groups that could be formed is equal to the total number of variables excluding the number of basic dimensions. Accordingly, eleven dimensionless numbers could be formed:

$$\begin{aligned}
\pi_1 &= d_i^{a1}\mu_l^{b1}C_{p,l}^{c1}\rho_l^{d1}\alpha_{tp}\\
\pi_2 &= d_i^{a2}\mu_l^{b2}C_{p,l}^{c2}\rho_l^{d2}G_{ref}\\
\pi_3 &= d_i^{a3}\mu_l^{b3}C_{p,l}^{c3}\rho_l^{d3}\Delta T_{ref-wall}\\
\pi_4 &= d_i^{a4}\mu_l^{b4}C_{p,l}^{c4}\rho_l^{d4}h_{fg}\\
\pi_5 &= d_i^{a5}\mu_l^{b5}C_{p,l}^{c5}\rho_l^{d5}k_l\\
\pi_6 &= d_i^{a6}\mu_l^{b6}C_{p,l}^{c6}\rho_l^{d6}\rho_v\\
\pi_7 &= d_i^{a7}\mu_l^{b7}C_{p,l}^{c7}\rho_l^{d7}\sigma\\
\pi_8 &= d_i^{a8}\mu_l^{b8}C_{p,l}^{c8}\rho_l^{d8}x\\
\pi_9 &= d_i^{a9}\mu_l^{b9}C_{p,l}^{c9}\rho_l^{d9}d_{coil}\\
\pi_{10} &= d_i^{a10}\mu_l^{b10}C_{p,l}^{c10}\rho_l^{d10}\delta_{coil}\\
\pi_{11} &= d_i^{a11}\mu_l^{b11}C_{p,l}^{c11}\rho_l^{d11}\mu_v
\end{aligned} \tag{5.2}$$

For each group the summation of a single dimension powers should be equal to zero. For instance:

$$\pi_1 = [L]^{a1}\left[ML^{-1}T^{-1}\right]^{b1}\left[L^2T^{-2}\theta^{-1}\right]^{c1}\left[ML^{-3}\right]^{d1}\left[MT^{-3}\theta^{-1}\right] \tag{5.3}$$

L: $a_1 - b_1 + 2C_1 - 3d_1 = 0.0$

M: $b_1 + d_1 + 1 = 0.0$

θ: $- c_1 - 1 = 0.0$

T: $- b_1 - 2C_1 - 3 = 0.0$

For each dimensionless group four equations are solved to determine four unknowns. Table 5.1 summarizes the values of the 44 constants in the dimensional analysis.

Table 5.1: Dimensional analysis constants.

Dimensionless group	a	B	c	d
π_1	1	-1	-1	0
π_2	1	-1	0	0
π_3	2	-2	1	2
π_4	2	-2	0	2
π_5	0	-1	-1	0
π_6	0	0	0	-1
π_7	1	-2	0	1
π_8	0	0	0	0
π_9	-1	0	0	0
π_{10}	-1	0	0	0
π_{11}	0	-1	0	0

This will lead to the following dimensionless groups:

$$\pi_1 = \frac{Nu_{tp}}{\Pr_l} \qquad \pi_2 = \mathrm{Re}_{lo} \qquad \pi_3 = \left(\frac{C_{p,l}\rho_l^2 \Delta T_{wall}}{G_{ref}^2}\right)\mathrm{Re}_{lo}^2$$

$$\pi_4 = \left(\frac{\rho_l^2 h_{fg}}{G_{ref}^2}\right)\mathrm{Re}_{lo}^2 \qquad \pi_5 = \frac{1}{\Pr_l} \qquad \pi_6 = \left(\frac{\rho_v}{\rho_l}\right) \tag{5.4}$$

$$\pi_7 = \left(\frac{\rho_l \sigma}{G_{ref}\mu_l}\right)\mathrm{Re}_{lo} \qquad \pi_8 = x \qquad \pi_9 = \left(\frac{d_{coil}}{d_i}\right) = fn(DeanNumber)$$

$$\pi_{10} = \left(\frac{\delta_{pitch}}{d_i}\right) \qquad \pi_{11} = \left(\frac{\mu_v}{\mu_l}\right)$$

It could be noted from this dimensional analysis that the boiling heat transfer coefficient may be correlated using the following dimensionless parameters:

$$Nu_{tp} = fn\left(\mathrm{Re}_{lo}, \mathrm{Pr}_l, \left(\frac{C_{p,l}\rho_l^2 \Delta T_{wall}}{G_{ref}^2}\right), \left(\frac{\rho_l^2 h_{fg}}{G_{ref}^2}\right), \left(\frac{\rho_v}{\rho_l}\right), \left(\frac{\rho_l \sigma}{G_{ref}\mu_l}\right), x, \left(\frac{d_{coil}}{d_i}\right), \left(\frac{\delta_{coil}}{d_i}\right), \left(\frac{\mu_v}{\mu_l}\right)\right) \quad \textbf{(5.5)}$$

These parameters could be combined to form common dimensionless groups as:

$$\left(\frac{\rho_l^2 h_{fg}}{G_{ref}^2}\right) / \left(\frac{C_{p,l}\rho_l^2 \Delta T_{wall}}{G_{ref}^2}\right) = \frac{h_{fg}}{C_{p,l}\Delta T_{wall}} = \frac{1}{Ja} \qquad \text{Ja = Jacob Number} \qquad \textbf{(5.6)}$$

$$\left(\frac{\rho_l \sigma}{G_{ref}\mu_l}\right) = \frac{\rho_l \sigma}{G_{ref}\mu_l} * \frac{G_{ref} d_i}{G_{ref} d_i} = \frac{\mathrm{Re}_{lo}}{We_{lo}} = fn(We_{lo}) \qquad \text{We= Weber number} \qquad \textbf{(5.7)}$$

Also the Martinelli number can be used to represent the effect of density ratio, viscosity ratios and vapour quality as reported by other researchers Zhao (2003) and Wongwises and Polsongkram (2006a):

$$X_{tt} = \left(\frac{1-x}{x}\right)^{0.9} \left(\frac{\rho_v}{\rho_l}\right)^{0.5} \left(\frac{\mu_l}{\mu_v}\right)^{0.1} \qquad \textbf{(5.8)}$$

The Helical coil dimensionless parameters that are mostly used in helical coils are the liquid only Dean Number (Dn_{lo}) and Helical number (He_{lo}):

$$He_{lo} = \frac{Dn}{\sqrt{\left(1 + \left(\frac{\delta_{coil}}{\pi d_{coil}}\right)^2\right)}} \qquad \text{Helical Number} \qquad \textbf{(5.9)}$$

$$Dn_{lo} = \mathrm{Re}_{lo}\sqrt{\left(\frac{di}{d_{coil}}\right)} \qquad \text{Liquid only Dean Number} \qquad \textbf{(5.10)}$$

Since the Helical Number combines both the Dean Number and dimensionless coil pitch, it will be utilized for correlating the data. Thus equation 5.5 can be rewritten as:

$$Nu_{tp} = fn\left(\mathrm{Re}_{lo}, \mathrm{Pr}_l, \frac{1}{Ja}, \frac{1}{We_{lo}}, X_{tt}, \frac{1}{He_{lo}}\right) \tag{5.11}$$

The analysis is further simplified by reducing the number of independent variables by using the Stanton Number as:

$$\left(\frac{Nu_{tp}}{\mathrm{Re}_{lo}\,\mathrm{Pr}_l}\right) = fn\left(\frac{1}{Ja}, \frac{1}{We_{lo}}, X_{tt}, \frac{1}{He_{lo}}\right) \tag{5.12}$$

$$St_{tp} = fn\left(\frac{1}{Ja}, \frac{1}{We_{lo}}, X_{tt}, \frac{1}{He_{lo}}\right) \tag{5.13}$$

5.2.1 Experimental data

Table 5.2 summarizes the collected experimental database and the number of data points. The table includes the number of data points N, position of the coil (Horizontal or vertical), fluid used, dimensions including tube diameter, coil diameter, pitch, and operating conditions including heat and mass fluxes and operating pressures. The data cover wide range of fluids, geometric parameters and operating conditions. It has been found from the experimental measurements for tube diameters less than 2 mm that early dry out occurs at vapour quality of 0.6 or less. This trend also has been proved by Kim et al. (2000) using R-22 through helical tubes with diameter of 1 mm and by current measurements for coils 2 mm, 1.55 mm and 1.1 mm. As a result, experimental data are split into data sets for tube diameters larger and smaller than 2 mm. Also, the transition diameter between macro boiling and micro boiling as proposed by Kew and Cornwell (Thome, 2010) and given in equation (5.14) for straight tube is 1.87 mm to 1.7 mm as depicted in figure (5.2) for R134a boiling at pressures of 3.5 bar to 6 bar respectively.

Kew and Cornwell criterion does not depend on the tube position (vertical or horizontal) since the flow is governed by surface tension and not gravity where the bubble is confined in channel. Assuming such criteria could be applied for helical coils, then when small diameter tubes are used, the bubbles after detaching from the surface will be confined and elongate in the axial direction rather than in the radial direction. Therefore transition diameter close to 2 mm can be used to take into account the confined bubble behaviour in small diameter channels.

$$d_{th} = 2\sqrt{\left(\frac{\sigma}{g(\rho_l - \rho_v)}\right)} \tag{5.14}$$

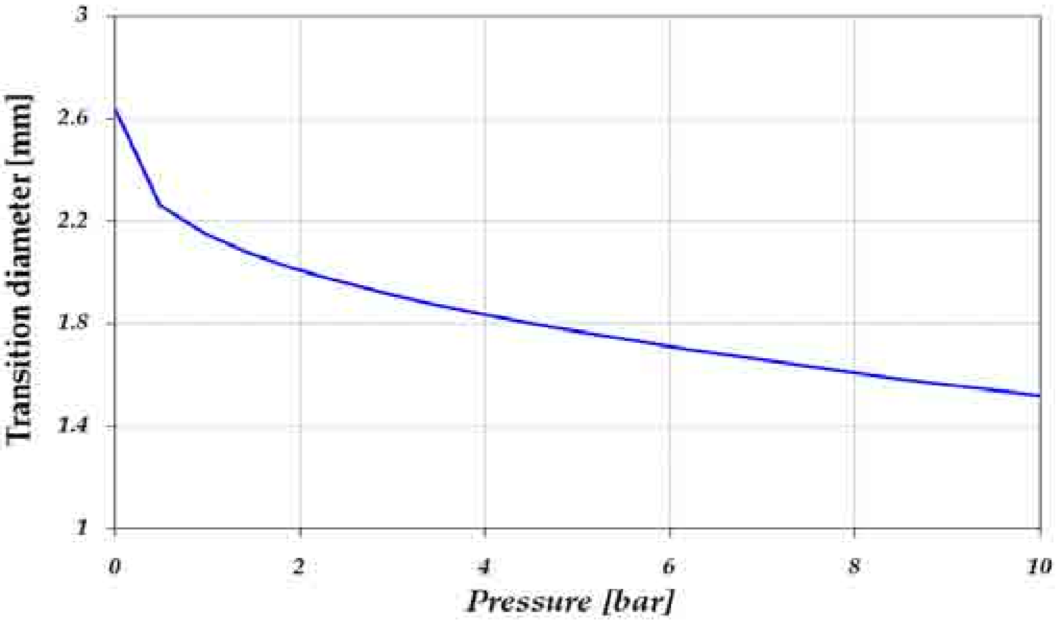

Figure 5.2: Transition diameter to micro-boiling based on confinement number proposed by Kew and Cornwell (Thome, 2010)

5.2.2 Regression analysis

The mathematical formula in equation (5.13) has been fitted using nonlinear multivariable regression analysis using datamaster 2003 software. Figure 5.3 shows the prediction of the experimental results using equation 5.15. The developed correlations are given in equation 5.15 where 88 % of data are predicted within ± 40% deviation.

Most of data scattered outside this boundary are from Kim (2000) data as more than 20 % of their data were above dryout where sharp reduction was observed in their data. Most of data scattered were found in the dryout after the peak as boiling mechanism before and after dryout is different. In case of the large tube diameters (d > 2mm), Some of Zhao et al. (2003) data were outside the 40% margin as some of their data were above dryout. They used large heat fluxes in their experiment (up to 900 kW/m^2).

For large tube diameters (2 <d_i <10 mm):

$$St_{tp} = 0.05473 \left(\frac{1}{Ja}\right)^{-0.55611} (X_{tt})^{-0.247552} \left(\frac{1}{We_{lo}}\right)^{0.22287} \left(\frac{1}{He_{lo}}\right)^{-0.17954} \qquad \textbf{(5.15a)}$$

For small tube diameters (1mm <$d_i \leq$ 2 mm):

$$St_{tp} = 0.1905 \left(\frac{1}{Ja}\right)^{-0.09422} (X_{tt})^{-0.131885} \left(\frac{1}{We_{lo}}\right)^{-0.025136} \left(\frac{1}{He_{lo}}\right)^{0.5446} \qquad \textbf{(5.15b)}$$

Table 5.2: Experimental data utilized in dimensional analysis.

Author	N (-)	Position (-)	Fluid (-)	d_i (mm)	D_{coil} (mm)	Pitch (mm)	G (kg/m^2.s)	q (kW/m^2)	P (bar)
Data for diameters larger than 2 mm									
Zhao (2003)	69	H	Steam	9	292	30	236-943	0-900	30
Jitian	144	H	R134a	7.6	600	30	50-500	5-20	3.5-5.6
Kaji (1998)	22	V	R113	10	165	82	305, 1564	53,188	3.9
Wongwises (2006)	118	V	R134a	7.2	305	35	400-800	5-10	4.15-5.87
Coil A	27	V	R134a	2.88	30	7	108-186	4-9.3	2.6-3.8
Data for diameters less than 2 mm									
Kim (2000)	71	V	R22	1	31 , 34	9.1, 7.5	150-500	1.5-3	5.88
Coil B	53	H	R134a	2	60	8	190-300	2.5,5	4-7
Coil C	69	H	R134a	1.55	60	8	190-300	5,12	3.4
Coil D	78	H	R134a	1.1	60	8	250-450	5,8,12	3.4-5

The dimensional analysis correlation has been established using 5 different experimental sources of data with ±40% deviation. Recently, artificial neural networks have been used as a prediction tool in many thermal engineering fields ranging from prediction of drying rates in food industries to prediction of temperature profiles. Many researchers recommended neural networks for more accurate prediction of the performance of thermal systems. In the next section, the application of neural networks in developing a more accurate predicting method of the two-phase heat transfer coefficient in helical coils will be described.

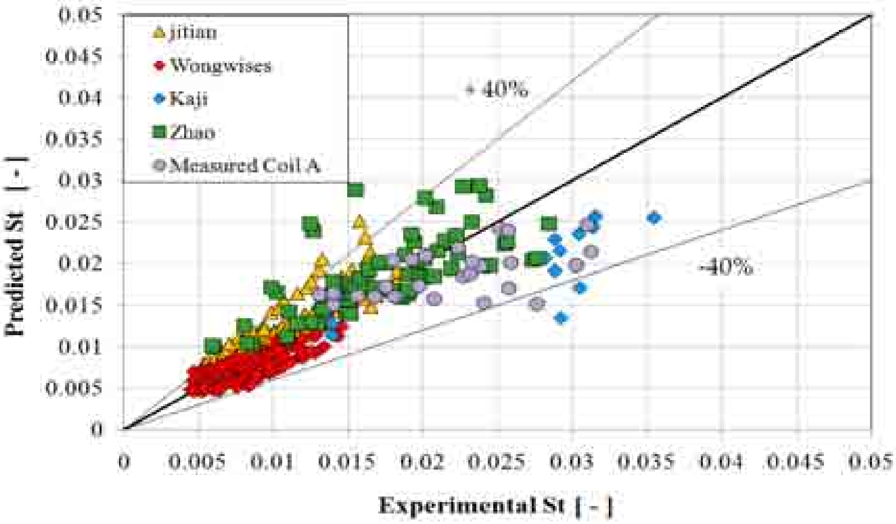

(A) Large diameter data validation

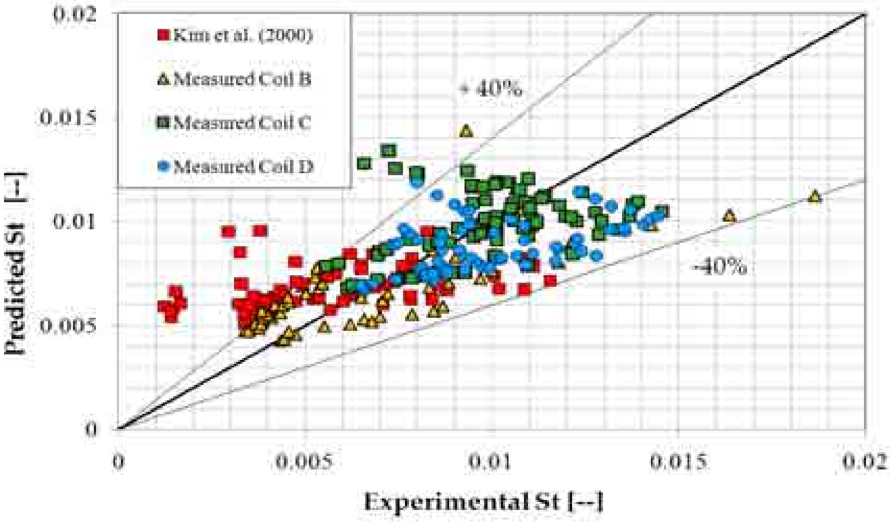

(B) Small diameter data validation

Figure 5.3: Validation of newly developed correlations.

5.3 Artificial neural network

Recently, Artificial Neural Networks (ANNs) technique have been used for system performance prediction in various thermal engineering applications such as drying rates in food industry, heat transfer rates in compact heat exchangers (Tan et al., 2009) and heat pumps performance (Esen et al., 2008). The ANNs methodology enables the design of useful nonlinear systems accepting large number of inputs, with the design based solely on input–output relationship and proved to be a powerful tool to analyze different heat transfer processes. ANN is used here to develop a prediction method for the flow boiling heat transfer coefficient inside helical coils that outperform existing empirical correlations including those developed in section 5.2.

5.3.1 Definition of network input and output parameters

The ratio between the two-phase heat transfer coefficient and liquid only or liquid heat transfer coefficient is widely utilized for determining the heat transfer coefficient in helical coils (Zhao et al., 2003; Kaji et al., 1998, Chen et al., 2011a and Isheda, 1981). The liquid heat transfer coefficient is a strong function of the following parameters:

$$\alpha_l = fn\left(\mathrm{Re}_l, \mathrm{Pr}_l, d_i / d_{coil}\right) \tag{5.16}$$

where $\mathrm{Re}_l = \dfrac{G(1-x)d_i}{\mu_l}$ and $\mathrm{Pr}_l = \dfrac{Cp_l \mu_l}{k_l}$

Rearranging:

$$\alpha_l = fn\left(\mathrm{Re}_l \sqrt{d_i / d_{coil}}, \mathrm{Pr}_l\right) = fn(Dn_l, \mathrm{Pr}_l) \tag{5.17}$$

where $Dn_l = \mathrm{Re}_l \sqrt{d_i / d_{coil}}$

The liquid heat transfer coefficient has been calculated from Mori-Nakayama correlation mentioned in chapter 2.

For flow boiling heat transfer coefficients, the two most important dimensionless parameters that express the different boiling mechanisms are the boiling number (Bo) and the convective number (Co) defined as:

$$\alpha_{tp} = fn(Bo, Co) \tag{5.18}$$

Where $Co = \left(\frac{1-x}{x}\right)^{0.8}\left(\frac{\rho_v}{\rho_l}\right)^{0.5}$ and $Bo = \frac{q}{Gh_{fg}}$

Therefore, the two-phase to liquid heat transfer coefficients ratio can be written as:

$$\frac{\alpha_{tp}}{\alpha_l} = fn(Bo, Co, \alpha_l) \tag{5.19}$$

Where the liquid heat transfer coefficient was calculated at the liquid flow G(1-x).

5.3.2 Network structure

A neural network consists of a large number of simple processing elements called neurons or nodes. Each neuron is connected to other neurons by means of direct communication links with associated weights. The input signal is multiplied by the weight of the link then a bias is added before conversion of signal through the transfer function. In this work, the artificial neural network (ANN) of two-phase to liquid heat transfer coefficients ratio was designed using the Boiling, Convective numbers and liquid heat transfer coefficient as given in equation 5.19 . The normalized Convective, Boiling numbers and liquid heat transfer coefficient were used as the inputs for the developed network while the normalized ratio of the two-phase to liquid heat transfer coefficients was set as the network output. Data processing using ANN is shown in figure 5.4 and equation 5.20 is used to normalise the data with normalisation range of 0.8 and the lower limit of 0.1.

$$R^{+} = \frac{R - R_{\min}}{R_{\max} - R_{\min}} * \text{Normalized range} + \text{lower limit of normalized range} \qquad \textbf{(5.20)}$$

Where R represent the actual value of the parameter that would be normalized to R^{+}.

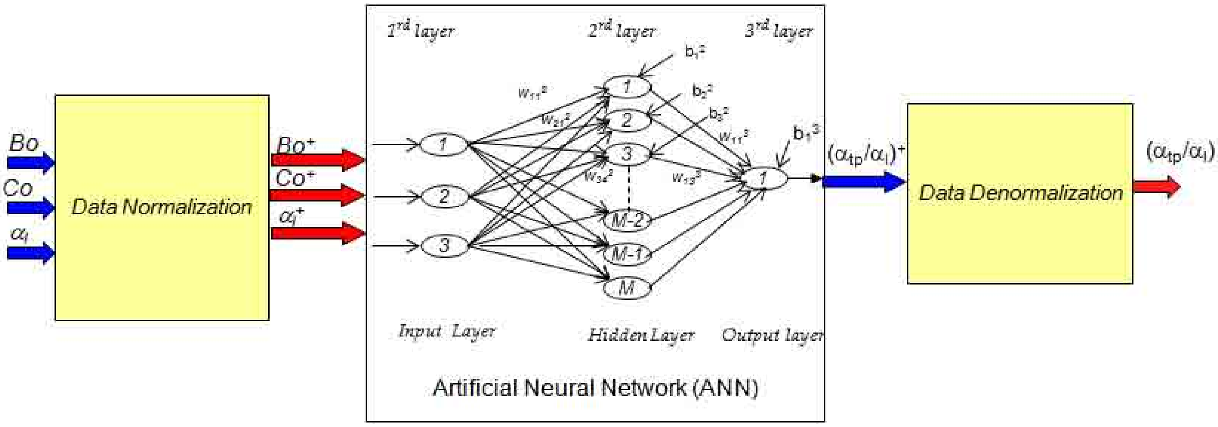

Figure 5.4: Neural network structure.

The central idea of neural networks is that the neuron's weights and biases can be adjusted so that the network exhibits some desired behaviour. There are several structures of neural networks including multilayer perceptron (MLP), radial basis function (RBF) and generalized regression neural network (GRNN). The multilayer perceptron (MLP) has become increasingly used in engineering applications (Wang *et al.*, 2006) due to its simplicity and effectiveness in tracking nonlinear behaviour of physical parameters. The number of neurons in the input layer and the number of the neurons in the output layer were determined by the number of the input and output parameters respectively. The neurons perform non-linear input-output transformation by means of selected activation functions. Each neuron in the input layer makes the weighted summation of all the neurons in the hidden layer, and then passes this summation through a transfer function. Likewise, the neurons in hidden layer makes the weighted summation of all the neurons in the output layer where the summation is passed through the transfer function in the output layer to obtain $(\alpha_{tp}/\alpha_l)^+$. The number of the neurons in the hidden layer is determined by a trial and error process together with cross-validation of the experimental data (Nafey, 2009). The most commonly used transfer functions are: log-sigmoid, tan-sigmoid and pure linear as shown in figure 5.5. With respect to log-sigmoid and tan-sigmoid transfer functions, the output should be normalized within interval (0,1) and (-1,1) respectively. Log-sig was used in both the hidden and output layers in the designed network as it produces better prediction of experimental data and consumes smaller training time (Wang et al., 2006). In addition, although the value of the ANNs input is unlimited in terms of log-sigmoid or tan-sigmoid transfer function, if the absolute value of the input is very large, the output of the hidden neuron will be very close either to 0 or 1 and not sensitive to the input (as shown in figure 5.5A). Therefore for the purpose of effective training, the input was also normalized within 0.1 to 0.9. After the training step, the output will be denormalized to produce values of the heat transfer coefficients.

The aim is to reduce the error by adjusting the interconnections between layers. The Back-propagation (Bp) algorithm is an iterative gradient algorithm, designed to minimize the mean square error (MSE) between the predicted output and the desired one (Naser *et al.*, 2010). Several back-propagation learning techniques exist in matlab toolbox including Levenberg-Marquardt (trainlm), scaled conjugate gradient learning algorithm (trainscg), Pola-Ribiere conjugate gradient (traincgp) and Bayesian regularization (trainbr). The difference between these algorithms is the method of adjusting the weights during iteration (epoch). Sigmoid transfer functions with Levenberg-Marquardt learning algorithm have been utilized in the training process as it requires small training time to reach a certain goal (MSE in the current study) and its robustness was proved by several researchers (Esen et al., 2008) and (Demir *et al.*, 2009). During the design of neural networks, the optimum number of neurons in the hidden layer and the training goal should be determined by minimizing the error function in both training and validation data. In this work, in order to find the suitable number of neurons in the hidden layer, the number of epochs has been set to 4000 and the performance of the network was evaluated based on the mean relative error (MRE).

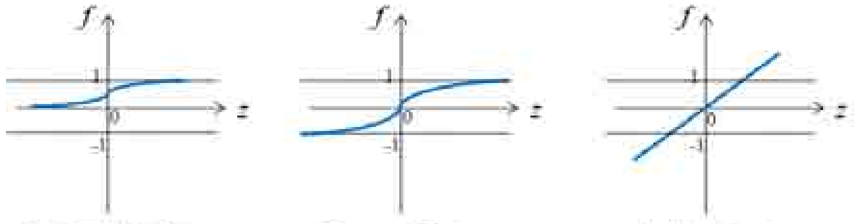

Log-sigmoid function Tan-sigmoid function Pure linear function

A. $f_{\log}(Z) = 1/(1+e^{-Z})$ B. $f_{\tan}(Z) = \left(2/\left(1+e^{-2Z}\right)\right) - 1$ C. $f_{line}(Z) = Z$

Figure 5.5: Common transfer functions utilized in neural networks.

The speed of learning is governed by the learning rate. Learning rate affects the convergence speed and stability of the weights and biases during learning. The larger the learning rate, the bigger the step. If the learning rate is made too large, the algorithm becomes unstable. If the learning rate is set too small, the algorithm takes a long time to converge. In this work, the learning rate and momentum constant have been set to 0.01 and 0.9 respectively as recommended by (Zhang and Wang, 2008). Several data sources have been selected to cover a wide range of operating conditions during training of the networks (see table 5.2). For tube diameters larger than 2 mm, the data from Jitian et al., Zhao (2003), Kaji (1998), Wongwises (2006) were utilized for training and Coil A data were utilized for validation. In case of small diameter tubes, Kim (2000), Coil B, Coil D has been selected for training and Coil C data for validation.

5.3.3 Network design

Several network designs have been tested using different number of neurons. The number of neurons in the hidden layer was optimised to reduce the mean relative error in the validation data at 4000 epochs (No change in training error after 4000 epochs). It has been found that 7 neurons were sufficient to give good prediction for both the training and validation data as shown in figure 5.6A and figure 5.6B with MRE (mean relative error) in the normalized validation data of 4.98 % and 7.53 % for the large and small coils network respectively. The mean relative error (MRE) and mean square error (MSE) in the normalized data were defined as:

$$MRE[\%] = \frac{1}{N}\sum_{i=1}^{N}\frac{\left|\left(\alpha_{tp}/\alpha_l\right)^{+}_{pre} - \left(\alpha_{tp}/\alpha_l\right)^{+}_{\exp}\right|}{\left(\alpha_{tp}/\alpha_l\right)^{+}_{\exp}} * 100 \qquad \textbf{(5.21)}$$

$$MSE = \frac{1}{N}\sum_{i=1}^{N}\left[\left(\alpha_{tp}/\alpha_l\right)^{+}_{pre} - \left(\alpha_{tp}/\alpha_l\right)^{+}_{\exp}\right]^2 \qquad \textbf{(5.22)}$$

The normalized heat transfer coefficient ratio in the designed neural network can be expressed in the following equation:

$$\left(\frac{\alpha_{tp}}{\alpha_{lo}}\right)^{+} = \frac{1}{1+e^{-Z_1^3}} \qquad \textbf{(5.23)}$$

Where $Z_1^3 = \left(w_{1-1}^3 f_1^2 + w_{1-2}^3 f_2^2 + w_{1-3}^3 f_3^2 + \ldots + w_{1-7}^3 f_7^2 + b_1^3\right)$ and $f_1^2,\ f_2^2, \ldots ,\ f_7^2$ are the logestic sigmoid (log-sig) transfer functions in the hidden layer expressed as:

$$f_1^2 = \frac{1}{1+e^{-Z_1^2}}, f_2^2 = \frac{1}{1+e^{-Z_2^2}}, \ldots, f_7^2 = \frac{1}{1+e^{-Z_7^2}} \qquad \textbf{(5.24)}$$

With values of hidden layer neurons:

$$\begin{aligned} Z_1^2 &= (w_{1-1}^2 Bo^+ + w_{1-2}^2 Co^+ + w_{1-3}^2 \alpha_l^{\ +} + b_1^2) \\ Z_2^2 &= (w_{2-1}^2 Bo^+ + w_{2-2}^2 Co^+ + w_{2-3}^2 \alpha_l^{\ +} + b_2^2) \\ &\vdots \\ Z_7^2 &= (w_{7-1}^2 Bo^+ + w_{7-2}^2 Co^+ + w_{7-3}^2 \alpha_l^{\ +} + b_7^2) \end{aligned} \qquad \textbf{(5.25)}$$

The weights w_{jk}^2, w_{jk}^3 and biases b_j^2 and b_j^3 of the input and output of the designed neural network are shown in table 5.3 and table 5.4 for large diameter and small diameter coils respectively where these values could be used through equations 5.23 to 5.25 to directly predict the normalized heat transfer coefficient ratio.

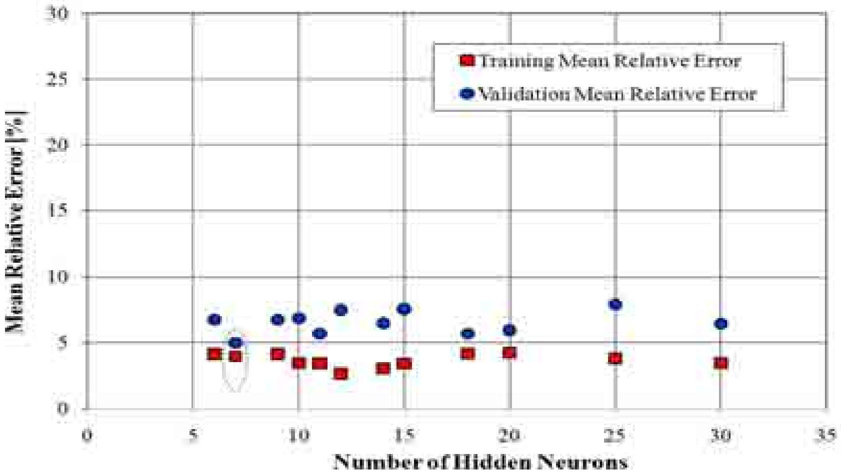

A. Large diameter coils

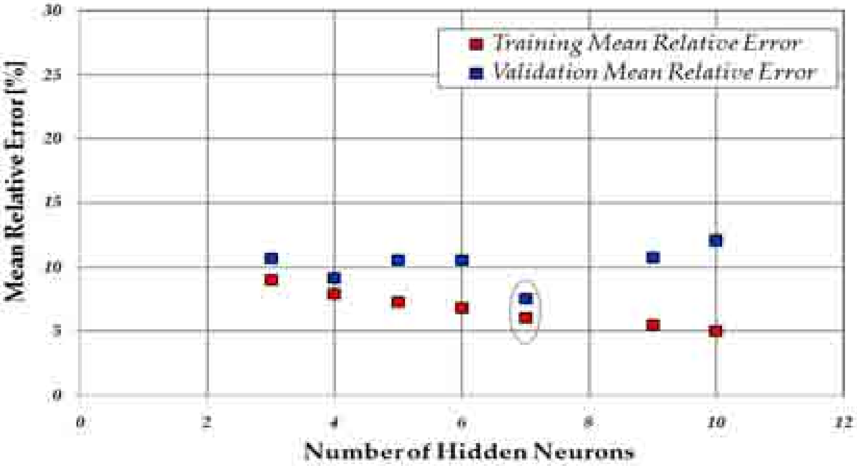

B. Small diameter coils

Figure 5.6: Design of Artificial Neural Network

Figure 5.7A shows that the ANN predicted the experimental results of coil A with diameter of 2.8mm with ±30% accuracy. However, the empirical correlation of Akhavan- Behabadi (2009) that was developed for R134a flow boiling in helical coils with tube diameter of 8.28 mm and given by equation (5.26) over predicted the current experimental results significantly. Also, the ANN prediction is better than the empirical correlation produced in section 5.2.

Table 5.3: Weight and biases of large coils neural network.

Weight of Hidden Neurons (Second layer) $w_{jk}^2/1000$	Input Neurons			Biases in hidden neurons b_j^2 (Second layer)
	$Bo^+(k=1)$	$Co^+(k=2)$	$Pr^+(k=3)$	
j=1	-0.0291	-0.0617	-0.0562	22.6416
j=2	0.0026	-0.0161	0.0019	0.4862
j=3	0.0076	-0.0014	-0.0042	-2.4439
j=4	0.5303	-3.0443	-1.1326	496.5046
j=5	0.0178	-0.1781	0.0152	6.1820
j=6	-0.0668	-0.3427	-0.1314	135.4904
j=7	0.0001	-0.1319	-0.0288	17.2062

Weight of output Neurons (Third layer) W_{jk}^3	k=1	k=2	k=3	k=4	k=5	k=6	k=7	Bias b_j^3
j=1	0.1756	0.7442	0.8268	0.1145	2.7574	0.0991	1.6056	-2.1060

Network Validity range	Min Value	Max Value
Bo	3.350E-05	1.375E-03
Co	1.794E-02	1.005E+00
α_l	65	9446

Table 5.4: Weight and biases of small coils neural network.

Weight of Hidden Neurons (Second layer) w_{jk}^2	Input Neurons			Biases in hidden neurons b_j^2 (Second layer)
	$Bo^+(k=1)$	$Co^+(k=2)$	$\alpha_l^+(k=3)$	
j=1	17.5274	-378.1403	-255.3984	72.4228
j=2	1.4786	-974.8637	164.8696	67.8774
j=3	0.4812	-9.8669	-0.4362	-3.3686
j=4	-190.6415	-191.9466	-21.0461	55.6331
j=5	-184.9329	-184.0135	-18.3622	53.0723
j=6	-4.5174	-81.1953	-0.0595	4.5663
j=7	-809.7390	364.1324	-246.3124	201.4254

Weight of output Neurons (Third layer) W_{jk}^3	k=1	k=2	k=3	k=4	k=5	k=6	k=7	Bias b_j^3
j=1	1.0415	38.6272	85.7453	-26.4968	26.099	205.1878	-0.3083	-1.7539

Network Validity range	Min Value	Max Value
Bo	2.3170 E-05	3.18400 E-04
Co	0.008636	1.032 E+00
α_l	33.2	1486

Figure 5.7B compares the ANN prediction of the experimental results of coil C with tube internal diameter of 1.55mm to the prediction using equation 5.15 for 1mm< $d_i \leq$ 2mm developed in section 5.2 predicts the experimental results within ±40%. The Akhavan-Behabadi empirical correlation over predicted coil C experimental results significantly. This indicates the superiority of the ANN in predicting the experimental heat transfer coefficients with good accuracy.

$$Nu_{tp} = 5980\, Dn_{eq}^{0.43}\, \Pr^{-5.055} \left(Bo \times 10^{4}\right)^{0.125} x_{tt}^{-0.036} \qquad \textbf{(5.26)}$$

Where $Dn_{eq} = \left[\mathrm{Re}_l + \mathrm{Re}_v \left(\frac{\mu_v}{\mu_l} \right) \left(\frac{\rho_v}{\rho_l} \right)^{0.5} \right] \left(\frac{d_i}{d_{coil}} \right)^{0.5}$

5.4 Summary

Two new generalized predictive methods of heat transfer flow boiling in helical coils were developed. The first one is based on dimensional and regression analysis. The second method is based on artificial neural network. Both developed techniques cover a wide range of operating conditions such as mass velocities, heat fluxes, coil diameters, tube diameters. The mass velocities, heat fluxes, pressures, tube diameters, coil diameters were up to 1600 kg/m^2.s, 900 kW/m^2, 30 bar, 10 mm, 600 mm respectively.

A normalized artificial neural network was trained by using the normalized liquid heat transfer coefficient, boiling number and convective number as the network inputs. The two-phase to liquid heat transfer ratio was utilized as the network output. Agreement between the validation experimental data and ANN prediction within ± 30% was obtained.

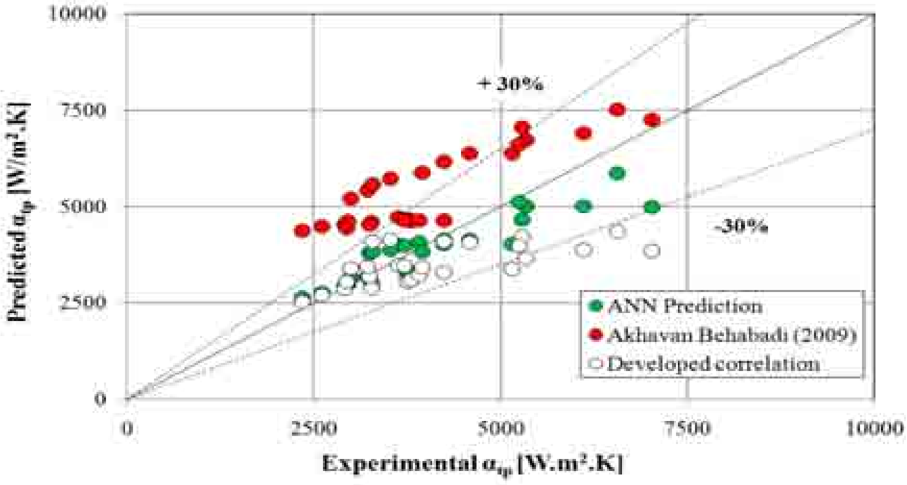

A. Comparison of coil A (d_i=2.8 mm) data against different prediction.

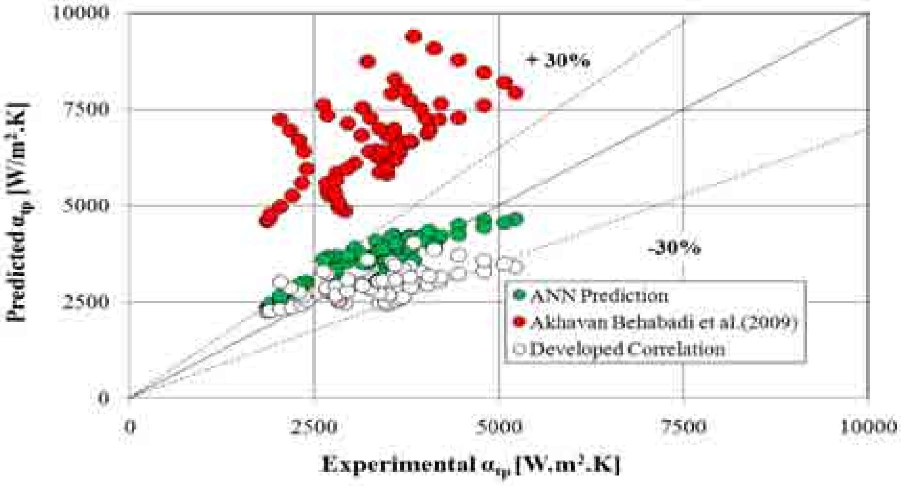

B. Comparison of coil C (d_i=1.55 mm) data against different prediction.

Figure 5.7: Validation of ANN against empirical correlations.

CHAPTER 6

Performance of Miniature Cooling Systems

6.1 Introduction

Utilizing helically coiled tubes evaporator and condenser in cooling applications is promising due to their higher heat transfer coefficients compared to straight tube. With growing interest in miniature and efficient refrigeration systems, the use of small diameter helically coiled tubes can offer significant advantages in terms of being compact, light weight and improved coefficient of performance. This chapter first describes a performance study of small scale vapour compression cooling system (100 W cooling capacity) equipped with shell and helically coiled tube evaporator and condenser. Afterwards, a detailed mathematical model has been developed for this system based on thermodynamic principles and relevant heat transfer correlations and will be described in section 6.3. The model was validated and then used to optimise the cooling system performance in terms of the evaporator and condenser geometric parameters including helical coil diameter, tube inside diameter, and surface area ratio.

6.2 Test methodology and data reduction

The test facility described in chapter 3 was used to determine the performance of the vapour compression cooling system equipped with helically coiled evaporator and condenser. The water cooled condenser and the water heated evaporator were used in the experimental study. Several parameters were investigated including the effect of refrigerant and water flow rate in both the condenser and evaporator. The refrigerant flow rate was varied from 21 to 25 ml/min while the degree of superheat ranged from 2

K to 18 K. The water flow rate through the evaporator was varied from 190 ml/min to 230 ml/min while the condenser water flow rate varied from 270 ml/min and 300 ml/min. All Data were collected at steady state conditions. Table 6.1 summarizes the controlling methods to achieve the test conditions.

Table 6.1: Adjustment of experimental test condition.

Tested parameter	Evaporating temperature	Refrigerant mass velocity	Water flow	Water inlet temperature
Controlling facility	Compressor speed	Manual expansion valve	Needle valves	Immersed heater

The heat transfer from water in the evaporator was calculated from:

$$Q_{evap,w} = \dot{m}_{evap,w} C_w (T_{evap,w,in} - T_{evap,w,out}) \quad \textbf{(6.1)}$$

The heat transfer to refrigerant in the evaporator was calculated from enthalpy difference calculated at the suction pressure:

$$Q_{evap,ref} = \dot{m}_{ref} (h_{evap,ref,out} - h_{evap,ref,in}) \quad \textbf{(6.2)}$$

Similarly the heat transfer between refrigerant and water in the condenser was calculated as:

$$Q_{cond,w} = \dot{m}_{cond,w} C_w (T_{cond,w,out} - T_{cond,w,in}) \quad \textbf{(6.3)}$$

$$Q_{cond,ref} = \dot{m}_{ref} (h_{cond,ref,in} - h_{cond,ref,out}) \quad \textbf{(6.4)}$$

Figure **6.1** compares the evaporator cooling capacity calculated from the refrigerant side to that of the water side and the condenser heat rejected calculated for the refrigerant and water sides. These results show that the heat balance of both the evaporator and condenser are within ± 20%. This deviation in heat balance is slightly higher than what has been reported by other researchers working on small scale evaporators and condensers (Trutassanawin et al., 2006) with 15% deviation. This difference could be attributed to the uncertainties in the measurements. Regarding the deviation on the positive side, there is no clear justification for this, though similar trend observed by (Trutassanawin et al., 2006).

Figure 6.2 shows variation of the cooling capacity with increasing the cooling water flow rate in the evaporator. The results were obtained at two condenser water flow rates namely 300 and 270 ml/min and two refrigerant volume flow rates namely 22 and 24 ml/min. It is depicted that the cooling capacity increases with the increase of cooling water in the evaporator which increases the suction pressure and suction density; however this increase is suppressed at high water flow rates due to the increase in the degree superheat of the refrigerant. Although there is a trend that the cooling capacity increases with the increase in condenser water flow due to the decrease in the discharge pressure and the vapour inlet quality to the evaporator thus enhancing the cooling effect, the uncertainty in the measurements may not support this conclusion.

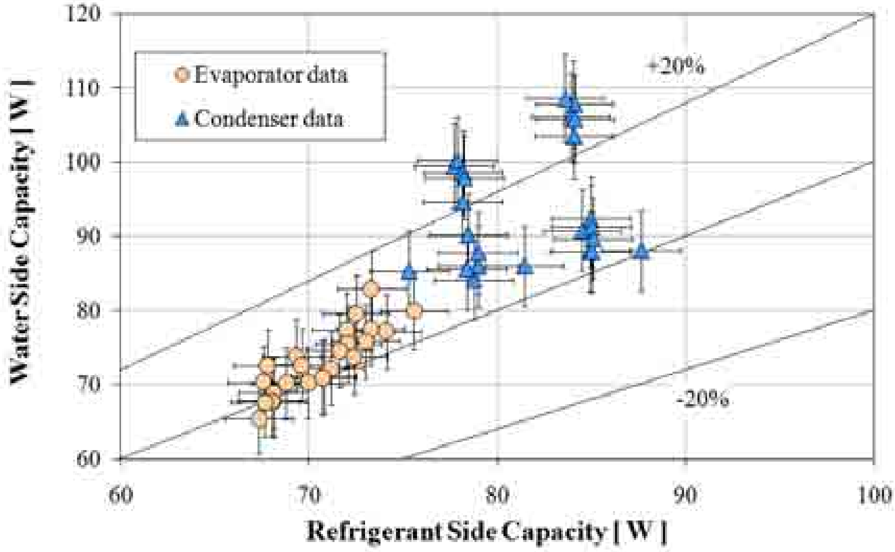

Figure 6.1: Heat balance in the evaporator and condenser.

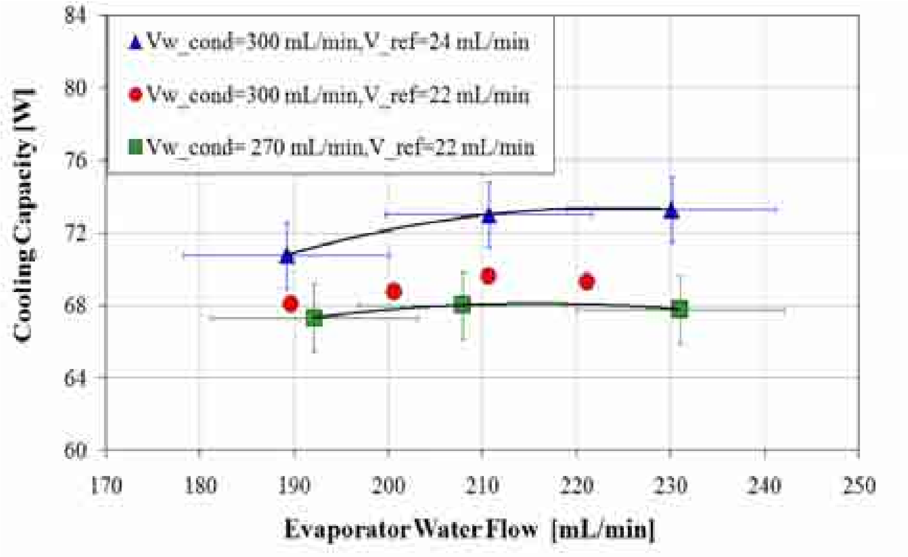

Figure 6.2: Variation of cooling capacity at different water and refrigerant flows.

The thermodynamic cycle *COP* is defined as the ratio between the evaporator cooling capacity to the compression power used to pump the refrigerant:

$$COP_{ref} = \frac{Q_{evap,ref}}{W_{polytropic}} \quad \textbf{(6.5)}$$

The compression process was assumed polytropic compression (general compression process) where the polytropic index (k =1.0246) has been found by fitting the suction and discharge experimental measurement in the following form:

$$P_{suc} v_{suc}^{k} = P_{dis} v_{dis}^{k} \quad \textbf{(6.6)}$$

The polytropic work has been calculated using the following form:

$$W_{polytropic} = \dot{m}_{ref} \frac{k}{k-1} P_{suc} v_{suc} \left(\left(P_{dis} / P_{suc} \right)^{\frac{k-1}{k}} - 1 \right) \quad \textbf{(6.7)}$$

After the ploytropic index was calculated from applying equation (6.6), the polytropic was determined from equation (6.7). The heat losses were determined experimentally by subtracting the refrigerant enthalpy difference across the evaporator from the polytropic work. The system COP is defined as the evaporator cooling capacity to the electrical power supplied including all losses such as mechanical friction between piston and compressor cylinder, compression heat loss, mechanical transmission in crankshaft and connecting rod:

$$COP_{system} = \frac{Q_{evap,ref}}{W_{elect}} \tag{6.8}$$

The electric compressor power was calculated by multiplying the supplied 12 voltage by the consumed current. The uncertainty associated with the electric power measurements were (± 0.5 W). Figure 6.3 shows the variation of the thermodynamic Cycle *COP* and the System *COP* versus the evaporating temperature where the thermodynamic Cycle *COP* varies between 5 to 6 and the System *COP* is nearly 2 due to the compression losses. Uncertainty of ±5% and ±3% Reading were calculated for both *COP*s respectively.

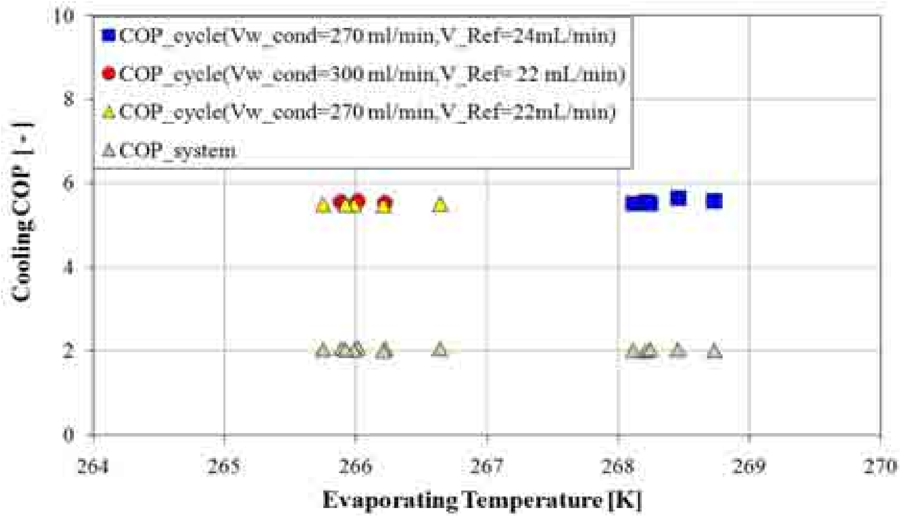

Figure 6.3: Cycle and system coefficient of performances.

The second law efficiency of the system was defined as the ratio between the systems COP to the Carnot COP. This efficiency represents the actual system performance compared to the ideal maximum performance that could be obtained:

$$\eta_{II} = \frac{COP_{system}}{COP_{carnot}} \tag{6.9}$$

$$COP_{carnot} = \frac{T_{evap}}{T_{cond} - T_{evap}} \qquad \textbf{(6.10)}$$

The temperatures in equation (6.10) are in Kelvins. The overall compressor efficiency accounting for the electrical motor losses and the reciprocating component thermal and mechanical losses (valves pressure drop, friction between the piston and wall and heat loss to environment) was defined as:

$$\eta_{overall} = \frac{W_{polytropic}}{W_{elect}} = \frac{COP_{system}}{COP_{ref}} \qquad \textbf{(6.11)}$$

The overall efficiency was found to be 36%, with uncertainty calculated as ±2%. The overall compressor efficiencies for miniature systems were found to be low due to the irreversibility in the compressor as found in the current study, Mongia et al. (2006) and Trutassanawin et al. (2006). Since the compressor shell volume was not small compared to other system component, significant amount of compression heat losses and friction was found in measurements. Additionally, selection of small diameter piping system (d_i=2.8 mm) made the compressor work at high pressure ratio leading to such small efficiencies. The compressor volumetric efficiency is defined as:

$$\eta_{vol} = \frac{\dot{m}_{ref}}{\dot{m}_{ref,theor}} = \frac{\rho_l \dot{V}_l}{\rho_{suc} V_{comp} Rpm} \qquad \textbf{(6.12)}$$

$\dot{V}_l$ is the refrigerant liquid volume flow rate measured by the flow meter. The measured volumetric efficiency was found to be 63% as shown in figure 6.4.

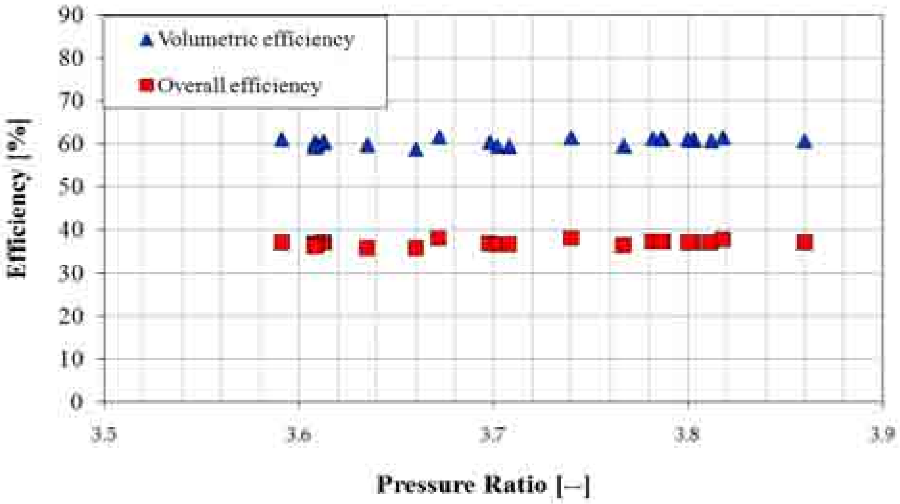

Figure 6.4: Volumetric and overall efficiencies.

Results from figures 6.3 and 6.4 show that the overall cycle efficiency of the tested miniature system (COP_{system}) is lower than the cycle coefficient of performance COP_{cycle} (2 to 5.5) which is mainly due to the lower compressor efficiency. The practical implication of using such system in small scale applications will be higher power consumption therefore; there is a need for further research work to develop miniature compressors with higher efficiencies.

6.3 Mathematical modelling of the cooling system

Based on thermodynamic principles and relevant heat transfer correlations, a detailed mathematical model has been developed for the refrigeration system. Figure 6.5 shows the thermodynamic modelling setup for the compressor, condenser, expansion device and the evaporator.

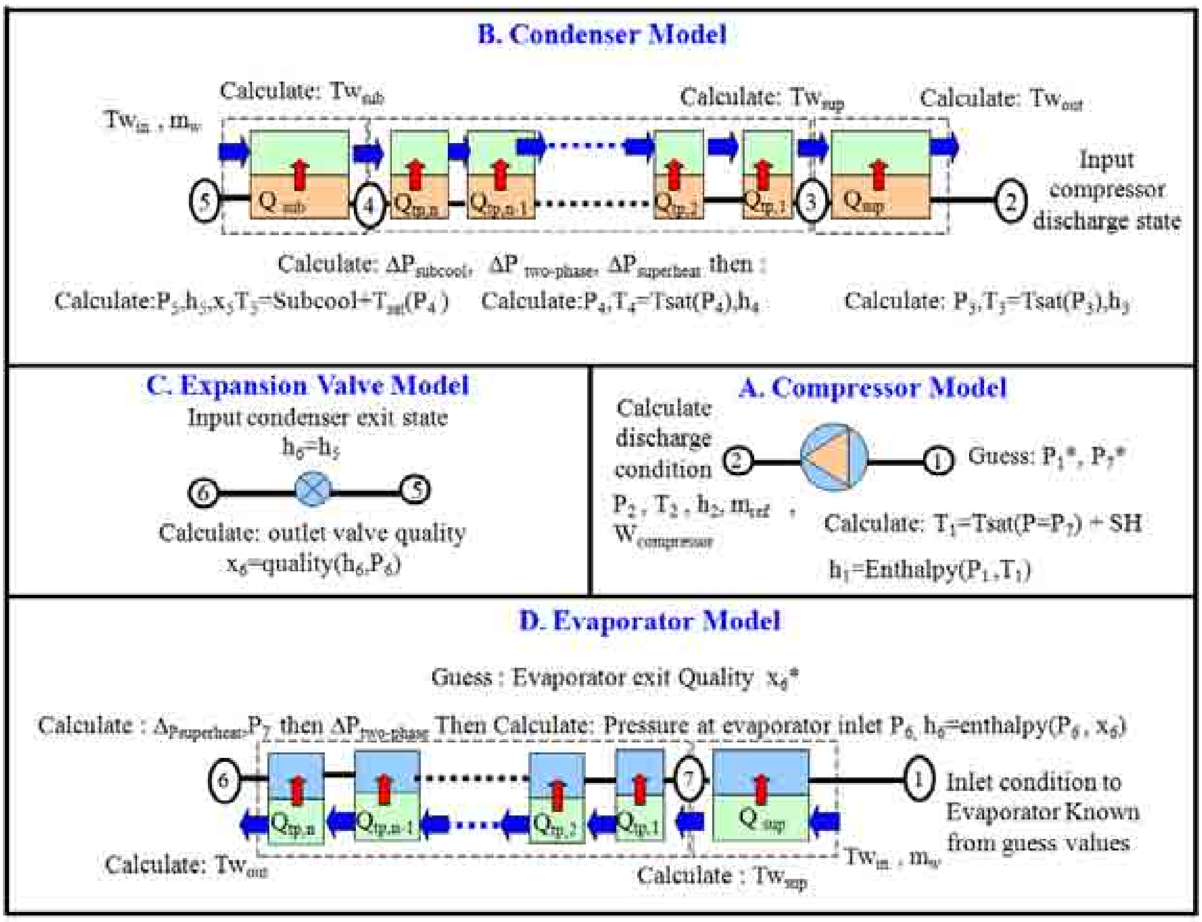

Figure 6.5: Integration between the refrigeration cycle components.

6.3.1 Compressor model

Figure 6.5A shows the thermodynamic model of the reciprocating compressor used with the mass flow calculated using its displacement volume as follows:

$$\dot{m}_{ref}=\rho_{suc}V_{disp}\eta_{vol}\frac{RPM}{60} \tag{6.13}$$

The compressor discharge condition was calculated from:

$$h_2 = h_1 + (W_{polytropic} - Q_{loss}) / \dot{m}_{ref} \tag{6.14}$$

According to the experimental tests performed; the volumetric efficiency, overall efficiency, and the heat loss to polytropic power ratio during compression were found to be 63%, 36 %, and 20% respectively.

6.3.2 Condenser model

Figure 6.5B shows the discretisation of the condenser where it was divided into three main regions; namely the superheated, the subcooled and the two-phase ones. The two-phase region was subdivided into small elements to take into account the effect of vapour quality on pressure drop and heat transfer. For calculating the single phase heat transfer coefficients in the superheated and subcooled refrigerant regions, the Manlapaz and Churchill (Kakaç and Liu, 2002) correlation for constant heat flux boundary conditions and laminar flow regime (Re<1500) was used

$$Nu_i = \left[\left(4.364 + \frac{4.636}{x3}\right)^3 + 1.816\left(\frac{Dn}{x4}\right)^{3/2}\right]^{1/3} \qquad \textbf{(6.15)}$$

$$x3 = \left(1 + \frac{1342}{Dn^2 \Pr}\right)^2 \quad \& \quad x4 = \left(1 + \frac{1.15}{\Pr}\right) \quad \& \quad Dn = \mathrm{Re}\left(d_i / d_{coil}\right)^{1/2}$$

For single phase turbulent flow, Pratt correlation (Kakaç and Liu, 2002) for low Reynolds turbulent flow was used:

$$Nu_i = Nu_{straight}\left[1 + 3.4\left(d_i / d_{coil}\right)\right] \qquad 1.5*10^3 < \mathrm{Re} < 2*10^4 \qquad \textbf{(6.16)}$$

$Nu_{straight}$ is the Nusselt number for turbulent flow inside straight tube for the same flow conditions. For highly turbulent single phase flow, Schmidt correlation (Kakaç and Liu, 2002) was used:

$$Nu_i = Nu_{straight}\left(1 + 3.6\left[1 - \left(d_i / d_{coil}\right)\right]\left(d_i / d_{coil}\right)^{0.8}\right) \qquad 2*10^4 < \mathrm{Re} < 1.5*10^5 \quad \textbf{(6.17)}$$

The Nusselt Number for straight tube was evaluated using Gnielinski correlation (Kakaç and Liu, 2002):

$$Nu_{straight} = \frac{f_{straight}}{8}(\mathrm{Re}-1000) * \mathrm{Pr} / \left(1.07 + 12.7\left(\frac{f_{straight}}{8}\right)^{0.5}\left(\mathrm{Pr}^{2/3}-1\right)\right) \tag{6.18}$$

Where $f_{straight} = (0.79\ln(\mathrm{Re}) - 1.64)^{-2}$

As for the pressure drop calculations, the friction factor was calculated using Schmidt correlation (Guo et al., 2001) for laminar flow:

$$f_c = f_{straight}\left(1 + 0.14(d_i / d_{coil})^{0.97}\,\mathrm{Re}\right)^{pp} \quad pp = 1 - 0.644\left(\frac{d_i}{d_{coil}}\right)^{0.312} \tag{6.19}$$

For turbulent flow, the friction factor was calculated using Ito correlation (Kakaç and Liu, 2002):

$$f_c = 1.216\,\mathrm{Re}^{-0.25} + 0.116\left(\frac{d_i}{d_{coil}}\right)^{0.5} \tag{6.20}$$

For condensation inside the helical coils, the correlation developed by Mosaad et al. (2009) that covered a mass velocity range between 95 to 710 kg/m^2.s for R134a was utilized:

$$\alpha_{cond} = 6.39\left[1 - 0.85\left(\frac{\Delta T_s}{T_s - 273.15}\right)^{0.9}\right]\overset{*}{\mathrm{Re}}^{0.4}\,\mathrm{Pr}_l^{1/3} * \frac{k_l}{d_i} \tag{6.21}$$

For $1200 \le \overset{*}{\mathrm{Re}} \le 95000$ and $0.3 \le \left(\frac{\Delta T_s}{T_s}\right) \le 0.6$

Reynold’s number was calculated as: $\overset{*}{\mathrm{Re}} = G\left((1-x) + x\sqrt{\frac{\rho_l}{\rho_v}}\right)\frac{d_i}{\mu_l}$

The two-phase pressure drop was calculated using Guo correlation (2001):

$$\Delta P_{tp} = \phi_l^2 \Delta P_l \qquad \textbf{(6.22)}$$

Where the liquid two-phase multiplier is given by:

$$\phi_l^2 = 1 + (4.25 - 2.55x^{1.5})G^{0.34}$$

The liquid pressure drop is calculated from the friction factor for liquid only flow as:

$$\Delta P_l = \frac{2 f_f L}{d_i} \frac{\left(G(1-x)\right)^2}{\rho_l}$$

f_f =fanning friction factor

6.3.3 Evaporator model

Figure 6.5D shows the discretisation of the evaporator where it was divided into two main regions; namely the superheated and the two-phase one. The two-phase zone was subdivided into small elements to take into account the effect of vapour quality on pressure drop and heat transfer. For calculating the single phase heat transfer coefficients in the superheated zone equations (6.15) to (6.18) were used. For the two-phase region, the correlation described in chapter 5 for flow boiling inside helical coils over a wide range of heat fluxes, mass velocities, pressures, and refrigerants was used:

$$St_{tp} = 0.05473\left(\frac{1}{Ja}\right)^{-0.55611}\left(\frac{1}{We_{lo}}\right)^{0.22287}\left(X_{tt}\right)^{-0.247552}\left(\frac{1}{He}\right)^{-0.17954} \qquad \textbf{(6.23)}$$

$$Ja = \frac{Cp_l \Delta T_{wall-ref}}{h_{fg}} \quad \& \quad \chi_{tt} = \left(\frac{1-x}{x}\right)^{0.9}\left(\frac{\rho_v}{\rho_l}\right)^{0.5}\left(\frac{\mu_l}{\mu_v}\right)^{0.1} \quad \& \quad St_{tp} = \frac{Nu_{tp}}{\mathrm{Re}_{lo}\,\mathrm{Pr}_l}$$

$$We_{lo} = \frac{G^2 d_i}{\rho_l \sigma} \quad \& \quad He = Dn / \sqrt{\left(1 + \left(\frac{\delta_{coil}}{\pi d_{coil}}\right)^2\right)} \quad \& \quad \mathrm{Re}_{lo} = \frac{\rho G d_i}{\mu_l} \quad \& \quad \alpha_{tp} = \frac{Nu_{tp} * k_l}{d_i}$$

For calculating the pressure drop in the single phase superheated refrigerant region, equations (6.19) and (6.20) were used and for the two-phase flow boiling region equation (6.22) was used.

6.3.4 Expansion device model

Figure 6.5C shows the thermodynamic model of the expansion device used. With no work done and assuming no heat transfer across the device, the enthalpy of the refrigerant remains constant.

6.3.5 Water side heat transfer coefficient

In order to develop a suitable correlation for the water side heat transfer coefficients for the current evaporator and condenser, the correlation developed by Salimpour et al (2009) for large scale diameters ($9 \le d_i \le 12$ and d_{coil}= 120 mm) was modified based on the experimental results (figure 6.1) to produce equation (6.24).

$$Nu_o = 24.55\,\mathrm{Re}_o^{0.513}\,\mathrm{Pr}^{0.129}\,\gamma^{0.938} \qquad \textbf{(6.24)}$$

Where $\gamma = \frac{\delta_{coil}}{\pi d_{coil}}$ & $\delta_{coil} = Coil\ pitch$

The heat transfer coefficient was then calculated as:

$$\alpha_o = \frac{Nu_o k_w}{d_h} \qquad d_h = \frac{d_{shell}^2 - \pi d_{coil} d_o^2 \gamma^{-1}}{d_{shell} + \pi d_{coil} d_o \gamma^{-1}} \qquad \textbf{(6.25)}$$

6.4 Solution methodology

Figure 6.6 shows the overall flow chart for the model setup where the system of equations has been reduced to seven non-linear equations solved simultaneously by iteration according to the following steps:

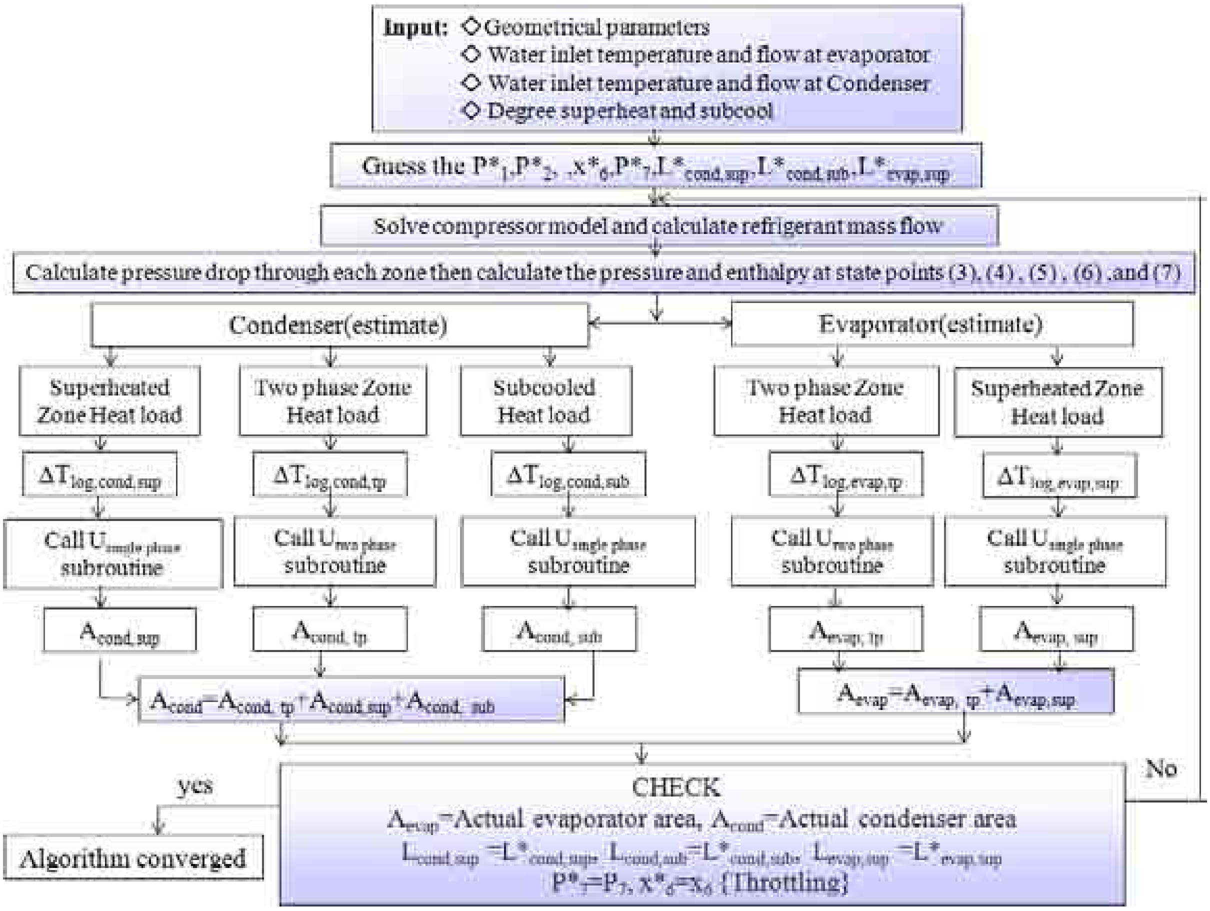

Figure 6.6: Program flow chart.

❶ Input the geometrical specifications, degree of superheat, degree of subcooling, water mass flow rates, and water inlet temperature for both the condenser and evaporator

❷ Guess the suction pressure (P^*_1), discharge pressure (P^*_2), evaporating pressure (P^*_7), the inlet quality to the evaporator x^*_6, length of superheated ($L^*_{cond,\ sup}$) and subcooled regions ($L^*_{cond,\ sub}$) in the condenser, and the length of superheated region in the evaporator ($L^*_{evap,\ sup}$).

❸Solve the compressor model to calculate the refrigerant mass flow and discharge condition at state 2 (i.e, inlet condition to the condenser).

❹Calculate the length of two-phase region in the evaporator ($L^*_{evap,tp}$) and condenser ($L^*_{cond,tp}$) by subtracting the length of other regions from the total length.

❺Calculate the pressure drop between state points (2) and (3) using the length ($L^*_{cond, sup}$), the pressure drop between point (3) and (4) using the length ($L^*_{cond, tp}$), the pressure drop between state (4) and (5) in the subcooled region using the length ($L^*_{cond, sub}$), the pressure drop in superheated region in the evaporator between state (1) and state (7) using length ($L^*_{evap, sup}$), and pressure drop between state (7) and (6) using length ($L^*_{evap, tp}$). See figure 6.5 for state points numbers.

❻Calculate the pressures (P_3), (P_4), (P_5), and the new value of (P_7) and (P_6). Then, the enthalpy of refrigerant at all state point in the cycle could be calculated from which the thermal load at each region could be calculated and the water temperature distribution produced.

❼Calculate the logarithmic mean temperature difference and overall heat transfer coefficient for each region. Then, solve the expansion device model and get the new vapour quality (x_6) at the expansion valve exit using evaporation pressure P_6 and enthalpy ($h_6=h_5$).

❽ Calculate the surface area and the new length of each region.

❾ Check if the following conditions are satisfied: If the guessed values of region length's are equal to those calculated from step 8 and if the summation of surface area regions equal to the actual surface area in both the evaporator and condenser, and if the pressure (P_7) calculated from step 6 equal to that guessed in step 2 (P^*_7) and inlet quality at the evaporator calculated in step 7 equal to that guessed in step 2.

❿ If all conditions given in step 9 are satisfied then end program and print result, otherwise, repeat the calculations using new initial guess, informed by the first attempt.

The Matlab software (2008) linked to the physical properties package REFPROP (2002) were used to solve the system of non-linear equation. Figure **6.7** compares the model results of the cooling capacity to the experimental ones with an agreement of ±5%.

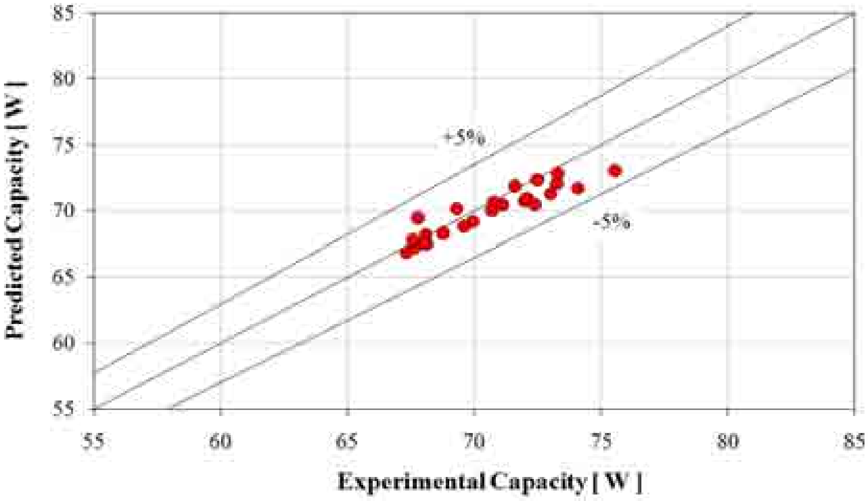

Figure 6.7: Model prediction and refrigerant measured capacities.

6.5 System performance and optimisation using the model

The validated model has been used to predict the performance of the system in terms of Cooling COP at various helically coiled condenser and evaporator configurations for fixed degrees of subcooling and superheat of 4 and 10 K respectively as recommended by Selbas et al. (2006). Water inlet temperatures of 15 °C, water flow rate to the condenser and the evaporator of 300 and 180 ml/min respectively were used. Figure 6.8 shows the effect of the surface area ratio (AR) of the condenser to evaporator on

Cooling COP at various compressor speeds. The effect of condenser coil design was investigated for a fixed evaporator design using different area ratios, coil and tube diameters. The evaporator is 1 m long with 3 mm tube diameter and 20 mm coil diameter. Figure 6.8 shows that for fixed compressor speed, as the area ratio increases, the system cooling COP increases. However, the rate of increase becomes lower at high area ratios due to the increase in pressure drop associated using longer condensers (Increasing in surface area ratio leads to longer condenser length). For fixed area ratio, the improvement in COP increases as the Rev/Min decreases. The compressor is the driving machine that pumps the fluid. The increase in compressor rotating speed would pump more refrigerant which increases the pressure drop and the power consumed and reduces the COP. Here it is worth mentioning that the area ratio was used as the base for the parametric variations since the coil surface area plays a major role in heat transfer between the refrigerant and water. Also surface area combines the effects of tube diameter and length.

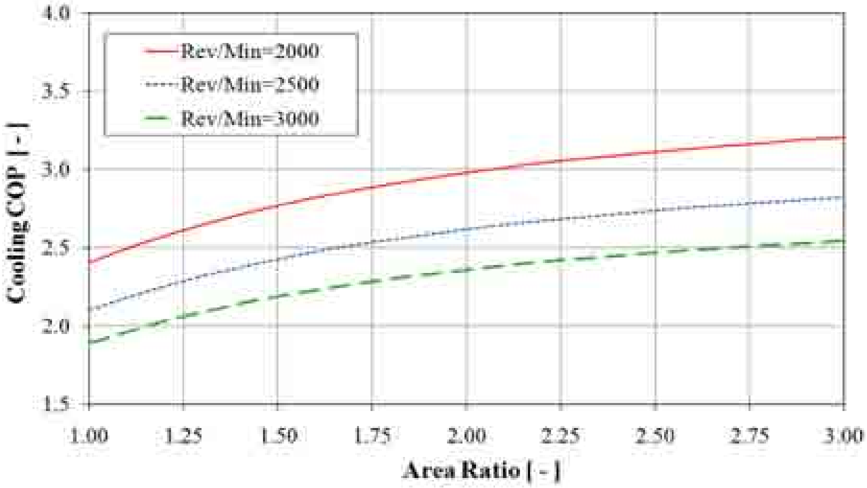

Figure 6.8: Effect of area ratio on cooling COP at various compressor speeds ($d_{i,evap}$=$d_{i,cond}$=3 mm & $d_{coil,evap}$= $d_{coil,cond}$=20 mm & L_{evap}=1 m).

Figure 6.9 illustrates the effect of the surface area ratio (AR) of the condenser to evaporator on cooling COP at various condenser coil diameters at compressor speed of 2000 Rev/Min. The figure shows that, at fixed surface area ratio, reducing the coil diameter gives higher COP values. Reducing the coil diameter increases the effect of centrifugal force on the fluid leading to better heat transfer and improves the cooling COP.

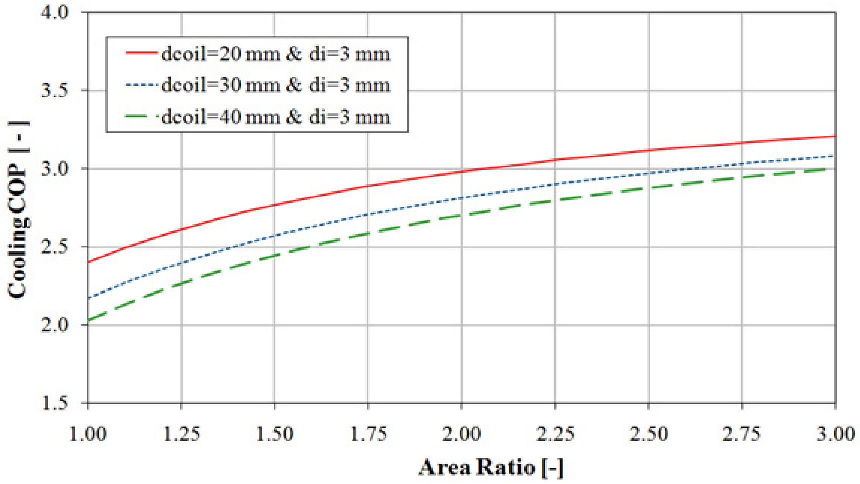

Figure 6.9: Effect of area ratio on cooling COP at various condenser coil diameters ($d_{i,evap}$=$d_{i,cond}$=3 mm & $d_{coil,evap}$=20 mm & Rev/Min=2000 & L_{evap}=1 m).

Figure 6.10 shows the effect of the surface area ratio (AR) on cooling COP at various condenser tube diameters at compressor speed of 2000 Rev/Min. The figure shows that at lower surface area ratio, reducing the tube diameter gives higher COP values. This is likely to be due to the increase in axial velocity. While at higher surface area ratio, adverse effect of reducing the tube diameter is noticed due to higher discharge pressures and required input power. Using high area ratio means using longer condenser length which will increase the pressure drop counteracting the enhancement of heat transfer in the coil. As a result, the COP decreases at high area ratios with decreasing the tube diameter.

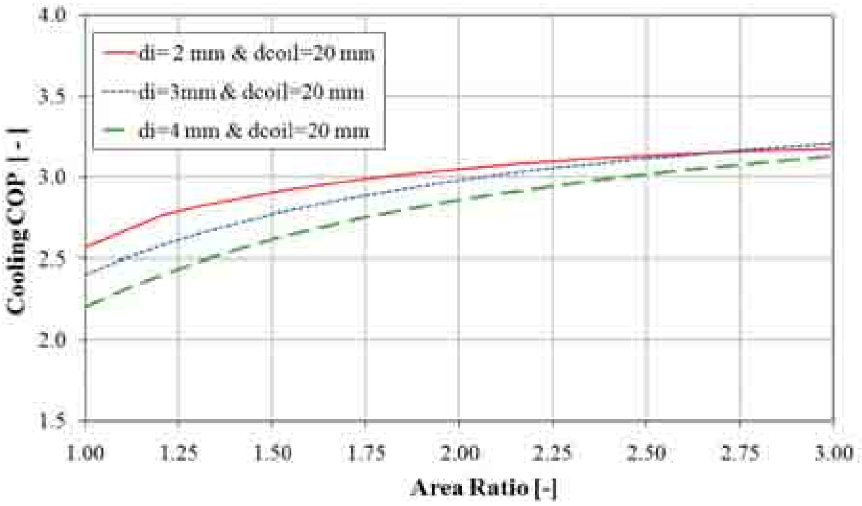

Figure 6.10: Effect of area ratio on cooling COP at various condenser tube diameters ($d_{i,evap}$= 3 mm& $d_{coil,evap}$= $d_{coil,cond}$=20 mm & Rev/Min=2000 & L_{evap}=1 m).

The above theoretical study indicated that both the geometry of the condenser and evaporator coils affect the *COP* of the cooling system. Therefore, an optimisation study was performed to determine the geometric parameters that produce maximum coefficient of performance of the miniature cooling system. The system performance has been optimised to maximize the cooling coefficient of performance for fixed evaporator length against condenser and evaporator coil diameters (20 to 40 mm), condenser and evaporator tube diameters (2 to 4 mm) and condenser to evaporator area ratio (1 to 3) for compressor speed of 2000 Rev/Min that produced the highest COP as shown in figure 6.8. The optimisation process was carried out using fmincon routine in Matlab for solving constrained optimisation problems. Starting with an initial estimate, the *fmincon* attempts to find a constrained minimum of a scalar function (-COP) of independent variables as expressed in equation 6.19.

$$-COP = fn(d_{coil,evap}, d_{coil,cond}, d_{i,evap}, d_{i,cond}, AR) \qquad \textbf{(6.19)}$$

The *fmincon* algorithm uses a sequential quadratic programming (*SQP*) technique at each iteration, for estimating the Hessian matrix of the Lagrangian function (Helgestad, 2009). *fmincon* is reliable and fast optimisation routine that is widely used for engineering applications (Rao, 2009 and Koeijer et al., 2004). The computational time needed for each optimisation run was 3 hrs on a 1.8GHz personal computer. Table 6.2 shows the geometrical parameters of the evaporator and condenser coils that produce the maximum system cooling COP at a given evaporator length. It can be seen that higher area ratio increase the COP as larger surface area and lower temperature difference across the heat exchanger could be used. Using smaller coil diameter leads to larger number of coil turns for the same evaporator length and better heat transfer characteristics and Cooling COP. Larger tube diameters offer larger surface area and better performance for the same evaporator length as the optimized evaporator tube moves to 4mm diameter. However, higher thermal performance using small tubes may be achieved at small area ratios as depicted in figure 6.10.

Table 6.2: Geometrical parameters of the helically coiled evaporator and condenser.

Evaporator length [m]	$d_{coil,cond}$ [mm]	$d_{coil,evap}$ [mm]	$d_{i,cond}$ [mm]	$d_{i,evap}$ [mm]	Area ratio [-]	COP [-]	Q_{evap} [W]
1	20	20	2.7	4	3	3.49	88.6
1.5	20	20	3.2	4	3	4.10	100.5
2	20	20	3.6	4	3	4.52	107.7
2.5	20	20	4	4	3	4.82	112.4
3	20	20	4	4	3	5.04	115.7

6.6 Summary

An optimisation study has been carried to study the performance of small scale cooling system and determine means of enhancing its performance. The smaller the coil diameter, the better the performance of cooling system can be. For the same evaporator length, the larger the tube diameter, the larger surface area and better COP. Smaller tube diameters showed better performance at lower AR. However, smaller tube diameters showed lower performance at high area ratios due to the large pressure drop caused by smaller tubes in case of using high AR. The optimised condenser diameter moves to the upper optimisation limit with increasing the evaporator coil length to avoid large pressure drop with increasing the condenser length as summarized in table 6.2.

CHAPTER 7

Numerical Heat Transfer in Helical Coils Using Nanofluids

7.1 Introduction

As reported in chapter 2 section 2.10, nanofluids have been reported to enhance heat transfer performance in heat exchangers. Additionally, the use of helical coils has shown to be another passive heat transfer enhancement technique as reported in chapter 2 section 2.3. This chapter presents a CFD modelling study to investigate the heat transfer through helical tubes with nanofluids. The developed CFD models were validated against published experimental results and empirical correlations in the literature. The effects of particles concentration and Reynolds number on heat transfer coefficient were then numerically investigated.

7.2 Laminar flow governing equations and thermophysical properties

Al_2O_3 nanofluid has been treated as incompressible, steady state, homogeneous and Newtonian fluid with negligible effect of viscous heating. The flow has been modelled using Navier-stokes equations using fluent package (2006). The single phase homogeneous flow governing equations in the Cartesian co-ordinates are:

Continuity: $$\rho\left(\frac{\partial u_x}{\partial x}+\frac{\partial u_y}{\partial y}+\frac{\partial u_z}{\partial z}\right)=0 \quad \textbf{(7.1)}$$

Momentum: $$\rho\left(u_x\frac{\partial u_x}{\partial x}+u_y\frac{\partial u_x}{\partial y}+u_z\frac{\partial u_x}{\partial z}\right)=-\frac{\partial P}{\partial x}+\rho g_x+\mu\left(\frac{\partial^2 u_x}{\partial^2 x}+\frac{\partial^2 u_x}{\partial^2 y}+\frac{\partial^2 u_x}{\partial^2 z}\right) \quad \textbf{(7.2)}$$

Energy: $\rho C\left(u_x\frac{\partial T}{\partial x}+u_y\frac{\partial T}{\partial y}+u_z\frac{\partial T}{\partial z}\right)=k\left(\frac{\partial^2 T}{\partial x^2}+\frac{\partial^2 T}{\partial y^2}+\frac{\partial^2 T}{\partial z^2}\right)$ **(7.3)**

The effective thermo-physical properties of the nanofluid were defined based on the measurements of Rea et al. (2009).

Density: $\rho_{nf}=(1-\phi)\rho_{bf}+\rho_p\phi$ **(7.4)**

Specific heat: $C_{nf}=\left((\rho C)_p\phi+(\rho C)_{bf}(1-\phi)\right)/\rho_{nf}$ **(7.5)**

Thermal conductivity: $k_{nf}=(1+4.5503\phi)k_{bf}$ **(7.6)**

Dynamic viscosity: $\mu_{nf}=\exp\left(4.91\phi/(0.2092-\phi)\right)\mu_{bf}$ **(7.7)**

Where *nf*, *bf* and *p* denote the nanofluid, base fluid, and particle respectively. The base fluid thermo-physical properties have been fitted as polynomial functions in temperature (Kelvins) using Engineering Equation Solver EES data as shown in equations 7.8 to 7.10.

$\rho_{bf}=2813.77E\left(\text{-}01\right)+6351.93E\left(\text{-}03\right)T-1761.03E\left(\text{-}05\right)T^2+1460.96E\left(\text{-}08\right)T^3$ **(7.8)**

$k_{bf}=-1056.42\ E\left(\text{-}03\right)+1011.33E\left(\text{-}05\right)T-1772.74E\left(\text{-}08\right)T^2+7994.88E\left(\text{-}12\right)T^3$ **(7.9)**

$\mu_{bf}=9684.22E\left(\text{-}05\right)-821.53\ E\left(\text{-}06\right)T+2345.21E\left(\text{-}09\right)T^2-2244.12\ E\left(\text{-}12\right)T^3$ **(7.10)**

These properties were formulated as UDF subroutine and incorporated into Fluent 6.3 solver.

7.2.1 Laminar heat transfer in straight tubes

7.2.1.1 Base fluids (water) heat transfer in straight tubes

The CFD analysis for the base fluid flow in straight tube was investigated to provide a reference case. Figure 7.1 shows the boundary conditions and mesh configuration for a straight tube with 4.5 mm internal diameter and 1.01 m long. The fluid enters at uniform velocity at the tube inlet and the tube wall exposed to uniform heat flux. The flow in the straight circular pipe is a three-dimensional problem in Cartesian coordinates which was reduced to a two-dimensional analysis via symmetry in cylindrical polar coordinates.

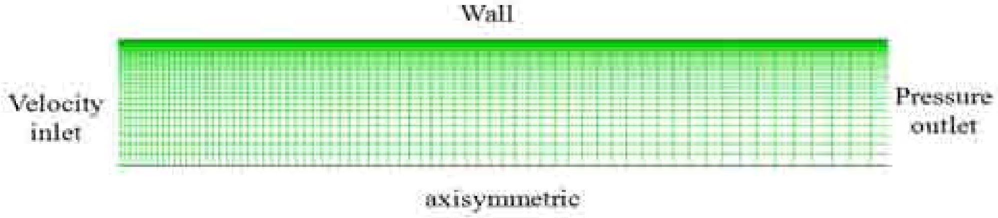

Figure 7.1: Meshing of the straight tube in laminar flow.

Enhanced mesh treatment was applied at inlet and wall boundaries with 50 x 700 nodes in the radial and axial directions respectively with successive ratio of grid in the radial direction of 1.1. Second order upwind scheme was utilized for discretizing the energy and momentum equations, and the SIMPLE algorithm was used for solving the pressure-velocity coupling. The average heat transfer coefficient was calculated as the arithmetic mean of the locally predicted heat transfer coefficients. Figure 7.2 shows the predicted heat transfer coefficient and those reported by Rea et al. (2009) at various Reynolds numbers with ±7% agreement.

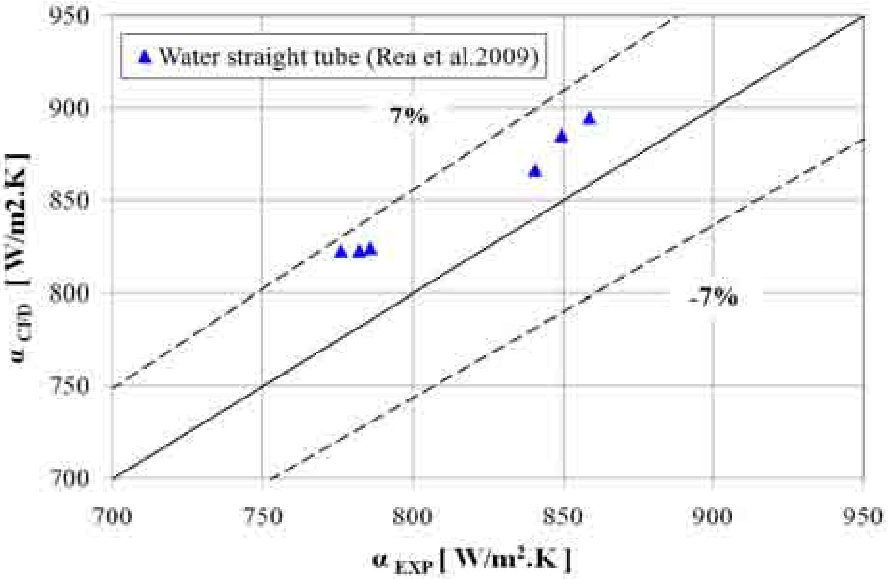

Figure 7.2: Laminar flow validation of water (base fluid) CFD model in straight tubes.

7.2.1.2 Al_2O_3 nanofluid heat transfer and pressure drop in straight tubes.

The flow governing equations describing nanofluids flow (equations 7.1 to 7.10) were used to simulate the Al_2O_3 nanofluid performance in straight tubes. Figure 7.3 presents the predicted heat transfer coefficient of Al_2O_3 nanofluid in straight tube compared to the experimental results of Rea et al. (2009) at volume concentration ratios of 0.65%, 1.32%, 2.76% and 6% and Reynolds numbers ranging from 400 to1800 with ±10% agreement. This supports the validity of using single phase approach to model the nanofluids using the effective thermophsyical properties of the nanofluid. The figure also shows that high Al_2O_3 volume concentration (ϕ=6%) has higher heat transfer coefficients compared to lower concentration (ϕ=1%).

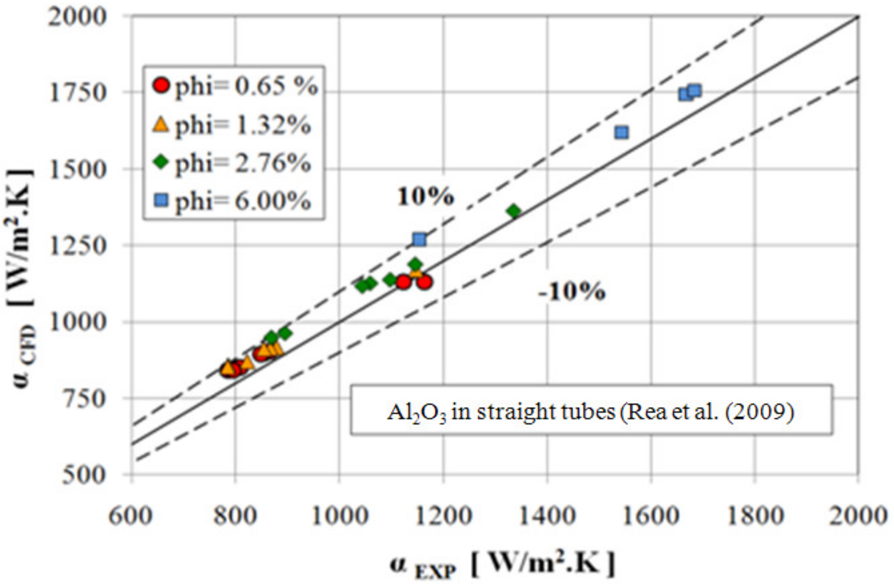

Figure 7.3 Laminar flow validation of Al_2O_3 nanofluid CFD model in straight tubes.

The developed CFD model has been used to investigate the effect of nanofluid volume fraction on the heat transfer enhancement ratio in straight tubes at various Reynolds Numbers. In this analysis, the heat transfer enhancement ratio is defined as the ratio of heat transfer coefficient of the nanofluid to that of the base fluid at the same Reynolds number. Figure 7.4 shows that the heat transfer enhancement ratio increases with the increase in nanofluid volume fraction and the increase in Reynolds number. However, for constant concentration, the increase in heat transfer enhancement ratio is more noticeable at low Reynolds numbers (Re<1000). An enhancement ratio up to 1.55 (55%) was predicted at volume fraction of 4% and Reynolds number of 2000.

Analytical prediction of the enhancement ratio for the same tube diameter, tube length, and flow Reynolds number for developing laminar flow was deduced based on modifying Rea et al. (2009) analysis for heat transfer coefficient at constant heat flux as shown in equations 7.11 and 7.12.

$$\alpha = fn\left(k^2 \rho u C / x d_i\right)^{1/3} \qquad \textbf{(7.11)}$$

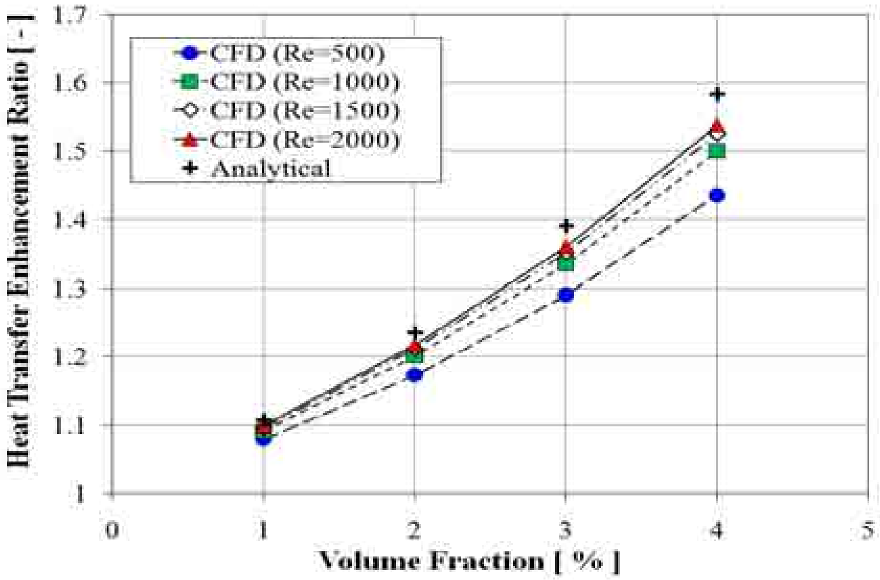

Figure 7.4: Straight tube Al_2O_3 nanofluid Laminar heat transfer enhancement ratio at different Reynolds Number ($q=5000\ W/m^2$).

$$Enhancement\ Ratio = \frac{\alpha_{nf}}{\alpha_{bf}} = \left(\frac{\left(k^2 \mu C\right)_{nf}}{\left(k^2 \mu C\right)_{bf}}\right)^{1/3} \tag{7.12}$$

Where x, d_i, u, α are the local distance from entrance, internal tube diameter, flow velocity and heat transfer coefficient respectively. In figure 7.4, results from the analytical prediction and the CFD were in agreement especially at higher Reynolds numbers as the developing length becomes significant where the developing length is calculated from $x/d_i=0.04RePr$ (Rea et al., 2009). The analytical enhancement ratio was developed for thermally developing flow. Since part of the tube would be in the thermally developing region, Reynolds number increases as the length of this developing part increases and the CFD prediction at higher Reynolds numbers becomes closer to this analytical line.

It has been shown that the friction factor of nanofluids agree with conventional theory (Li and Xuan, 2002). Therefore the ratio of pressure drop (also known as penalty factor, PF) for nanofluid and base fluid in straight tube for constant tube length, tube diameter and Reynolds number is expressed as:

$$PF = \frac{\Delta p_{nf,ST}}{\Delta p_{bf,ST}} = \frac{\left(\mu^2 / \rho\right)_{nf}}{\left(\mu^2 / \rho\right)_{bf}} \tag{7.13}$$

Where Δp is defined as:

$$\Delta p = \frac{fL}{d_i}\frac{G^2}{2\rho} = \frac{fL}{d_i^3}\frac{\mu^2}{2\rho}\mathrm{Re}^2 \tag{7.14}$$

Figure 7.5 shows the pressure drop ratio (PF) for the same Reynolds numbers and volume concentrations equals to those used in figure 7.4, where close agreement shown between the CFD and the analytical prediction. Excessive pressure drop was obtained using high volume fraction of Al_2O_3 nanofluids where the pressure drop exceeds four times that of the base fluid in straight tube for the same flow condition. This increase in pressure drop is due to the significant increase in the viscosity of the nanofluid as measured by Rea et al.(2009).

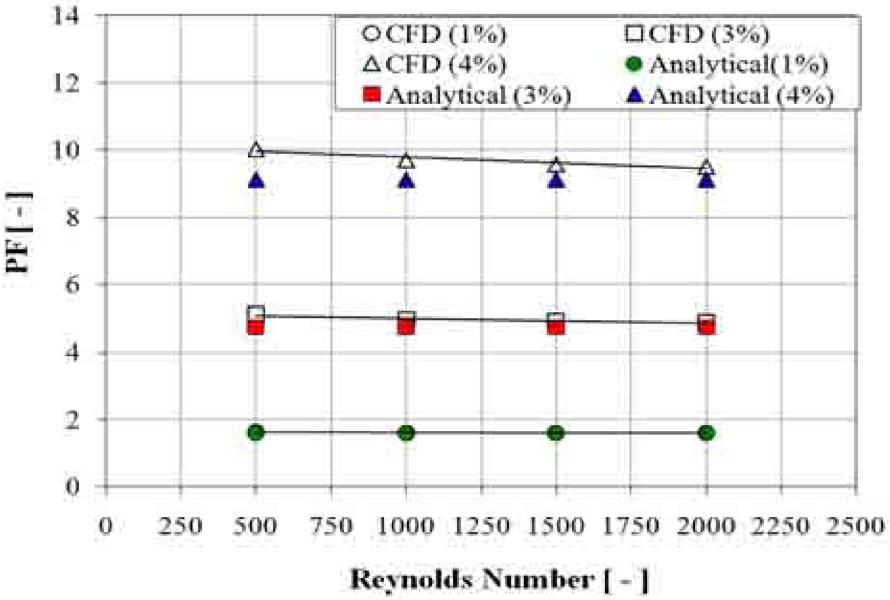

Figure 7.5: Pressure drop penalty factor (PF) in straight tubes.

7.2.2 Laminar heat transfer in helical coils

7.2.2.1 Base fluid (water) heat transfer in helical tubes

A helical coil with coil length and tube diameter similar to those used in the straight tube (Coil-A: 4.5 mm internal diameter and 1.01 m long) has been modelled. The coil pitch was selected as 15 mm and number of turns of 4 leading to a coil diameter of 80.4 mm. Figure 7.6 shows the mesh used where tri-quad meshing has been utilized to mesh the inlet face and hex/wedge cooper mesh used to mesh the coil volume with 10 layers close to wall with growth factor of the grid in the radial direction of 1.3 and first layer thickness of 0.01 mm. The discritization schemes utilized were second order for energy, first order for momentum, SIMPLEC algorithm with skewness factor of one for coupling the velocity and pressure.

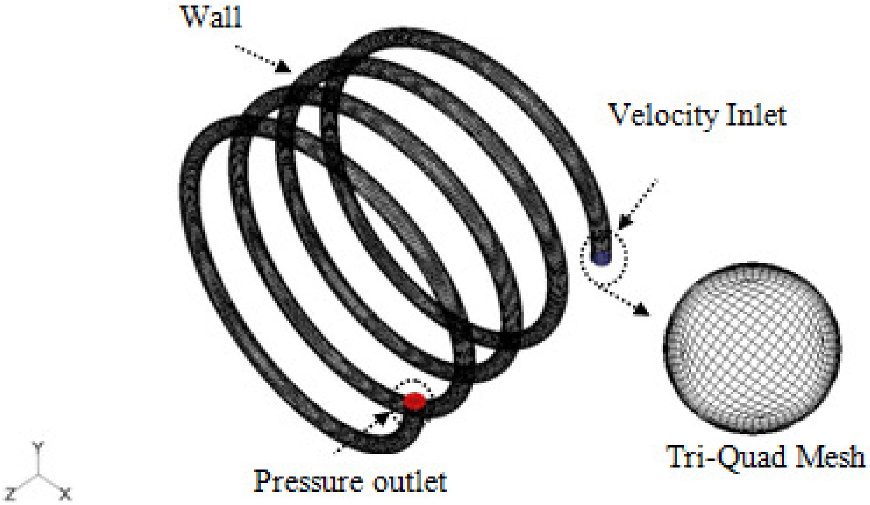

Figure 7.6: Three dimensional mesh of helical coil using tri-quad mesh in laminar flow.

A grid sensitivity analysis was carried out to determine the appropriate mesh density (number of cells per unit volume (cells/mm^3)). Table 7.1 compares the simulation results of four grid densities of 14.28, 22.60, 31.74, 52.37, 63.86 cells per mm^3. Grid densities larger than 60 nodes in the angular direction do not improve the prediction significantly in terms of average Nusselt number and wall temperature. As a result 60 nodes in the angular direction were utilized in the analysis with 5 hours simulation time required for each test condition.

Table 7.1 Grid dependency analysis at water velocity=0.1 m/s.

Nodes in angular direct.	20	30	40	60	70
Cell density cell/mm3	14.28	22.60	31.74	52.37	63.86
No. of Cells*1000	227.7	360.27	506	834.9	1018.1
ΔP (pa)	219.1	225.1	227.3	229.3	229.98
Avg.wall temp. (K)	301.21	301.35	301.44	301.55	301.52
Avg. Nusselt Number	16.17	14.85	13.95	13.17	13.15

Figure 7.7 shows the close agreement between the CFD predicted heat transfer coefficient and those predicted using Manlapaz-Churchill (Kakaç and Liu, 2002) described in chapter 6 and Kalb-Seader (1972) correlations given in equations 6.15. Manlapaz-Churchill validated their correlation for water, air and other fluids in helical coils exposed to constant heat flux with Reynolds numbers in the laminar flow regime. They correlated the Nusselt number as a function of Dean and Prandtl as mentioned in chapter 6. Also Kalb-Seader numerically developed the following correlation (1972):

$$Nu_c = 0.913 Dn^{0.476} \Pr^{0.2} \qquad 0.7 \le \Pr \le 5 \qquad 80 \le Dn \le 1200 \qquad \textbf{(7.15)}$$

The maximum deviation between the CFD prediction and empirical correlations was found to be less than ±3.5%.

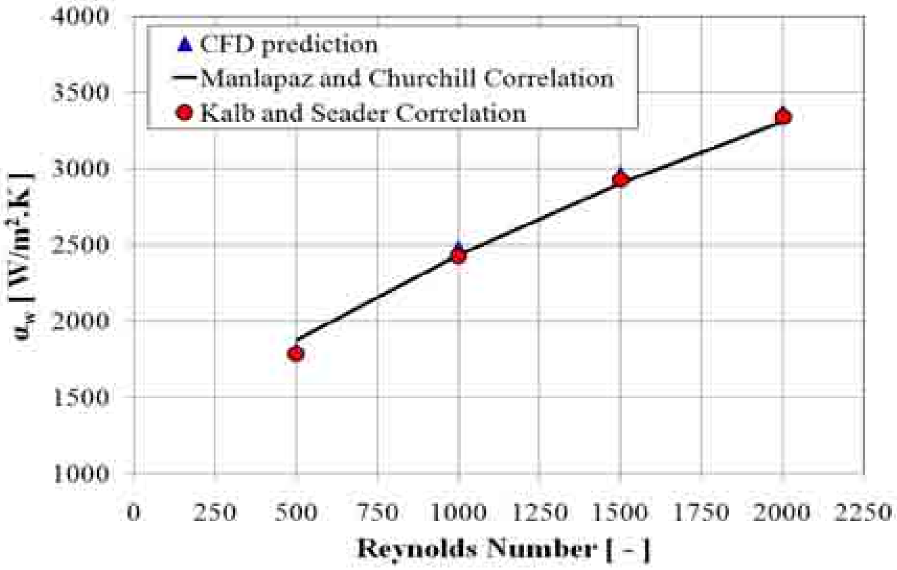

Figure 7.7: Laminar flow validation of CFD against empirical correlations for water flow in helical coils (q=5000 W/m^2).

Figure 7.8 shows velocity contours at successive cross section in a plane parallel to the coil inlet. The flow enters the coil with uniform velocity of 0.11 m/s (Re=500) then the fluid elements with high velocities are pushed to the outer side of the coil due to the centripetal force. This will generate a secondary flow with vortices that enhance fluid mixing and heat transfer.

Figure 7.9 shows the heat transfer coefficient distribution on the circumference of the tube at cross section of 3.5 turns from the coil entrance with flow velocity of 0.11 m/s. The heat transfer coefficient was found to be lowest at the coil inner surface (position 1) where the wall temperature is highest compared to other positions in the section. The heat transfer coefficient at the bottom of the tube is slightly lower than that at the top due to the effect of gravity. The above described heat transfer coefficient variation around the circumference of helical coils is in agreement with the findings of Jayakumar et al. (2010).

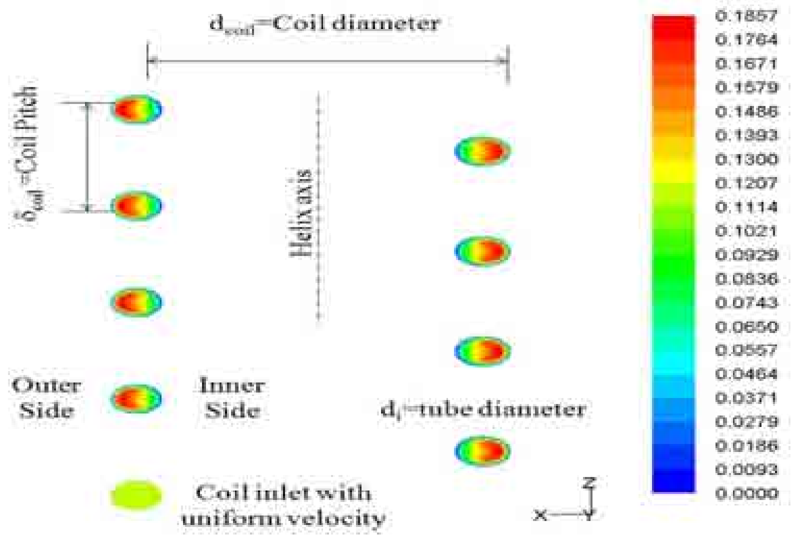

Figure 7.8: Velocity contours in laminar flow regime at cross section parallel to coil inlet.

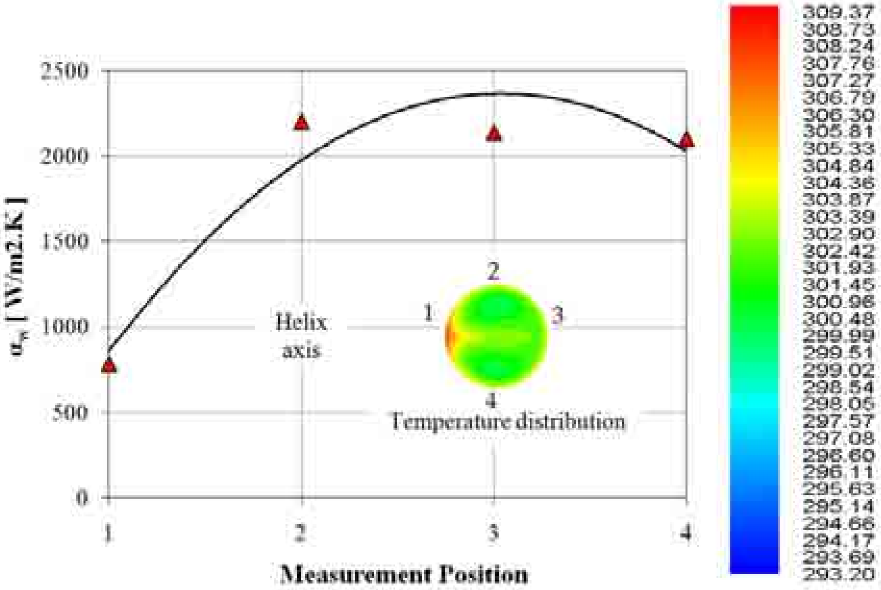

Figure 7.9: Water heat transfer coefficient distribution on the circumference of the coil at 3.5 turns from entrance.

Figure 7.10 shows the heat transfer enhancement ratio versus Reynolds number. The enhancement ratio is defined as the heat transfer coefficient of base fluid in helical coils compared to that of water flow inside straight tube with the same surface area. Three coils have been modelled with geometric characteristics shown in Table 7.2.

Table 7.2: Dimensions of helically coiled tubes in mm.

Coil Number	d_i	d_{coil}	N_{turn}	δ_{coil}
Coil A	4.5	80.373	4	15
Coil B	4.5	40.1866	8	15
Coil C	6	80.373	3	15

Coil A shows that heat transfer enhancement ratios of 2.5 to 3.25 times that in straight tube was achieved. Figure 7.10 shows that decreasing the coil diameter increases the heat transfer enhancement ratio due to better mixing caused by the larger number of turns. Increasing the tube diameter reduces the heat transfer enhancement ratio due to reduction in the flow velocity for the same Reynolds number.

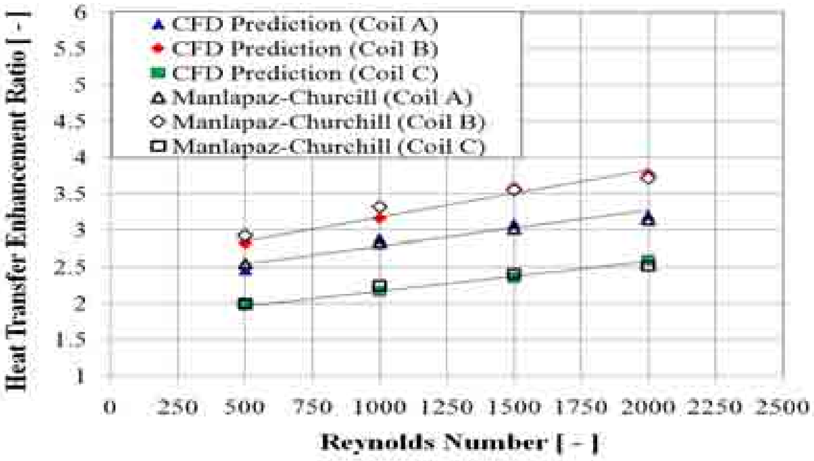

Figure 7.10: Laminar heat transfer enhancement ratio in helical coils using water at different Reynolds number with different coils.

Comparing figure 7.10 to figure 7.4 indicates that the heat transfer enhancement ratio of helical coils using the base fluid is 2 to 3.25 for coil A which is higher than that using Al_2O_3 nanofluid in straight tube with enhancement of 1.55.

7.2.2.2 Al_2O_3 nanofluids heat transfer in helical coils

The flow governing equations describing nanofluids flow (equations 7.1 to 7.10) and the geometry described in section 7.2.2.1 (Coil A) were used to simulate the Al_2O_3 nanofluid thermal performance in helical coil. With similar mesh configurations and boundary conditions, figure 7.11 shows the heat transfer enhancement ratio (heat transfer coefficient of nanofluid in the helical coil divided by the heat transfer coefficient of the base fluid in the straight tube with the same internal diameter and length) versus the nanofluid volume fraction at various Reynolds numbers. Contrary to the straight tube results, it is clear from this figure that as Reynolds number increases, the heat transfer enhancement ratio increases at all volume fractions.

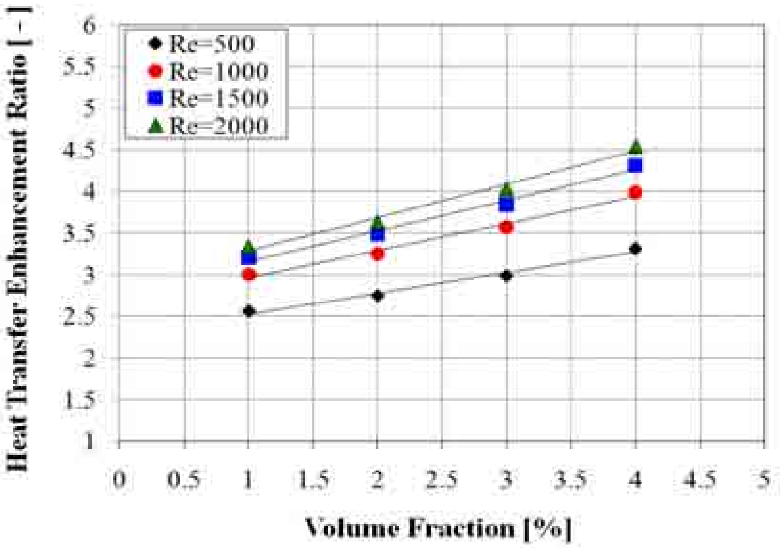

Figure 7.11: Laminar heat transfer enhancement ratio in helical coil using Al_2O_3 nanofluid at different Reynolds Number (Coil A).

The heat transfer using both nanofluids and helical coil effect was found to be very effective. The enhancement ratio was found to vary from 2.5 to 4.5 times that of base fluid (water) in straight tubes at Reynolds number of 500 to 2000 respectively. The combined enhancement technique was found to be better than using helical coils with base fluids or using nanofluids in straight tubes.

For the same tube length and Reynolds number, the pressure drop ratio of nanofluid flow in helical coil to the base fluid in straight tube can be expressed as:

$$\frac{\Delta p_{nf,Hc}}{\Delta p_{bf,St}} = \frac{f_{nf,Hc}}{f_{bf,St}} \left(\frac{\mu_{nf}}{\mu_{bf}}\right)^{2} \left(\frac{d_{nf}}{d_{bf}}\right)^{-3} \left(\frac{\rho_{nf}}{\rho_{bf}}\right)^{-1} \tag{7.16}$$

The friction factor of nanofluid in helical coil $f_{nf,Hc}$ was calculated using White correlation (Welti-Chanes et al. , 2003) while the friction factor of nanofluid in the straight tube was taken as equal to that of the base fluid in straight tube at the same Reynolds number (Li and Xuan, 2002). Thus:

$$\frac{f_{nf,Hc}}{f_{bf,St}} = \frac{f_{nf,Hc}}{f_{nf,St}} = \left(1 - \left(1 - \left(11.6 / Dn_{nf}\right)^{0.45}\right)^{2.2}\right)^{-1} \tag{7.17}$$

Figure 7.12 shows that the pressure drop ratio increases with increasing Reynolds number at all concentrations used with close agreement between CFD predictions and those of equation (7.16). The pressure drop in helical coils using pure water (0% volume concentration is 2 times that in straight tubes. The pressure drop in helical coils using Al_2O_3 for volume fraction larger than 2% exceeds 5 times that of water in straight tubes.

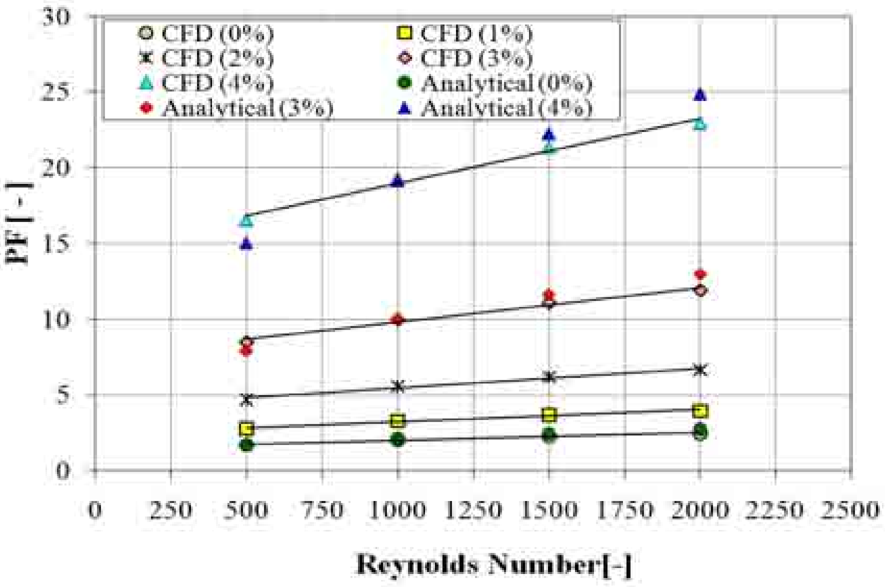

Figure 7.12: Pressure drop penalty factor in helical coils Laminar flow.

7.3 Turbulent flow governing equations

Similar to the laminar flow, Al_2O_3 nanofluid has been treated as incompressible, steady state, homogeneous and Newtonian fluid with negligible effect of viscous heating. The single phase homogeneous flow governing equations including the turbulent terms in the Cartesian co-ordinates are:

Continuity: $$\frac{\partial}{\partial x_i}(\rho u_i) = 0 \qquad \textbf{(7.18)}$$

Momentum: $$\frac{\partial}{\partial x_j}(\rho u_i u_j) = -\frac{\partial P}{\partial x_i} + \rho g_i + \frac{\partial}{\partial x_j}\left[\mu\left(\frac{\partial u_i}{\partial x_j} + \frac{\partial u_j}{\partial x_i}\right)\right] + \frac{\partial}{\partial x_j}\left(-\rho \overline{u_i' u_j'}\right) \qquad \textbf{(7.19)}$$

Energy: $$\frac{\partial}{\partial x_i}(\rho u_i T) = \frac{\partial}{\partial x_j}\left((\Gamma + \Gamma_t)\frac{\partial T}{\partial x_j}\right) \qquad \Gamma = \frac{\mu}{\Pr}\, and\ \Gamma_t = \frac{\mu_t}{\Pr_t} \qquad \textbf{(7.20)}$$

Γ, Γ_t are the molecular thermal diffusivity and turbulent thermal diffusivity respectively. The Boussinesq hypothesis is used to relate the Reynolds stresses (last term in momentum equation) to the mean velocity as:

$$\left(-\rho\overline{u_i' u_j'}\right)=\mu_t\left(\frac{\partial u_i}{\partial x_j}+\frac{\partial u_j}{\partial u_i}\right) \tag{7.21}$$

The Turbulent viscosity term is to be computed from an appropriate turbulence model. In the present numerical analysis, k-ε turbulent model introduces two additional equations namely turbulent kinetic energy (k) and turbulent dissipation rate (ε) so that:

$$\mu_t=\rho C_\mu\frac{k^2}{\varepsilon} \tag{7.22}$$

Where C_μ is empirical constant. The modelled equation of the turbulent kinetic energy (TKE), k is written as:

$$\frac{\partial}{\partial x_i}(\rho k u_i)=\frac{\partial}{\partial x_j}\left[\left(\mu+\frac{\mu_t}{\sigma_k}\right)\frac{\partial k}{\partial x_j}\right]+G_k+\rho\varepsilon \tag{7.23}$$

$\rho\varepsilon$ is the turbulence destruction rate of TKE and G_k is the rate of generation of the TKE given by:

$$G_k=-\rho\overline{u_i' u_j'}\frac{\partial u_j}{\partial x_i} \tag{7.24}$$

Similarly the dissipation rate (TDR), ε is given by the following equation:

$$\frac{\partial}{\partial x_i}(\rho\varepsilon u_i)=\frac{\partial}{\partial x_j}\left[\left(\mu+\frac{\mu_t}{\sigma_\varepsilon}\right)\frac{\partial\varepsilon}{\partial x_j}\right]+C_{1\varepsilon}\frac{\varepsilon}{k}G_k+C_{2\varepsilon}\rho\frac{\varepsilon^2}{k} \tag{7.25}$$

The boundary values for the turbulent quantities near the wall are specified with the two layers (Enhanced wall treatment). The values of empirical constants in the turbulence transport equations were as follow:

$C_\mu=0.009, C_{1\varepsilon}=1.44, C_{2\varepsilon}=1.92, \sigma_k=1, \sigma_\varepsilon=1.3$ and $\Pr_t=0.85$

Pr_t is the turbulent Prandtl number at the wall. The effective thermo-physical properties of the nanofluid have been calculated using equations (7.4) to (7.10) similar to laminar flow.

7.3.1 Turbulent heat transfer in straight tubes

7.3.1.1 Base fluids (water) heat transfer in straight tube

The CFD analysis for the base fluid flow in straight tube was used as a reference case. Figure **7.13** shows the boundary conditions and mesh configuration for a straight tube with 9.4 mm internal diameter and 2819 mm long (Williams et al., 2008). Two adiabatic sections with 1 m and 0.5 m long respectively were positioned before and after the heated section. The heated section was meshed with 40 and 1600 nodes in the angular and axial direction respectively. The 1 m and 0.5 m adiabatic sections were meshed with 40x800 and 40x 400 nodes in the angular and axial directions. Second order upwind scheme was utilized for discretizing the energy and momentum equations, turbulence kinetic energy and turbulence dissipation rate. Uniform heat flux was applied to the heated section with uniform velocity at 1 m adiabatic straight tube inlet. The coupled algorithm was used with Courant number set to one for solving the pressure-velocity coupling since the solver was stable in convergence (Kelecy, 2008).

The average heat transfer coefficient was calculated using the average heated wall temperature and average fluid temperature at the inlet and outlet of the heated tube. Figure **7.14** shows the predicted heat transfer coefficient and those reported by (Williams et al., 2008) at various Reynolds numbers with ±9 % agreement of both experimental data and those predicted by Petukhov correlation (Bejan, and Kraus, 2003). Petukhov correlated the Nusselt number as a function of Reynolds and Prandtl numbers in the following form.

$$Nu = \frac{(f/8)\,\mathrm{Re}\,\mathrm{Pr}}{1.07 + 12.7(f/8)^{0.5}(\mathrm{Pr}^{(2/3)} - 1)} \tag{7.26}$$

Where $f = (1.82\log_{10}(\mathrm{Re}) - 1.64)^{-2}$

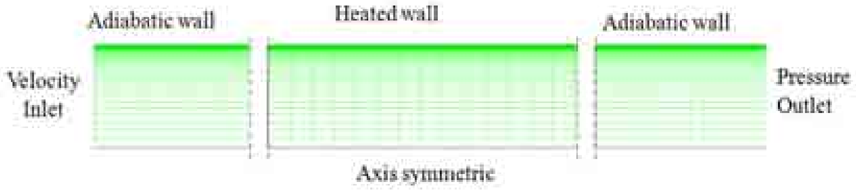

Figure 7.13: Straight tube meshing and boundary conditions in turbulent flow.

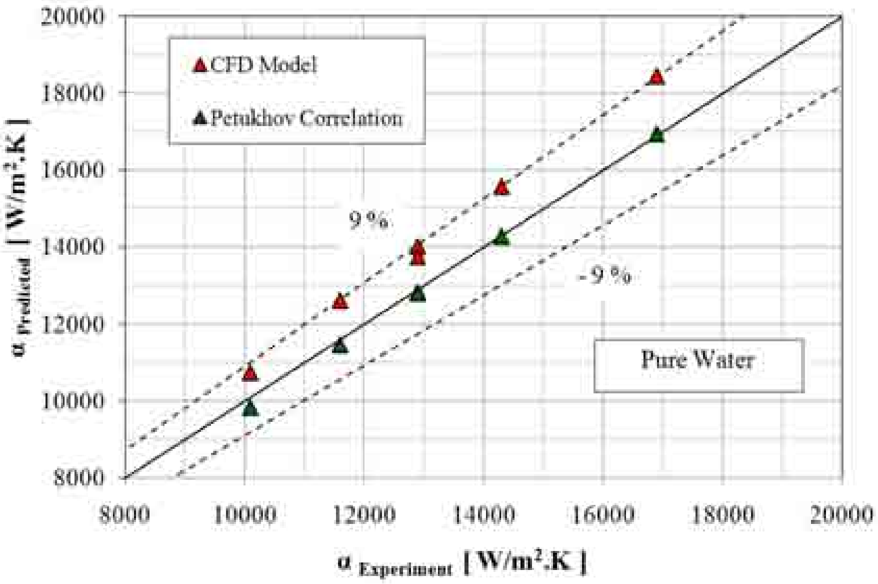

Figure 7.14: CFD Validation of pure water turbulent flow in straight tubes.

7.3.1.2 Al_2O_3 nanofluid heat transfer and pressure drop in straight tubes.

Figure 7.15 presents the predicted heat transfer coefficient of Al_2O_3 nanofluid in straight tube compared to the experimental results of (Williams et al., 2008) at volume concentration ratios of 0.9%, 1.8 % and 3.6% at Reynolds numbers ranging from 8000 to 60000 with ±12% agreement. Pak and Cho (1998) correlation was in a good agreement with the CFD prediction. On the other hand, Vajjha et al. (2010) correlation tends to under predict the experimental measurement and Maiga correlation (2006) was found to over predict the experimental results.

Pak and Cho correlation: $Nu_{nf} = 0.021\mathrm{Re}_{nf}^{\;0.8}\,\mathrm{Pr}_{nf}^{\;0.5}$ **(7.27)**

Maiga correlation: $Nu_{nf} = 0.085\mathrm{Re}_{nf}^{\;0.71}\,\mathrm{Pr}_{nf}^{\;0.35}$ **(7.28)**

Vajjha correlation: $Nu_{nf} = 0.065(\mathrm{Re}_{nf}^{\;0.65} - 60.22)(1 + 0.0169\phi^{0.15})\,\mathrm{Pr}_{nf}^{\;0.542}$ **(7.29)**

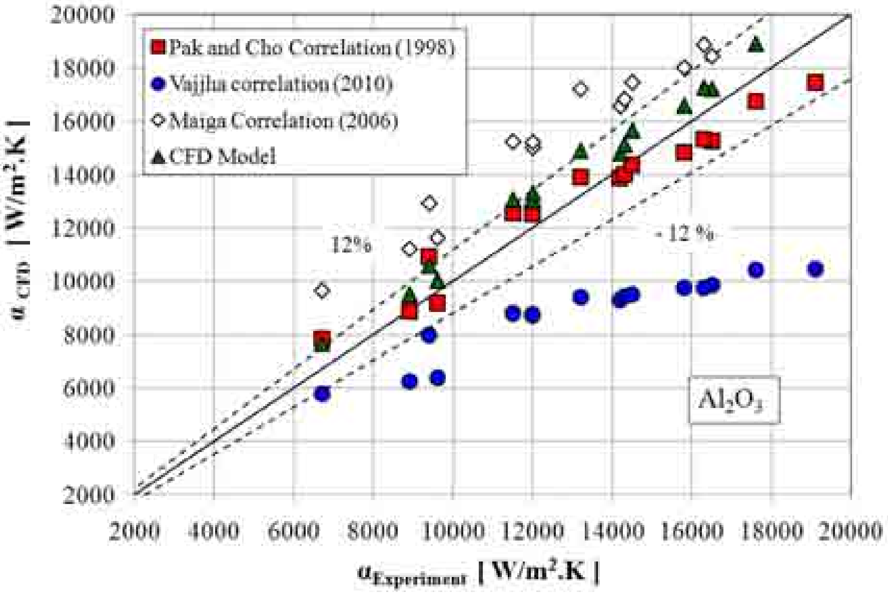

Figure 7.15: Al_2O_3 CFD and empirical correlation prediction with Williams et al. (2008) measurements of turbulent flow regime.

The developed CFD model was used to investigate the effect of nanofluid volume fraction on the heat transfer enhancement ratio in straight tubes at various Reynolds Numbers with 30 kW/m^2 heat flux. In this analysis, the heat transfer enhancement ratio is defined as the ratio of heat transfer coefficient of the nanofluid to that of the base fluid at the same inlet Reynolds number.

Figure 7.16 shows that the heat transfer enhancement ratio increases with the increase in nanofluid volume fraction. The enhancement was close to 40% for concentrations of 3%. The maximum deviation between the Pak and Cho correlation and CFD prediction was less than 7 %. The effect of Reynolds number was found to be insignificant which agrees with most experimental measurements in the turbulent flow regime (Li and Xuan (2002); Celeta (2008)).

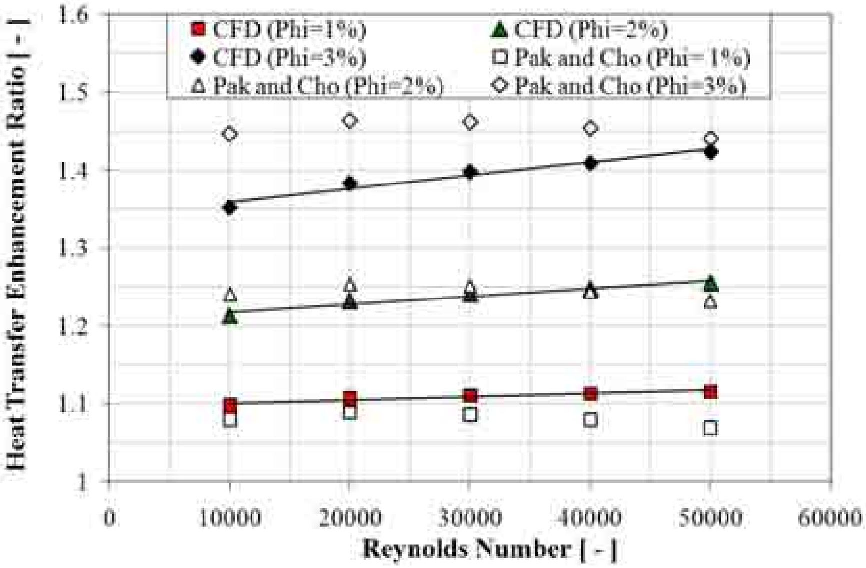

Figure 7.16: Turbulent heat transfer enhancement ratio with the nanofluid volume fraction.

It has been shown that the friction factor of nanofluids agrees with that predicted by conventional theory (Li and Xuan, 2002). Therefore the ratio of pressure drop for nanofluid and base fluid in straight tube for constant tube length, tube diameter and Reynolds number is expressed using equations (7.13) and (7.14).

Figure 7.17 shows the pressure drop ratio for the same Reynolds numbers and volume concentrations. It can be seen tha tthe Reynolds number has insignificant effect on the pressure drop penalty ratio. On the other hand, increasing the volume fraction leads to higher penalty ratio due to the increase in the nanofluid viscosity. Figure 7.17 also shows a close agreement between the CFD and the analytical predictions using equation (7.13).

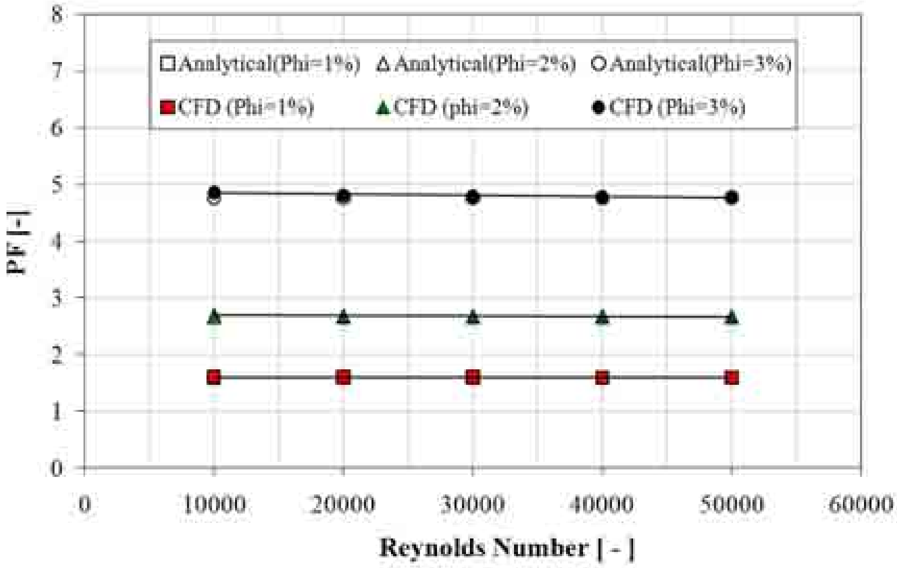

Figure 7.17: Turbulent flow heat transfer in helical coils.

7.3.1.3 Base fluid (water) heat transfer in helical coils

A helical coil with coil length and tube diameter similar to those used in the straight tube (9.4 mm internal diameter and 2819 mm long) with 1 m and 0.5 m adiabatic sections has been modelled (Williams et al., 2008). The coil pitch was selected as 15 mm and number of turns of 5 leading to a coil diameter of 179.5 mm. The discritization schemes utilized were second order for energy, first order for momentum and SIMPLEC algorithm with skewness factor of one for coupling the velocity and pressure.

The mesh contains 1,026,000 elements where the number of nodes in the axial direction were 500, 1500, and 250 for the inlet straight, helically coiled, outlet straight tubes respectively. Figure 7.18 shows the mesh used where tri-quad meshing has been utilized to mesh the inlet face and hex/wedge cooper mesh used to mesh the coil volume with 6 layers close to the wall.

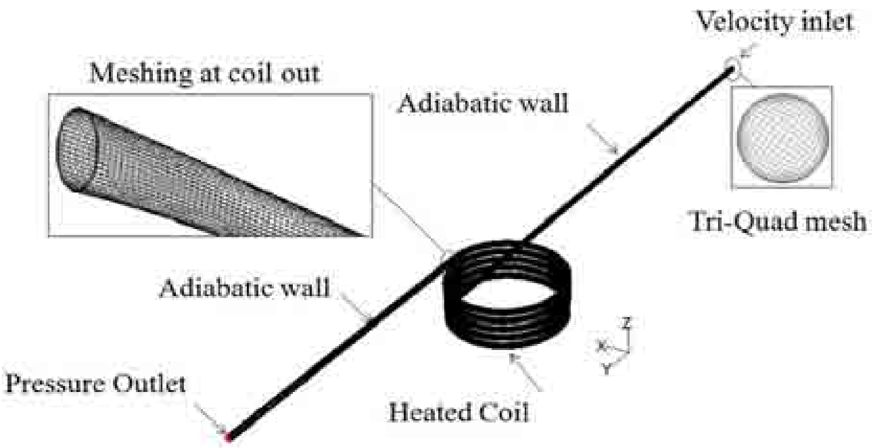

Figure 7.18: Turbulent flow 3D mesh of helical coil using tri-quad mesh.

The mesh quality has been checked by revising the turbulent wall function y^+ value (less than 5 as depicted in figure 7.19 and comparison to pure water empirical correlations. The required simulation time for each case was 8 hours using 2.4 GHz core Quad processor with 2GB RAM memory computer.

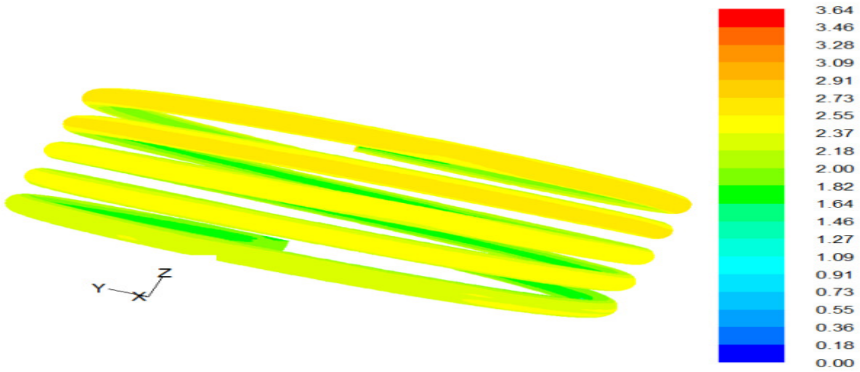

Figure 7.19: Turbulence wall function y^+.

Figure 7.20 shows close agreement between the CFD predicted heat transfer coefficients with 30 kW/m^2 heat flux and empirical correlations using Seban and Mclaughlin correlation (1963) and Mori and Nakayam (1967) correlations described in equations (7.30) and (7.31) respectively. Seban and Mclaughlin (1963) tested two coils using water with 7.37 mm internal diameter with coil to diameter ratios of 17 and 104 using direct electrical heating with constant heat flux. In their correlation, the thermophysical properties were calculated based on the film temperature (the average between bulk fluid temperature and wall temperature). Mori and Nakayama (1967) tested two coils with tube diameter to coil ratio of 18.7 and 40 with the thermophysical properties calculated using the bulk average temperature in implementing their correlation.

$$\alpha_{Seban-Mclaughlin} = 0.023\mathrm{Re}^{0.85}\,\mathrm{Pr}^{0.4}\left(\frac{d_i}{d_{coil}}\right)^{0.1}\frac{k_l}{d_i} \qquad \textbf{(7.30)}$$

$$6000 \le \mathrm{Re} \le 65{,}600 \qquad 2.9 < \mathrm{Pr} < 5.7$$

$$\alpha_{Mori-Nakayama} = \frac{1}{41}\mathrm{Re}^{5/6}\,\mathrm{Pr}^{0.4}\left(\frac{d_i}{d_{coil}}\right)^{(1/12)}\left(1+0.061/\left(\mathrm{Re}(d_i/d_{coil})^{2.5}\right)^{(1/6)}\right)\frac{k_l}{d_i} \qquad \textbf{(7.31)}$$

$$10{,}000 \le \mathrm{Re} \le 200{,}000 \qquad \mathrm{Pr} > 1$$

The absolute mean relative deviation between the CFD prediction and those of the Seban and Mclaughlin (1963) correlation was found to be less than ± 3.2 %.

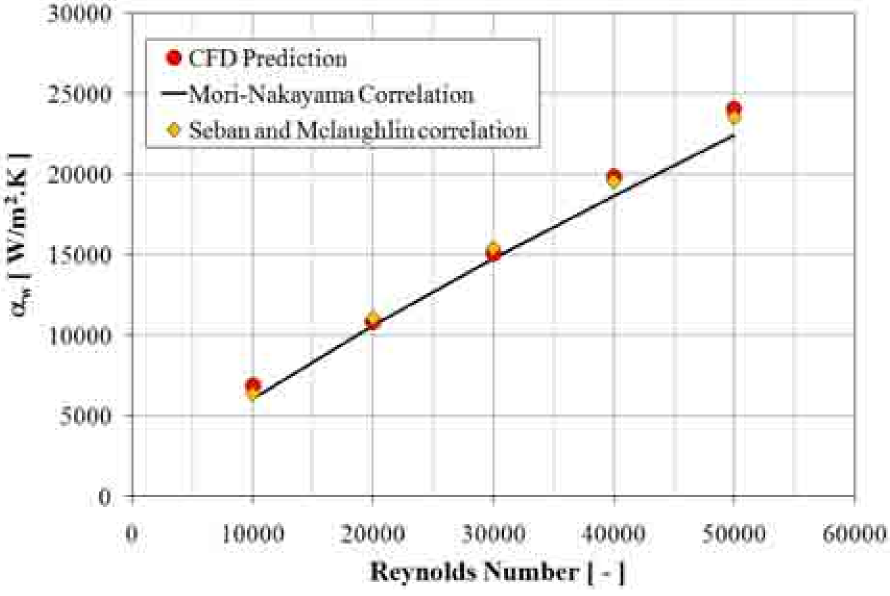

Figure 7.20: Comparison between turbulent CFD prediction and water flow empirical correlations in helical coils.

Figure 7.21 shows the velocity contours at successive cross sections at coil inlet, 1, 2.5, and 5 turns at Reynolds number of 20,000. The flow enters the coil as hydrodynamically fully developed turbulent. Inside the helical coil, the fluid elements with high velocities are pushed to the outer side of the coil due to centripetal force and generating secondary flow in the coil.

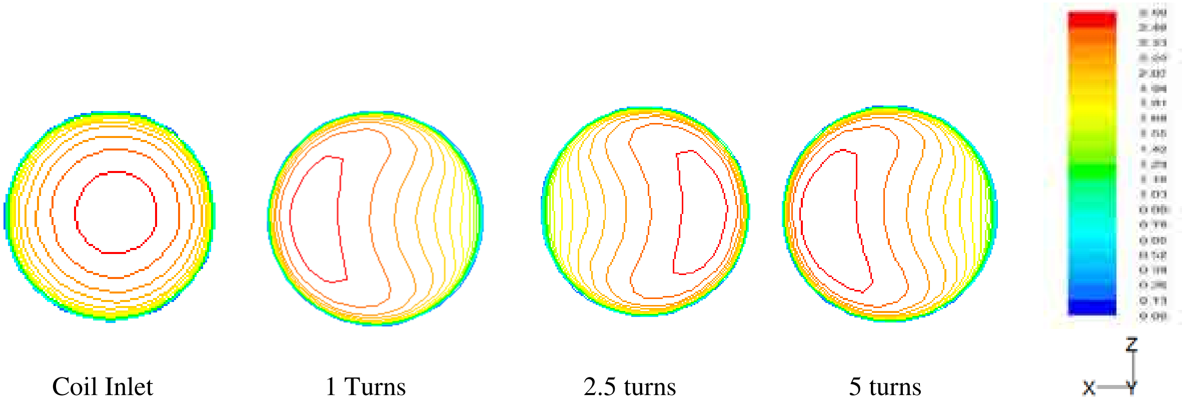

Coil Inlet 1 Turns 2.5 turns 5 turns

Figure 7.21: Turbulent velocity contours cross section parallel to coil inlet(y=0) at Re=20,000.

Figure **7.22** shows the heat transfer enhancement ratio versus the flow Reynolds number. Here the enhancement ratio is defined as the heat transfer coefficient of water in helical coils compared to that of water flow inside straight tube with the same diameter and length. It is clear from this figure that the enhancement ratio ranges from 1.07 to 1.12 which is considerably lower than those reported for the laminar flow as described in section 7.2.2.1, and Kumar et al. (2006). Also, the heat transfer enhancement ratio increases slightly with Reynolds number in agreement with the findings of Naphon (2011) and Kumar et al.(2008).

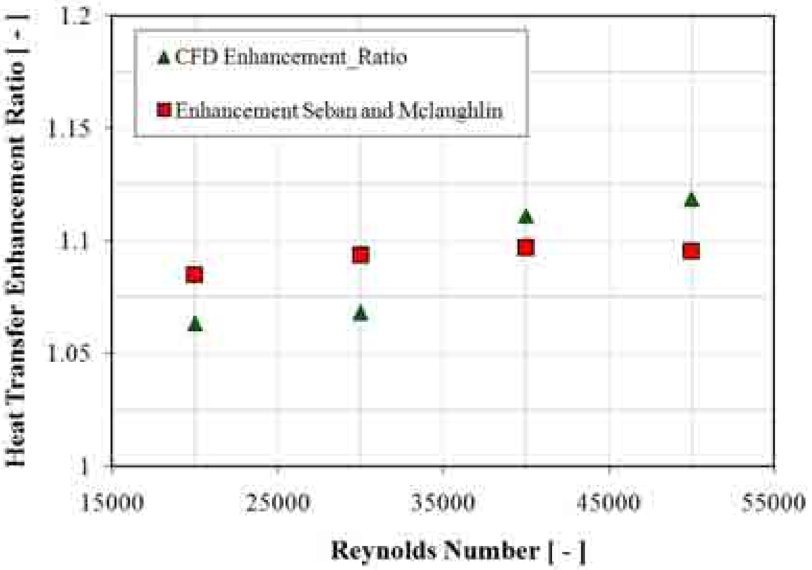

Figure 7.22: Helical coil heat transfer enhancement ratio in turbulent flow using water.

7.3.1.4 Al_2O_3 nanofluids turbulent heat transfer in helical coils

The flow governing equations describing nanofluids flow and the geometry described in section 7.3 were used to simulate the Al_2O_3 nanofluid performance in helical coil with similar mesh configurations and boundary conditions. Figure **7.23** shows the heat transfer enhancement ratio (heat transfer coefficient of nanofluid in the helical coil divided by the heat transfer coefficient of the base fluid in the straight tube with the same internal diameter and length) versus the nanofluid volume fraction at various Reynolds numbers. It is clear from this figure that for the studied Reynolds number range 20000-50000, the heat transfer enhancement ratio increases with both Reynolds number and volume fractions.

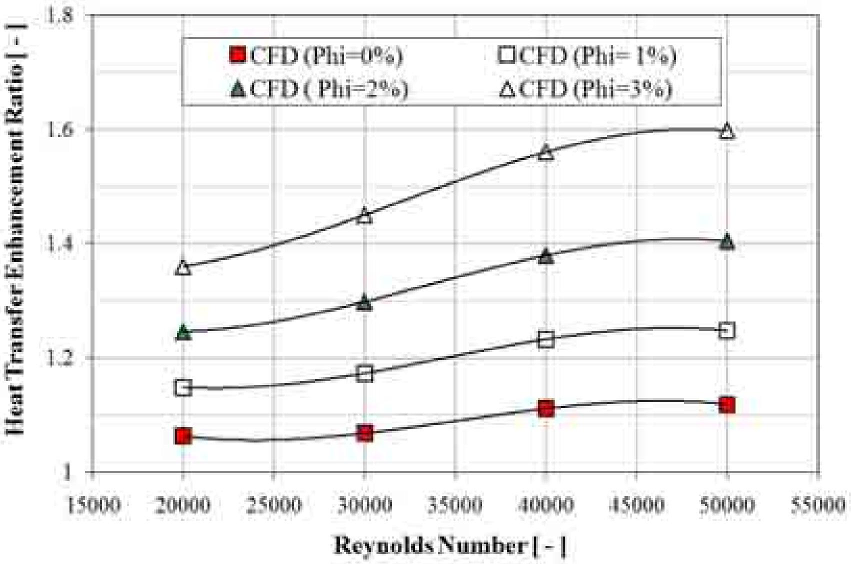

Figure 7.23: Helical coil Al_2O_3 nanofluid heat transfer enhancement ratio.

Regarding the velocity contours in case of nanofluids, the velocity contours at volume concentration of 2% with Reynolds number of 20000 has been presented. No significant change in behaviour with respect to base fluid was observed. Since the viscosities of nanofluids are higher than those of base fluids, the flow velocities to achieve the same Reynolds number were higher as depicted in figure 7.24.

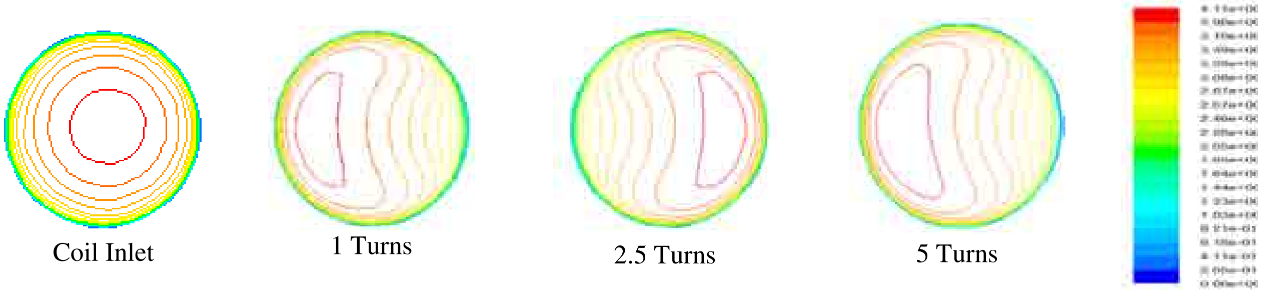
Coil Inlet 1 Turns 2.5 Turns 5 Turns

Figure 7.24: Turbulent velocity contours cross section parallel to coil inlet(y=0) at Re=20,000.

The effect of nanoadditives on heat transfer in helical coils was found to be close to that of nanoadditives in straight tubes in the turbulent flow regime. However, the pressure drop penalty was found to be larger in the case of helical coils as depicted in figure 7.25. Additionally an analytical pressure drop ratio (Penalty factor, PF) expression has been developed based on White correlation (Welti-Chanes et al., 2003) for friction factor in the turbulent flow regime and was found to be in a close agreement with the CFD prediction. The pressure drop in helical coils using Al_2O_3 for volume fraction larger than 2% exceeds 4 times that of water in straight tubes.

For the same tube length and Reynolds number, the pressure drop ratio of nanofluid flow in helical coil to the base fluid in straight tube (pressure drop Penalty Factor, PF) can be expressed as:

$$\frac{\Delta P_{nf,Hc}}{\Delta P_{bf,St}} = PF = \frac{f_{nf,Hc} L_{Hc} + f_{nf,St}\left(L_{tube} - L_{Hc}\right)}{f_{bf,St}} \left(\frac{\mu_{nf}}{\mu_{bf}}\right)^{2} \left(\frac{d_{nf}}{d_{bf}}\right)^{-3} \left(\frac{\rho_{nf}}{\rho_{bf}}\right)^{-1} \qquad \textbf{(7.32)}$$

Where L_{tube} and L_{Hc} are the total straight tube length including the adiabatic parts and the coil heated length with 4319 mm and 2819 mm respectively. The friction factor of nanofluid in helical coil $f_{nf,Hc}$ was calculated using White correlation (Welti-Chanes et al., 2003) for turbulent flow while the friction factor of nanofluid in the straight tube was taken as equal to that of the base fluid in straight tube at the same Reynolds number. Thus

$$\frac{f_{nf,Hc}}{f_{bf,St}} = \frac{f_{nf,Hc}}{f_{nf,St}} = \frac{4\left(0.08\,\mathrm{Re}_{nf}^{-0.25} + 0.012\left(d_i / d_{coil}\right)^{0.5}\right)}{0.316\,\mathrm{Re}_{nf}^{-0.25}} \qquad 15000 < \mathrm{Re} < 100000 \qquad \textbf{(7.33)}$$

$f_{nf,Hc}$, $f_{nf,St}$ are the friction factor of nanofluids in helical coils and straight tubes based on White (Welti-Chanes et al., 2003) and Blasius (Kakaç and Liu, 2002) correlations respectively using the nanofluid thermophysical properties.

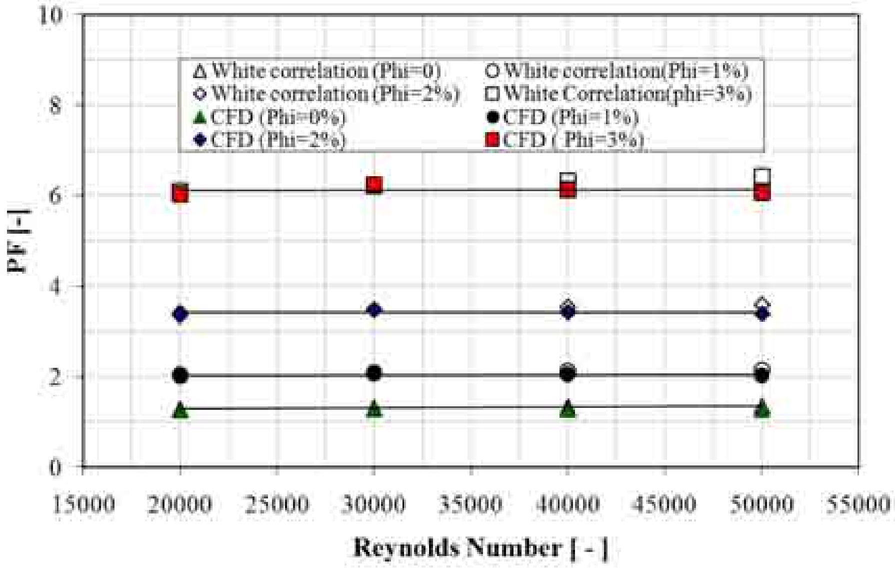

Figure 7.25: Turbulent pressure drop penalty factor in helical coils.

7.4 Summary

Different strategies have been investigated to enhance the heat transfer in single phase fluid flow by coiling the tubes or using nanofluids. The main findings could be summarized:

- For pure fluids, the heat transfer enhancement due to tube coiling in the laminar flow (ER=2 to 3) was much higher than that in turbulent flow (ER=1.1) due to the secondary flow effect.
- Nanofluid additives was found to cause higher enhancement in turbulent flow (ER=1.5) compared to coiling the tube (ER=1.1).
- White friction factor correlations were found to predict the pressure drop in both the laminar and turbulent flow with good agreement within ± 5%.
- Using volume concentration of Al_2O_3 is recommended up to 2% to avoid substantial pressure drop.

CHAPTER 8

Conclusions and Recommendation for Future work

8.1 Introduction

Due to the need to develop efficient miniature cooling systems for portable and electronic cooling applications, helical coils have attractive features for heat exchanger manufacturers due to their compactness and heat transfer enhancement. Understanding the heat transfer mechanism through helical coils is important to design efficient thermal system. The present study is an investigation of different strategies to augment the heat transfer in helical coils for miniature cooling applications. The effect of coil geometry on the boiling heat transfer was investigated experimentally by testing four different coils with tube diameters of 2.8 mm, 2 mm, 1.55 mm, and 1.1 mm respectively. All coils have 60 mm coil diameter except the first one has 30 mm coil diameter. Based on the boiling experimental results the first coil was recommended for experimental investigation for the design of miniature cooling vapour compression system equipped with helical coils as the reduction in coil diameter proved to effectively enhance the boiling heat transfer rate. Afterwards, a theoretical model to simulate the cooling system using Matlab 2008 was developed and validated against the experimental measurements. This model was then used to find optimum configuration of condenser and evaporator helical coils to enhance the performance of miniature cooling systems. Finally, combined passive heat transfer techniques using nanofluids and tube coiling were investigated numerically using Fluent CFD package.

8.2 Conclusions

Both the heat flux and mass velocities were found to have significant effect on flow boiling in small helical coils using R134a for coil diameter range of 30 mm to 60 mm for tube diameter range down to 1 mm based on the current measurements. This indicates that both nucleate and convective boiling mechanisms coexist and affect the heat transfer process in such small tube diameter helical coils. Dimensional analysis and neural network methods have been implemented for flow boiling in helical coils where selection of parameters affecting the boiling process has been identified. The data used in the analysis covered a wide range of fluids, diameters, heat fluxes, and mass velocities. The two-phase heat transfer coefficient was correlated through Stanton number as a function of Jacob number, Martnielli parameter, Weber number and Helical number in the following form.

$$St_{tp} = 0.05473 \left(\frac{1}{Ja}\right)^{-0.55611} \left(X_{tt}\right)^{-0.247552} \left(\frac{1}{We_{lo}}\right)^{0.22287} \left(\frac{1}{He}\right)^{-0.17954} \qquad (2\text{mm} < d_i < 10\text{ mm})$$

$$St_{tp} = 0.1905 \left(\frac{1}{Ja}\right)^{-0.09422} \left(X_{tt}\right)^{-0.131885} \left(\frac{1}{We_{lo}}\right)^{-0.025136} \left(\frac{1}{He}\right)^{0.5446} \qquad (1\text{mm} < d_i \leq 2\text{ mm})$$

Parametric study has been made to study the effect of geometrical parameters on overall performance of miniature cooling system. Opportunities of achieving better performance were found using smaller helical coils where the effect of centrifugal force is significant. Different strategies have been investigated to enhance the heat transfer in single phase fluid flow by coiling the tubes or using nanofluids. The main findings could be summarized:

- For pure fluids, the heat transfer enhancement due to tube coiling in the laminar flow was much higher than that in turbulent flow due to the secondary flow effect. Enhancement ratio of up to 3.25 was found in laminar flow while only a ratio of up to 1.1 was found in the turbulent flow.
- Nanofluid additives were found to cause higher enhancement in turbulent flow compared to coiling the tube. Up to 50 % increase in the heat transfer coefficient was found by using 3% concentration of Al_2O_3 in water while 10% increase in heat transfer coefficient was found by coiling the tube using pure water.
- White friction factor correlations were found to predict the pressure drop in both the laminar and turbulent flow with good agreement within ± 5% for both pure and nanofluids.
- While the addition of nanoparticles to pure fluids can improve the heat transfer performance, significant pressure drop penalty are obtained. Therefore, using volume concentration of Al_2O_3 can be recommended up to 2% to avoid substantial pressure drop. Higher Al_2O_3 concentrations are proved to produce pressure drop penalty higher than 5 times that without nanoparticles.

8.3 Future work

The present study is a step in developing efficient helical coil heat exchangers for small scale applications. However much research is required to cover the following aspects:

- It is desirable to experimentally test more coil geometry for accurately defining the optimum designs. Additionally, more accurate prediction methods could be developed using the generated data by applying different test conditions.
- It is desirable to experimentally test more fluids in helical coils for better understanding of the flow behaviour. Due to the environmental regulations,

some of the current refrigerant will be banned such as R134a, R22. Some refrigerant such as Propane (R290) and CO_2 (R744) are currently under extensive research in flow boiling through straight tubes due to their negligible global warming potential. Therefore, testing these environmental friendly refrigerants is recommended.

- The effects of helical cross-sections such as elliptical, square or rectangular on the heat transfer augmentation need to be investigated. Researchers reported that flow boiling in straight rectangular channels is better than circular ones due to the hold up of liquid at the corners of the channel and thinning the liquid film causing better heat transfer coefficient (Thome, 2004). Such effects should be considered for designing efficient helical coil evaporators.
- The thermal model of miniature cooling system was performed incorporating the empirical correlation developed using the dimensional analysis. As the artificial neural network method predicted the boiling heat transfer coefficient more accurately, it is recommended to incorporate the ANN method in the thermal model to produce more accurate prediction of the system performance with the various helical coil evaporators.
- Different nanoadditive materials such as Cu, CNT, CuO need to be investigated to assess the effect of nanoparticle material on improving heat transfer. It is desirable to engineer the nanoparticles material that could produce high thermal performance with insignificant pressure drop.
- Comparing between different nanofluids modelling approaches such as mixture model, particle dispersion model, Eulerian-Eulerian model and single phase approach is also needed. Although multiphase modelling approaches requires much computational effort, the multiphase modelling approaches does not

requires the measurement of effective thermophysical properties of the nanofluids. This will be beneficial for investigating the new particle materials by specifying more general modelling approach.

- The effect of nanoadditives on the flow boiling process. The research of nanoparticles on the flow boiling process is in its initial stage. More experimental and numerical investigation is required for understanding the boiling process using nanoadditives as some researchers proved it improves the critical heat flux of the heated surface.

References

Agostini, B., Bontemps, A. (2005). Vertical flow boiling of refrigerant R134a in small channels. *International Journal of Heat and Fluid Flow* 26: 296-306.

Akhavan-Behabadi, M. A., Aria, H., and Shemirani, F. M. (2009). Flow boiling heat transfer of HFC-134a inside helically coiled tubes. *In Proceedings of International Conference on Applications and Design in Mechanical Engineering* (ICADME), Malaysia.

Akhavan-Behbadi, M.A., Hashemi, S.M.(2010).Pressure drop characteristics of nanofluid flow in horizontal coiled tube under constant heat flux. In: *Biennial Conference in Engineering Systems Design and Analysis*, ASME, Turkey.

Balakrishnan, R., Santhappan, J. S. and Dhasan, M. L. (2009). Heat transfer correlation for a refrigerant mixture in a vertical helical coil evaporator. *Thermal Science* 13(4), 197-206.

Bradshaw, C., Groll, E.A.,Garimella, S.V.(2011). A comprehensive model of a miniature-scale linear compressor for electronics cooling. *International Journal of Refrigeration* (2011), 34:63-73.

Bergles, A. E. (2002). ExHFT for fourth generation heat transfer technology. *Experimental Thermal and Fluid Science*, 26: 335–344.

Bejan, A., and Kraus, A. (2003). Heat Transfer Handbook. J. Wiley.

Bell, K. J. and Owhadi, A.(1969) . Local heat transfer measurements during forced convection boiling in a helically coiled tube. *Proceedings of the Institution of Mechanical Engineers*, 184(3C): 52-58.

Bi, Q., Chen, T., Tian, Y., Chen, X. (1997). Experimental Study on steam-water two-phase flow frictional pressure drops in helical coils. *Nuclear Science and Techniques* 8(3): 149-153.

Bianco, V., Manca,O., and Nardini, S. (2011). Numerical investigation on nanofluids turbulent convection heat transfer inside a circular tube. *International Journal of Thermal Sciences* 50: 341-349.

Cary,V.P. (1992).Liquid-vapor phase-change phenomena: an introduction to the thermophysics of vaporization and condensation processes in heat transfer equipment. Hemisphere publisher.

Cavallini, A. and Zecchin, R. (1974). A dimensionless correlation for heat transfer coefficient in forced convection condensation. *Proceedings of the Sixth International Heat Transfer Conference*, Tokyo, 309-31.

Celata, G.P.,(2008). Nanofluids – A further chance for heat transfer enhancement. Nanotec2008, Venezia,. http://www.nanotec2008.it/Homeeng/Download/

Chen, C.N., Han, J.T., Jen, T.C. and Shao, L.(2011a). Thermo-chemical characteristics of R134a flow boiling in helically coiled tubes at low mass velocity and low pressure. *Thermochimica Acta* 512: 163–169.

Chen, C.N., Han, J.T., Jen, T. C., Shao, L., Chen, W.W. (2011b). Experimental study on critical heat flux characteristics of R134a flow boiling in horizontal helically-coiled tubes. *International Journal of thermal Sciences* 50:169-177.

Chen, C.N., Han, J.T., Jen, T.C., and Shao, L.(2011c). Dry-out CHF correlation for R134a flow boiling in a horizontal helically-coiled tube. *International Journal of Heat and Mass Transfer* 54: 739–745.

Cheng, L. (2009). Nanofluid heat transfer technologies. *Recent Patents on Engineering* 3, 1-7.

Choi,K., Pamitran, A.S., and Oh, J.T.(2007). Two-phase flow heat transfer of CO_2 vaporization in smooth horizontal minichannels. *International Journal of Refrigeration* 30(5): 767-777.

Choi, K., Pamitran, A. S., Oh,J.T., Saito,K.(2009). Pressure drop and heat transfer during two-phase flow vaporization of propane in horizontal smooth minichannels. International Journal of Refrigeration. 32(5), 837-845.

Chowdhury, S. (2008) Study of condensation of refrigerants in micro-channels for development of future compact micro-channel condensers. PhD thesis, University of Maryland, College Park, USA.

Chung, W.S., Sa, Y.C., Lee, J. S. (2002). An experimental Study on Dryout of Two-phase Flow in helically coiled tubes. *KSME International Journal* 16(11), 1540-1549.

Cioncolini, A., Cammi, A., Cinotti, L., Castelli, G., Lombardi, C., Luzzi, L., Ricotti, M.E.(2003). Thermal and hydraulic analysis of IRIS reactor coiled tube steam generator. *Nuclear Mathematical and Computational Sciences*, Tennessee.

Cioncolini, A., Santini, L., and Ricotti, M. E. (2008). Subcooled and saturated water flow boiling pressure drop in small diameter helical coils at low pressure. *Experimental Thermal and Fluid Science* 32: 1301–1312.

Cui, W., Li, L., Xin, M., Jen, T.-C., Chen, Q. and Liao, Q. (2006). A heat transfer correlation of flow boiling in micro-finned helically coiled tube. *International Journal of Heat and Mass Transfer* 49(17-18): 2851-2858.

Cui , W., Li, L., Xina, M., . Jenb, T-C , Liaob, Q. and Chen, Q. (2008) . An experimental study of flow pattern and pressure drop for flow boiling inside microfinned helically coiled tube. *International Journal of Heat and Mass Transfer* 51(1-2): 169-175.

Data master 2003. http://www.datamaster2003.com/

Del Col, D., Cavallini, A., Bortolin, S., Matkhovic, M., and Rosseto L.(2008). Heat transfer coefficient during flow boiling of r134a in a circular minichannel. In proceedings of *fifth European Thermal-Science conference*, Netherland.

Domanski, P. A. and Hermes, C. J. L.(2006). An improved correlation for two-phase pressure drop of R-22 and R-410a in 180° return bends. *Proceedings of the eleventh Brazilian Congress of Thermal Sciences and Engineering*, Brazil.

Elsayed, A., Al-dadah, R., Mahmoud, S., and Mahrous, A. (2011). Numerical investigation of laminar flow heat transfer through helically coiled tubes using Al_2O_3 nanofluid. *Third Micro and Nano Flows Conference*. Thessaloniki, Greece.

Engineering Equation Solver EES, (2008) software.www.fchart.com

Ernst, T. (2005). Design, fabrication and testing of a wearable cooling system. MSc. Thesis, Georgia Institute of Technology.

Fernando, P., Palm, B., Ameel, T., Lundqvist, P., and Granryd, E. (2008). A minichannel aluminium tube heat exchanger – Part II: Evaporator performance with propane. *International journal of Refrigeration* 31: 681–695.

FLUENT 6.3 User's Guide, 2006.

García-Cascalesa, R., Vera-Garcíaa, F., Corberán-Salvadorb, J.M., Gonzálvez-Maciáb, J., and Fuentes-Díaz, D. (2007). Assessment of boiling heat transfer correlations in the modelling of fin and tube heat exchangers. *International Journal of Refrigeration* 30(6): 1004-1017.

Gungor, K. E. (1986). A general correlation for flow boiling in tubes and annuli. PhD. Thesis, University of Birmingham, UK.

Gungor, K. E. and Winterton, R.H.S. (1986). Simplified general correlation for saturated flow boiling and comparisons of correlations with data. Chemical Engineering Research & Design. The Canadian Journal of Chemical Engineering 65 (2): 148–156.

Guo, L., Feng, Z., and Chen, X. (2001). An experimental investigation of the frictional pressure drop of steam-water two-phase flow in helical coils. *International Journal of Heat and Mass Transfer* 44 (14): 2601-2610.

Hart, J., Ellenberger, J., and Hamersma, P. J. (1988). Single and Two-Phase Flow Through Helically Coiled Tubes. Chemical Engineering Science 43: 775-783.

Helgestad, D. (2009). Modelling and optimisation of the C3MR process for liquefaction of natural gas. Process Systems Engineering (Specialization Project).

Heris, S.Z., Etamad, S. Gh., Esfahani, M. N.(2006). Heat transfer enhancement of nanofluid laminar flow. In: 14th Annual International Mechanical Engineering Conference, Isfahan, Iran.

Heydari, A.(2002). Miniature vapor compression refrigeration systems for active cooling of high performance computers. *In The Eighth Intersociety Conference Thermal and Thermomechanical* Phenomena, Electronic Systems, ITHERM, 371 – 378.

Huo, X., D. Shiferaw, Karayiannis,T.G., Tian, Y.S. and Kenning, D.B.R. (2007). Boiling Two-phase Pressure Drop In Small Diameter Tubes. Retrieved 6 April, 2009, from http://bura.brunel.ac.uk/

Ishida, K.(1981). Two-phase flow with heat transfer in helically-coiled tubes. PhD thesis, Imperial College. London, UK.

Jayanti, S. and Berthoud, G. (1990). High-quality dryout in helical coils. *Nuclear Engineering and Design* 122: 105-118.

Jayakumar, J.S., Mahajani, S.M., Mandal, J.C., Iyer, K.N., Vijayan, P.K.(2010).CFD analysis of single-phase flows inside helically coiled tubes. Computers and Chemical Engineering 34: 430–446.

Jensen, M. K.(1980). Boiling heat transfer and critical heat flux in helical coils. PhD thesis, Iowa state university, USA.

Jitian, H., Li, S., Wenwen, C., and Changnianm, C. Study on Flow Boiling Heat Transfer of R134a in Horizontal Helical Coils. *Chinese Engineering Thermophysics*. ID 093191, http://www.docin.com/p-37703731.html.

Jokar, A., Hosni, M. H., and Eckels, S. (2006). Dimensional Analysis on the evaporation and Condensation of Refrigerant R-134a in minichannel plate heat exchangers. *Applied Thermal Engineering* 26(17-18): 2287-2300.

Kaew-on, J. and Wongwises, S. (2009). Experimental investigation of evaporation heat transfer coefficient and pressure drop of R-410A in a multiport mini-channel. *International Journal of Refrigeration* 32: 124-137.

Kaji, M., Mori, K., Matsumoto, T., Oishi, M., Sawai, T. O., and Nakanishi, S. (1998). Forced convection boiling heat transfer characteristics and critical heat flux in helically coiled tubes. *JSME* 64(626): 203-209.

Kalb, C. E., and Seader, J. D. (1972). Heat and mass transfer phenomena for viscous flow in curved circular tubes. *International Journal of Heat and Mass Transfer* 15: 801-817.

Kakaç, S.and Liu, H. (2002). Heat exchangers: selection, rating and thermal design. CRC Press, Second edition.

Kelecy, F. J. (2008).Coupling momentum and continuity increases CFD robustness. ANSYS Advantage 2 (2): 49- 51.

Kim, J.W, Im, Y., and Kim, J.S. (2006). A study on Performance analysis of helically coiled evaporator with circular minichannels. *Journal of Mechanical Science and Technology* 20(7): 1059-1067.

Kim, J.W., Kim, J.H., and Kim, J.S.(2001). A study on the helically coiled heat exchanger of small diameter tubes. KSME series B 25(11), 1492-1499.

Kim, J.W., Kim, J.H., Seo, S. K., Kim, J. H., and Kim, J. S. (2000). Characteristics of heat transfer and pressure drop of R-22 inside an evaporating tube with small diameter helical coil. KSME series B 24(5), 699-708.

Klimenko, V.V. (1988). A generalized correlation for two-phase forced flow heat transfer, *International Journal of Heat and Mass Transfer* 31 (3): 541–552.

Kozeki, M., Nariai, H., Furukawa, T., and Kurosu, K. (1970). A study of helically-coiled once-through steam generator. *Bulletin of the JSME* 13(66): 1485-1495.

Koeijer, G. De, Røsjorde, A., and Kjelstrup, S.(2004). Distribution of heat exchange in optimum diabatic distillation columns. *Energy* 29, 2425–2440.

Kumar, V., Faizee, B., Mridh, M., and Nigam, K.D.P.(2008). Numerical studies of a tube-in-tube helically coiled heat exchanger. *Chemical Engineering and Processing* 47: 2287–2295.

Kumar, V., Saini, S., Sharma, M., and Nigam, K.D.P. (2006). Pressure drop and heat transfer study in tube-in-tube helical heat exchanger. *Chemical Engineering Science* 61: 4403 – 4416.

Li, Q., and Xuan, Y.(2002). Convective heat transfer and flow characteristics of Cu-water nanofluid. *International Journal of Nanotechnology and Applications*, Science in China 45(4)-Series E: 408-416.

Li, S., Jitian, H., Wenwen, C., Changnian, C., and Jihong, P. Study on flow boiling pattern and pressure drop of R134a in horizontal helical coils. *Chinese Engineering Thermophysics*. Heat and mass transfer.

Lie, Y. M., Su, F. Q., Lai, R.L. and Lin , T.F. (2006). Experimental study of evaporation heat transfer characteristics of refrigerants R-134a and R-407C in horizontal small tubes. *International Journal of Heat and Mass Transfer* 49(1-2): 207-218.

Maiga, S.E.B., Nguyen, C.T., Galanis, N., Roy, G., Mare, T., and Coqueux, M.(2006). Heat transfer enhancement in turbulent tube flow using Al2O3 nanoparticle suspension. *International Journal of Numerical Methods for Heat and Fluid Flow* 16 (3): 275–292.

Matlab (2008). http://www.mathworks.com/

Matsui, G., Suzuki, M. and Kaji, M. (2008). Characteristics of Boiling flow in Helically Coiled Heat-Transfer Tube. JSEM, 72-77.

Mikielewicz, D.(2004). Modelling of convective heat transfer in flow boiling. Minsk International Heat & Mass Transfer Forum (MIF).

www.imamod.ru/~serge/arc/conf/MIF_2004/S05/5-55.pdf

Mongia, R., Masahiro, K., DiStefano, E., Barry, J., Chen, W., Izenson, M., Possamai, F., Zimmermann, A., and Mochizuki, M.(2006). Small scale refrigeration system for electronics cooling within a notebook computer. *In Tenth Intersociety Conference, Thermal and Thermomechanical Phenomena in Electronics Systems*-ITHERM, 751-758.

Mori, Y. and Nakayama, W. (1967). Study on forced convective heat transfer in curved pipes. *International Journal of Heat and Mass Transfer* 10(5): 681–695.

Mosaad, M., Al-Hajeri, M. Al-Ajmi, R. , and Koliub, Abo. M.(2009). Heat transfer and pressure drop of R-134a condensation in a coiled double tube. *Heat Mass Transfer* 45: 1107-1115.

Murshed, S. M., Leong, K.C., Yang, C., and Nam-Trung, N. (2007). Convective heat transfer of nanofluids in minichannel under laminar flow conditions. *In:*

Proceedings of the International Conference on Mechanical Engineering, ICME2007, Bangladesh.

Nariai, H., Kobayashi, M., and Matsuoka T.(1982) Friction pressure drop and heat transfer coefficient of two-phase flow in helically coiled tube once through steam generator for integrated type marine water reactor. *Journal of Nuclear Science and Technology*, 19(11): 936-947.

Naphon, P. (2011). Study on the heat transfer and flow characteristics in a spiral-coil tube. *International Communications in Heat and Mass Transfer* 38: 69–74.

Nnanna, A. G. A. (2006). Application of refrigeration system in electronics cooling. *Applied Thermal Engineering* 26(1):18-27.

Nguyen, C. T., Roy, G., Lajoie, P.-R., and Maiga, S. E. B.(2005). Nanofluids heat transfer performance for cooling of high heat output microprocessor. Proceedings of the Third IASME/WSEAS International Conference on heat transfer, Corfu, Greece: 160-165.

Oh, J.T., Pamitran, A.S., Choi, K., Hrnjak, P. (2011). Experimental investigation on two-phase flow boiling heat transfer of five refrigerants in horizontal small tubes of 0.5, 1.5 and 3.0 mm inner diameters. *International journal of heat and mass transfer* 54(9-10): 2080-2088.

Ong, C. L. and Thome, J. R. (2009). Flow boiling heat transfer of R134a, R236fa and R245fa in a horizontal 1.030 mm circular channel. *Experimental Thermal and Fluid* Science 33(4): 651-663

Owhadi, A., Bell, K. J. and Crain, B.(1968). Forced convection boiling inside helically-coiled tubes. International Journal of Heat and Mass *Transfer*, 11(12): 1779-1793.

Owhaib, W. (2007). Experimental heat transfer, pressure drop, and flow visualization of R134-a in vertical mini/micro tubes. PhD thesis, Royal Institute of Technology, KTH, Stockholm, Sweden, 2007.

Pamitran, A.S., Choi, K., Oh, J.K.,Oh, H.K.(2008). Two-phase pressure drop during CO_2 vaporization in horizontal smooth minichannels. *International Journal of Refrigeration* 31(8): 1375-1383.

Pak, B., and Cho, Y.I. (1998). Hydrodynamic and heat transfer study of dispersed fluids with submicron metallic oxide particle. *Journal of Heat Transfer* 11: 151-170.

Rao, S.(2009). Engineering optimisation: theory and Practice Engineering Optimisation, John Wiley & Sons, Inc.

Refprop(2002), NIST Reference Fluid Thermodynamic and Transport Properties Database, version 7.

Rashid Ali., Björn Palm. (2010). Dryout Characteristics during Flow Boiling of R134a in Vertical Circular Minichannels. International Journal of Heat and Mass Transfer, 54 (11-12):2434-2445.

Rea, U., McKrell, T., Hu, L., and Buongiorno, J. (2009). Laminar convective heat transfer and viscous pressure loss of alumina-water and zirconia-water nanofluid. *International Journal of Heat and Mass Transfer* 52(7-8), 2042-2048.

Ribatski, G., L. Wojtan, Thome,J.R.(2006). An analysis of experimental data and prediction methods for two-phase frictional pressure drop and flow boiling heat transfer in micro-scale channels. Experimental Thermal and Fluid Science 31(1):1-19.

Rohsenow, W. M., Hartnett, J. R., and Cho, Y. I. (1998). Handbook of heat transfer. McGraw-Hill, Third edition, Chapter 5.

Rostamani, M., Hosseinizadeh, S.F. , Gorji, M., Khodadadi, J.M.(2010). Numerical study of turbulent forced convection flow of nanofluids in along Horizontal duct considering variable properties. *International Communications in Heat and Mass Transfer* 37:1426–1431

Saitoh,S., Daiguji, H. and Hihara, E.(2007). Correlation for boiling heat transfer of R-134a in horizontal tubes including effect of tube diameter. *International Journal of Heat and Mass Transfer* 50: 5215–5225.

Saitoh,S., Daiguji, H. and Hihara, E.(2005). Effect of tube diameter on boiling heat transfer of R134a in horizontal small-diameter tubes. International Journal of heat and Mass transfer 48: 4973-4984.

Salimpour, M. R. (2009) .Heat transfer coefficients of shell and coiled tube heat exchangers. *Experimental Thermal and Fluid Science*, 33: 203–207.

Sathe,A., Groll, E.A., Garimella, S.V.(2009). Optimization of electrostatically actuated miniature compressors for electronics cooling. *International Journal of Refrigeration* , 32: 1517-1525.

Santini, L., Cioncolini, A., Lambardi, C., and Ricotti, M.(2008). Two-phase pressure drops in helically coiled steam generator. *International Journal of Heat and Mass Transfer* 51: 4926-4939.

Saripella, S.K., Routbort, J. L., Yu, W., France, D.M., Rizwan-Uddin (2007). Effects of nanofluid coolant in a class 8 truck engine. Retrieved April 5, 2011 from http://papers.sae.org/2007-01-2141

Seban, R. A., and Mclaughlin, E. F (1963). Heat transfer in tube coils with laminar and turbulent flow. *International Journal of Heat and Mass Transfer* 6(5): 387-395.

Selbas, R., KizIlkan, Ö. and Sencan, A.(2006). Thermoeconomic optimisation of subcooled and superheated vapor compression refrigeration cycle. *Energy*, 31(12): 2108-2128.

Shao, L., Han, J.-t., Su,G.-p., and Pan, J.-h. (2007). Condensation heat transfer of R-134A in horizontal straight and helically coiled tube-in-tube heat exchangers. *Journal of Hydrodynamics, Ser. B*, 19(6): 677-682.

Shiferaw, D., Mahmoud, M. M., Karayiannis, T. G., and Kenning D. B. R. (2008). Experimental flow boiling study in a 0.52 mm diameter vertical tube using R134A. *In Proceedings of the fifth European Thermal-Sciences Conference*. Netherlands.

Shiferaw, D., Karayiannis, T. G. and Kenning, D. B. R.(2006). A comparison with the three-zone model for flow boiling heat transfer in small diameter tubes. *In Proceedings of the thirteenth International Heat Transfer Conference*, Sydney, Australia.

Skousen,P.L.(2004). Valve Handbook. chapter 7, McGraw-Hill.

Styrikovich, M.A., Polonsky, V.S., and Reshetov, V.V. (1984). Experimental investigation of the critical heat flux and post-dryout temperature regime of helical coils. *International Journal of Heat and Mass Transfer* 27(8): 1245-1250.

Sundar, L.S., Ramanathan, S., Sharma K.V., Sekhar Babu, P.(2007). Temperature Dependent Flow Charecteristics of Al_2o_3 Nanofluid. *International Journal of Nanotechnology and Applications* 1(2), 35-44.

Suzuki, M., Kaji, M., and Matsui G. (2009). Heat flux Measurement of boiling heat transfer in a helically coiled tube heated by oil bath. *Japan Society of Mechanical Engineers JSEM* 9: 60-65.

Thome, J. (2004). Boiling in microchannels: a review of experiment and theory. *International Journal of Heat and Fluid Flow* 25(2), 128-139.

Thome, J. (2010). Wolverine databook III. Wolverine Tube.

Torii, S.(2007). Experimental study on convective heat transfer of aqueous suspension of nano-diamond particles. International Symposium on EcoTopia Science. Japan: 352-357.

Trutassanawin, S., Groll, E.A., Garimella, S.V., and Cremaschi, L.(2006). Experimental investigation of a miniature-scale refrigeration system for electronics cooling. *Components and Packaging Technologies*, IEEE Transactions, 29(3):678-687.

Vajjha, R.S., Das, D.K., and Kulkarni, D.P.(2010). Development of new correlations for convective heat transfer and friction factor in turbulent regime for nanofluids. *International Journal of Heat and Mass* Transfer 53:4607-4618.

Vasu, V., Krishna, K. R., and Kumar, A.C.S.(2008). Application of nanofluids in thermal design of compact heat exchanger. Research India Publications, *International Journal of Nanotechnology and Applications* 2(1):75–87.

Wadekar, V. (2001). Compact exchangers for phase change. *Fifth World Conference on Experimental Heat Transfer, Fluid Mechanics and Thermodynamics, Greece.*

Wallace, K. G. (2010). Research in heat transfer with nanofluids. M.Sc. in Technology, Purdue University Calumet School of Technology.

Welti-Chanes, J., Vélez-Ruiz, J., and Barbosa-Cánovas, J.V. (2003). Transport Phenomena in Food Processing. CRC Press, Chapter 25.

Wessapan, T., Borirak, T., Teeksap, S., and Somsuk, N. (2010). A development of a portable air conditioning-heat pump unit using helical coil heat exchanger. *Second International Conference of Computer Engineering and Technology* (ICCET), 5: 186-190.

Whalley, P. B. (1996). Two-Phase Flow and Heat Transfer. Oxford Science Publications.

Williams, W., Buongiorno,J., and Hu, L.(2008). Experimental investigation of turbulent convective heat transfer and pressure loss of alumina/water and zirconia/water nanoparticle colloids (nanofluids) in horizontal tubes. *Journal of Heat Transfer* 130(4).

Wongwises, S. and Polsongkram, M. (2006a) .Evaporation heat transfer and pressure drop of HFC-134a in a helically coiled concentric tube-in-tube heat exchanger. *International Journal of Heat and Mass Transfer*, 49(3-4): 658-670.

Wongwises, S. and Polsongkram, M. (2006b). Condensation heat transfer and pressure drop of HFC-134a in a helically coiled concentric tube-in-tube heat exchanger. *International Journal of Heat and Mass Transfer*, 49: 4386–4398.

Wu, Y., Ma, C., and Zhong, X.(2010). Development and experimental investigation of a miniature-scale refrigeration system. *Energy Conversion and Management*, 51, 81–88.

Wu, Z. and Du, R. (2011). Design and experimental study of a miniature vapor compression refrigeration system for electronics cooling. *Applied Thermal Engineering*: 31, 385-390.

Xiande, F., Rongrong, S., Zhanru, Z.(2011). Correlations of flow boiling heat transfer of R-134a in minichannels: comparative study. *Energy Science and Technology* 1(1),1-15.

Yan, Y.Y. and Lin, T.F. (1998). Evaporation heat transfer and pressure drop of refrigerant R-143a in a small pipe. *International Journal of Heat and Mass Transfer* 41: 4183- 4194

Young, M. A. and Bell, K. J.(1991). Review of two-phase flow and heat transfer phenomena in helically coiled tubes. *American Institute of Physics,* 217: 1214-1222.

Yi, J., Liu, Z.-H., and Wang, J. (2003). Heat Transfer Characteristics of the evaporator Section using small helical coiled pipes in a looped heat pipe. *Applied Thermal Engineering* 23: 89-99.

Zhao, L., Guo, L., Bai, B., Hou, Y., and Zhang , X. (2003). Convective boiling heat transfer and two phase flow characteristics inside a small horizontal helically coiled tubing once-through steam generator. *International Journal of Heat and Mass Transfer* 46: 4779-4788.

Zhong, X.H., Gou,Y. J.,Wu, Y.T. and Ma, C. F.(2008) Development and experimental study of a miniature vapor compression refrigeration equipment. *Science In China Series E: Technological Sciences* 51(5): 632-640.

Appendix A: Instrument Calibration Uncertainties

1. Thermocouples

The uncertainty in thermocouples is defined as:

$$U_{Tc} = \sqrt{U_{st}^2 + U_{curve\_fit}^2} \qquad \textbf{(A.1)}$$

Where U_{TC} , U_{st}, U_{curve_fit} are the uncertainties of thermocouple, standard instrument utilized in the calibration (RTD= Resistance temperature detector), and the curve fit error respectively. The RTD was positioned in ice water mixture and the temperature was recoreded as shown in figure A-1. It seems that the error of the standard RTD (resistance thermometer) is within ± 0.025 which is negligible.

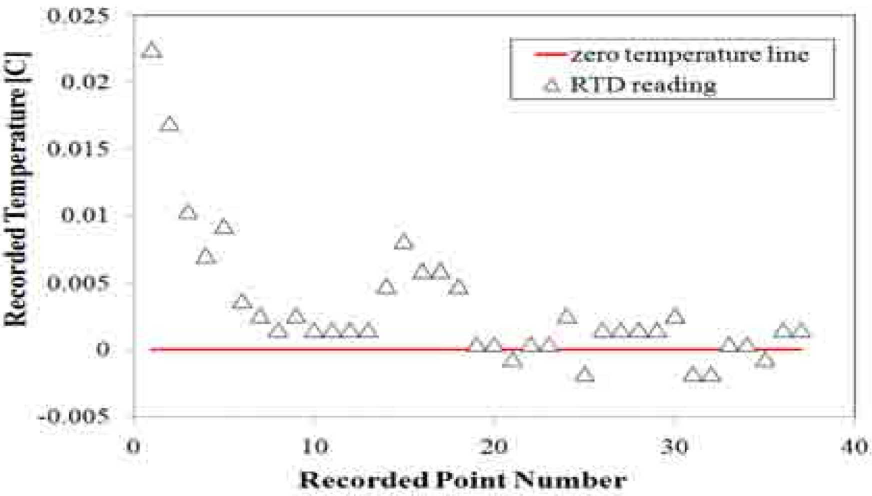

Figure A-1: Uncertainty in RTD thermocouple

So the uncertainty in the thermocouples is equals to the uncertainty associated with curve fitting process between the thermocouple and RTD readings:

$$U_{Tc} \approx U_{curve\_fit} \qquad \textbf{(A.2)}$$

The uncertainty of curve fitting was defined from the standard deviation of the mean as: $U_{curve\_fit} = t_{N-1,95\%} S_{\bar{x}}$ **(A.3)**

For instance the uncertainty associated with thermocouple SURF-8 is depicted in table A.1.

Table A.1: Calculation of SURF-8 thermocouple associated curve fitting uncertainty

Data Point(N)	RTD	average measured Temperature ($TC_{measured}$)	Curve fit temperature [C] $TC_{corrected}=1.003*TC_{measured}$	Deviation^2
1	2.903	3.4185	3.4287555	0.276
2	5.08475	4.95375	4.96861125	0.0134
3	12.428	12.19975	12.23634925	0.036
4	17.897	17.75	17.80325	0.009
5	37.62775	37.693	37.806079	0.032
6	64.476	64.352	64.545056	0.005
7	77.42875	77.24975	77.48149925	0.003
8	100.04425	99.622	99.920866	0.015
Degree of freedom(N-1)=7				
Standard deviation of the mean $S_{\bar{x}}$ =0.0834				
Student distribution factor $t_{N-1,95\%}$ = 2.365				
U_{curve_fit} =0.19 K				

2. Pressure Transducers

The pressure transducer calibration has been repeated four times. In the first to third calibration experiments the pressure was raised from atmospheric pressure to 11 barg. In the fourth calibration the pressure was decreased from 11 barg to atmospheric pressure to estimate the hysteresis in the transducer. The uncertainty of pressure transducer includes the uncertainties associated with repeatability, standard, curve fit, stability per year after calibration, operating temperature and hysteresis.

$$U_{trans} = \sqrt{(\mathrm{U}_{\mathrm{Repeatability}})^2 + (U_{standard})^2 + (U_{curve\_fit})^2 + (U_{stability})^2 + (U_{temp})^2 + (U_{Hysteresis})^2} \quad \textbf{(A.4)}$$

The repeatability has been calculated by subtracting the first calibration reading from the second and third calibration reading and taking the maximum difference. The repeatability found to be ± 0.03bar.

A certified accurate pressure gauge has been used to as a standard to calibrate the transducer through a water dead weight tester. The gauge has uncertainty of ± 0.0397 bars. From the manufacturer catalogue the uncertainty associated with operating temperature was 1 % FS giving ±0.1 bar and the stability error per one year is 0.1% F.s giving uncertainty of ±0.01bar.

The hysteresis was defined as the maximum difference between the readings at different pressures when the transducer loaded and unloaded with pressure. The uncertainty associated with the hysteresis found to be ±0.044 bar. Lastly, the uncertainty associated with the curve fitting was found to be 0.0192 bar. The overall uncertainty of the pressure transducer fitted before the electrically heated evaporator was found to be ±0.122 bar. The overall uncertainty in the water heated evaporator and the discharge pressure transducers were ±0.12 bar and ±0.17 respectively.

3. Water flow meter uncertainty

The volume flow rate has been calculated using:

$$\overset{\bullet}{V}_{w,st} = \frac{collected\ volume}{time} = \frac{V_{w,st}}{t} \qquad \textbf{(A.5)}$$

The uncertainty associated with estimating the tank volume and collecting time is ±1 sec and ±5 mL.

Using the rule of square root sum to calculate the uncertainty of the volume flow rate:

$$U_{\dot{V}_{w,st}} = \sqrt{\left(\frac{\partial U_{\dot{V}_{w,st}}}{\partial V}\Delta V\right)^2 + \left(\frac{\partial U_{\dot{V}_{w,st}}}{\partial t}\Delta t\right)^2} \qquad \textbf{(A.6)}$$

$$U_{\dot{V}_{w,st}} = \sqrt{\left(\frac{1}{t}\Delta V\right)^2 + \left(\frac{-V_w}{t^2}\Delta t\right)^2} \qquad \textbf{(A.7)}$$

The measurement was taken for flow rate less than 500 ml/min flow. So the uncertainty would be:

$$U_{\dot{V}_{w,st}} = \pm\sqrt{\left(\frac{1}{1\min}\times 5mL\right)^2 + \left(\frac{-500mL}{(1\min)^2}\times(1/60)\min\right)^2} = \pm 9.71 mL/\min \qquad \textbf{(A.8)}$$

The uncertainty associated with collecting tank method was found to be ± 9.71mL/min. The overall uncertainty in the flow meter measurement includes both the uncertainty in the collecting volume method and curve fit error as given by equation (A.9).

$$\begin{aligned} U_{\dot{V}_w} &= \sqrt{U^2_{\dot{V}_{w,st}} + U^2_{\dot{V}_{w,curve\_fit}}} \\ &= \sqrt{9.71^2 + 3.336^2} = \pm 10.26 mL/\min = \pm\frac{10.26}{500} * 100 = \pm 2.053\% Fs \end{aligned} \qquad \textbf{(A.9)}$$

The uncertainty associated with water heated evaporator was found to be 2% of the full scale. The calibration has been done at excitation voltage of 15 volt and supply current of 0.02 amp which were fixed during experiment to ensure accurate measurements.

Appendix B: Miniature Cooling System Experimental Measurements

Rpm	Power[w]	Evap. water flow [ml/min]	Cond. water flow [ml/min]	Refrigerant flow[ml/min]	Water inlet temp.[c]	Evap. Outlet water temp.[c]	cond. Outlet water temp.[c]	Suction temp[c]	Discharge temp[c]	Cond outlet temp[c]	Suction press.[bar]	Discharge press.[bar]
2000	33.9	227.6	298	22	16.3766	11.85	20.6791	4.336	43.54	32.47	2.2612	8.3456
2000	33.7	221.1	306.3	22	17.1044	12.31	21.33118	5.867	43.29	32.32	2.2743	8.6489
2000	33.5	210.7	302.5	22	16.8053	11.86	20.88381	5.818	43.64	32	2.2628	8.5576
2000	33.3	200.6	302	22	16.586	11.56	20.75839	3.85	43.74	32.11	2.2448	8.5012
2000	33.1	189.6	302	22	16.4763	11.35	20.47399	2.448	43.52	32.3	2.2339	8.4578
2000	33.8	231	272.8	22	16.227	11.72	21.45941	4.539	43.95	33.49	2.2995	8.6627
2000	33.6	218.8	272.8	22	16.1373	11.62	21.41786	4.769	43.89	33.27	2.2615	8.62
2000	33.4	207.9	269.9	22	16.1073	11.43	21.35116	3.768	43.73	32.96	2.2423	8.5281
2000	33.2	200.4	267.1	22	16.0974	11.25	21.18339	2.715	43.54	32.92	2.2366	8.4998
2000	33.1	192.1	272	22	16.0076	11.12	21.17181	1.378	43.32	32.76	2.2219	8.4443
2000	35.8	226.2	293.4	25	17.7924	12.72	22.10091	4.17	45.61	34.56	2.5168	9.0373
2000	34.9	225.9	299.7	24	17.8822	12.98	22.22992	6.916	45.44	34.19	2.4359	8.9445
2000	34.3	225.7	305	23	17.9819	13.06	22.02921	8.306	45.34	33.79	2.3633	8.8385
2000	33.8	225.4	303.6	22	17.9221	13.45	21.96929	9.788	45.13	33.26	2.2835	8.719
2000	33.4	224.8	300	21	17.8024	13.31	21.88521	10.64	44.99	32.73	2.223	8.5802
2000	34.9	230.1	303.7	24	17.613	12.44	21.97908	4.434	45.69	33.93	2.4592	8.874
2000	34.8	222	299.7	24	17.4933	12.48	21.70586	4.269	45.52	33.91	2.457	8.877
2000	34.7	210.7	298.8	24	17.3836	12.22	21.6064	3.252	45.33	33.74	2.4458	8.8334
2000	34.6	200	299.7	24	17.244	11.83	21.61359	0.6569	45	33.63	2.438	8.7981
2000	34.4	189.2	300.2	24	17.1244	11.73	21.41047	-3.096	44.54	33.39	2.4206	8.7338
2000	36	232	278	24	16.9848	12.06	22.55147	3.044	44.6	34.19	2.4637	8.9566
2000	35.8	221.9	268.4	24	17.0247	12.2	22.83168	2.248	45.06	34.76	2.4894	9.1125
2000	35.4	209.4	269.3	24	17.0845	12.03	22.6034	3.188	45.09	34.39	2.441	9.0267
2000	35.2	199.9	257.7	24	17.1742	11.99	23.08572	0.5741	45.16	34.58	2.4441	9.0477
2000	35	187.6	275.3	24	17.254	11.83	22.77196	-1.035	45.1	34.36	2.432	9.0173

Appendix C: Matlab Miniature Cooling System Code

OPTIMISER

```
clc;clear


lower_bound=[20/1000 20/1000 2/1000 2/1000 1]
upper_bound=[40/1000 40/1000 4/1000 4/1000 3]
yy= fmincon(@mainprogram,xo,[],[],[],[],lower_bound,upper_bound)
```

MAINPROGRAM

```
function optimiziation=mainprogram(x)
L_evap=3;
D_coil_cond=x(1);
D_coil_evap=x(2);
di_cond=x(3);
di_evap=x(4);
Area_ratio=x(5);
design=[L_evap,D_coil_cond,D_coil_evap,di_cond,di_evap,Area_ratio]
media='r134a';
Vs=2/1000/1000;
RPM=2000;
superheat=10;
subcool=4;
mw_gc=5/1000;
mw_evap=3/1000;
tw_cond_in=15+273.15;
tw_evap_in=15+273.15;
di_annulus_cond=50/1000;
%D_coil_cond=20/1000
pitch_cond=7/1000;
%di_cond=3/1000
do_cond=di_cond+2/1000;
k_wall_cond=340;
di_annulus_evap=50/1000;
%D_coil_evap=20/1000
pitch_evap=7/1000;
%di_evap=3/1000
do_evap=di_evap+2/1000;
k_wall_evap=340;
A_evap=3.14*L_evap*di_evap;
A_cond=A_evap*Area_ratio;
L_cond=A_cond/(3.14*di_cond);
%xxo=[P_disP P_ref_evap_sup P_suc l_cond_sub l_cond_sup l_evap_sup  quality_evap_in]
xxo= [5.95*100 2*100 1.78*100 0.1 0.1 0.1 0.3];%initial guess of refrigeration cycle
variables
sol_vector=fsolve(@solver,xxo,[],media,Vs,RPM,superheat,subcool,mw_gc,mw_evap,
tw_cond_in,tw_evap_in,di_annulus_cond,D_coil_cond,pitch_cond,do_cond,k_wall_co
nd,di_cond,L_cond,di_annulus_evap,D_coil_evap,pitch_evap,do_evap,k_wall_evap,d
i_evap,L_evap)
load Q_evap;
load Cop_c;
optimiziation=-1*Cop_c
return
```

SOLVER

```
function
y=solver(zz,media,Vs,RPM,superheat,subcool,mw_gc,mw_evap,tw_cond_in,tw_evap_in
,di_annulus_cond,D_coil_cond,pitch_cond,do_cond,k_wall_cond,di_cond,L_cond,di_
annulus_evap,D_coil_evap,pitch_evap,do_evap,k_wall_evap,di_evap,L_evap)
P_dis=zz(1);
PP_ref_evap_sup=zz(2);
P_suc=zz(3);
l_cond_sub=zz(4);
l_cond_sup=zz(5);
l_evap_sup=zz(6);
quality_evap_in=zz(7);
%y_guess=zz
%save y_guess
[Q_evap,Cop_c,error]=heatpump_function(media,Vs,RPM,superheat,subcool,mw_gc,mw
_evap,tw_cond_in,tw_evap_in,di_annulus_cond,D_coil_cond,pitch_cond,do_cond,k_w
all_cond,di_cond,L_cond,di_annulus_evap,D_coil_evap,pitch_evap,do_evap,k_wall_
evap,di_evap,L_evap,P_suc,P_dis,PP_ref_evap_sup,l_cond_sub,l_cond_sup,l_evap_s
up,quality_evap_in)
save Q_evap;
save Cop_c;
y=error';
return
```

HEATPUMP_FUNCTION

```
function
[Q_evap,Cop_c,error]=heatpump_function(media,Vs,RPM,superheat,subcool,mw_gc,mw
_evap,tw_cond_in,tw_evap_in,di_annulus_cond,D_coil_cond,pitch_cond,do_cond,k_w
all_cond,di_cond,L_cond,di_annulus_evap,D_coil_evap,pitch_evap,do_evap,k_wall_
evap,di_evap,L_evap,P_suc,P_dis,PP_ref_evap_sup,l_cond_sub,l_cond_sup,l_evap_s
up,quality_evap_in)
%[Q_evap,Cop_c,error]=heatpump_function('r134a',2/1000/1000,2000,10,4,5/1000,3
/1000,16+273.15,16+273.15,50/1000,30/1000,7/1000,4/1000,340,3/1000,1.5,50/1000
,30/1000,7/1000,4/1000,340,3/1000,1,3*10^5,6*10^5,3*10^5,0.1,0.1,0.1,0.1)
%{Surface Area Calculations}
A_evap_actual=pi*di_evap*L_evap;
A_cond_actual=pi*di_cond*L_cond;
T_evap_sup=refpropm('T','P',PP_ref_evap_sup,'Q',1,media);
T_suc=T_evap_sup+superheat ;
[m_ref,W_comp,h_dis,h_ref_evap_out,T_dis]=compressor(media,RPM,Vs,P_suc,P_dis,T_suc);
h_ref_cond_in=refpropm('H','T',T_dis, 'P',P_dis,media);
dp_ref_cond_sup=dp_singlephase_function('sup',media,l_cond_sup,m_ref,D_coil_co
nd,di_cond,P_dis,h_ref_cond_in);
P_ref_cond_sup=P_dis-dp_ref_cond_sup;
T_cond_sp=refpropm('T','P',P_ref_cond_sup,'Q',1,media);
h_ref_cond_sup=refpropm('H','P',P_ref_cond_sup,'Q',1,media);
l_evap=A_evap_actual/(pi*di_evap);
l_cond=A_cond_actual/(pi*di_cond);
l_cond_tp=l_cond-l_cond_sub-l_cond_sup;
dp_ref_cond_tp=dp_tp_function(media,l_cond_tp,m_ref,di_cond,P_ref_cond_sup,D_c
oil_cond,0.00001);
P_ref_cond_sub=P_ref_cond_sup-dp_ref_cond_tp;
h_ref_cond_sub=refpropm('H','P',P_ref_cond_sub,'Q',0,media);
T_cond_sub=refpropm('T','P',P_ref_cond_sub,'Q',0,media);
%{condenser routine}
T_ref_cond_out=(T_cond_sub-subcool);
%{state points}
dp_ref_cond_sub=dp_singlephase_function('sub',media,l_cond_sub,m_ref,D_coil_co
nd,di_cond,P_ref_cond_sub,h_ref_cond_sub);
P_ref_cond_out=P_ref_cond_sub-dp_ref_cond_sub;
h_ref_cond_out=refpropm('H','T',T_ref_cond_out,'P',P_ref_cond_out,media);
%{evaporator routine}
```

```
dp_ref_evap_sup=dp_singlephase_function('sup',media,l_evap_sup,m_ref,D_coil_ev
ap,di_evap,P_suc,h_ref_evap_out);
P_ref_evap_sup=P_suc+dp_ref_evap_sup;
h_ref_evap_sup=refpropm('H','P',P_ref_evap_sup,'Q',1,media);
l_evap_tp=l_evap-l_evap_sup;
dp_ref_evap_tp=dp_tp_function(media,l_evap_tp,m_ref,di_evap,P_ref_evap_sup,D_c
oil_evap,quality_evap_in);
P_evap_in=P_ref_evap_sup+dp_ref_evap_tp;
h_ref_evap_in=h_ref_cond_out;
quality_evap_inx=refpropm('Q','P',P_evap_in,'H',h_ref_evap_in,media);
T_evap_in=refpropm('T','P',P_evap_in,'H',h_ref_evap_in,media);
%{Condenser equations}
Q_cond_sup=m_ref*(h_ref_cond_in-h_ref_cond_sup);
Q_cond_tp=m_ref*(h_ref_cond_sup-h_ref_cond_sub);
Q_cond_sub=m_ref*(h_ref_cond_sub-h_ref_cond_out);
tw_cond_sub=Q_cond_sub/(mw_gc*4180)+tw_cond_in;
tw_cond_sup=Q_cond_tp/(mw_gc*4180)+tw_cond_sub;
tw_cond_out=Q_cond_sup/(mw_gc*4180)+tw_cond_sup;
dT_log_cond_sup=((T_dis-tw_cond_out)-(T_cond_sp-tw_cond_sup))/log(((T_dis-
tw_cond_out)/(T_cond_sp-tw_cond_sup)));
dT_log_cond_tp=((T_cond_sp-tw_cond_sup)-(T_cond_sub-
tw_cond_sub))/log(((T_cond_sp-tw_cond_sup)/(T_cond_sub-tw_cond_sub)));
dT_log_cond_sub=((T_cond_sub-tw_cond_sub)-(T_ref_cond_out-
tw_cond_in))/log(((T_cond_sub-tw_cond_sub)/(T_ref_cond_out-tw_cond_in)));
%{evaporator equations}
Q_evap_sup=m_ref*(h_ref_evap_out-h_ref_evap_sup);
Q_evap_tp=m_ref*(h_ref_evap_sup-h_ref_evap_in);
tw_evap_sup=tw_evap_in-Q_evap_sup/(mw_evap*4180);
tw_evap_out=tw_evap_sup-Q_evap_tp/(mw_evap*4180);
dT_log_evap_sup=((tw_evap_in-T_suc)-(tw_evap_sup-T_evap_sup))/log((tw_evap_in-
T_suc)/(tw_evap_sup-T_evap_sup));
dT_log_evap_tp=((tw_evap_sup-T_evap_sup)-(tw_evap_out-
T_evap_in))/log((tw_evap_sup-T_evap_sup)/(tw_evap_out-T_evap_in));
%{Single Phase Regions}
%{Overall Heat transfer Coefficient in superheated condenser region}
tw_avg_cond_sup=(tw_cond_out+tw_cond_sup)/2;
T_ref_avg_cond_sup=(T_dis+T_cond_sp)/2;
U_cond_sup=U_singlephase_function('water',media,P_dis,T_ref_avg_cond_sup,mw_gc
,tw_avg_cond_sup,di_annulus_cond,D_coil_cond,pitch_cond,do_cond,di_cond,k_wall
_cond,m_ref);
%{Overall Heat transfer Coefficient in subcooled condenser region}
tw_avg_cond_sub=(tw_cond_in+tw_cond_sub)/2;
T_ref_avg_cond_sub=(T_ref_cond_out+T_cond_sub)/2;
U_cond_sub=U_singlephase_function('water',media,P_ref_cond_sub,T_ref_avg_cond_
sub,mw_gc,tw_avg_cond_sub,di_annulus_cond,D_coil_cond,pitch_cond,do_cond,di_co
nd,k_wall_cond,m_ref);
%{Overall Heat transfer Coefficient in superheated evaporator}
tw_avg_evap_sup=(tw_evap_in+tw_evap_sup)/2;
T_ref_avg_evap_sup=(T_suc+T_evap_sup)/2;
U_evap_sup=U_singlephase_function('water',media,P_suc,T_ref_avg_evap_sup,mw_ev
ap,tw_avg_evap_sup,di_annulus_evap,D_coil_evap,pitch_evap,do_evap,di_evap,k_wa
ll_evap,m_ref);
%{Two-phase Regions}
%{Overall Heat transfer Coefficient in two-phase evaporator Region}
T_ref_avg_evap_tp=(T_evap_sup+T_evap_in)/2;
U_evap_tp=U_tp_function('evap','water',media,P_ref_evap_sup,T_ref_avg_evap_tp,
mw_evap,tw_evap_sup,tw_evap_out,di_annulus_evap,D_coil_evap,pitch_evap,do_evap
,di_evap,k_wall_evap,m_ref);
%{Overall Heat transfer Coefficient in two-phase condenser Region}
T_ref_avg_cond_tp=(T_cond_sub+T_cond_sp)/2;
U_cond_tp=U_tp_function('cond','water',media,P_ref_cond_sup,T_ref_avg_cond_tp,
mw_gc,tw_cond_sub,tw_cond_sup,di_annulus_cond,D_coil_cond,pitch_cond,do_cond,d
i_cond,k_wall_cond,m_ref);
%{Condenser calculated areas}
A_cond_sup=(Q_cond_sup)/(U_cond_sup*dT_log_cond_sup);
l_cond_supx=A_cond_sup/(pi*di_cond);
A_cond_tp=Q_cond_tp/(U_cond_tp*dT_log_cond_tp);
l_cond_tpx=A_cond_tp/(pi*di_cond);
```

```
A_cond_sub=Q_cond_sub/(U_cond_sub*dT_log_cond_sub);
l_cond_subx=A_cond_sub/(pi*di_cond);
%{evaporator calculated areas}
A_evap_sup=(Q_evap_sup)/(U_evap_sup*dT_log_evap_sup);
l_evap_supx=A_evap_sup/(pi*di_evap);
A_evap_tp=Q_cond_tp/(U_evap_tp*dT_log_evap_tp);
l_evap_tpx=A_evap_tp/(pi*di_evap);
Q_evap=Q_evap_sup+Q_evap_tp;
Q_cond=Q_cond_sup+Q_cond_tp+Q_cond_sub;
Cop_c=Q_evap/W_comp;
%{errors}
error(1)=quality_evap_inx-quality_evap_in;  %{expansion valve}
error(2)=l_cond_supx-l_cond_sup;
error(3)=l_cond_tpx-l_cond_tp;
error(4)=l_cond_subx-l_cond_sub;
error(5)=l_evap_supx-l_evap_sup;
error(6)=l_evap_tpx-l_evap_tp;
error(7)=P_ref_evap_sup-PP_ref_evap_sup;

return
```

COMPRESSOR

```
function [m_ref, W_comp,h_dis,h_suc,T_dis]=compressor(media,RPM,Vs,P_suc,P_dis,T_suc)
%
[m_ref,W_comp,h_dis,T_dis]=compressor('r134a',2000,2/1000/1000,3*10^5,6*10^5,-
10+273)
%Compressor Model
%RPM=Revolution per minute
%Input parameters
%Vs=stroke volume
%Pressure Ratio
PR=P_dis/P_suc;
%volumetric efficiency
eta_vol=0.63;
%Density at compressor suction
rho(1)=refpropm('D','T',T_suc,'P',P_suc,media);
%mass flow rate
m_ref=rho(1)*eta_vol*Vs*RPM/60;
%discharge enthalpy
h(1)=refpropm('H','T',T_suc,'P',P_suc,media);
h_suc=h(1);
n_polytropic=1.0246 ;  % from fitting the data
specific_volume_suc=1/rho(1);
%Heat balance on compressor first law
W_polytropic=m_ref*(n_polytropic/(n_polytropic-
1))*(P_suc*10^3)*specific_volume_suc*((P_dis/P_suc)^((n_polytropic-
1)/n_polytropic)-1) ;
heat_fraction=0.2;
h(2)=(W_polytropic-heat_fraction*W_polytropic+m_ref*h(1))/m_ref;
eta_overall=0.36;
T_dis=refpropm('T','P',P_dis','H',h(2),media);
h_dis=h(2);
%compressor power
W_comp=W_polytropic/eta_overall;
return
```

DP_SINGLEPHASE_FUNCTION

```
function
[dp_singlephase]=dp_singlephase_function(zone,media,L_segment,m_ref,D_coil,di,
P_ref,h_ref)
G=m_ref/(pi*di^2/4);
if (zone =='sub') %subcool
mu_ref=refpropm('V','P',P_ref,'Q',0,media) ;    %{refrigerant dynamic
viscosity}
rho_ref=refpropm('D','P',P_ref,'Q',0,media) ;     %{refrigerant density}
else
mu_ref=refpropm('V','P',P_ref,'H',h_ref,media);     %{refrigerant dynamic
viscosity}
rho_ref=refpropm('D','P',P_ref,'H',h_ref,media);      %{refrigerant density}
end
Re_ref=G*di/mu_ref;
%{Blasius equation}
if (Re_ref<=2*10^4)
friction_straight=0.316*Re_ref^(-0.25);
end
if (Re_ref>2*10^4)
friction_straight=0.184*Re_ref^(-0.2);
end
transition=2100*(1+12*(di/D_coil)^0.5);
if (Re_ref>transition)
friction=(1.216*Re_ref^(-0.25)+0.116*(di/D_coil)^0.5 ); %{ turbulent friction
factor =Ito correlation}
end
%{laminar region}
if (Re_ref<=transition)
friction_straight=64/Re_ref;
pp=1-0.644*(di/D_coil)^0.312;
friction=friction_straight*(1+0.14*(di/D_coil)^0.97*Re_ref)^pp;   %{Schmidt
Correlation}
end
dp_singlephase=(G^2/(2*rho_ref))*(friction*L_segment/di)/1000;  % pressure
drop in kpa
return
```

DP_TP_FUNCTION

```
function
[dp_tp]=dp_tp_function(media,L_segment,m_ref,di,P_ref,D_coil,quality_mix)
index=0;
N_step=20;
quality_v=0.999;
dquality=(quality_v-quality_mix)/N_step;
quality=quality_v;
dp_tp_quality=0;
while (index~= N_step)
G=m_ref/(pi*di^2/4);
%{liquid only friction factor}
mu_ref_l=refpropm('V','P',P_ref,'Q',0,media) ;    %{refrigerant dynamic
viscosity}
rho_ref_l=refpropm('D','P',P_ref,'Q',0,media) ;     %{refrigerant density}
Re_ref_l=G*(1-quality)*di/mu_ref_l;
transition=2100*(1+12*(di/D_coil)^0.5);
if (Re_ref_l>transition)
friction_l=(1.216*Re_ref_l^(-0.25)+0.116*(di/D_coil)^0.5 )/4 ;  %{ turbulent
fanning factor =Ito correlation}
end
if (Re_ref_l<=transition)
friction_straight=64/Re_ref_l;
pp=1-0.644*(di/D_coil)^0.312;
friction_l=friction_straight/4*(1+0.14*(di/D_coil)^0.97*Re_ref_l)^pp;
%{Schmidt Correlation}  {Fanning factor }
```

```
end
%{gas only friction factor}
mu_ref_g=refpropm('V','P',P_ref,'Q',1,media);     %{refrigerant dynamic
viscosity}
rho_ref_g=refpropm('D','P',P_ref,'Q',1,media) ;    %{refrigerant density}
Re_ref_g=G*quality*di/mu_ref_g;
%{Guo Evaporation pressure drop Model}
phi_l=1+(4.25-2.55*quality^1.5)*G^0.34;
dp_l=2*friction_l*(G*(1-quality))^2/(di*rho_ref_l)/1000; % pressure drop in
kpa    %{liquid only pressure drop per unit length}
dp_tp_quality=dquality*(phi_l*dp_l)+dp_tp_quality ;       %{integration of the
two phase pressure drop per unit quality}
quality=quality-dquality;
index=index+1;
end    % end while loop
dp_tp=(dp_tp_quality*L_segment)/(quality_v-quality_mix);
end
```

U_SINGLEPHASE_FUNCTION

```
function
[U_singlephase]=U_singlephase_function(secondary_fluid,media,P_ref,T_ref_avg,m
w_gc,Tw_avg,di_annulus,D_coil,pitch,do,di,k_wall,m_ref)
%calculations of U_single phase
%water side heat transfer
%di_annulus=inner shell diameter
gamma=pitch/(pi*D_coil) ;  %{dimensionless pitch}
d_h=(di_annulus^2-D_coil*pi*do^2*gamma^(-1))/(di_annulus+D_coil*pi*do*gamma^(-
1));
k_w=refpropm('L','T',Tw_avg,'Q',0,secondary_fluid);    %{water thermal
conductivity}
mu_w=refpropm('V','T',Tw_avg,'Q',0,secondary_fluid);     %{water dynamic
viscosity}
C_w=refpropm('C','T',Tw_avg,'Q',0,secondary_fluid) ;
Prand=C_w*mu_w/k_w;   %{Prandtl number}
A_flow=pi/4*(di_annulus^2-((D_coil+do)^2-(D_coil-do)^2));
Re_w=(mw_gc/A_flow)*d_h/mu_w;
%{water side is in annulus}
Nu=1.25*19.64*Re_w^0.513*Prand^0.129*gamma^0.938;
alpha_w=Nu*k_w/d_h ;   %{water heat transfer coefficient at each segment}
%{Refrigerant side calculations}
d_h=di  ;    %{hydraulic diameter}
rho_ref_b=refpropm('D','T',T_ref_avg,'P',P_ref,media) ;     %{refrigerant
density}
k_ref_b=refpropm('L','T',T_ref_avg,'P',P_ref,media) ;   %{refrigerant  thermal
conductivity}
mu_ref_b=refpropm('V','T',T_ref_avg,'P',P_ref,media)  ;   %{refrigerant
dynamic viscosity}
CP_ref_b=refpropm('C','T',T_ref_avg,'P',P_ref,media) ; % heat capacity
Prand_ref=CP_ref_b*mu_ref_b/k_ref_b;  %{Prandtl number}
Re_ref=4*m_ref/(pi*mu_ref_b*d_h);
%{Gienlinski equation}
f=(0.79*log(Re_ref)-1.64)^(-2) ;  %{friction factor}
%{Nusselt number at the bulk temperature}
Nu_ref_straight=(f/8)*(Re_ref-
1000)*Prand_ref/(1.07+12.7*(f/8)^0.5*(Prand_ref^(2/3)-1));
if((20000<Re_ref) & (Re_ref<1.5*10^5));
Nu_ref=Nu_ref_straight*(1+3.6*(di/D_coil)^0.8*(1-(di/D_coil)))  ;  %{schmidt's
correlation}
end
if((1500<Re_ref) & (Re_ref<20000))
Nu_ref=Nu_ref_straight*(1+3.4*(di/D_coil)) ;       %{Pratt's Corrletion}
end
if (Re_ref<1500)
%{Manlapaz and churchill correllation= heat exchanger selection, rating
(kakac)}
```

```
D_e_ref= Re_ref*(di/D_coil)^(1/2)    ;               %{refrigerant Dean
Number}
x3=(1+1342/(D_e_ref^2*Prand_ref))^2;
x4=1+1.15/Prand_ref       ;
Nu_ref=((4.364+4.636/x3)^3+1.816*(D_e_ref/x4)^(3/2))^(1/3);
alpha_ref=(Nu_ref*k_ref_b)/d_h;
%{overall heat transfer coefficient}
U_singlephase=1/((di/(alpha_w*do))+di*log(do/di)/(2*k_wall)+1/alpha_ref);
flux=U_singlephase*abs((T_ref_avg-Tw_avg));
return
```

U_TP_FUNCTION

```
function
[U_tp]=U_tp_function(Heat_exchanger,secondary_fluid,media,P_ref,T_ref,mw,tw_in
,tw_out,di_annulus,D_coil,pitch,do,di,k_wall,m_ref)
N_step=20;
tw=max(tw_in,tw_out);
quality=0.999;
dt_w=abs(tw_in-tw_out)/N_step;
index=1 ; %{local index through heat exchanger}
%{begin discretization of two phase region}
U_avg=0; %{variable for storing sum of overall heat transfer coefficient}
h_g=refpropm('H','P',P_ref,'Q',1,media) ;
h_f=refpropm('H','P',P_ref,'Q',0,media) ;
h_fg=h_g-h_f;
while ((tw-min(tw_in,tw_out))>0.000001)   % checking the end of heat exchnager
%{di_annulus=inner shell diameter}
gamma=pitch/(pi*D_coil) ;  %{dimensionless pitch}
d_h=(di_annulus^2-D_coil*pi*do^2*gamma^(-1))/(di_annulus+D_coil*pi*do*gamma^(-
1));
k_w=refpropm('L','T',tw,'Q',0,secondary_fluid) ; %{water thermal conductivity}
mu_w=refpropm('V','T',tw,'Q',0,secondary_fluid) ;    %{water dynamic
viscosity}
c_w=refpropm('C','T',tw,'Q',0,secondary_fluid) ;
Prand=c_w*mu_w/k_w ; %{Prandtl number}
A_flow=pi/4*(di_annulus^2-((D_coil+do)^2-(D_coil-do)^2));
Re_w=(mw/A_flow)*d_h/mu_w;
%{water side is in annulus}
Nu=1.25*19.64*Re_w^0.513*Prand^0.129*gamma^0.938;
alpha_w=Nu*k_w/d_h  ;  %{water heat transfer coefficient at each segment}
A_c=pi/4*di^2;
G=m_ref/A_c;    %{mass velocity}
flux=5000 ; %{initial guess for the flux}
error_flux=1000;
while (error_flux>0.00001)
if (Heat_exchanger=='cond')
T_ref_sat=refpropm('T','P',P_ref,'Q',1,media);
dt_cond=T_ref_sat-tw;
alpha_ref=alpha_cond_function(media,flux,P_ref,G,quality,di,D_coil,dt_cond);
else
    %evaporator
alpha_ref=alpha_evap_function(media,flux,P_ref,G,quality,di,D_coil,pitch);
end % endif
%{overall heat transfer coefficient}
U_tp=1/((di/(alpha_w*do))+di*log(do/di)/(2*k_wall)+1/alpha_ref);
%{heat flux from refrigerant to water}
if (Heat_exchanger=='cond')
flux_cc=U_tp*(T_ref-tw);
else
 %evaporator
    flux_cc=U_tp*(tw-T_ref);
end   %endif
error_flux=abs((flux_cc-flux)/flux);
flux=(flux_cc+flux)/2;
end  % end the inner while loop
U_avg=U_tp+U_avg;
```

```
Q_element=mw*4180*dt_w ; %{heat load perelement}
tw=tw-dt_w;
quality=quality-Q_element/(m_ref*h_fg) ;
end   % end the upper while loop

U_tp=U_avg/N_step; % average overall heat transfer coefficient
return
```

ALPHA_COND_FUNCTION

```
function
[alpha_cond]=alpha_cond_function(media,flux,P_ref,G,quality,di,D_coil,dt_cond)
%[alpha_cond]=alpha_cond_function('r134a',100,10*10^5,300,0.1,3/1000,30/1000,3
)
%Mosaad and Al-Hajeri correlation
T_ref=refpropm('T','P',P_ref,'Q',0,media);
k_l=refpropm('L','P',P_ref,'Q',0,media);
roh_l=refpropm('D','P',P_ref,'Q',0,media);
roh_v=refpropm('D','P',P_ref,'Q',1,media);
mu_l=refpropm('V','P',P_ref,'Q',0,media);
mu_v=refpropm('V','P',P_ref,'Q',1,media);
Cp_l=refpropm('C','P',P_ref,'Q',0,media);
Prand_l=Cp_l*mu_l/k_l;
T_ref=T_ref-273.15 ; % converting the temperature into celsius
Re_star=G*((1-quality)+quality*sqrt(roh_l/roh_v))*di/mu_l;
alpha_cond=6.39*k_l/di*Prand_l^(1/3)*Re_star^0.4*(1-0.85*(
dt_cond/T_ref)^0.9);
return
```

ALPHA_EVAP_FUNCTION

```
function
[alpha_evap]=alpha_evap_function(media,flux,P_ref,G,quality,di,D_coil,coil_pit
ch)
%[alpha_evap]=alpha_evap_function('r134a',100,12*10^5,300,0.3,3/1000,30/1000,7
/1000)
%Dean Number
mu_l=refpropm('V','P',P_ref,'Q',0,media);
roh_l=refpropm('D','P',P_ref,'Q',0,media);
Re_l=G*(1-quality)*di/mu_l;
cp_l=refpropm('C','P',P_ref,'Q',0,media);
mu_v=refpropm('V','P',P_ref,'Q',1,media);
roh_v=refpropm('D','P',P_ref,'Q',1,media);
k_l=refpropm('L','P',P_ref,'Q',0,media);
Prand_l=cp_l*mu_l/k_l;
T_ref=refpropm('T','P',P_ref,'Q',0,media);
sigma_l=refpropm('I','T',T_ref,'Q',0,media);
Re_lo=G*di/mu_l;
%Martinelli Number
X_tt=((1-quality)/quality)^0.9*(roh_v/roh_l)^0.5*(mu_l/mu_v)^0.1;
h_l=refpropm('H','P',P_ref,'Q',0,media);
h_v=refpropm('H','P',P_ref,'Q',1,media);
h_fg=h_v-h_l  ;  %latent heat of vaporization
dtwallx=0.2;
error=1000;
while (abs(error)>0.001)
ja_inv=h_fg/(cp_l*dtwallx);
we_lo_inv=((roh_l*sigma_l)/(G^2*di)) ;
He_inv=(Re_lo*(di/D_coil)^0.5/(1+(coil_pitch/(3.14*D_coil))^2)^(0.5))^(-1);
j1=0.054729;
j2=-0.556109;
j3=-0.24755185;
j4=0.22287;
j5=-0.17954258;
```

```
Nu_tp=(j1*ja_inv^j2*X_tt^j3*we_lo_inv^j4*He_inv^j5)*Re_lo*Prand_l;
alpha_evap=Nu_tp*k_l/di;
dtwall=flux/alpha_evap;
error=dtwallx-dtwall;
dtwallx=(dtwall+dtwallx)/2;
end  % end while loop
return
```

Appendix F: Fluent User Defined Code (UDF)

```
/**************************************************************/
/* User-Defined Function for temperature-dependent density for Al2O3 nanofluid
*/
/* Mechanical Engineering Department*/
/* University of Birmingham*/
/*Author: Eng Ahmed Elsayed*/
/**************************************************************/
#include "udf.h"
#define density_nano_particle 3920
#define v_fraction 3*pow(10,-2)

DEFINE_PROPERTY(user_density, cell, thread)
{
float temp,density_w,density_nf;
temp = C_T(cell, thread);
{
/* Density of water as a function temperature */
density_w=281.377 + 6.35193*temp- 0.0176103*temp*temp +
0.0000146096*temp*temp*temp;
density_nf= density_w * (1-v_fraction) + v_fraction*density_nano_particle;
}
return density_nf;
}
/**************************************************************/
/* User-Defined Function for temperature-dependent viscosity for Al2O3
nanofluid */
/**************************************************************/
DEFINE_PROPERTY(user_viscosity, cell, thread)
{
float temp,viscosity_w,viscosity_nf;
temp = C_T(cell, thread);
{

/* viscosity of water as a function temperature */
viscosity_w=0.0968422- 0.00082153*temp + 0.00000234521*temp*temp -
0.00000000224412*temp*temp*temp;
viscosity_nf= viscosity_w *exp(4.91*v_fraction/(0.2092-v_fraction));
}
return viscosity_nf;
}
/**************************************************************/
/* User-Defined Function for temperature-dependent conductivity for Al2O3
nanofluid */
/**************************************************************/
DEFINE_PROPERTY(user_conductivity, cell, thread)
{
float temp,coductivity_w,coductivity_nf;
temp = C_T(cell, thread);
{
/* conductivity of water as a function temperature */
coductivity_w=-1.05642 + 0.0101133*temp- 0.0000177274*temp*temp +
0.00000000799488*temp*temp*temp;
coductivity_nf=coductivity_w*(1+4.5503*v_fraction);
}
return coductivity_nf;
}
```

Appendix G: EES Code for Boiling Heat Transfer Calculations

```
procedure boiling(index,r$,k_wall,v_ref,volt_evap,current_evap,p_suc,
p_dis,t_before_throttle,l_evap,do,di,d_coil,twall_out_exp1,twall_out_exp2,twal
l_out_exp3,twall_out_exp4,twall_out_exp5,twall_out_exp6,twall_out_exp7,twall_o
ut_exp8,twall_out_exp9,twall_out_exp10,volt_preheat,current_preheat,tevap_in,t
evap_out:q_evap,alpha_ref_exp,twall_exp,latentload,q_preheat,dtmetal)
t_cond=t_sat(r134a,p=p_dis)
roh_l=density(r$,t=t_before_throttle, p=p_dis)
m_ref=roh_l*v_ref/(60*10^6)
q_evap=volt_evap*current_evap
q_preheat=volt_preheat*current_preheat
twall_out_exp=(twall_out_exp1+twall_out_exp2+twall_out_exp3+twall_out_exp4+twa
ll_out_exp5+twall_out_exp6+twall_out_exp7+twall_out_exp8+twall_out_exp9+twall_
out_exp10)/10
flux_tp_exp=q_evap/(pi*di*l_evap)
coil_metal_volume=pi/4*(do^2-di^2)*l_evap
heat_generation=q_evap/coil_metal_volume
{twall_exp = inner  wall temperature  form thermocouples}
twall_exp=twall_out_exp+(heat_generation/k_wall)*(  ((do/2)^2-( di/2)^2)/4-
(do/2)^2/2*ln(do/di))
t_ref_exp=(tevap_in+tevap_out)/2
h_g=enthalpy(r$,t=t_ref_exp,x=1)
h_f=enthalpy(r$,t=t_ref_exp,x=0)
h_fg=h_g-h_f
dtmetal=twall_out_exp_avg-twall_exp
latentload=(m_ref*h_fg)
h_ref_cond_out=enthalpy(r$,p=p_dis, t=t_before_throttle)
h_ref_exp[1]=h_ref_cond_out {throttling process}
x_ref_preheat=quality(r$,p=p_suc,h=h_ref_exp[1])      {evaporator inlet}
x_ref_exp[1]=x_ref_preheat+q_preheat/(m_ref*h_fg)
x_ref_out=x_ref_exp[1]+q_evap/(m_ref*h_fg)
x_ref_mean=(x_ref_out+x_ref_exp[1])/2
alpha_ref_exp=flux_tp_exp/(twall_exp-t_ref_exp)       {twall =wall temperature at refrigerant
side}
number=index
g_ref=m_ref/(pi*di^2/4)
t_ref_exp=(tevap_in+tevap_out)/2
p_ref_exp=p_sat(r134a,t=t_ref_exp)
lookup('heat transfer',number,1)=m_ref
lookup('heat transfer',number,2)=x_ref_out
lookup('heat transfer',number,3)=q_evap
lookup('heat transfer',number,4)=x_ref_mean
lookup('heat transfer',number,5)=g_ref
lookup('heat transfer',number,6)=p_ref_exp
lookup('heat transfer',number,7)= alpha_ref_exp
lookup('heat transfer',number,8)=x_ref_exp[1]
lookup('heat transfer',number,9)=twall_exp
lookup('heat transfer',number,10)=flux_tp_exp
end

Call  boiling(index,r$,k_wall,v_ref,volt_evap,current_evap,p_suc,
p_dis,t_before_throttle,l_evap,do,di,d_coil,twall_out_exp1,twall_out_exp2,twal
l_out_exp3,twall_out_exp4,twall_out_exp5,twall_out_exp6,twall_out_exp7,twall_o
ut_exp8,twall_out_exp9,twall_out_exp10,volt_preheat,current_preheat,tevap_in,t
evap_out:q_evap,alpha_ref_exp,twall_exp,latentload,q_preheat,dtmetal)
flux=q_evap/(pi*di*l_evap)
dtwall=flux/(alpha_ref_exp)
```

Appendix H: Flow Boiling Experimental Measurements

Coil B data

P_{suc} [bar]	P_{dis} [bar]	$T_{trottle}$ [°C]	$Tcond_{out}$ [°C]	Twall1 [°C]	Twall2 [°C]	Twall3 [°C]	Twall4 [°C]	Twall5 [°C]	Twall6 [°C]	Twall7 [°C]	Twall8 [°C]	Twall9 [°C]	Twall10 [°C]	V ref [ml/min]	Ievap	Vevap	Ipreheat	Vpreheat	$Tevap_{in}$	$Tevap_{out}$
6.231	12.239	40.52	48.05	25.89	24.78	24.61	23.35	24.23	25.4	26.24	27.17	27.67	27.02	30.43	9.2	1.93	0	0	23.47	22.3
6.269	12.3886	41.05	48.73	26.54	25.18	24.94	23.47	23.95	25.2	26.57	27.9	28.05	27.24	30.43	9.2	1.93	2	1.13	23.64	22.18
6.282	12.3579	41.12	48.63	26.29	24.96	24.68	23.27	23.87	25.14	26.48	27.74	27.95	27.17	30.43	9.2	1.93	4	2.29	23.84	22.27
6.224	12.1936	40.65	47.87	25.52	24.67	24.53	23.01	23.65	24.58	25.42	26.47	27.52	26.87	30.43	9.2	1.93	5	2.9	23.79	22.3
6.255	12.1801	40.62	48.03	25.86	24.68	24.29	22.6	23.29	24.43	25.56	26.87	27.55	26.71	30.43	9.2	1.93	6	3.54	23.67	22.01
6.208	12.0566	40.29	47.73	25.42	24.19	23.7	21.97	22.73	23.91	25.05	26.39	27.08	26.21	30.43	9.2	1.93	7	4.15	23.34	21.57
6.251	12.0805	40.31	47.78	25.39	24.16	23.68	22.04	22.86	24.07	25.21	26.49	27.1	26.23	30.43	9.2	1.95	8	4.7	23.56	21.8
6.213	12.0178	40.13	47.65	25.09	23.73	23.18	21.52	22.29	23.58	24.91	26.23	26.7	25.79	30.43	9.2	1.95	9	5.33	23.28	21.37
6.22	11.8826	39.46	47.12	24.75	23.47	22.91	21.27	22.39	23.7	24.85	25.72	26.69	25.83	30.43	9.2	1.95	10	5.99	23.44	21.51
6.948	11.2998	36.1	44.79	29.37	28.72	28.51	27.1	27.91	28.8	29.53	30.03	31.49	30.92	40	9.19	1.95	0	0	27.39	26.36
7.004	11.4058	36.31	45.06	29.61	28.91	28.72	27.27	28.16	29	29.77	30.29	31.62	31.17	40	9.19	1.95	2	1.15	27.96	26.88
7.023	11.4527	36.44	45.29	29.65	28.94	28.83	27.24	27.86	28.77	29.8	30.39	31.71	31.11	40	9.19	1.95	4	2.32	28.2	26.65
6.995	11.3397	35.92	44.99	29.38	28.66	28.52	26.94	27.56	28.5	29.57	30.19	31.45	30.81	40	9.19	1.95	5	2.94	27.9	26.39
7.019	11.3638	35.73	45.26	29.38	28.61	28.4	26.8	27.53	28.45	29.49	30.16	31.71	30.89	40	9.19	1.95	6	3.55	27.81	26.05
7.075	11.4603	35.56	45.59	29.52	28.76	28.47	26.82	27.58	28.48	29.47	30.1	31.95	31.1	40	9.19	1.95	7	4.2	28.11	26.18
7.089	11.4796	35.32	45.65	29.37	28.64	28.3	26.64	27.41	28.31	29.27	29.91	31.86	31.01	40	9.19	1.95	8	4.83	28.21	26.22
7.083	11.4573	34.82	45.61	29.18	28.42	28.06	26.35	27.16	28.11	29.06	29.69	31.56	30.66	40	9.19	1.95	9	5.47	28.05	26.14
7.076	11.3427	34.29	45.3	28.92	28.15	27.78	26.14	27.06	27.95	28.83	29.41	31.39	30.48	40	9.19	1.95	10	6.17	27.98	25.88
5.937	7.9068	25.1	32.28	24.44	23.62	22.9	21.39	22.74	23.61	24.02	24.63	27.03	26.06	16	9.2	1.95	0	0	21.86	20.48
5.911	7.8767	24.75	32.14	24.24	23.49	22.68	21.28	22.59	23.36	23.75	24.34	26.69	25.77	16	9.2	1.95	2	1.13	21.69	20.31
5.841	7.7824	24.09	31.7	23.85	23.09	22.9	21.45	22.11	22.91	23.78	24.43	26.07	25.19	16	9.2	1.95	4	2.28	21.38	19.93
5.835	7.7754	23.68	31.68	23.49	22.77	22.53	21.13	21.73	22.49	23.29	23.82	25.66	24.74	16	9.2	1.95	6	3.51	21.41	19.93
5.856	7.7441	23.44	31.55	23.07	22.34	21.94	20.55	21.47	22.2	23.04	23.5	25.3	24.3	16	9.2	1.95	7	4.1	21.31	19.88
5.863	7.7523	23.38	31.57	22.79	22.03	21.88	20.42	21.09	21.8	23.07	23.67	25.17	24.28	16	9.2	1.95	8	4.74	21.43	19.98

6.573	8.3133	29.05	33.44	27.36	26.65	26.59	25.58	26.1	26.8	27.66	28.33	29.49	28.86	47	9.18	1.96	0	0	25.08	23.96
6.56	8.2596	28.99	33.22	27.23	26.52	26.51	25.46	25.99	26.84	27.72	28.37	29.35	28.68	47	9.18	1.96	2	1.11	25.14	23.88
6.493	8.4605	29.71	34.17	26.61	25.85	25.94	24.79	25.59	26.62	27.66	28.22	28.82	28.09	47	9.18	1.96	4	2.25	25.07	23.38
6.477	7.9554	26.33	32.28	26.52	25.7	25.74	24.36	25.16	26.31	27.58	28.34	28.48	27.68	47	9.18	1.96	6	3.44	24.74	23.1
6.488	7.8292	26.28	31.66	26.25	25.44	25.45	24.07	25.22	26.39	27.62	28.34	28.34	27.51	47	9.18	1.96	7	4.05	24.7	23
6.436	7.9694	26.49	32.18	25.39	24.88	24.97	23.49	24.8	25.94	27.13	27.72	27.85	27.12	47	9.18	1.96	8	4.68	24.6	22.83
6.446	7.9635	26.26	32.11	25.18	24.83	24.86	23.33	24.86	25.85	26.83	27.36	27.75	27.04	47	9.18	1.96	9	5.33	24.75	22.89
6.471	7.9641	26.11	32.06	25.01	24.79	24.82	23.22	25	25.98	26.91	27.3	27.65	26.97	47	9.18	1.96	10	6.02	24.92	23.01
4.93	9.0345	28.32	37	17.09	16.39	16.06	15.34	16.02	16.74	17.18	17.71	18.66	18.04	16	6.48	1.37	0	0	15.4	14.46
4.883	9.0562	28.45	37.12	16.87	16.1	15.86	15.07	15.67	16.44	17.2	17.86	18.56	17.86	16	6.48	1.37	2	1.08	15.16	14.05
4.851	9.1459	28.12	37.62	16.58	15.64	15.34	14.35	15.42	16.52	17.49	18.14	18.47	17.67	16	6.48	1.37	4	2.18	15.12	13.8
4.916	9.2012	27.88	37.84	16.64	15.67	15.27	14.18	15.61	16.82	17.81	18.46	18.64	17.81	16	6.48	1.37	6	3.35	15.55	14.1
4.776	9.2957	27.87	38.25	15.45	14.53	14.18	13.06	14.8	15.97	16.95	17.53	17.56	16.78	16	6.48	1.37	7	3.93	14.76	13.26
4.813	9.3406	27.66	38.32	15.38	14.54	14.36	13.32	15	15.89	16.94	17.61	17.8	16.91	16	6.48	1.37	8	4.65	14.9	13.26
4.773	9.332	27.36	38.23	15.09	14.29	14.21	13.06	14.85	15.72	17.08	18	17.99	17.06	16	6.48	1.37	9	5.22	14.69	12.92
4.841	9.4638	27.52	38.83	21.63	20.82	25.1	23.92	30.19	31.23	36.17	36.96	40.45	39.5	16	6.48	1.37	10	5.88	15.14	32.35
4.874	8.1632	27.37	33.34	16.69	15.82	15.63	14.72	15.38	16.07	16.87	17.67	18.92	17.9	30.43	6.48	1.37	0	0	15.15	13.52
4.886	8.1291	27.09	33.21	16.65	15.78	15.67	14.81	15.51	16.19	17.06	17.85	18.88	17.87	30.43	6.48	1.37	2	1.08	15.2	13.55
4.901	8.1155	27.06	33.19	16.7	15.73	15.53	14.46	15.39	16.5	17.67	18.43	18.72	17.8	30.43	6.48	1.37	4	2.21	15.43	13.76
4.897	8.0935	26.93	33.01	16.4	15.46	15.15	13.97	15.2	16.35	17.45	18.19	18.36	17.46	30.43	6.48	1.37	6	3.36	15.36	13.67
4.816	8.146	27.02	33.24	15.62	14.74	14.41	13.17	14.7	15.83	16.96	17.66	17.64	16.79	30.43	6.48	1.37	7	3.96	14.89	13.07
4.849	8.177	27.1	33.38	15.7	14.77	14.41	13.07	14.7	15.9	17.1	17.84	17.63	16.75	30.43	6.48	1.37	8	4.58	14.99	13.11
4.915	8.2683	27.25	33.82	16.07	15.1	14.72	13.3	15.28	16.59	17.86	18.63	18.03	17.12	30.43	6.48	1.37	9	5.23	15.47	13.48
4.812	8.234	27.21	33.64	15.31	14.43	14	12.47	14.64	15.94	17.18	17.94	17.22	16.29	30.43	6.48	1.37	10	5.89	14.8	12.73
4.919	8.6627	29.47	35.37	16.85	15.97	15.71	14.59	15.32	16.32	17.38	18.12	18.68	17.85	40	6.48	1.37	0	0	15.48	13.92
4.768	8.6943	29.56	35.48	15.8	14.94	14.66	13.5	14.17	15.17	16.29	17.03	17.49	16.67	40	6.48	1.37	2	1.08	14.5	12.89
4.792	8.6599	29.5	35.27	15.75	14.89	14.6	13.46	14.32	15.36	16.47	17.19	17.49	16.68	40	6.48	1.37	4	2.2	14.77	12.92
4.853	8.672	29.53	35.31	15.86	15.08	14.77	13.55	14.66	15.7	16.76	17.45	17.68	16.88	40	6.48	1.37	6	3.36	15.09	13.24
4.806	8.6318	29.51	35.09	15.33	14.57	14.21	12.82	14.23	15.33	16.42	17.15	17.06	16.22	40	6.48	1.37	8	4.58	14.75	12.61
4.834	8.6104	29.45	34.96	15.29	14.47	14.1	12.8	14.6	15.87	16.93	17.61	17.14	16.34	40	6.48	1.37	9	5.22	15.06	12.79

4.857	8.5984	29.46	34.89	15.29	14.46	14.08	12.76	14.77	16.1	17.17	17.83	17.16	16.38	40	6.48	1.37	10	5.89	15.22	12.77
4.717	8.5702	29.88	34.75	15.41	14.37	14.07	13.02	13.84	15.04	16.17	16.93	17.24	16.46	47	6.48	1.37	0	0	14.26	12.59
4.908	8.5147	29.78	34.55	16.75	15.78	15.47	14.43	14.92	16.06	17.19	17.99	18.3	17.55	47	6.48	1.37	2	1.08	15.46	13.87
4.87	8.5392	29.86	34.75	16.33	15.26	14.89	13.82	14.62	15.88	17.11	17.9	17.96	17.19	47	6.48	1.37	4	2.2	15.36	13.53
4.881	8.5446	29.86	34.64	16.04	15.11	14.76	13.64	14.71	15.88	16.98	17.69	17.77	17	47	6.48	1.37	6	3.37	15.29	13.38
4.819	8.4819	29.51	34.34	15.32	14.43	14.1	12.85	14.35	15.56	16.69	17.41	17.19	16.39	47	6.48	1.37	8	4.57	14.94	12.72
4.791	8.4122	29.22	34.02	15	14.03	13.67	12.44	14.23	15.55	16.72	17.46	16.83	16.05	47	6.48	1.37	9	5.21	14.84	12.46
4.86	8.472	29.4	34.21	15.31	14.51	14.13	12.83	14.77	16.01	17.07	17.78	17.03	16.23	47	6.48	1.37	10	5.88	15.22	12.69
4.918	8.0042	27.23	32.05	18.84	18.8	18.61	18.28	18.14	18.8	18.57	18.9	20.24	20.13	30.4	14.3	2.95	0	0	15.6	13.97
4.83	8.0745	27.57	32.36	18.53	18.01	17.62	17.08	17.14	17.88	17.67	18.1	19.53	19.35	30.4	14.3	2.95	2.04	1.14	15.15	13.19
4.857	8.0255	27.4	32.3	18.26	17.52	16.96	16.26	16.51	17.36	17.26	17.84	19.15	18.95	30.4	14.3	2.95	3.98	2.23	15.43	12.88
4.804	8.0589	27.26	32.5	16.17	15.62	14.86	13.97	14.73	15.86	15.93	16.78	17.7	17.48	30.4	14.3	2.95	5.97	3.41	15.1	11.47
4.804	8.0589	27.26	32.5	16.17	15.62	14.86	13.97	14.73	15.86	15.93	16.78	17.7	17.48	30.4	14.3	2.95	8	4.57	15.1	11.47
4.825	8.0514	27.15	32.55	11.98	11.01	10.1	8.849	11.06	12.51	13.22	14.27	15.25	14.62	30.4	14.3	2.95	9.77	5.74	15.4	8.182
4.721	9.0246	30.51	36.54	16.89	16.01	15.03	13.73	14.33	15.76	16.19	17.25	18.06	17.59	40	14.3	2.95	0	0	14.58	10.82
4.774	9.0469	30.94	36.72	16.92	16.01	15	13.71	14.19	15.61	16.09	17.22	18.05	17.56	40	14.3	2.95	1.98	1.09	14.88	10.85
4.866	9.0541	31.14	36.64	16.51	15.73	14.81	13.48	13.97	15.32	15.68	16.68	17.83	17.4	40	14.3	2.95	4.02	2.25	15.75	10.95
4.817	9.0488	31.05	36.66	13.45	12.23	11.31	9.945	11.14	12.52	12.9	13.98	14.7	14.32	40	14.3	2.95	6.65	3.87	15.35	8.22
4.749	8.7455	30.74	35.32	10.52	9.026	8.024	6.639	8.233	9.681	10.02	11.1	11.55	11.19	40	14.3	2.95	8.08	4.63	14.8	5.251
4.894	8.6995	30.35	35.14	7.169	5.563	4.527	3.052	5.202	6.687	6.914	8.049	8.171	7.815	40	14.3	2.95	9.74	5.74	15.73	2.007
4.815	7.492	25.85	29.84	21.02	20.84	19.42	18.95	18.33	19.16	19.2	20.19	19.3	19.04	16	14.3	2.92	0	0	15.18	14.22
4.96	7.6424	25.94	30.56	21.82	21.49	19.7	19.25	18.82	19.88	20.08	21.12	20.1	19.79	16	14.3	2.92	2.01	1.09	15.94	14.78
4.902	7.7391	26.24	31.11	21.63	21.15	19.19	18.53	18.27	19.54	19.9	20.97	19.99	19.54	16	14.3	2.92	3.05	1.66	15.8	14.43
4.743	7.759	26.41	31.21	19.62	19.53	17.89	17.17	16.49	17.6	18.63	19.39	19.95	19.16	16	14.3	2.92	4.55	2.5	14.92	13.49
4.659	7.6814	26.36	30.72	18.81	18.67	17.22	16.43	16.22	17.28	17.6	17.83	18.06	17.65	16	11.7	2.42	0	0	14.3	13.1
4.697	7.7447	26.57	31.06	19.26	18.77	17.11	16.36	16.11	17.41	18.04	18.49	18.13	17.63	16	11.7	2.42	1.99	1.1	14.44	13.13
4.722	7.7689	26.73	31.21	19.03	18.93	17.41	16.52	16.04	17.17	17.59	17.89	18.08	17.7	16	11.7	2.42	2.99	1.66	14.74	13.35
4.755	7.798	26.95	31.28	19.06	18.58	16.88	16.09	15.97	17.29	17.88	18.36	17.85	17.47	16	11.7	2.42	3.98	2.23	14.9	13.38
4.948	7.8444	27.59	31.53	19.27	18.64	17.24	16.34	16.29	17.59	18.43	19.51	18.89	18.43	16	11.7	2.42	5.87	3.38	16.25	14.33
3.545	7.0785	25.79	27.91	8.652	8.803	7.395	7.083	6.464	7.224	7.256	8.054	7.853	7.902	16	9.3	1.89	0	0	5.953	4.603

3.563	7.0866	25.9	27.98	8.573	8.707	7.258	6.998	6.478	7.23	7.256	8.063	7.78	7.821	16	9.3	1.89	2.16	1.14	6.047	4.632
3.658	7.1637	26.23	28.34	8.613	8.941	7.608	7.589	7.045	7.551	7.36	8.07	7.837	8.022	16	9.3	1.89	4.02	2.21	6.688	5.314
3.585	7.1552	26.21	28.19	7.07	7.277	5.957	5.985	5.527	6.131	6.2	6.84	6.445	6.659	16	9.3	1.89	6	3.37	6.065	4.083
3.484	7.1247	26.12	27.81	5.47	5.55	4.306	4.256	3.973	4.607	5.097	5.655	6.009	5.728	16	9.3	1.89	7.46	4.14	5.246	2.596